To the Graduate Council:

I am submitting herewith a dissertation written by Kyu Jeong Song entitled "Superconducting Study of the Intermetallic YNi_2B_2C Single Crystal and Several High-T_c Materials." I have examined the final copy of this dissertation for form and content and recommend that it be accepted in partial fulfillment of the requirements for the degree of Doctor of Philosophy, with a major in Physics.

James R. Thompson, Major Professor

We have read this dissertation

and recommend its acceptance:

Accepted for the Council:

Associate Vice Chancellor

and Dean of The Graduate School

Superconducting Study of the Intermetallic YNi_2B_2C Single Crystal and Several High-T_c Materials

A Dissertation

Presented for

the Doctor of Philosophy

Degree

The University of Tennessee, Knoxville

Kyu Jeong Song

August 1999

To

My family

ACKNOWLEDGMENTS

I would like to express my sincere appreciation to my advisor, Professor James R. Thompson, for his excellent guidance, invaluable help, and enormous encouragement throughout the research of this thesis. I would also like to express my deepest gratitude to Dr. David K. Christen for his help and encouragement. In addition, I am indebted to Dr. D. G. Mandrus, who performed the heat capacity experiments, and to Mr. S. K. Kang, who helped the electrical resistivity measurements.

My appreciation also goes to my other committee members, Prof. T. A. Callcott, Prof. M. Breinig, and Prof. A. J. Pedraza for their careful review of this thesis and useful suggestions. I would like to thank to my colleges: Dr. H. R. Kerchner, Dr. J. G. Ossandon, Dr. M. Yethiraj, Dr. H. R. Khan, Dr. Q. He, Dr. D. T. Verebelyi, Dr. M. Paranthaman, Dr. C. Park, and Mrs. N. F. Delene.

I wish to give special thanks to my wife, Hayoung, my son, Seongwoo, my daughter, Dain, my father, the late Mr. W. S. Song, my mother, Mrs. J. R. Choi, my parent-in-law, and my sisters and brother, for their unending support, patience, and understanding of my educational endeavors throughout the years.

I would like to acknowledge the financial support of the Solid State Division of the Oak Ridge National Laboratory, operated by Lockheed Martin Energy Research Corp. for United State Department of Energy.

ABSTRACT

Magnetization studies on a single crystal of YNi_2B_2C superconductor have revealed significant effects of nonlocality in the superconductive state and have displayed a significant angular variation in normal state. The 17 mg crystal was studied at temperatures T from above T_c (15 K) to 2 ~ 3 K, in magnetic fields H applied parallel and perpendicular to the (001)-crystal axis, within magnetic fields from zero to $H > H_{c2}$, the upper critical field. The material exhibited little magnetic irreversibility, with a critical current density ~ $10^{-4} \times J_o$, the depairing current density. This nearly reversible behavior has allowed an analysis of its equilibrium properties: the thermodynamic critical field $H_c(T)$, $H_{c2}(T)$, and the magnetization $M(H,T)$ in both the normal and superconductive states. Near T_c, the equilibrium magnetization M of the clean single crystal of YNi_2B_2C was standard London-like with $M \propto \ln(H)$. Well below T_c, however, M is shown to deviate significantly from this simple "local" London predictions, but the behavior is well described by "non-local" London theory, which is a more general theory derived by Kogan et al. [Phys. Rev. B **54**, 12386 (1996)]. The non-local analysis yields reasonable values for the nonlocality radius ρ and London penetration depth λ. The T dependence of λ was obtained from both non-local London analysis at low temperatures and a standard local-London analysis near T_c. Contrary to the exponential dependence expected for simple *s*-wave pairing, the nearly T^3 behavior for $\lambda(T)$ below 10 K seems to give evidence for a more complex, perhaps non-*s*-wave pairing scheme. In addition, the normal state magnetic susceptibility was measured

in the temperature regime between 16 K and 295 K in an applied field of 10 kG, for the magnetic field applied parallel or perpendicular to the crystalline (001)-direction. The material exhibited a large anisotropy between the two field orientations, particulary in the low temperature regime. Furthermore, according to heat capacity studies of YNi_2B_2C, the material appears to deviate from both weak- and strong-coupling superconductive mechanisms, but agrees relatively well with predictions [$C_{e,\,super} \propto t^3$] of a medium-coupling formalism. From magnetization and heat capacity studies, the deduced values of the Ginzburg-Landau parameters κ_1 and κ_2 increase considerably as T decreases. This is consistent with the material's long electronic mean free path and the observation of non-local electrodynamics.

Several features of high temperature superconductors were investigated in complementary work. In studies of the effects of adding elemental Ag to high T_c superconducting $HgBa_2CuO_{4+\delta}$ materials, a series of polycrystalline $Ag_xHgBa_2CuO_{4+\delta}$ materials (with molar fraction x = 0, 0.05, 0.1, 0.3, and 0.5) were investigated. The processing with Ag at elevated temperatures led to changes in superconducting properties. These are consistently interpreted in terms of the superconducting hole density, calculated from the London penetration depth λ by analysis of the equilibrium magnetization M using standard London theory. The irreversible magnetic properties of these materials are dominated by surface barrier effects and are well described in terms of thermally activated tunneling of pancake vortices through a surface barrier.

For practical applications, vortex pinning in high-T_c superconducting (HTS) materials is very important. To pin vortices strongly, splayed columnar tracks produced

using a fission process, induced by high energy (GeV) proton irradiation, have been formed in several HTS materials. Overall, the magnetic hysteresis ΔM ($\propto J$) of the materials is greatly increased by the splayed columnar defects. The hysteresis or persistent current density first increases with increasing the proton fluence Φ_p, then passes through an optimal proton fluence, and finally decreases at much higher Φ_p. In contrast with ΔM ($\propto J$) that is enhanced significantly by the columnar defects, the superconducting transition temperature T_c is suppressed somewhat, with a material-dependent rate. By analyzing the decay rate of J with a time in a Maley analysis, the effective pinning energy $U(J)$ was obtained with both irradiated and unirradiated materials. The net pinning potential barrier of vortices is clearly enhanced by the splayed columnar tracks, from 0.8 GeV proton irradiation. In general, these splayed columnar defects lead to significant enhancements in the vortex pinning effect within the HTS materials investigated.

CONTENTS

CHAPTER **PAGE**

1. INTRODUCTION 1

2. THE SUPERCONDUCTING AND MAGNETIC PROPERTIES OF YNi_2B_2C SINGLE CRYSTAL 6

2.1 Experimental Aspects 7

2.2 Experimental and Theoretical Background 11

2.2.1 SQUID-based Magnetometer System 11

2.2.2 Small Angle Neutron Scattering (SANS) Experiment 23

2.2.3 Thermodynamic Properties for Reversible Superconductors 25

2.2.4 From London to Ginzburg-Landau Theory 30

2.2.5 Kogan's Standard Local and Non-local London Formalisms 41

2.3 Experimental Results and Analysis 51

2.3.1 Magnetization studies in the Superconducting State 51

2.3.2 Magnetic Susceptibility, Magnetization, and Electrical Resistivity in Normal State 70

2.3.3 Heat Capacity for Normal and Superconducting state 76

2.3.4 Thermodynamic Critical Field H_c 85

2.3.5 Lower Critical Field H_{c1} 90

2.3.6 Upper Critical Field H_{c2} 94

2.3.7 Ginzburg-Landau Parameter κ

- Beyond the Constant-κ Approximation 99

2.4 Summary 102

3. THE MIXED STATE PROPERTIES OF HIGH-T_C SUPERCONDUCTORS 105

3.1 The Influence of Ag-Additions to $HgBa_2CuO_{4+\delta}$ Materials 107

3.1.1 Experimental Aspects 107

3.1.2 Experimental Results and Analysis 110

3.2 The Effects of Artificially Created Defects by Irradiation Methods: Splayed Columnar Effects in Several HTS materials 124

3.2.1 Experimental Aspects 124

3.2.2 Experimental and Theoretical Background 128

3.2.2.1 The Formation of Defects in HTS Materials by Particle Irradiation 128

3.2.2.2 Bean Critical State Model 133

3.2.2.3 The Measurement of Magnetic Relaxation 138

3.2.2.4 From Classical Anderson-Kim to Collective Flux Creep Theory .. 141

3.2.3 Experimental Results and Analysis 148

3.3 Summary 163

4. CONCLUSIONS 166

REFERENCES and BIBLIOGRAPHY 169

APPENDICES 184

Appendix 1. The calculation of mass density of YNi_2B_2C 185

Appendix 2. Useful BCS relationships 186

Appendix 3. The calculation of the mass of free Ag in $Ag_xHgBa_2CuO_{4+\delta}$ and the volume of $Ag_xHgBa_2CuO_{4+\delta}$ superconductor 188

Appendix 4. The calculation of the critical current density J_c of a spherical superconductor of radius R by Bean critical state model 189

Appendix 5. Published papers and presentations in these works 192

VITA 196

List of Tables

2.3.5-1 The comparison of superconductive mass anisotropy for YNi_2B_2C: $\gamma = \sqrt{m_c/m_{ab}} = \lambda_c/\lambda_{ab} = \xi_{ab}/\xi_c = H_{c2\text{-}ab} / H_{c2\text{-}c}$. 92

List of Figures

2-1 The structure of YNi_2B_2C. 8

2-2 The system components of the SQUID magnetometer of Quantum Design's MPMS-7. 12

2-3 The functional control diagram of the SQUID magnetometer of Quantum Design's MPMS-7. 13

2-4 The MPMS temperature control module. 15

2-5 The MPMS gas control system. 16

2-6 The MPMS transverse SQUID system; inset: the detector array for longitudinal system. 19

2-7 The configuration and location of the pick up coils. 20

2-8 (a) The plot of critical field, H_c, as a function of the temperature. (b) The magnetization M of a type-I superconductors versus magnetizing field H: the figure pertains to a long specimen with field applied parallel to the long axis (zero demagnetizing factor). At critical field H_c, the sample reverts to the normal state. 27

2-9 Parameter γ versus reduced temperature t which determines the temperature

dependence of nonlocality radius ρ for the scattering parameter (impurity parameter) $\xi_2/l = 0$ (the upper curve), 0.2, 0.5, 1, 2, and 10 (the bottom curve). . 48

2-10 ZFC and FC magnetization curves as the function of temperature, for YNi_2B_2C. ..55

2-11 The magnetization M of YNi_2B_2C versus H (a) at $T = 3$ K and (b) $T = 5$ K, for magnetic field H applied parallel to c-axis (001). 56

2-12 A semilogarithmic plot of equilibrium magnetization M_{eq} versus H, for temperatures from 14 K to 3 K. The local London theory, equation (2.3.1-1), predicts the linear dependence seen at higher temperature (above 10 K). The nonlocal London theory, equation (2.3.1-2), describes the data well at lower temperature. 57

2-13 A semilogarithmic plot of equilibrium magnetization M_{eq} versus H at several temperatures. The solid lines show the nonlocal London theory fitted to the data, with parameters M_o, H_o, and ζ. 59

2-14 Parameters from non-local London analysis versus temperature T: (a) the field scale $H_o \sim \phi_o/\rho^2$ and product $\gamma(T)H_o(T) \sim \phi_o/\xi_o^2$, (b) the magnetization $M_o \sim \phi_o/32\pi^2\lambda^2$, and (c) dimensionless quantity ζ. 60

2-15 The London penetration depth λ, obtained with field $H \parallel$ (001)-axis; (a) open squares came from magnetization analysis, standard London near T_c and nonlocal London far below T_c (below 10 K), dotted line from empirical function $(1-t^{3/2})$, cross circles from neutron scattering intensity, and straight solid line is Ginzburg-Landau dependence near T_c. (b) $[\lambda(0)/\lambda(T)]^2$ versus $t = T/T_c$, with several theoretical lines. 62

2-16 (a) The plots of $S = dM/d\ln H$, as the function of the field H.
(b) The temperature dependence of dS/dH. 64
2-17 Temperature dependence of the irreversibility field, H_{irr}, for the field H parallel to (open squares) and perpendicular to (open triangles) (001)-axis. Solid and dot lines are fits to the function $H_{irr}(T) = H_{irr}(0)(1-T/T_c)^n$. 65
2-18 (a) Isothermal *dc*-magnetization M versus field H for $H \parallel c$-axis at $T = 5$ K. Inset indicates the "anomalous peak effect" in an expanded scale. The open squares and circles denote values for increasing and decreasing field history. (b) Semilogarithmic plot of the critical density J_c versus field H at several temperatures. 67
2-19 H versus T phase diagram in the high field region, from *dc*-magnetization measurement with field H parallel to c-axis. 69
2-20 Susceptibility ($\chi = M/H$) versus temperature T measured in magnetic field H = 10 kG, parallel and perpendicular to (001)-direction. The inset shows the temperature dependence of $1/\chi$, where lines are linear curves above $T = 200$ K. 71
2-21 Susceptibility (χ) versus $1/T$, for both field directions. 73
2-22 The magnetization M versus magnetic field H at several temperatures (above T_c) for fields applied parallel to or perpendicular to (001)-direction. 74
2-23 The electrical resistivity ρ versus temperature T, for YNi_2B_2C. 77
2-24 C_p/T versus T^2 in the temperature regime 2 K to 30 K for normal state (with $H = 70$ kG) and superconducting state with zero magnetic field. 78
2-25 The electronic heat capacity C_{es} versus T in superconducting state with

$H = 0$. The inset shows the t^3-dependence of C_{es}, where $t = T/T_c$. 80

2-26 A plot of entropy S as a function of temperature T for both normal and superconducting states. 83

2-27 A plot of free energy F as the function of temperature T for both normal and superconducting states. 84

2-28 The temperature dependence of thermodynamic critical field H_c. The fitting curve is given by $H_c(T) = H_c(0)[1-(T/T_c)^2]$, according to heat capacity results, where H_c is about 2556 G, and T_c = 14.5 K. Open circles results from heat capacity study, and close squares come from the magnetization analysis. 86

2-29 A plot of the deviation function $D(t)$ as the function of $t = T/T_c$. 88

2-30 The magnetization M versus field H with the applied field parallel to c-axis in an expanded low field region. The inset shows $(\Delta M)^{1/2}$ versus H, which indicate the deviation point from linearity. 91

2-31 The temperature dependence of H_{c1} for both field directions. The smooth curves are given by $H_{c1} = H_{c1}(0)[1-(T/T_c)^2]$. 93

2-32 Plots of equilibrium magnetization M as a function of temperature T (a) in the reversible region and (b) in the limited scale up to $4\pi M$ = -10 G. 95

2-33 The temperature dependence of H_{c2} using several analytic methods. 96

2-34 Plots of (a) M_{eq} vs. H and (b) M_{eq} vs. ln(H) at several temperatures. 98

2-35 The temperature dependence of Ginzburg-Landau parameters κ_i. 101

3-1 The structure of Hg-1201 in the unit cell. 108

3-2 Field cooled magnetization M versus temperature T in an applied

field H = 4 G. 111

3-3 (a) T_c versus x (Ag-mole fraction) and (b) J_c versus x (Ag-mole fraction) at T = 10 and 30 K for H = 1 T. 113

3-4 Zero field cooled magnetization M versus temperature T in an applied field H = 4 G. 114

3-5 The magnetization M versus magnetic field H, for polycrystalline $Ag_xHgBa_2CuO_{4+\delta}$ superconductor with x = 0.05. Inset in (b) shows a semilogarithmic plot of M versus H. 115

3-6 Plots of $1/\lambda^2$ as a function of temperature T, for polycrystalline Ag_xHg-1201 materials. The intersections at $[1/\lambda^2] = 0$ show T_c, which are very similar to the values measured in low fields (Field Cooled measurement). 117

3-7 T_c of the materials versus hole density p, deduced from the London penetration depth using effective mass ratio $(m^*/m_e) = 1.07$. The solid line shows the general relation, Eq. (3.1.2-3), with $T_{c,max}$ = 96 K. 119

3-8 Semilogarithmic plot of the penetration field H_p versus T. 121

3-9 Semilogarithmic plot of the magnetic hysteresis ΔM, measured in different magnetic fields, versus T. 123

3-10 A schematic magnetic phase diagram for type-II, high T_c superconductors. 125

3-11 General behavior of the damage efficiency as observed in magnetic insulators. In the upper part of the figure, the evolution of the damage efficiency versus (dE/dx) is shown. 130

3-12 The formation of splayed columnar defects by the fission process. 132

3-13 TEM of 0.8 GeV proton-induced splayed columnar defects in Bi-2212. 134

3-14 The Bean critical state model. 135

3-15 The hysteresis loop ($M(H)$ curve) and profiles for a slab of thickness r. 137

3-16 The procedure for measurement of magnetic relaxation. 140

3-17 The schematic diagram about the collective pinning. 145

3-18 Magnetization M versus field H for both virgin and irradiation samples. 150

3-19 The persistent current density $J = (15 \times \Delta M)/r$ versus (a) the magnetic field H and (b) the temperature, for both virgin and irradiated samples. 152

3-20 The current density J versus proton fluence Φ_p. Results are for Hg-1223 polycrystalline HTS with $H = 1$ T. 154

3-21 The dependence of T_c on the fluence of 0.8 GeV protons, for several cuprate HTS materials. 155

3-22 The irreversibility field H_{irr} versus $(1-T/T_c)$, where H_{irr} is defined by $J_{criterion} = 10^3$ A/cm^2. 156

3-23 The flux creep rate S versus temperature T for Bi-2212/Ag tapes, both virgin and proton-irradiated with 4.7 x 10^{16} p/cm^2. 158

3-24 The pinning potential energy U versus current density J in both increasing and decreasing field history for magnetic field $H = 1$ T. 161

3-25 The log plots of $U_{eff}/g(T)$ versus J in both increasing and decreasing field regions for magnetic field $H = 1$ T, where $g(T) = [1-(T/T_c)^2]^m$ with $T_c =$ 135 K, $m = 0.4$(inc.), 0.8(dec.) for unirradiated sample, and $m = 0.8$(inc.), 1.0(dec.) for irradiated sample. 162

List of Symbols and Abbreviations

ac	Alternating Current
B	magnetic flux density / magnetic induction
BCS	Bardeen-Cooper-Schrieffer
CEF	Crystalline Electric Field
C_p	heat capacity
D	demagnetizing factor
dc	Direct Current
$D(t)$	Deviation function
E	Energy / Electric field
emu	electromagnetic unit
F	free energy
FC	Field Cool
FFLO	Fulde-Ferrell-Lakin-Ovchininikov
F_L	Lorenz force
FLL	Flux Line Lattice
F_{pin}	pinning force
$F(q_{hk})$	magnetic form factor
G	Gibbs free energy
GL	Ginzburg-Landau

GPIB	General Purpose Interface Bus
H	magnetic field
H_c	thermodynamic critical field
H_{c1}	lower critical field
H_{c2}	upper critical field
H_{irr}	irreversibility field
H_p	penetration field
HP	Hewlett Packard
HTS	High-T_c Superconductivity / Superconductor / Superconducting
IBAD	Ion-Beam-Assisted Deposition
I_{hk}	the intensity of scattered neutrons
J_c	critical current density
J_o	depairing current density
J_s	supercurrent density
ℓ	electronic mean free path
LAMPF	Los Alamos Meson Production Facility
LTS	Low-T_c Superconductor
m	magnetic moment
M	Magnetization
M_{eq}	equilibrium Magnetization
M_{irr}	irreversible Magnetization
MPMS	Magnetic Property Measurement System

n_s	the number of superconducting electrons
ORNL	Oak Ridge National Laboratory
P	Power
PC	Personal Computer
PIT	Powder-In-Tube
PPMS	Physical Properties Measurement System
RABiTS™	Rolling-Assisted Biaxially Textured Substrates
rf	radio frequency
S	entropy / normalized creep rate
SANS	Small Angle Neutron Scattering
SQUID	Superconducting QUantum Interference Device
T	Temperature
t	reduced temperature / time
t_o	the fundamental time scale for vortex oscillations
T_c	critical temperature / transition temperature
T_o	characteristic temperature
U	activation energy / effective pinning energy
WHH	Werthamer-Helfand-Hohenberg
WNR	Weapons Neutron Research
YSZ	Yttria-Stabilized Zirconia
ZFC	Zero Field Cool
κ	Ginzburg-Landau parameter

ξ	coherence length
λ	London penetration depth
ϕ_o	quantized flux line = ch/2e = 2.07×10^{-7} G·cm^2
$\Psi(r)$	the order parameter
$\Delta(0)$	superconducting energy gap
Φ_p	proton fluence
ρ	nonlocality radius / electrical resistivity
γ	impurity scattering / the coefficient of the electronic heat capacity (Sommerfeld parameter) / superconductive mass anisotropy
χ	magnetic susceptibility
χ^{Pauli}	Pauli spin susceptibility
AgHg-1201	$Ag_xHgBa_2CuO_{4+\delta}$
Bi-2212	$Bi_2Sr_2CaCu_2O_8$
Hg-1201	$HgBa_2CuO_{4+\delta}$
Hg-1223	$HgBa_2Ca_2Cu_3O_9$
Tl-1223	$TlBa_2Ca_2Cu_3O_9$
Tl-2212	$Tl_2Ba_2CaCu_2O_{8+\delta}$
(TlBi)-1223	$(Tl_{0.8}Bi_{0.2})Ba_2Ca_2Cu_3O_{9+\delta}$
(TlPb)(SrBa)-1223	$(TlPb)(SrBa)_2Ca_2Cu_3O_{9+\delta}$
Y-123	$YBa_2Cu_3O_{7-\delta}$
YNBC	YNi_2B_2C

CHAPTER 1

INTRODUCTION

In 1908, H. Kamerlingh-Onnes first liquified helium and then discovered the phenomenon of superconductivity just three years later, in 1911.[1] A superconductor has an important property, which is Meissner effect. The Meissner effect, a spontaneous expulsion of magnetic flux upon cooling through the superconductive transition temperature T_c, was found by Meissner and Ochsenfeld in 1933.[2] It required, however, a long time to understand clearly the microscopic mechanism of superconductivity. The first theoretical explanation of the magnetic properties of superconductors was given in 1935 by F. London and H. London.[3] After that, in 1950, L. D. Landau and V. L. Ginzburg suggested a more general theory of superconductivity.[4] At last, the microscopic mechanism of the phenomenon of superconductivity, so-called BCS theory, was discovered in 1957 by J. Bardeen, L. Cooper, and J. R. Schrieffer.[5] The mechanism of BCS theory itself is often called Cooper pairing.[6]

Following Kamerlingh-Onnes' discovery of superconductivity in metallic mercury, more than 20 metallic elements were found to be superconductive. Subsequently, various

alloys including ordered binary, ternary, and intermetallic compounds played a key role in increasing the superconducting transition temperature up to about 20 K by the middle of the 20th century. In 1973, a record high-T_c of 23.3 K was found in the compound Nb_3Ge.[7,8] Many years then passed with no further increase in the superconducting transition temperature. At last, in 1986 J. G. Bednorz and K. A. Müller first discovered superconductivity in a layered perovskite material, $(La\text{-}Ba)_2CuO_4$, which had an astonishingly high T_c, above 30 K.[9] For this remarkable discovery, Bednorz and Müller received the 1987 Nobel Prize in Physics. This marked the discovery of new classes of so-called high temperature superconducting (HTS) materials. Finally, the dream of superconductivity at the temperature of liquid-nitrogen (77 K) came very quickly. Like an explosion, several series of cuprate materials were quickly discovered: a Y-based family with T_c up to 90 K, Bi-based family with T_c up to 110 K, Tl-based family with T_c up to 125 K, and Hg-based family with T_c up to 133 K.[10-15] At the time, science appeared to be on the threshold of a technological revolution and the discovery of room temperature superconducting materials before the 21st century. However, contrary to our expectation, a dozen years have passed since the discovery of high-T_c superconductivity, with no technological revolution to date.

Having materials that superconduct at remarkably high temperatures, it was thought somewhat naively that practical applications of the new materials would be easily developed. However, many obstacles soon became apparent. First, applications such as superconducting wires, magnets, and so on are hindered by the fact that the high-T_c superconductors are ceramics, which are brittle and not flexible. Second, the high-T_c

superconductors have highly anisotropic properties; in polycrystalline materials, the current flow across grain boundaries is quite poor (the "weak link" problem); in the presence of a large magnetic field, which is necessary for many applications, the movement of flux lines ("giant flux creep") generates heat and makes current conduction to be dissipative; and so on. Since discovery of high-T_c materials, many scientists have expended great effort to overcome these challenges. Therefore, it seems that these innovative HTS materials have enormous potential for new technological applications in the near future. Surely, their future seems bright at the beginning of the 21st century.

As mentioned, all of the high-T_c superconducting materials are ceramics, cupric oxides. In one approach, many scientists tried to solve the ceramic problem by growing HTS layers on some substrate or backing. High-T_c superconducting wires were made by a powder-in-tube (PIT) technique;[16] films were prepared by various deposition methods; flexible tapes were formed by ion beam-assisted deposition (IBAD)[17-19] and the recently developed Rolling-Assisted Biaxially Textured Substrate (RABiTS™) technique.[20,21] Second, other material scientists have searched for new classes of more metallic superconductors possessing greater flexibility. Recently in early 1994, the intermetallic borocarbide family (RNi_2B_2C, where R = rare earth, Y, and so on) was discovered by many research groups.[22-26] This new class of intermetallic RNi_2B_2C superconductors has held a great attention during recent years because of very interesting physical properties, such as the coexistence of magnetism and superconductivity,[27-31] phase transitions in the lattice of magnetic flux lines, e.g., changing from a simple hexagonal vortex array to a square array,[31-35] and their modestly high transition temperatures, comparable with well-studied A-15

structure materials. Though these new materials were first thought to be similar to conventional low-T_c superconductors (LTS), they have some unconventional properties. Therefore, the nickel borocarbide family may provide a connecting line between conventional low-T_c superconductors and unconventional high-T_c materials.

From a basic perspective, there are two kinds of superconductors, known as type-I and type-II according to their responses to magnetic field. The type-I superconductors exclude magnetic field up to a critical field (H_c), which destroys superconductivity. For type-II superconductors, there are two additional critical fields, the lower critical field H_{c1} and the upper critical field H_{c2}. The relation between H_c and H_{c1} (and H_{c2}) is more complicated. The Meissner state with flux density $B = 0$ exists only below H_{c1}. When the applied field exceeds H_{c1}, flux starts to penetrate into the material in the form of quantized flux lines called vortices (each with flux $\phi_0 = ch/2e = 2.07 \times 10^{-7}$ G·cm^2). Finally the material reverts to the normal state at field H_{c2}. The field regime between H_{c1} and H_{c2} is called the mixed state or vortex state. Several structural phases have been identified, including the vortex liquid, vortex glass, and vortex solid; these have differing dynamic behaviors.[36] The mixed state plays a key role in practical applications of HTS materials, for the mixed state covers a very large part of the magnetic phase diagram, and the H_{c2} is much larger (and the coherence length is much shorter) than those in conventional low-T_c superconductors. As noted, the HTS materials suffer from highly anisotropic properties, weak link current flow, and giant flux creep (magnetic relaxation) in the mixed state. To overcome giant flux creep and weak current density (J_c) in the mixed state, many scientists have studied vortex pinning effects of HTS materials. Fortunately, vortices can be "pinned"

in the mixed state by intrinsic or extrinsic imperfections (defects) that prevent movement of vortex. In 1991, L. Civale et al. showed that introducing columnar defects, formed by heavy-ion irradiation, greatly increase the critical current density J_c in single crystals of $YBa_2Cu_3O_7$.[37] In other words, parallel columnar defects produce strong vortex pinning and reduce the decay rate of magnetization. More recently, T. Hwa et al. suggested that splayed (slightly dispersed in angle) columnar defects should create even stronger pinning effects than those of simple parallel columnar defects.[38] Therefore, Krusin-Elbaum et al. devised a mechanism to produce splayed columnar defects using a fission process, in which heavy constituent nuclei inside a material were induced to fission by high energy (GeV) proton irradiation. They found remarkable increases in the critical current density J_c and decreases in the decay rate of magnetic relaxation, due to strong vortex pinning.[39,40] The key point for useful applications lies in creating means to pin the vortices against dissipative motion, due to a current flow in a magnetic field. This is a necessary condition for many practical applications to emerge.

The present study is directed in part to understanding the superconducting properties of the new class of intermetallic Ni-borocarbides. Chapter 2 deals with the physical, thermodynamic, and superconducting properties of these materials and with some theoretical background for understanding them. The second major topic deals with strong vortex pinning. Thus, Chapter 3 presents the pinning effects due to artificially created defects, such as simple parallel columnar tracks and splayed columnar tracks, and describes some flux creep models as well. Chapter 4 contains the conclusions of this work.

CHAPTER 2

THE SUPERCONDUCTING AND MAGNETIC PROPERTIES OF YNi_2B_2C SINGLE CRYSTAL

In this era of high-T_c superconductors, a new class of perhaps more conventional intermetallic borocarbide materials has been discovered,[22-26] with transition temperatures in the range of 7 K - 20 K. The nickel-borocarbide superconductors are proving to be a rich and complex system of materials. In the past few years, these materials have received great attention from many scientists, because they show so many remarkably interesting physical phenomena. For example, they display a coexistence of magnetism and superconductivity,[27-31] the vortex lattice changes from simple hexagonal to square symmetry,[31-35] and the transition temperatures are comparable with the well studied A-15 compounds. In general, the superconducting parameters of YNi_2B_2C single crystal are not

easily determined magnetically because of the paramagnetic properties of normal state. In addition, the "clean" single crystal of YNi_2B_2C studied here shows deviations from simple standard London formalism,[41] which provides important evidence for more complex superconductivity. There are still many physical properties, that are not fully understood in the $\boldsymbol{R}Ni_2B_2C$ family (where $\boldsymbol{R}$ represents any rare earth ion and Y).

2.1 Experimental Aspects

The recently discovered superconductor YNi_2B_2C is one member in the series of several new intermetallic borocarbide superconductors.[22-24] The single crystal of YNi_2B_2C was grown by a high temperature flux method using Ni_2B flux with isotopic ^{11}B to reduce neutron absorption (in small angle scattering studies). The 17 mg single crystal whose dimensions are $0.29 \times 0.23 \times 0.06$ cm^3 had a mosaic spread of less than 0.2°, as determined by neutron diffraction.[33] The structure of YNi_2B_2C was determined by Siegrist et al.[24] and is shown in Figure 2-1. These intermetallic borocarbides have a layered crystal structure, but they do not contain superconductive CuO_2 layers as with all of the high-T_c superconducting cuprates. In the structure of $\boldsymbol{R}Ni_2B_2C$, Ni_2B_2 layers alternate with $\boldsymbol{R}C$ layers, repeating along the crystallographic c-axis. These new type quaternary $\boldsymbol{R}Ni_2B_2C$ (where $\boldsymbol{R}$ = rare earth and Y) compounds build up in the well known tetragonal $ThCr_2Si_2$-type structure and belong to the space group I4/mmm.[23,24,30]

Small Angle Neutron Scattering (SANS) has become a very useful method for

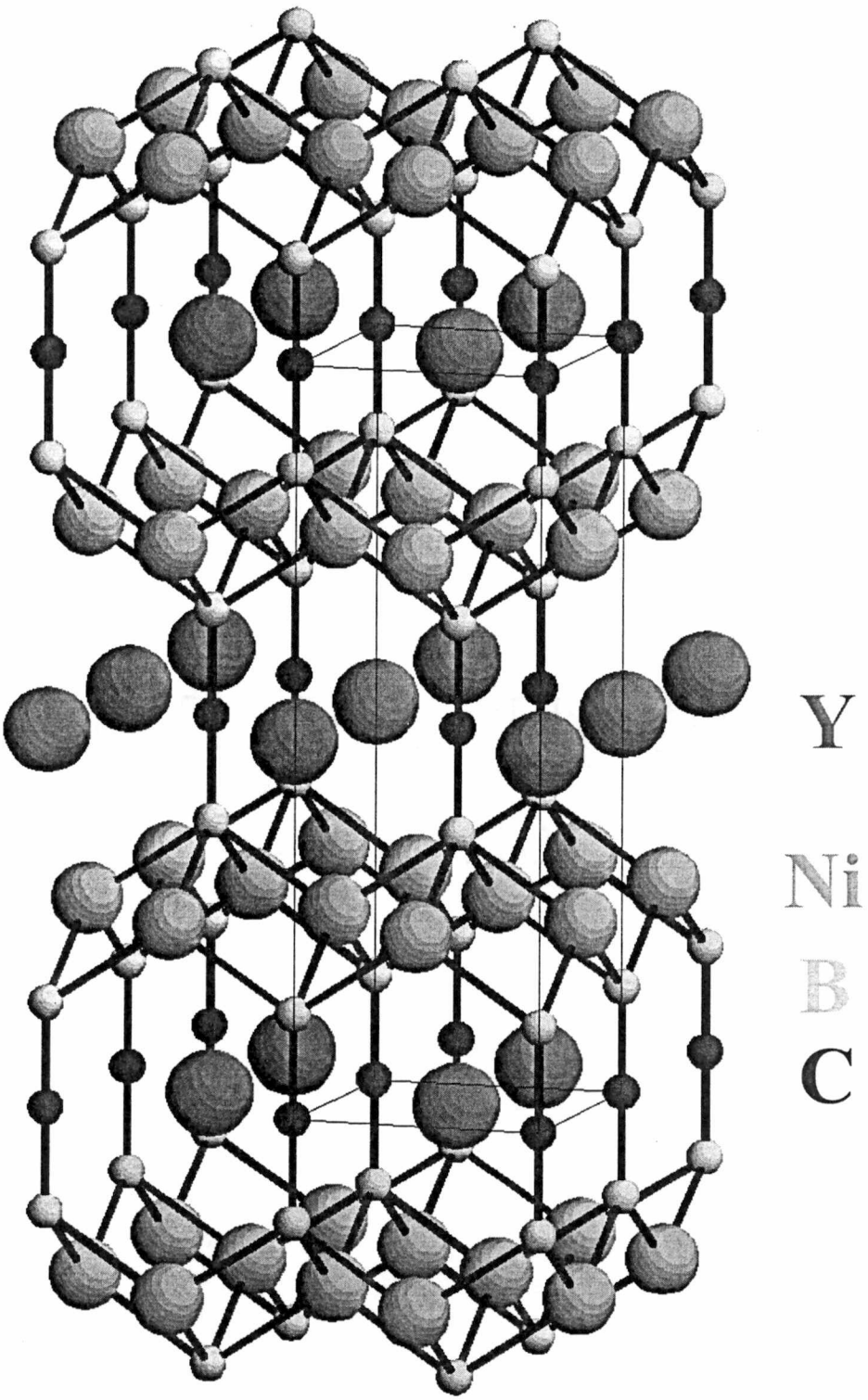


Figure 2-1. The structure of YNi_2B_2C. B.C.Chakoumakos and M. Paranthaman, Physica C **227**,143 (1994)

investigating the vortex structures in the superconducting mixed state. Overall, isotropic superconductors have a simply hexagonal flux line lattice (FLL) with vortices forming equilateral triangles. Neutron scattering studies have shown, however, that the FLL in borocarbides is more complex: the symmetry changes from simply hexagonal to square form, even for YNi_2B_2C that contains no magnetic rare earth ions.[33-35,42] The FLL is nearly hexagonal in low fields H where vortices are far apart. As the magnetic field increases to modest field levels, the FLL becomes rhombohedral and appears to undergo a first order structure transition. At still higher fields, the lattice becomes square. This seemingly strange behavior has been explained in terms of non-local London theory (as discussed below)[43] or generalized Ginzburg-Landau theory.[44] If the superconductivity in "clean" YNi_2B_2C is indeed non-local, then its equilibrium mixed state properties should be modified significantly. Recently, K. J. Song et al. have shown that the equilibrium magnetization of the single crystal of YNi_2B_2C deviates significantly from simple London predictions, and it is well described by a non-local generalization of London theory.[41]

Magnetic studies were conducted in a SQUID (Superconducting QUantum Interference Device)-based magnetometer (Quantum Design model MPMS-7). Generally the sample for study was glued onto a thin Si-disk using a *Duco* cement and mounted in a *Mylar* tube for measurement. The equilibrium magnetization M of the single crystal of YNi_2B_2C superconductor has been studied with magnetic field H parallel and perpendicular to c-axis. Prior to studies in low magnetic fields, the superconducting magnet in the magnetometer was "reset" to release trapped flux in its windings, by heating it above its T_c. The Meissner state magnetic moment m was measured under zero-field-cooled (ZFC) and

field-cooled (FC) conditions in an applied field H = 10 G. In all case, the magnetization M[G] = m[G·cm^3] / V[cm^3] was based on the volume V, using the theoretical mass density $\rho_{X\text{-}ray}$ = 6.05 gm/cm^3, which was calculated from the lattice parameters (Appendix 1).[23,24]

These magnetization studies have been carried out in order to understand the superconducting properties of YNi_2B_2C and its magnetic field-temperature (H vs. T) phase diagram. The following topics are discussed. First, the reversible magnetization of the single crystal of YNi_2B_2C are analyzed, for field orientation H parallel and perpendicular to (001)-direction, using the theoretical formalisms of standard simple London-limit[45] near T_c and the non-local London theory of V. G. Kogan et al.[46] at low temperature. Here, the temperature dependence of the penetration depth, λ, is discussed. In addition, the upper critical field, H_{c2}, is treated as well. Second, the normal state magnetic properties, primarily paramagnetism due to paramagnetic Ni^{2+} ions, have been investigated for both field directions. Third, the thermodynamic critical field of the superconductor, H_c, is established from the magnetic study. This is possible, since the superconducting state magnetization in this material is remarkably reversible magnetically. For comparison with this thermodynamic analysis, the heat capacity of the YNi_2B_2C single crystal has been investigated as well, using a Physical Properties Measurement System (Quantum Design PPMS). Fourth, the lower critical field, H_{c1}, is established by determining the field at which the magnetization first deviates from initial linearity, which field H parallel and perpendicular to (001)-direction. Finally, the dimensionless Ginzburg-Landau parameter κ for YNi_2B_2C single crystal will be discussed. In addition, we go beyond the constant-κ approximation and investigate the temperature dependence of the more detailed parameters κ_1, κ_2, and κ_3,

according to K. Maki theory.[47]

These topics are discussed in detail to Section 2.3 "Experimental results and discussions." Before discussing explicit results, however, the magnetic measurement system is described in following section. Next, the principle of SANS (small angle neutron scattering) will be introduced, since neutron scattering experimental results are playing a key role in understanding the vortex physics in these borocarbide families. However, SANS experiments were not performed directly in this work. Following that, some theoretical background will be presented: the thermodynamic properties of reversible superconductors, the London theory,[3,48,49] the Ginzburg-Landau theory,[4,49] and Kogan's standard simple local limit and non-local London formalisms.[45,46,50]

2.2 Experimental and Theoretical Background

2.2.1 SQUID-based Magnetometer System

Quantum Design's Magnetic Property Measurement System (MPMS) is a highly integrated instrument system. The model MPMS sample magnetometer is designed to detect the magnetic moment of a sample, from which the magnetization and magnetic susceptibility can be determined. Figure 2-2 and 2-3 show the system components and the functional control diagram of the SQUID magnetometer of Quantum Design's MPMS-7. The principal components of this measurement system are comprised of the following subsystems.[51,52]

SYSTEM COMPONENTS

1. Sample Rod
2. Sample Rotator
3. Sample Transport
4. Probe Assembly
5. Helium Level Sensor
6. Superconducting Solenoid
7. Flow Impedance
8. SQUID Capsule with Magnetic Shield
9. Superconducting Pick-up Coil
10. Dewar Isolation Cabinet
11. Dewar
12. HP Thinkjet Printer
13. Magnet Power Supply
14. Model 1802 Temperature Controller
15. Console Cabinet
16. Power Distribution Unit
17. Model 1822 MPMS Controller
18. Gas/Magnet Control Unit
19. HP Vectra Computer
20. Monitor

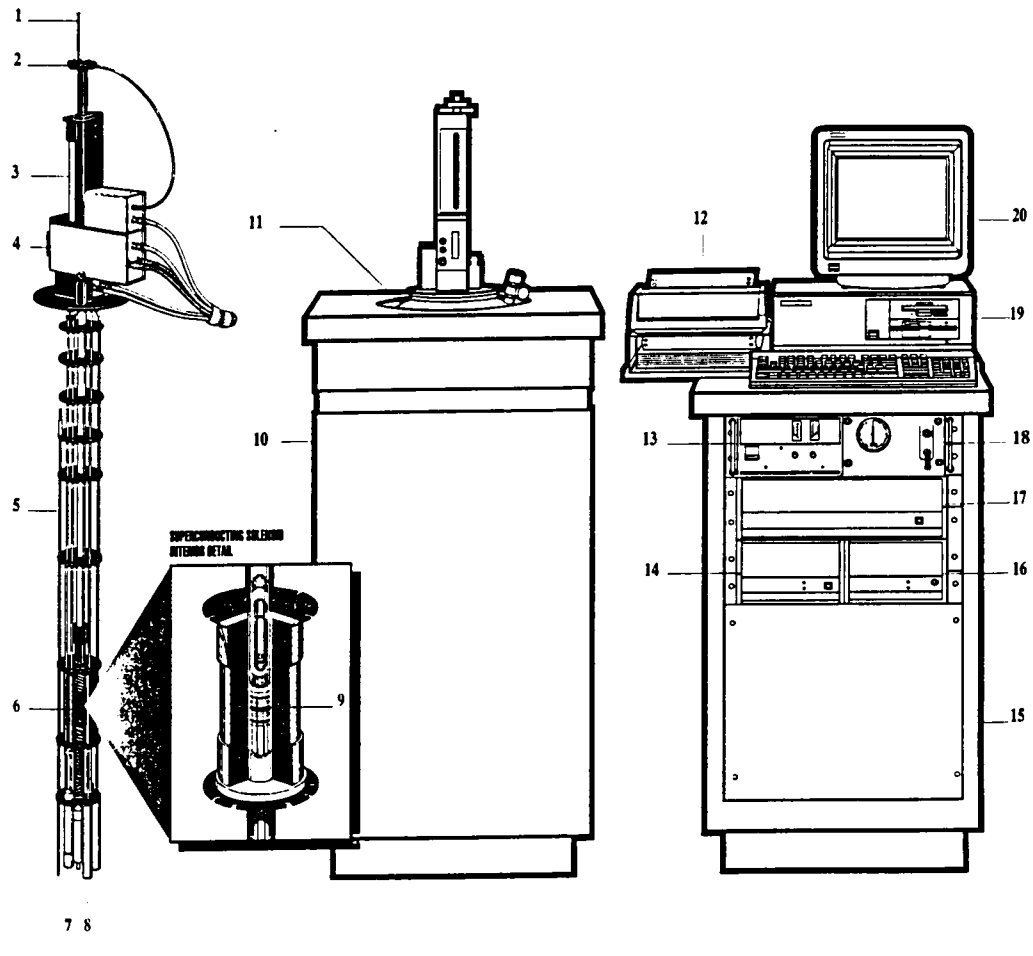


Figure 2-2. The system components of the SQUID magnetometer of Quantum Design's MPMS-7.

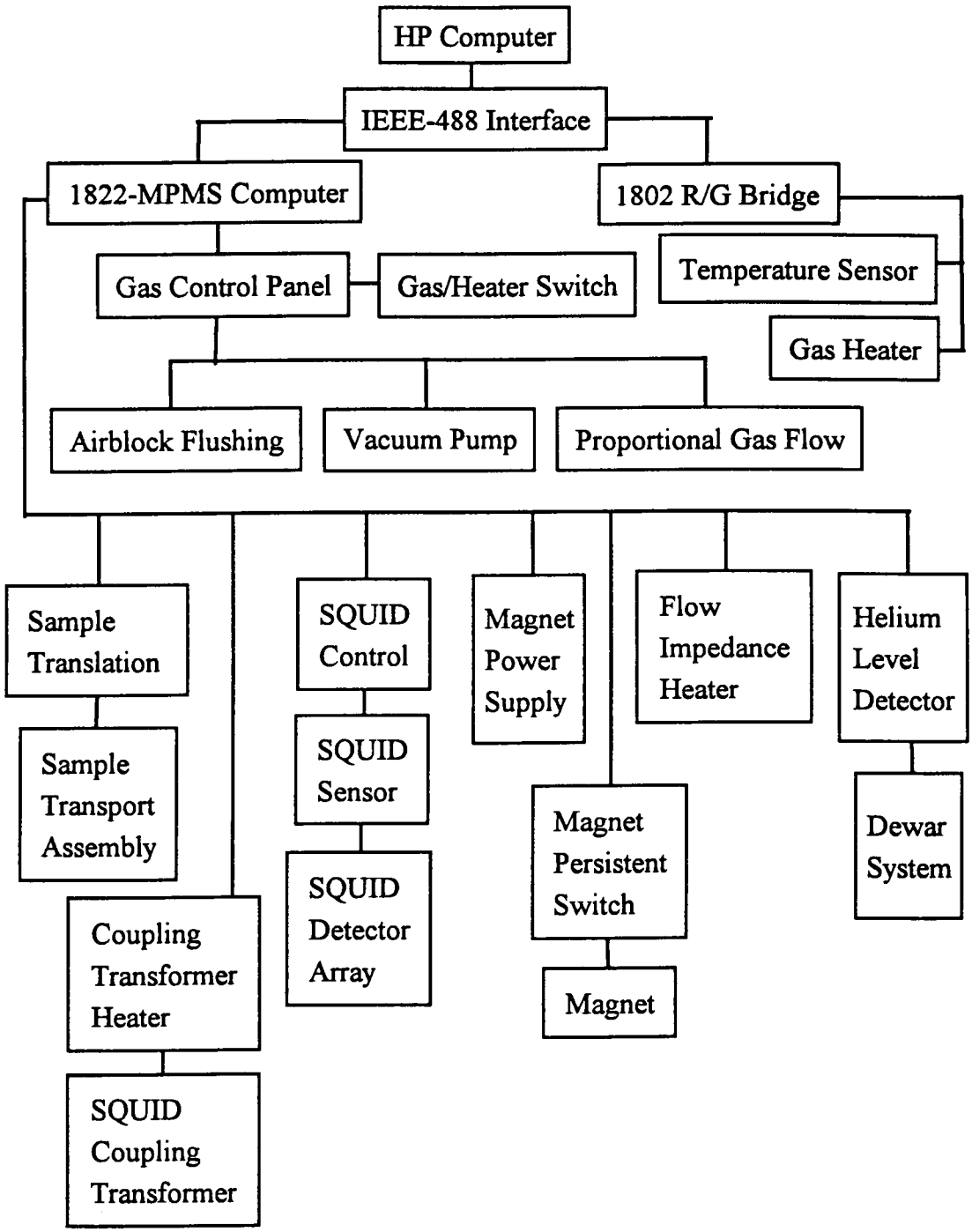


Figure 2-3. The Functional Control Diagram of the SQUID magnetometer of Quantum Design's MPMS-7

(1) Temperature Control System

The principal components of the temperature control system are the liquid helium dewar, the variable impedance assembly, the temperature control module, the proportional flow control valve, and the vacuum pump. Figure 2-4 and 2-5 show the Temperature Control Module and the Gas Control System of MPMS-7. The system has two thermometers, a germanium resistor for the low temperature regime below 40 K and a platinum resistance thermometer for the regime above 40 K, to cover the whole temperature range from 2 K (-271 °C) to 400 K (127 °C). An important feature is the fully automated temperature control system. The Model 1802 R/G Bridge controls the heat flow into the sample space to establish a target temperature between 4.4 K and 400 K. Also, one requires no special modification of the MPMS hardware to operate for a limited time at temperatures below 4.4 K. The principle of the operation of the MPMS at temperature below 4.4 K is not complicated. To do so, the system adjusts the proportional flow control valve to get a lower pressure in the helium reservoir. Therefore, liquid helium will flow through the impedance assembly and into the helium reservoir via the connecting tube. Maintaining this condition for short period time (about 15 minutes) will result in the accumulation of about 20 cc of liquid helium in a reservoir. One can start automatically this mode of operation by the following steps: (1) set temperature to 5 K, (2) pause 600 seconds, (3) set the target temperature below 4.4 K, and (4) turn impedance heater off. The first two steps are included to make sure that the sample chamber and helium reservoir are relatively cool before the system tries to fill the reservoir with liquid helium. However, during step 3, the

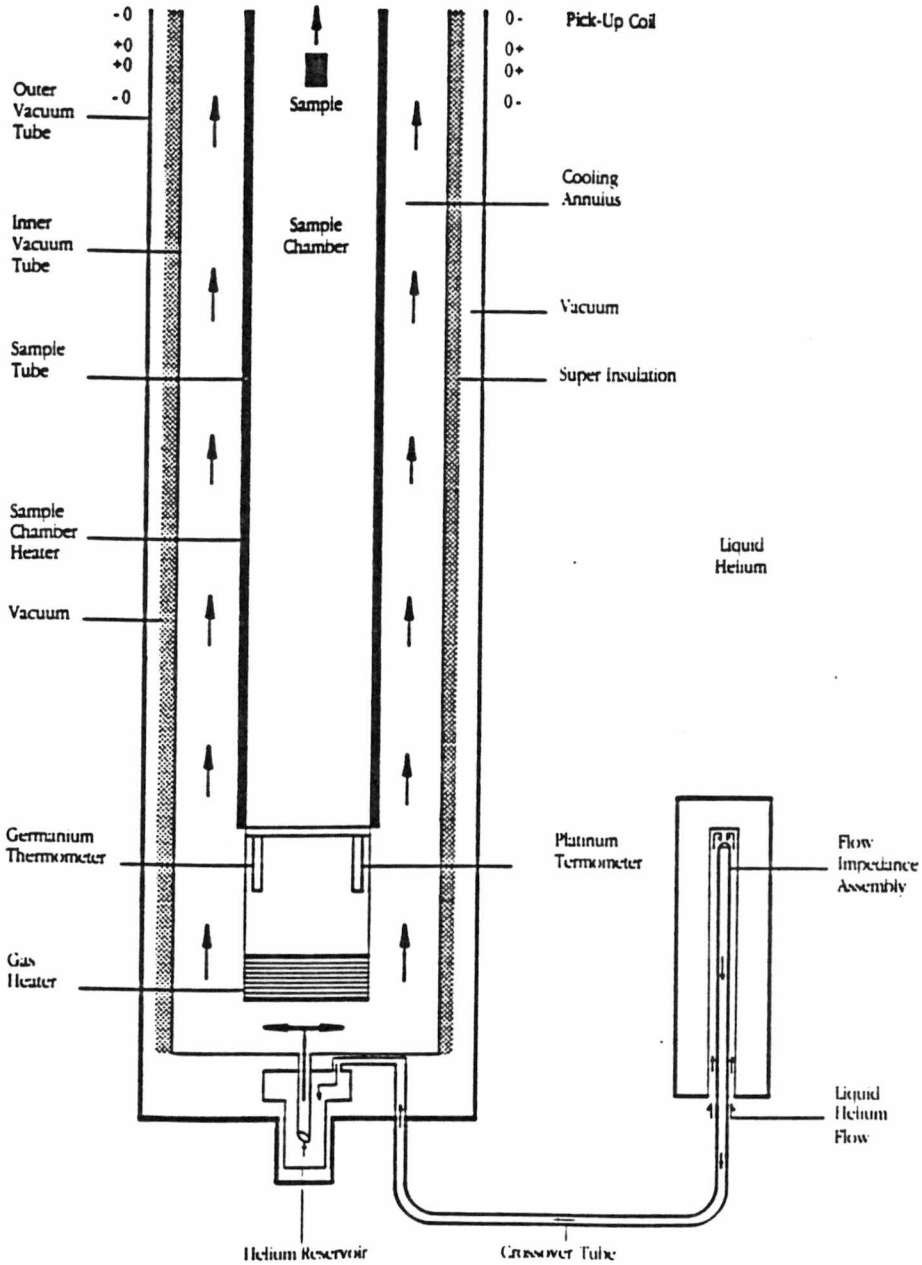


Figure 2-4. The MPMS temperature control module.

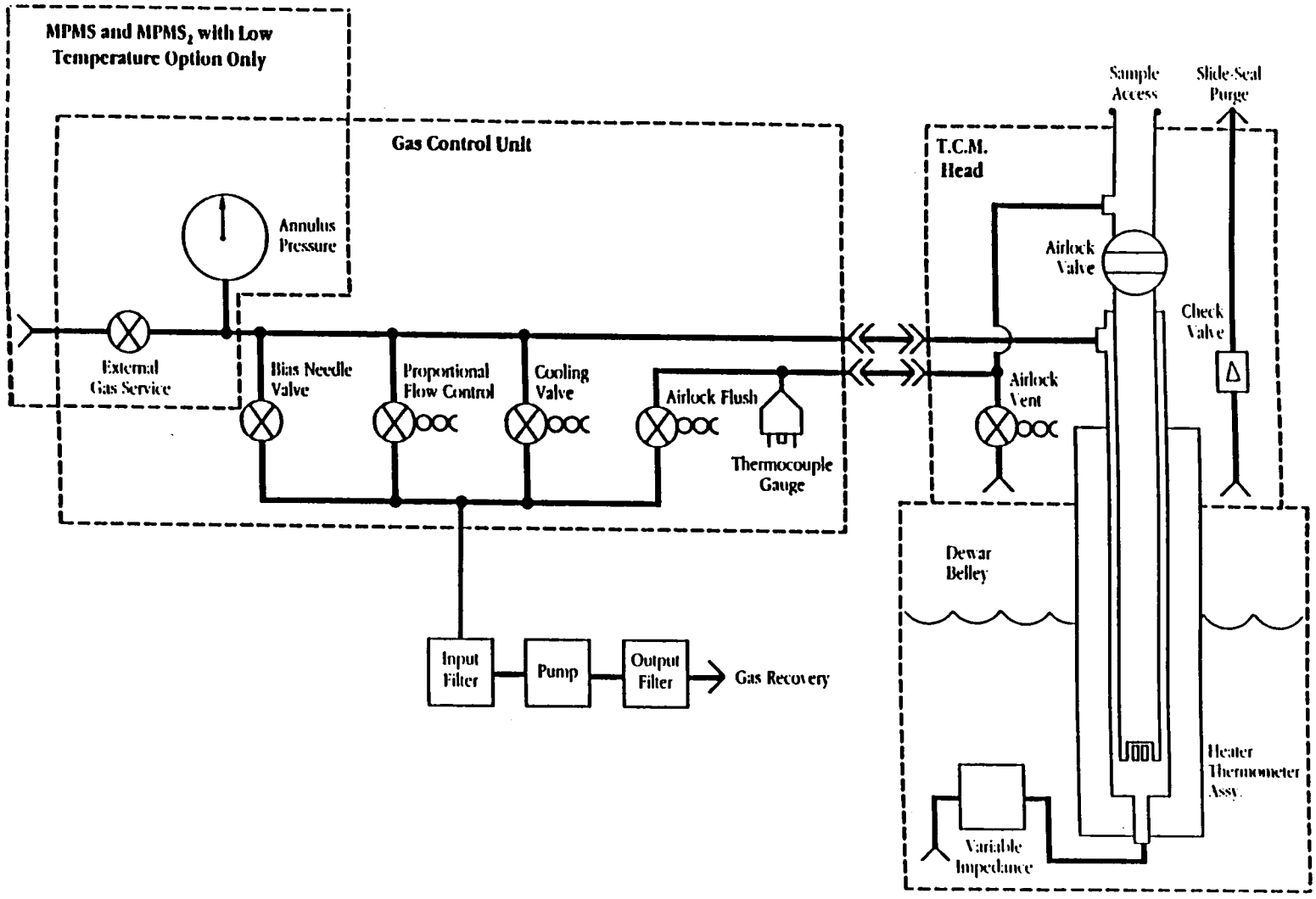


Figure 2-5. The MPMS gas control system.

reservoir fills with liquid helium, the impedance is closed, the proportional flow control valve is opened, and the temperature is controlled at temperature below 4.4 K using both the proportional flow control valve and heater. One charge of liquid helium can maintain target temperature in the range 2 ~ 4 K for about 2 or 3 hours.

(2) Magnet Control System

A high homogeneity superconductive magnet provides magnetic fields up to ±7 T. It is energized with current from a power supply. Thus, the field is provided and sustained by charging or trapping an amount of current in the superconducting magnet that is wound in a solenoidal configuration and is constructed as a completely closed superconducting loop. The entire sequence of the MPMS magnetic field control is processed entirely by the Model 1822 Main Controller without detailed attention from the HP host computer. To establish a target magnetic field, the magnet current can be controlled in two ways: the *Oscillating* and the *No Overshoot* mode. The *Oscillating* mode oscillates the current back and forth around target value with decreasing amplitude of oscillation, after passing the target value at first. In contrast, the *No Overshoot* mode guides the current to get the target value very monotonically without passing the target value. Sometimes, it is very important to choose the *Oscillating* mode or *No Overshoot* mode according to experimental objectives. Usually, the *Oscillating* mode reduces greatly the magnetic field relaxation in the magnet, which arises from residual magnetic forces on the magnetic flux pinned in the magnet windings. The current oscillation helps minimize these relaxation effects, which appears as drift in the output of the SQUID detector with its extreme sensitivity. However,

when one measures a material exhibiting irreversible magnetic behavior, the *Oscillating* mode cannot be used; the *No Overshoot* mode should be used so that the sample experiences a monotonically changing field. Finally, it should be noted that, when the magnet is charged to a high field, some magnetic flux becomes trapped in the superconducting windings. To eliminate trapped flux that gives a remnant magnetic field, the MPMS system allows one to warm (with an electric heater) the magnet above its superconducting transition temperature for a short time period, releasing the trapped fields. In addition, the homogeneity of magnet is important, since the movement of superconducting sample in inhomogeneous field induces currents that can drastically change the sample magnetization. Usually, a scan of 3 cm, properly centered, gives a field excursion of δH ~ 3 G at H = 5 T, i.e., 60 ppm for our MPMS system. The MPMS-7 model has 1 ppm/hour of field stability and 0.01% over (at a scan of 4 cm) of intrinsic field uniformity.

(3) Superconducting SQUID Amplifier System

The detection system for magnetic moment consists of a highly balanced second-derivative pickup coil, reset circuitry, auto-ranging capability, a superconducting transformer and *rf* SQUID sensor with a Model 2000 SQUID Amplifier. Figure 2-6 shows the transverse SQUID system. The *rf* SQUID detector is the most important part in the magnetic moment detection system. The thin film SQUID device of Josephson junctions essentially functions as an extremely sensitive current-to-voltage convertor. Figure 2-7 shows the configuration and location of the pickup coil set. The longitudinal pickup coils

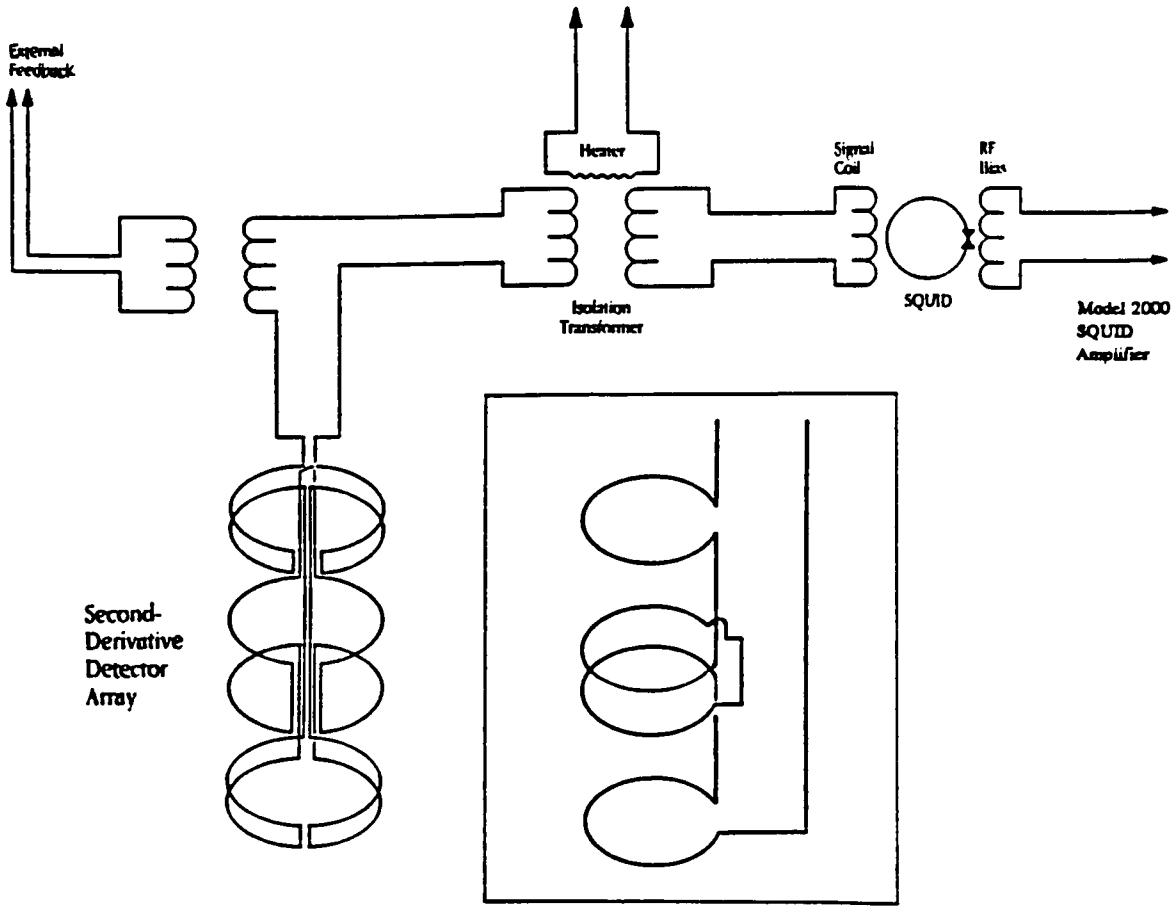


Figure 2-6. The MPMS transverse SQUID system; inset: the detector array for longitudinal system.

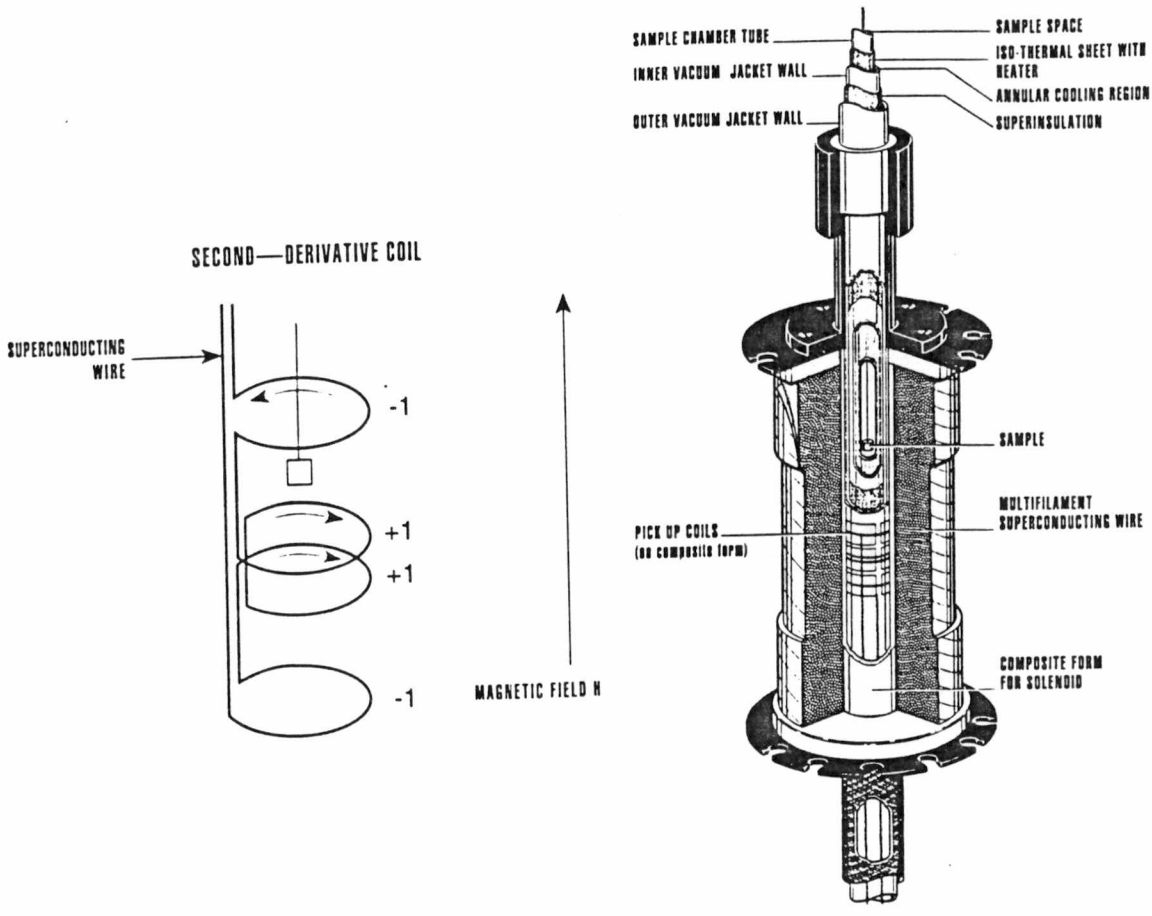


Figure 2-7. The configuration and location of the pick up coils.

are a highly balanced second-derivative coil set with a 2.02 cm diameter and a total length of 3.02 cm. The upper coil is a single turn wound clockwise, the center coil comprises two turns wound counter-clockwise, and the bottom coil is a single turn wound clockwise. This second-order gradiometer configuration, which will provide more noise cancellation than a first-order gradiometer, rejects noise in the detection circuit caused by fluctuations in the large magnetic field of the superconducting magnet. A measurement is performed in the MPMS system by moving a sample through the superconducting detection (pickup) coils. When the sample moves through the pickup coils, the magnetic moment of the sample induces an electric current in the pickup coils. The pickup coils, the connecting wires, and the SQUID input coil form a closed superconducting loop. Therefore, any change of magnetic flux in the pickup coils produces a change in the persistent current in the pickup detection circuit, which is proportional to the change in magnetic flux. Since the SQUID functions as a highly linear current-to-voltage convertor, the variations in the current in the pickup coils produce corresponding variations in the SQUID output voltage which is proportional to the magnetic moment of the sample.

(4) Sample Holding System

The sample holding system composes of the sample holder (*Mylar* tube and Si- or Al-disk), the sample rod, a special slide seal assembly, and a stepper-motor-controlled platform. The sample is attached with "*Duco*" cement on the Si-disk, which seats in a *Mylar* tube that is connected in turn to the end of a rigid sample rod. After loading the sample into magnetometer, the top of the sample transport rod is attached to a stepper-motor-controlled

platform and this drives the sample through the pickup coils in a series of discrete steps. At each step, the SQUID system measures a voltage proportional to the induced current. The resulting "scan", which typically is 3 ~ 4 cm in length, is converted to magnetic moment electrically, using an experimentally determined calibration factor, and automatically controlled attenuation factors.

(5) Computer Operating System.

All operating features of the MPMS are under automated and computer control. The user interface at the PC console provides the option of working under standard sequence controls, or diagnostic controls which are invoked individually. For the experimental studies reported here, specific sets of instructions ("sequences") were written. The Model 1822 Main Controller is a standard bus on-board computer that controls probe functions and SQUID data acquisition. This unit is consisted of a 6809-microprocessor operating in a STD bus configuration, with an IEEE-488 General Purpose Interface Bus (GPIB) card to handle communications between the 1822 microprocessor and the host computer. In addition, the Model 1802 Digital R/G Bridge is a multi-channel, microprocessor controlled, a programmable measurement and control instrument.

The model MPMS sample magnetometer is currently used in many research laboratories. It is configured to detect the magnet moment of various materials. The MPMS can measure a magnetic moment with a range of sensitivity from about 10^{-8} emu to 2 emu in the standard configuration and can measure over 300 emu with the extended range

option, as included in this instrument. Usually, the MPMS reports the magnetic moment data in emu (electromagnetic units [G·cm^3]). Therefore, we get the magnetization M by dividing the value of the magnetic moment by volume, mass, or the number of moles in the sample to obtain M in units of emu/cm^3 = G, emu/gm = G·cm^3/gm, and emu/mol = G·cm^3/mol, respectively.

2.2.2 Small Angle Neutron Scattering (SANS) Experiment

In recent years, Small Angle Neutron Scattering (SANS) has become a very useful method for investigating the vortex array in the superconducting mixed state. In particular, a phase transition in vortex symmetry, from simply hexagonal to square symmetry, was discovered in SANS experiments on RNi$_2$B$_2$C compounds.[31-35] In general, scattering experiments are one of the main sources of information on the structure of matter. A beam of particles, such as electrons, neutrons, alpha particles, other atomic nuclei, etc., is deflected by elastic collisions with atomic nuclei. In addition, to get useful information from scattering experiments, specialized techniques are needed for detecting the scattering particles. The use of neutron diffraction is relatively new compared to electron and X-ray diffraction. Neutron scattering is a unique tool for the study of a variety of magnetic phenomena, because the magnetic moment of neutron interacts with magnetic moments or spatial variations in the magnetic field within matter.

Usually, flux lines start to enter into superconducting materials when the applied field H reaches the lower critical field H_{c1}. These flux lines inside a material can form a periodic lattice, due to their repulsive interaction. One can understand the principle of small

angle neutron scattering (SANS) from a flux line lattice (FLL), following the treatment of C. M. Aegerter et al.[53] If the flux density $B \approx \phi_o/a_o^2$ in superconducting material is 1 T (which is much larger than H_{c1}), the typical spacing a_o between FLL planes will be about 50 nm. Thus, to observe the structure of the FLL, neutrons with long wavelengths are required to get even small angle scattering. For example, if the beam has wavelengths between 1.2 and 1.5 nm, scattering angles $2\theta \approx 2°$ can be estimated from the Bragg condition,

$$\lambda_n = 2d_{hk} \sin(\theta), \qquad (2.2.2\text{-}1)$$

where λ_n is the wavelength, d_{hk} is the layer spacing, and θ is scattering angle. Because a neutron has a magnetic moment, $\mu_n = -1.913\mu_N$, it may interact not only with the nuclei in a sample, but also with magnetic field modulation due to FLL in superconducting mixed state. Thus small angle neutron scattering, due to interactions between neutrons and magnetic spatial inhomogeneities, gives information about the structure of the FLL within superconductors.[54,55]

The intensity of scattered neutrons in a Bragg reflection (integrated over angle rocking curve, when the sample is rocked through the Bragg condition) is estimated from the magnetic cross section to be[56]

$$I_{hk} = [(\pi\mu_n^2 \Phi \lambda_n^2 V)/(8\phi_o^2 q_{hk})]\, |F(q_{hk})|^2 \qquad (2.2.2\text{-}2)$$

where Φ is the flux of incoming neutrons, λ_n is the neutron wavelength, V is the sample volume, $\phi_o = h/2e$ is the magnetic flux quantum, and $F(q_{hk})$ is the magnetic form factor, which is a measure of the q_{hk} Fourier component of the spacial variation of the magnetic field in the sample. For extreme type-II superconductors (HTS materials) with high κ values, which indicate long magnetic penetration depths and short coherence lengths, the

$F(q_{hk})$ can be easily calculated in the London approximation:

$$F(q_{hk}) = B / (1 + \lambda_L^2 q_{hk}^2). \quad (2.2.2\text{-}3)$$

Here λ_L is the magnetic penetration depth, which is temperature dependence, and B is the average of magnetic induction field. Finally, one can obtain the relation between I and λ_L from equations (2.2.2-2 and -3):[33]

$$(I/I_o) = V(2\pi/q)(\gamma/2)^2\lambda_n^2(1/\phi_o)^2\{[B/(1+q^2\lambda_L^2)]\exp(-2\pi^2 B\xi^2/\phi_o)\}^2, \quad (2.2.2\text{-}4)$$

where γ is the neutron gyromagnetic ratio, and ξ is the coherence length. Thus, the London penetration depth λ_L of the sample in the mixed state can be estimated from the scattered intensity where $I \propto \lambda^{-4}$. Because the HTS materials have long penetration depths, $\lambda_{ab} \approx 150 \sim 200$ nm at low temperature and much longer close to T_c, the scattered intensities are very weak and hard to obtain, compared with conventional low-T_c type-II superconductors. Therefore, in SANS experiments on HTS materials, long counting times are required generally. In addition, there is very strong background scattering from various defects in the sample. For experimental data in the mixed state, the background correction is obtained by subtracting normal state results, measured above its T_c, just as the magnetization data were corrected by this method.

2.2.3 Thermodynamic Properties for Reversible Superconductors

For reversible superconductors, the most fundamental thermodynamics quantities, which are the electronic specific heat ($C_{electronic}$) and the thermodynamic critical field (H_c), are directly related to the superconducting energy gap. The superconducting state has lower entropy, which is a higher degree of order, than that of the normal state. One expects a

reduction in energy as a result of the transition from the normal to superconducting state. Thus, the superconducting condensation energy (which is proportional to H_c^2, as noted below) associated with the superconducting transition can be calculated easily. Figure 2-8-a shows the typical relation between the critical field H_c and temperature T. Figure 2-8-b shows the corresponding magnetization curve $M(H)$ for a simple type-I superconductor. The curve of H_c versus T separates two phases, the normal and superconducting states. As we see the Figure 2-8-a, when the superconducting specimen starts at point S and ends at point N with taking the vertical path SN, that is gradually increasing the field, with keeping constant temperature T_S (below T_c), it results to the normal state at the point N. In the above processing, the condensation energy is $\Delta E = E_N - E_S$. In addition, ΔE is equal to the demagnetization energy because the sample acts as perfect diamagnet, due to the Meissner effect, along the path SN; see the Figure 2-8-b. Finally, we can write the following expression for the condensation energy per unit volume,

$$\Delta E = -\int_0^{Hc} M\, dH = -(1/4\pi)\int_0^{Hc} (-H)\, dH = (1/8\pi)H_c^2 \qquad (2.2.3\text{-}1)$$

where B (magnetic flux density) = H (magnetic field strength) + $4\pi M = 0$ (in the Meissner state). In other words, this ΔE is the amount of energy needed to convert a system from the superconducting to the normal state or the amount of energy lost by the system when it makes the transition from the normal to the superconducting state.

To apply thermodynamics, the transition from the superconducting to the normal state must be reversible. In other words, the magnetization of a superconducting sample can depend only on the values of the applied magnetic field and temperature, but not on the processes for establishing these external conditions. Generally, the stable state in any system

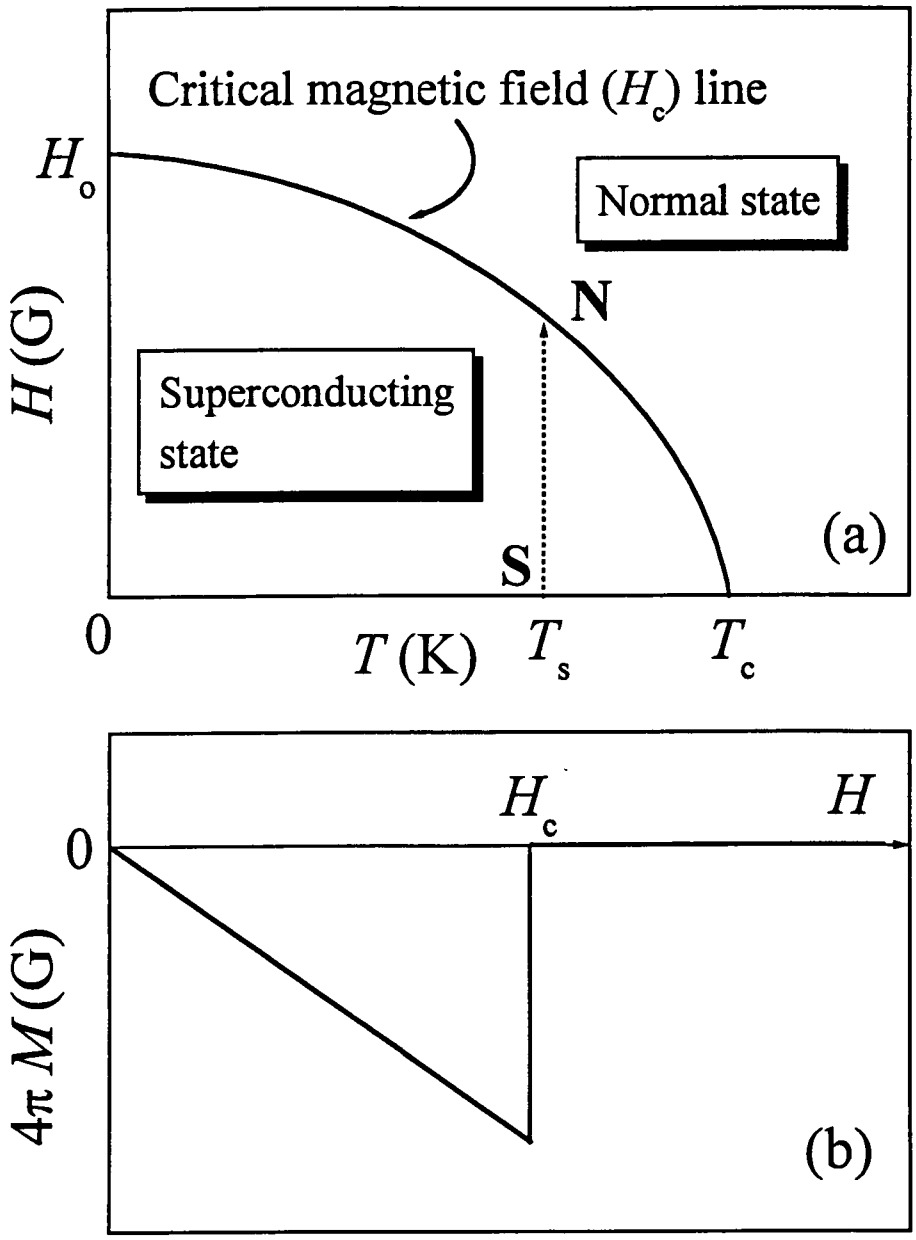


Figure 2-8. (a) The plot of critical field, H_c, as a function of the temperature. (b) The magnetization M of a type-I superconductor versus magnetizing field H: the figure pertains to a long specimen with field applied parallel to the long axis (zero demagnetizing factor). At critical field H_c, the sample reverts to the normal state.

belongs to the lowest free energy. It is very useful to compare the difference in the magnetic contribution to the free energy of two phases, which are superconducting and normal states, due to the applied magnetic field. The free energy of the superconducting state must be less than that of the normal state because the superconducting state has lower entropy. In addition, the application of magnetic field does not change the free energy of the normal state because of the non-magnetic properties of the normal state. In contrast, the free energy of the superconducting state will increase as the applied magnetic field increases.

Therefore, for both type-I and type-II superconductors, the thermodynamic critical field is defined by the relation,[49,57,58]

$$H_c^2\,(\mathrm{T}) / 8\pi = [\, F_n\,(T) - F_s\,(T)\,] / V_{\mathrm{molar}}\,, \qquad (2.2.3\text{-}2)$$

where $F_n(T)$ (or $F_s(T)$) is the molar free energy of the normal state (or superconducting state), V_{molar} is molar volume. The relation of free energy of a system is $F(T) = U(T) - TS(T) + pV$, without magnetic field, where $U(T)$ is the internal energy, $S(T)$ is the entropy per mole, p is the pressure, and V is the volume. Thus, the free energy of a magnetic body within magnetic field can be written

$$F(T) = U(T) - T\,S(T) + p\,V - (1/4\pi)\,H_a M\,, \qquad (2.2.3\text{-}3)$$

where H_a is the applied magnetic field, and M is the magnetic moment. If the pressure and the applied magnetic field are kept constant but the temperature T is varied by an amount dT, the change of the free energy is

$$dF(T) = dU(T) - T\,dS(T) - S(T)\,dT + p\,dV - (1/4\pi)\,H_a\,dM. \qquad (2.2.3\text{-}4)$$

However, using the first law of thermodynamics, $dU = T\,dS - p\,dV + (1/4\pi)\,H_a\,dM$, one can get

$$dF(T) = -S(T)\,dT \quad \text{and} \quad S(T) = -[\partial F / \partial T]_{p,Ha} \tag{2.2.3-5}$$

per unit volume. In addition, the molar specific heat is defined by $C_p = T\,[dS/dT]$. Finally, one obtains for a superconductor,

$$\begin{aligned} C_n - C_s &= T\,(\partial/\partial T)[S_n(T) - S_s(T)] \\ &= T\,(\partial/\partial T)\{-(\partial/\partial T)[F_n - F_s]\} \\ &= -(T\,V_{molar}/8\pi)(\partial^2/\partial T^2)[H_c(T)]^2, \end{aligned} \tag{2.2.3-6}$$

where C_n, S_n, and F_n are the specific heat, the entropy and the free energy of the normal state, and C_s, S_s, and F_s is the specific heat, the entropy, and the free energy of the superconducting state, respectively. Therefore, we can derive the thermodynamic critical field by the specific heat experiment due to following relation,[57,59]

$$H_c^2(T) = (8\pi/V_{molar}) \int_T^{Tc} dT' \int_{T'}^{Tc} dT'' \{[C_s(T'') - C_n(T'')]/T''\}. \tag{2.2.3-7}$$

Therefore, in the framework of thermodynamics, we can obtain the thermodynamic critical field from specific heat measurements, using above relations.

On the other hand, we can obtain the thermodynamic critical field from a magnetization experiment as well. Usually, in the regime near H_{c2}, the vortices are packed very tightly. According to Abrikosov calculations, the local flux density is less than the applied field by an amount proportional to the local value of $|\psi(r)|^2$. Thus, the magnetization, $M = (B - H)/4\pi$ is proportional to $\langle\psi^2(r)\rangle$ which goes to zero linearly with $(H_{c2} - H)$ in the second order phase transition at H_{c2}. As an explicit result,[49,57]

$$B = H + 4\pi M = H - (H_{c2} - H) / [(2\kappa^2 - 1)\,\beta_A], \tag{2.2.3-8}$$

where $\beta_A = 1.16$ for the triangular lattice and 1.18 for the square lattice.

Meanwhile, let us define the Gibbs free energy $G = F - BH/4\pi$. Using the thermodynamic relation, $(\partial G/\partial H)_T = -B/4\pi$, one can get easily following relation by integrating, where $F = G$ when $H = 0$, and $G_s = G_n$ when $H > H_{c2}$,

$$H_c^2 / 8\pi = F_n(0) - F_s(0) = -\int_o^{Hc2} M\, dH, \qquad (2.2.3\text{-}9)$$

having nothing to do with the value of κ. This indicates that the area under the magnetization curve is given by the condensation energy $H_c^2/8\pi$ in all case, in spite of changing of the shape of magnetization curve.

2.2.4 From London to Ginzburg-Landau Theory

(1) London theory

At first, let us consider the behavior of superconducting electrons under a constant electric field $\boldsymbol{E}$, in a superconducting metal. The superconducting electrons will be accelerated by the electronic field $\boldsymbol{E}$:

$$m(d\mathbf{v}_s/dt) = -e\boldsymbol{E}. \qquad (2.2.4\text{-}1)$$

The supercurrent density is $\boldsymbol{J}_s = -n_s e\mathbf{v}_s$, where n_s is the number of superconducting electrons per unit volume, and $\mathbf{v}_s$ is the velocity of the superconducting electrons; from equation (2.2.4-1), one then has

$$d\boldsymbol{J}_s / dt = (n_s e^2/m)\boldsymbol{E}. \qquad (2.2.4\text{-}2)$$

Using Maxwell's equations inside a superconductor, $\nabla \times \boldsymbol{E} = -(1/c)(\partial \boldsymbol{B}/\partial t)$ and $\nabla \times \boldsymbol{B} = (4\pi/c)\boldsymbol{J}_s$, we can deduce the following relation describing magnetic fields:

$$(\partial/\partial t)[\nabla \times \boldsymbol{J}_s + (n_s e^2/mc)\boldsymbol{B}] = 0 \qquad (2.2.4\text{-}3)$$

and

$$(\partial/\partial t)[\nabla \times \nabla \times \boldsymbol{B} + (4\pi n_s e^2/mc^2)\boldsymbol{B}] = 0. \qquad (2.2.4\text{-}4)$$

However, the one of the basic physical features of superconductors is the Meissner effect,[2] which indicates that the flux density $\boldsymbol{B}$ inside a superconductor is zero in small magnetic fields $H < H_{c1}$, the lower critical field. This Meissner effect is incompatible with the above relation (2.2.4-4), which shows that constant magnetic fields can be exist within a perfect conductor. Therefore, F. and H. London suggested that the magnetic properties of superconductors could be explained by restricting the equation (2.2.4-3 and 4), whose the solution is not only constant but also always zero, to the following forms,[3,48]

$$\nabla \times \boldsymbol{J}_s + (n_s e^2/mc)\boldsymbol{B} = 0 \qquad (2.2.4\text{-}5)$$

and

$$\nabla \times \nabla \times \boldsymbol{B} + (4\pi n_s e^2/mc^2)\boldsymbol{B} = 0. \qquad (2.2.4\text{-}6)$$

From the vector identities $\nabla \times \nabla \times \boldsymbol{B} = \nabla(\nabla \cdot \boldsymbol{B}) - \nabla^2\boldsymbol{B}$ and Maxwell's equation $\nabla \cdot \boldsymbol{B} = 0$, the equation (2.2.4-6) becomes

$$\nabla^2\boldsymbol{B} - (4\pi n_s e^2/mc^2)\boldsymbol{B} = 0. \qquad (2.2.4\text{-}7)$$

This equation predicts that the magnetic flux density dies away exponentially inside a superconductor, falling to 1/e of its value at the distance λ_L from the surface. The quantity λ_L, known the London penetration depth, is given by

$$\lambda_L = (mc^2/4\pi n_s e^2)^{1/2}. \qquad (2.2.4\text{-}8)$$

The penetration depth λ_L is temperature dependent due to the temperature dependence of n_s, the density of superconducting electrons. The Gorter-Casimir theory,[60] which is an empirical two fluid model, provides that $n_s \propto (1 - t^4)$, where $t = T/T_c$ is reduced temperature.

Therefore, we can get the relation of $\lambda_L \propto (1- t^4)^{-1/2}$ in the framework of two fluid model.

A key point of the London theory is that the supercurrent is always determined by the local magnetic field. The London theory assumes that the total current J is the sum of a supercurrent J_s and a normal current J_n. In summary, we can now write the current relations and the London equations for superconductors:

$$J = J_n + J_s \text{ and } J_n = \sigma' E \tag{2.2.4-9}$$

$$\nabla \times J_s = - (n_s e^2/mc) B \tag{2.2.4-10}$$

$$dJ_s / dt = (n_s e^2/m) E \tag{2.2.4-11}$$

Meanwhile, if we introduce a vector potential A for the magnetic field B, where $B = \nabla \times A$, then the London relation between J_s and A is $A(r) = - (mc/n_s e^2) J_s(r)$ from the London equation (2.2.4-10). Therefore, the q^{th} Fourier components of A and J_s are related by $A(q) = - (mc/n_s e^2) J_s(q)$. Using Maxwell's equation $\nabla \times B = (4\pi/c) J$, vector potential $B = \nabla \times A$, and London gauge $\nabla \cdot A = 0$, we can get

$$\nabla^2 A = - (4\pi/c)(J_e + J_s), \tag{2.2.4-12}$$

where J_e is external current, and J_s is supercurrent. After taking a Fourier integral, the equation (2.2.4-12) can be rewritten

$$- q^2 A(q) = - (4\pi/c) J_e(q) + K(q) A(q) \tag{2.2.4-13}$$

where we define $K(q)$ from $J_s(q) = - (4\pi/c) K(q) A(q)$. Finally, we can derive the London kernel, by comparing two J_s equations, as

$$K_L(q) = 4\pi n_s e^2/mc^2 = 1/(\lambda_L)^2. \tag{2.2.4-14}$$

This London kernel is independent of q.

In general, the London theory, which is a macroscopic or phenomenological theory

of superconductivity, treats well the Meissner effect in bulk superconductors as well as the magnetic properties of superconducting thin films with dimensions comparable to the penetration depth. However, there are some serious discrepancies between the London theory and some experimental results,[61] such as the variation of the London penetration depth λ_L with orientation in a single crystal, the near-independence of the London penetration depth λ_L with respect to H_a near T_c, an increase in λ_L as the electronic mean free path ℓ decreases, and the need for a negative surface energy between the normal and superconducting phases.

(2) Pippard theory

The London relation for penetration depth, $\lambda_L = (mc^2/4\pi n_s e^2)^{1/2}$, does not explain well the observed anisotropy of the penetration depth in dilute alloying materials. To understand this anisotropy, A. B. Pippard made many measurements of the penetration depth[61] and reached the important conclusion that the London equation for pure superconductors should be replaced by a non-local equation, like the non-local form of Ohm's law for the anomalous skin effect in a normal metal. Therefore, Pippard introduced a new size scale, the coherence length, while deriving a non-local generalization of the London equation.[61] Just as the local form of Ohm's law in the normal skin effect,

$$\boldsymbol{J}(0) = \sigma \boldsymbol{E}(0), \tag{2.2.4-15}$$

should be replaced by a non-local relation for the anomalous skin effect,

$$\boldsymbol{J}(0) = (3\sigma/4\pi\ell)/\{[\boldsymbol{r}(\boldsymbol{r}\cdot\boldsymbol{E})e^{-r/\ell}]/r^4\}d\tau, \tag{2.2.4-16}$$

so also should the local London equation,

$$J_s(0) = -(n_s e^2/mc)A(0), \qquad (2.2.4\text{-}17)$$

be replaced by the Pippard non-local relation

$$J_s(0) = -(3n_s e^2/4\pi\xi_o m)\int [r(r\cdot A)e^{(-r/\xi)}]\, d\tau. \qquad (2.2.4\text{-}18)$$

The coherence length ξ is given by

$$1/\xi = 1/\xi_o + 1/\ell \qquad (2.2.4\text{-}19)$$

where ξ_o is a constant for a given pure superconductors and ξ depends on the mean free path ℓ; $\xi = \xi_o$ in pure superconductors, and $\xi = \ell$ for $\ell << \xi_o$. The microscopic BCS theory[5] gives

$$\xi_o = 0.18\hbar v_F / k_B T_c, \qquad (2.2.4\text{-}20)$$

where v_F is the Fermi velocity.

Continuing, the kernel $K_P(q)$, defined through the equation $J_s(q) = -(4\pi/c)K(q)A(q)$, is given by

$$K_P(q) = (\xi/\xi_o\lambda_L^2)(3/2(q\xi)^3)[(1 + q^2\xi^2)\tan^{-1}q\xi - q\xi] \cdots . \qquad (2.2.4\text{-}21)$$

From this, we can get the following limiting forms:

$$K_P(q) = (1/\lambda_L^2)(\xi/\xi_o)[1 - q^2\xi^2/5 + \cdots] \quad \text{for } q\xi << 1 \qquad (2.2.4\text{-}22)$$

$$K_P(q) = (1/\lambda_L^2)(\pi/4q\xi_o)[1 - 4/\pi q\xi + \cdots] \quad \text{for } q\xi >> 1. \qquad (2.2.4\text{-}23)$$

The Pippard kernel for $q\xi >> 1$ belongs to $\ell \to \infty$, with $\xi \to \xi_o$ and $\xi_o > \lambda$. The Pippard kernel goes over to a London kernel for $q\xi << 1$, which is satisfied when $q \to 0$. If we consider the Fourier component with $q \sim 1/\lambda$, then $\xi << \lambda$ leads to London behavior. This corresponds to two types of superconductors: the type-I or Pippard superconductors with $\xi > \lambda$, and the type-II or London superconductors with $\xi < \lambda$.

In summary, the Pippard theory demonstrates well the potential non-local

relationship current density and vector potential, and the properties of the coherence length. Pippard gave up a local concept, a "rigidity" of the superconducting wave function, and introduced the non-local concept of a coherence length ξ, which requires an integration averaging over a finite region surrounding the perturbing point.

(3) Ginzburg-Landau theory

The macroscopic electromagnetic London equations play a key role in understanding some phenomenology of superconducting materials. However, they do not explain fully the macroscopic picture, as mentioned previously. In 1950, Ginzburg and Landau developed a macroscopic, phenomenological theory based on thermodynamics to overcome some deficiencies of London theory.[4] In the pre-BCS era, the Ginzburg-Landau theory provided important understanding of the macroscopic picture of superconducting materials.

The Ginzburg-Landau theory is based on second-order phase transitions. This is based on quantum mechanics, unlike London theory which was truly classical. A main point of the theory is that Ginzburg-Landau introduces an effective wave function, $\Psi(r)$, which is called the order parameter. The order parameter is defined to be zero in the normal state and unity for a purely superconducting state at zero temperature.

In analogy with an ordinary wave function, $\Psi(r)$ for a superconductivity is taken as a complex function. Therefore, the density of superconducting electrons, $N_s(r)$, is related to the order parameter via the relation $N_s(r) = |\Psi(r)|^2$. In addition, Ginzburg-Landau wrote the free energy of the material, F_s, as a function of $\Psi(r)$ and $\Psi(r)^*$. They incorporated in F_s dependencies on a spatial variation of $\Psi(r)$ as well as a magnetic field H,

$$F_s = F_n + \int d^3r \{- F(|\Psi(r)|^2) + (1/8\pi)|H(r) - H_a|^2$$

$$+ (1/2m^*)|[(\hbar/I)\nabla - (e^*/c)A(r)]\Psi(r)|^2\}. \qquad (2.2.4\text{-}24)$$

The term F_n is the free energy of the normal state. The function F has always positive value (≥ 0), which represents a lowering of the free energy of the system due to the superconducting correlation. Since $|\Psi(r)| \rightarrow 0$ in the normal state, then $F(0) = 0$. For temperatures just below T_c when $(T_c - T) << T_c$, the term $F(|\Psi(r)|^2)$ can be expanded in a power series, keeping just the first two nonvanishing terms:

$$F(|\Psi(r)|^2) \approx \alpha|\Psi(r)|^2 + (\beta/2)|\Psi(r)|^4; \qquad (2.2.4\text{-}25)$$

odd powers of $|\Psi(r)|$ are excluded because they are not analytic at $\Psi(r) = 0$. The next term in equation (2.2.4-24) is the magnetic field energy, which increases the superconducting free energy due to the Meissner effect; H_a is the external applied field. The final term in equation (2.2.4-24) comes from the spatial variation of the order parameter and from current flow, which increase the free energy.

In the simple case of zero applied magnetic field and spatial homogeneity, we have

$$F_s - F_n = \alpha|\Psi|^2 + (\beta/2)|\Psi|^4. \qquad (2.2.4\text{-}26)$$

In the framework of thermodynamics, the free energy F_s should be a minimum. Therefore, β should be positive to be an adequate theory. If $\alpha > 0$, the minimum free energy takes place at $|\Psi|^2 = 0$. If $\alpha < 0$, one can differentiate with respect to $|\Psi(r)|^2$ to get the minimum values of F_s,

$$\partial F_s/\partial|\Psi|^2 = \alpha + \beta|\Psi_\infty|^2 = 0, \qquad (2.2.4\text{-}27)$$

the minimum free energy occurs at $|\Psi|^2 = |\Psi_\infty|^2 = -\alpha/\beta$, where Ψ_∞ indicates a value far from any boundaries. Substituting $|\Psi|^2 = |\Psi_\infty|^2 = -\alpha/\beta$ into equation (2.2.4-26) and using the

definition of the thermodynamic critical field H_c, one finds

$$F_s - F_n = \alpha |\Psi_\infty|^2 + (\beta/2)|\Psi_\infty|^4 = -\alpha^2/2\beta = -H_c^2/8\pi. \qquad (2.2.4\text{-}28)$$

In addition, if we eliminate α and β by solving equations (2.2.4-27) and (2.2.4-28) simultaneously, we get the following form,

$$F(|\Psi|^2) = (H_c^2/8\pi)\,(2|\Psi|^2/|\Psi_\infty|^2 + |\Psi|^4/|\Psi_\infty|^4). \qquad (2.2.4\text{-}29)$$

The coefficient $\alpha\,(T)$ must change from positive to negative value at $T = T_c$. By keeping only the leading term in a Taylor's series expansion of $\alpha\,(T)$ about T_c, one has

$$\alpha\,(t) = \alpha_o\,(t - 1), \qquad (2.2.4\text{-}30)$$

where α_o is positive and $t = T/T_c$. If β is constant at $T = T_c$, then we have $H_c \propto (1\text{-}t)$ as well as $|\Psi|^2 \propto (1\text{-}t)$. In London theory, the density of superconducting electrons, $n_s \propto \lambda^{-2} \propto (1\text{-}t)$ when $T \rightarrow T_c$. Using the identification $N_s = n_s/2 = |\Psi|^2$ and recalling that the simple London penetration depth $\lambda_L^2 = mc^2/4\pi e^2 n_s$, we can define a Ginzburg-Landau penetration depth $\lambda_{GL}^2 = m^* c^2 / 4\pi(e^*)^2 |\Psi|^2$. In addition, we can derive the parameters of the theory by solving (2.2.4-28),

$$|\Psi|^2 = |\Psi_\infty|^2 = -\alpha/\beta, \text{ and } \lambda_{GL}^2 = \lambda^2 = m^* c^2 / [4\pi(e^*)^2 |\Psi|^2]:$$

$$|\Psi_\infty|^2 = N_s = n_s/2 = m^* c^2/4\pi e^{*2}\lambda^2 = mc^2/8\pi e^2\lambda^2 \qquad (2.2.4\text{-}31)$$

$$\alpha(T) = -(e^{*2}/m^* c^2)H_c^2(T)\lambda^2(T) = -(2e^2/mc^2)H_c^2(T)\lambda^2(T) \qquad (2.2.4\text{-}32)$$

$$\beta(T) = (4\pi e^{*4}/m^{*2}c^4)H_c^2(T)\lambda^4(T) = (16\pi e^4/m^2 c^4)H_c^2(T)\lambda^4(T). \qquad (2.2.4\text{-}33)$$

Consider now the full expression for the overall free energy, equation (2.2.4-24). In minimizing F_s with respect to variations in Ψ and A (in addition to the obvious requirement of $F_s \leq F_n$), we get two additional equations, the so-called Ginzburg-Landau differential equations,

$$\{\alpha + \beta |\Psi|^2 + (1/2m^*) [(\hbar/I)\nabla - (e^*/c)A]^2\}\Psi = 0 \qquad (2.2.4\text{-}34)$$

$$J = (c/4\pi)\nabla\times H = (e^*\hbar/2m^*I)(\Psi^*\nabla\Psi - \Psi\nabla\Psi^*) - [(e^*)^2/m^*c]\Psi^*\Psi A. \qquad (2.2.4\text{-}35)$$

The former equation (2.2.4-34) has the form of a Schrödinger equation with an eigenvalue $-\alpha$, apart from the nonlinear term. The latter equation (2.2.4-35) has the form of the usual quantum mechanical expression of the current density for particles of mass m^*, charge e^*, and wave function $\Psi(r)$. In addition, a boundary condition at the surface of the specimen

$$n \cdot [(\hbar/I)\nabla - (e^*/c)A]\Psi = 0 \qquad (2.2.4\text{-}36)$$

where n is the normal surface, should be considered with these equations. In particular, for the case of spatial uniformity where $\nabla\Psi = 0$, one has $J = -[(e^*)^2/m^*c]\Psi^*\Psi A = -[(e^*)^2|\Psi|^2/m^*c]A$ from the equation (2.2.4-35), which is exactly identical to $J = -(e^2n_s/mc)A$ from London equation if we take $e^* = 2e$, $m^* = 2m$, and $|\Psi|^2 = N_s = n_s/2$. These relations agree very well with the microscopic BCS theory with Cooper pairs, consisting of two paired electrons.

Meanwhile, if we consider a simplified case of zero field ($A = 0$), take Ψ to be real, and introduce a normalized wavefunction $w = \Psi/\Psi_\infty$, then the differential equation (2.2.4-34) takes the form

$$(\hbar^2/2m^*|\alpha|)\nabla^2 w + w - w^3 = 0. \qquad (2.2.4\text{-}37)$$

Therefore, we can define a coherence length $\xi(T)$ for variation of Ψ such as

$$\xi^2(T) = \hbar^2/2m^*|\alpha(T)| \propto (1-T/T_c)^{-1}. \qquad (2.2.4\text{-}38)$$

This means that the small disturbance of Ψ from Ψ_∞ decays in a coherence length of order $\xi(T)$. By substituting equation (2.2.4-32) into equation (2.2.4-38), we get

$$\xi(T) = \phi_0 / [(2\sqrt{2})\pi H_c(T)\lambda(T)] \qquad (2.2.4\text{-}39)$$

where $\phi_0 = hc/e^* = hc/2e = 2.07 \times 10^{-7}$ [G-cm^2] is the quantum of flux. Moreover, we find the famous Ginzburg-Landau parameter κ, the ratio of the characteristic lengths near T_c,

$$\kappa = \lambda(T) / \xi(T) = (2\sqrt{2})\pi H_c(T)\lambda^2(T) / \phi_0. \qquad (2.2.4\text{-}40)$$

In general, pure superconductors have $\kappa << 1$, and dirty superconductors have $\kappa >> 1$. The value $\kappa = 1/\sqrt{2}$ is the boundary between type-I and type-II superconductors: type-I is $\kappa < 1/\sqrt{2}$, and type-II is $\kappa > 1/\sqrt{2}$.

Finally, we treat the linearized Ginzburg-Landau equations to avoid the difficulty of solving the coupled nonlinear partial differential equations. By dropping the term $\beta|\Psi|^2\Psi$ in equation (2.2.4-34), we can get the linearized Ginzburg-Landau equation,

$$(\nabla/I - 2\pi A/\phi_0)^2\Psi = (-2m^*\alpha/\hbar^2)\Psi = \Psi/\xi^2(T). \qquad (2.2.4\text{-}41)$$

Suppose that we apply the field H along the z-axis and take a convenient gauge, $A_y = Hx$. We have the following results from equation (2.2.4-41):

$$[-\nabla^2 + (4\pi i/\phi_0)Hx(\partial/\partial y) + (2\pi H/\phi_0)^2 x^2]\Psi = (1/\xi^2)\Psi. \qquad (2.2.4\text{-}42)$$

Since the effective potential depends only on x, we can choose the trial solution, $\Psi = \exp(ik_y y)\exp(ik_z z)f(x)$. Substituting the trial solution into equation (2.2.4-42), we can derive

$$-f''(x) + (2\pi H/\phi_0)^2 (x - x_0)^2 f = (1/\xi^2 - k_z^2) f \qquad (2.2.4\text{-}43)$$

where $x_0 = k_y\phi_0/2\pi H$. This is similar to the Schrödinger equation of a harmonic oscillator, particularly that giving quantized states for a normal charged particle in a magnetic field. These so-called Landau levels, which are separated by the cyclotron energy $\hbar\omega_c$, have eigenvalues $E_n = (n + 1/2)\hbar\omega_c = (n + 1/2)\hbar(2eH/m^*c)$. Meanwhile, the eigenvalues of the equation (2.2.4-43) are to be equated to $E_n = (\hbar^2/2m^*)(1/\xi^2 - k_z^2)$. Thus, we can find

$$H = [(\hbar^2/2m^*)(1/\xi^2 - k_z^2)]/[(n+1/2)\hbar(2e/m^*c)]$$

$$= [\phi_o /2\pi(2n+1)](1/\xi^2 - k_z^2). \qquad (2.2.4\text{-}44)$$

In this equation, H has the highest value if $n = 0$ and $k_z = 0$. The corresponding value which is the largest possible field strength H_{max} while remaining in the superconducting state, defined as $H_{max} = H_{c2}$ (upper critical field), is $H_{c2} = \phi_o /2\pi\xi^2(T)$. Using the equations (2.2.4-39 and -40), the relation between H_{c2} and the thermodynamic critical field H_c is found to be

$$H_{c2} = \phi_o /2\pi\xi^2(T) = 4\pi\lambda^2 H_c^2 /\phi_o = \sqrt{2}\kappa H_c. \qquad (2.2.4\text{-}45)$$

Let us consider the mixed state of a type-II superconductor in an applied magnetic field. There are vortex cores which can be described the lowering of the free energy and decreasing of superelectron density. We can consider the vortex core as a cylinder of normal state material with radius ξ. An increase of local free energy of $(\pi\xi^2)(H_c^2/8\pi)$ per unit length of a core comes from the appearance of a normal state core. However, there is the decreasing of local free energy of $(\pi\lambda^2)(H_a^2/8\pi)$ per unit length, because the material is not diamagnetic over a radius of the penetration depth $\approx \lambda$. To drive the superconductor into the mixed state, a minimum applied field, H_{c1}, is required. Therefore, H_{c1} is defined as the applied field at which there is no net gain of local free energy. By equating $(\pi\xi^2)(H_c^2 /8\pi) = (\pi\lambda^2)(H_a^2 /8\pi)$, we estimate that $H_a = H_{c1} \approx H_c /\kappa$. A more accurate treatment of the core energy provides the following relationship:

$$H_{c1} = [H_c \ln(\kappa + 1/2)] / (\kappa\sqrt{2}). \qquad (2.2.4\text{-}46)$$

Using equation (2.2.4-40), to eliminate H_c, we have

$$H_{c1} = \phi_o \ln(\kappa + 0.5)/4\pi\lambda^2. \qquad (2.2.4\text{-}47)$$

Finally, the three critical magnetic fields for type-II superconductors are related by the expression

$$H_{c1}H_{c2} = H_c^2 \ln(\kappa + 0.5). \qquad (2.2.4\text{-}48)$$

2.2.5 Kogan's Standard Local and Non-local London Formalisms

(1) Kogan's Standard Simple Local Limit London Formalism

In high-T_c superconductors (HTS), the values of the Ginzburg-Landau parameter κ (= λ/ξ) are much higher (>> 1) than those of conventional low-T_c superconductors. This means that we can estimate $H_{c2} >> H_{c1}$ as formed from equations (2.2.4-45, -46, and -47). In addition, there exists a broad field domain $H_{c1} << H << H_{c2}$ in which the average intervortex distance L obeys the inequality $\xi << L << \lambda$. In 1988, V. G. Kogan et al. showed that the reversible magnetization M is linear in the logarithm of the applied field H_a.[45] The argument proceeds as follows.

First, the free energy density of an individual vortex line and the repulsive interaction energy between vortex lines were calculated by A. Abrikosov.[62] For simple materials, Abrikosov theory leads to a hexagonal vortex lattice, shown by P. G. de Gennes.[63] Therefore, in a field domain $H_{c1} << H << H_{c2}$, the free energy density F, deduced using the London approach, is given by de Gennes[63] as

$$8\pi F = B^2 + (B\phi_o/2\pi\lambda^2) \ln(L\beta/\xi) \qquad (2.2.5\text{-}1)$$

where B is the magnetic induction, ϕ_o is the flux quantum (= 2.07×10^{-7} G-cm^2), β is a geometric factor of the order unity which depends on the flux lattice structure, and L is the average vortex separation which is defined $L = (\phi_o/B)^{1/2}$. A typical value of L is about 50 nm for B = 1 T. Using $L = (\phi_o/B)^{1/2}$ and equation (2.2.4-45) where $H_{c2} = \phi_o/2\pi\xi^2(T)$, the logarithm in equation (2.2.5-1) can be driven the following ways:

$$\ln(L\beta/\xi) = \ln[(\phi_o/B)^{1/2}\beta/\xi] = (1/2)\ln[(\phi_o/B)(\beta/\xi)^2] = (1/2)\ln(\beta_1 H_{c2}/B) \quad (2.2.5\text{-}2)$$

where $\beta_1 = 2\pi\beta^2$. From the differentiation of the free energy density (equation (2.2.5-1)) with respect to the magnetic induction B, we can get easily H as follows:

$$\begin{aligned} H = 4\pi(\partial F/\partial B) &= 4\pi(\partial/\partial B)[(B^2/8\pi + (B\phi_o/16\pi^2\lambda^2)\ln(L\beta/\xi)] \\ &= (\partial/\partial B)[(B^2/2 + (B\phi_o/4\pi\lambda^2)(1/2)\ln(\beta_1 H_{c2}/B)] \\ &= B + (\phi_o/8\pi\lambda^2)\ln(\beta_1 H_{c2}/B) + (B\phi_o/8\pi\lambda^2)(-1/B) \\ &= B + (\phi_o/8\pi\lambda^2)\ln(\beta_1 H_{c2}/eB) \\ &= B + (\phi_o/8\pi\lambda^2)\ln(\beta_2 H_{c2}/B) \end{aligned} \quad (2.2.5\text{-}3)$$

where $\beta_2 = \beta_1/e$. The pre-ln factor, $(\phi_o/8\pi\lambda^2)$, is equal to $H_{c1}/2\ln(\kappa + 0.5)$ from equation (2.2.4-47). This is small as compared to both H and B because of $H >> H_{c1}$ by initial assumption. Therefore, B in the $\ln(\beta_2 H_{c2}/B)$ can be set $\approx H$ and replaced by H under the ln sign. Using $B = H + 4\pi M$ relationship, finally we can deduce the relation for the magnetization M:

$$\mathbf{-4\pi M = (\phi_o/8\pi\lambda^2)\ln(\beta_2 H_{c2}/H)} \quad (2.2.5\text{-}4)$$

for pinning-free isotropic superconductors in the field domain $H_{c1} << H << H_{c2}$.

Now consider the influence of demagnetizing effects. In the field region ($H_{c1} << H << H_{c2}$), M is the order of H_{c1}. Since $H_{app} = H_{eff} + 4\pi DM$ where D is the demagnetization factor, the difference between H_{app} and H is small. Therefore, the field H in equation (2.2.5-4) can be regarded as the applied field, H_{app}. Thus, equation (2.2.5-4) shows that in the field domain ($H_{c1} << H << H_{c2}$), ***the reversible magnetization (M) should be linear in the logarithm of the applied field*** **(ln(H))**.

This formalism can be generalized to the case of anisotropic materials, eg. layered

compounds. V. G. Kogan generalized the London equation, using an anisotropic superconductive mass tensor.[64] Proceeding like the previous isotropic case, one can deduce the free energy for a lattice of vortices tilted at an angle θ with respect to the c-axis of the crystal:[65]

$$8\pi F = B^2 + (\phi_o/4\pi\lambda^2)(m_1 B_X^2 + m_3 B_Z^2)^{1/2} \ln(H_{c2}\,\beta/B), \qquad (2.2.5\text{-}5)$$

where the direction Z coincides with the c-axis of the single crystal, and the direction X is taken as the intersection of the Z-B (magnetic field) plane with the basal plane normal to the direction Z. By differentiating the free energy F with respect to B with the consideration of the components of B, we can get the field H and the magnetization M for uniaxial superconductor in the thermodynamic equilibrium:

$$-M_Z = (H_Z - B_Z)/4\pi = M_o\,[m_3 \cos\theta/\sqrt{m(\theta)}] \text{ and}$$

$$-M_X = (H_X - B_X)/4\pi = M_o\,[m_3 \sin\theta/\sqrt{m(\theta)}], \qquad (2.2.5\text{-}6)$$

where $M_o = (\phi_o/32\pi^2\lambda^2)\ln(H_{c2}\beta/H)$, $m(\theta) = m_1 \sin^2\theta + m_3 \cos^2\theta$, and θ is the angle between the applied field H (the direction of the vortices) and c-axis. Therefore, the component parallel to the applied field, M_p, and the component normal to the applied field, M_n, can be derived from equation (2.2.5-6):

$$M_p = M_Z \cos\theta + M_X \sin\theta = -M_o \sqrt{m(\theta)} \text{ and}$$

$$M_n = M_X \cos\theta - M_Z \sin\theta = -M_o\,[(m_3 - m_1)/\sqrt{m(\theta)}]\sin\theta\cos\theta. \qquad (2.2.5\text{-}7)$$

In the case of a polycrystal, with considering the randomly oriented crystalline grains which have magnetic moment $\boldsymbol{m}$ and summation over all possible azimuthal orientations, we can obtain the magnetization, M_{pc}, along the applied field:

$$M_{pc} = N\int_0^{\pi/2} \boldsymbol{m}_p(\theta)\sin\theta\, d\theta = \int_0^{\pi/2} M_p(\theta)\sin\theta\, d\theta, \qquad (2.2.5\text{-}8)$$

where N is the number of densities of grains and the magnetic moment $\boldsymbol{m} = V\boldsymbol{M}$. Using the equation (2.2.5-7), we can deduce the slope $dM_{pc}/d(\ln H)$:

$$dM_{pc}/d(\ln(H/H_o)) = (\phi_o/32\pi^2\lambda^2)\int_0^{\pi/2}[\sqrt{m(\theta)}]\sin\theta\, d\theta$$

$$= (\phi_o/64\pi^2\lambda^2)(\sqrt{m_1})f(\gamma), \qquad (2.2.5\text{-}9)$$

where H_o is an arbitrary scaling field,

$$\gamma^2 = m_3/m_1, \text{ and } f(\gamma) = \gamma + (\gamma^2 - 1)^{-1/2}\ln[(\gamma^2 - 1)^{1/2} + \gamma]. \qquad (2.2.5\text{-}10)$$

If we take $\gamma = m_1 = f/2 = 1$ for the isotropic materials, the slope of equation (2.2.5-9) coincides with the result of the slope from equation (2.2.5-4).

As we know that from equations (2.2.5-4 and -9), we can obtain the average penetration depth λ from the slope $dM/d(\ln H)$ of the reversible magnetization M as a function of $\ln H$: $dM/d(\ln H) \propto \lambda^{-2}$. In addition to the average penetration depth λ, we can estimate the upper critical field H_{c2} from the extrapolation of the linear parts of $M(\ln H)$ to $M = 0$, with assumption $\beta_2 = 1$. To summarize, this simple London formalism gives a simple method for obtaining the penetration depth λ and the upper critical field H_{c2} for clean superconducting materials having high values of the Ginzburg-Landau parameter κ.

(2) Kogan's Non-local London Formalism

As described previously, we can explain relatively well the magnetic properties near T_c by the Ginzburg-Landau theory. However, it is hard to apply GL theory in the low temperature region of far from T_c. On the other hand, the London formalism applies to high-κ materials at any temperature, because the contribution of vortex cores to the total

energy is small. As we know from equation (2.2.5-4), the simple local London model predicts a linear relationship between magnetization (M) and the logarithm of the applied field ($\ln H$). However, at low temperatures, the plots of M versus $\ln(H)$ deviated from the predicted linearity, for some samples of high-κ, high-T_c superconducting materials from the Bi- and Tl-based families. Therefore, Kogan et al. reconsidered in detail the London approach at low temperatures and rederived more general London equations that contain a nonlocality in the current-field relation.[46] As mentioned in the previous section, a nonlocal current-field relation was first suggested by Pippard. After that, BCS theory extensively developed nonlocal electrodynamics by providing an integral equation with a Kernel extending to distances $\sim\xi_o$, the coherence length at $T = 0$ K (a finite size of Cooper pairs). Those studies of nonlocality focused mainly on the vortex core region for materials with $\kappa \sim 1$. Below we show the current-field relations from several theories: GL, local London, and BCS nonlocal theory. At first, the current-field relation of the GL theory which introduced the order parameter is

$$(4\pi/c)\, j(r) = -(|\Psi|^2/\lambda^2)[A + (\phi_0/2\pi)\nabla\theta]_r. \qquad (2.2.5\text{-}11)$$

Second, the current-field relation of the local London theory with $|\Psi|^2 = 1$ is

$$(4\pi/c)\, j(r) = -(1/\lambda^2)\, a(r). \qquad (2.2.5\text{-}12)$$

Third, the current-field relation of the BCS nonlocal theory is

$$(4\pi/c)\, j(r) = -\int Q(r-r')\, a(r')\, dr', \qquad (2.2.5\text{-}13)$$

where near T_c nonlocality is irrelevant because $\xi(T) >> \xi_o$. Recently, Kogan et al. have developed relatively simple corrections to London equation to allow for limited nonlocality in high-κ superconducting materials at low temperatures.[46]

The main assumption in Kogan's recent approach is that the spatial dependence of the order parameter Δ, the gap function, due to supercurrents can be ignored. The starting point for the nonlocal extensions is the quasiclassical Eilenberger equation of the BCS theory,[66]

$$\mathbf{v}\cdot\prod f = 2\Delta\, g/\hbar - 2\omega f + (g\langle f\rangle - f\langle g\rangle)/\tau, \tag{2.2.5-14}$$

$$g^2 = 1 - ff^+, \tag{2.2.5-15}$$

$$(\Delta/2\pi T)\ln(T_c/T) = \sum_{\omega>0}(\Delta/\hbar\omega - \langle f\rangle), \tag{2.2.5-16}$$

$$j = -4\pi|e|N(0)T\,\mathrm{Im}\sum_{\omega>0}\langle \mathbf{v}g\rangle, \tag{2.2.5-17}$$

where $\mathbf{v}$ is the Fermi velocity, $\Pi = \nabla + 2i\pi A/\phi_o$, $\Delta(r)$ (due to condensate of pairs) is the gap function, $f(r,\mathbf{v},\omega)$ (due to condensate of pairs), $f^+ = f^*(r,\mathbf{v},\omega)$, and g (due to normal electrons) are Eilenberger Green's functions, $N(0)$ is the total density of states at the Fermi level per one spin, $\hbar\omega = \pi T(2n+1)$ with an integer n, $\langle \ldots. \rangle$ means the average over the Fermi surface, and τ is the scattering time due to nonmagnetic impurities. In the absence of current and field, we have

$$f_0 = \Delta_0/\beta_0,\ g_0 = \hbar\omega/\beta_0,\ \text{and}\ \beta_0 = (\Delta_0^2 + \hbar^2\omega^2)^{1/2}. \tag{2.2.5-18}$$

If a weak supercurrent flows ($j = \phi_o/\xi\lambda^2$), one can search for solutions of equations (2.2.5-14, -15, -16) in the form (with small f_1 and g_1):

$$\Delta = \Delta_0 e^{i\theta},\ f = (f_0 + f_1)e^{i\theta},\ f^+ = (f_0 + f_1^+)e^{-i\theta},\ \text{and}\ g = g_0 + g_1. \tag{2.2.5-19}$$

Therefore, when we solve for f_1 and g_1, the first order corrections (f_1 and g_1) for f and g in Fourier space are

$$g_1(k) = (I\hbar\pi\Delta_0^2/\beta_0\phi_o)\{1/[\beta_0^2 + \hbar^2(\mathbf{v}\cdot k)^2/4]\}(\mathbf{v}\cdot a), \tag{2.2.5-20}$$

$$f_1(k) = -(I\hbar\pi\Delta_0/\beta_0\phi_o)\{[\omega - I\hbar(\mathbf{v}\cdot k)/2]/[\beta_0^2 + \hbar^2(\mathbf{v}\cdot k)^2/4]\}(\mathbf{v}\cdot a). \tag{2.2.5-21}$$

Substituting g_1 in equation (2.2.5-17), one can deduce the BCS current-field relation

$$j_i(k) = - [4\pi e^2 N(0) T\Delta_0^2/c] a_i(k) \sum_{\omega>0} (\beta'/\beta_0^2) \langle v_i v_l / [\beta'^2 + \hbar^2 (\mathbf{v}\cdot k)^2/4] \rangle, \quad (2.2.5\text{-}22)$$

where $\beta' = \beta_0 + \hbar/2\tau$ and $a = \phi_o P/2\pi = A + \phi_o \nabla\theta/2\pi$. Finally, keeping the first order correction in small k's, one can find the current-field relation

$$(4\pi/c) j_i = - (1/\lambda^2)(m_{ij}^{-1} - \lambda^2 n_{ijlm} k_l k_m) a_j, \quad (2.2.5\text{-}23)$$

where $1/\lambda^2 = (16\pi^2 e^2 N(0) T\Delta_0^2 \langle v^2 \rangle/3c^2) \sum_{\omega>0} (1/\beta_0^2 \beta')$, $m_{ij}^{-1} = 3\langle v_i v_j \rangle / \langle v^2 \rangle$, and

$$n_{ijlm} = (4\pi^2 e^2 \hbar^2 N(0) T\Delta_0^2 / c^2) \langle v_i v_j v_l v_m \rangle \sum_{\omega>0} (1/\beta_0^2 \beta'^3). \quad (2.2.5\text{-}24)$$

If $v^2 k^2 << \beta_0^2$, or $k^2 \xi_0^2 << 1$, then the equation (2.2.5-23) can be reduced the standard local limit anisotropic London equation (the first term on the right side of equation (2.2.5-23):

$$(4\pi/c) j_i = - (1/\lambda^2) m_{ij}^{-1} a_j \quad (2.2.5\text{-}25)$$

Meanwhile, the last term on the right side of the equation (2.2.5-23) is due to nonlocality.

For an isotropic system in the layer planes, from the equation (2.2.5-24) one can obtain and define the followings:

$$n_0 \lambda^2 = (\hbar^2 v^2 / 16\Delta_0^2) \gamma(T) \equiv \rho^2(T), \quad (2.2.5\text{-}26)$$

where ρ is a nonlocality radius, which is the order of the coherence length at $T = 0$ K. The temperature dependence of ρ is given by

$$\gamma(T) = \Delta_0^2 \sum(1/\beta_0^2 \beta'^3) / \sum(1/\beta_0^2 \beta'). \quad (2.2.5\text{-}27)$$

Values of γ, calculated from equation (2.2.5-27), are plotted versus reduced temperature $t = T/T_c$ in Figure 2-9. The various curves refer to progressively more "dirty" materials with shorter and shorter electronic mean free path ℓ. From the Figure, one sees that the

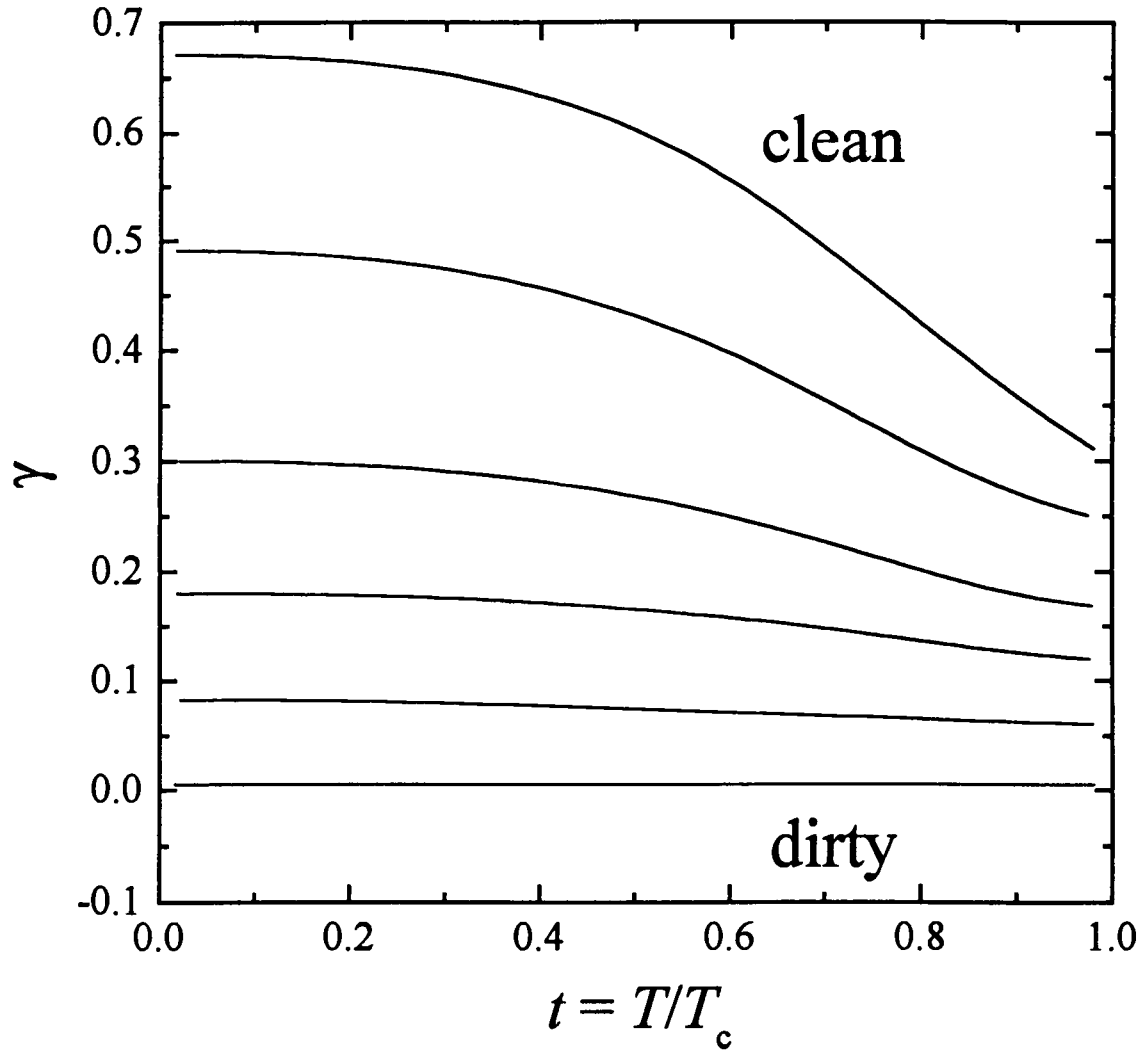


Figure 2-9. Parameter γ versus reduced temperature t which determines the temperature dependence of nonlocality radius ρ for the scattering parameter (impurity parameter) $\xi_2 / l = 0$ (the upper curve), 0.2, 0.5, 1, 2, and 10 (the bottom curve). (V.G. Kogan et al., Phys. Rev. **B 54**, 12386 (1996))

nonlocality radius, $\rho \propto \sqrt{\gamma}$, is reduced by temperature and by impurity scattering. In the clean limit ($\xi / \ell << 1$), the nonlocal effects are significant at low temperatures. However, in the dirty limit, γ becomes T-independent, that is, all nonlocal effects disappear.

If we apply the equation to a vortex along the z-axis, then the equation (2.2.5-23) reduces to $(4\pi j_\alpha / c) = - (1 - \rho^2 k^2)\, a_\alpha / \lambda^2$. Isolating the vector potential $\boldsymbol{a}$, using $\nabla \times \boldsymbol{a} = \boldsymbol{H} - \phi_o(z/z)\delta(r)$ of the flux quantization condition, and neglecting ~ $\rho^4 k^4$ terms, one obtains for the magnetic field:

$$H(k) = \phi_o / (1 + \lambda^2 k^2 + \rho^2 \lambda^2 k^4); \qquad (2.2.5\text{-}28)$$

this differs from the corresponding single vortex expression ($H(k) = \phi_o / (1 + \lambda^2 k^2)$) in simple local London theory. Next substitute $H(\boldsymbol{G})$ at reciprocal lattice vectors $\boldsymbol{G}$ (from equation (2.2.5-28)) into the expression $F = B^2 \sum_G H(G)/8\pi\phi_o$ for the free energy density of a flux line lattice; then for fields $H_{c1} << B << H_{c2}$, integrate from $G_{min} = [(2\pi^2\sqrt{3})B/\phi_o]^{1/2}$ (for a hexagonal vortex lattice) to $G_{max} = 2\pi/\xi'$, one then obtains the following results, ignoring terms of order ~ $O(\kappa^{-2})$.

$$\boldsymbol{F'} = \boldsymbol{M}_0\, B\{\ln[(H_0/B + 1) / (H_0/\eta_2 H_{c2} + 1)] + \eta_1\}, \qquad (2.2.5\text{-}29)$$

where $H_0 = \phi_o / 2\pi^2\sqrt{3}\rho^2$, $\boldsymbol{M}_0 = \phi_o / 32\pi^2\lambda^2$, and the constants η_1 and η_2 absorb uncertainties in the core energy and in the cutoff. Finally, from $\boldsymbol{M} = \boldsymbol{B}/4\pi - \partial\boldsymbol{F}/\partial\boldsymbol{B} = - \partial\boldsymbol{F'}/\partial\boldsymbol{B}$, one can obtain the following result for the magnetization, within Kogan's nonlocal London formulation:[46]

$$\boldsymbol{M} = - \boldsymbol{M}_0\, [\ln(\boldsymbol{H}_0/\boldsymbol{B} + 1) - \boldsymbol{H}_0/(\boldsymbol{H}_0 + \boldsymbol{B}) + \zeta(T)], \qquad (2,2.5\text{-}30)$$

where $\zeta(T) = \eta_1 - \ln(H_0/\eta_2 H_{c2} + 1)$. Therefore, the nonlocal London formula for the

reversible magnetization in intermediate fields contains the field scale $H_0 \sim \phi_o/\rho^2$ instead of $H_{c2} \sim \phi_o/\xi^2$, which the local limit London formula (2.2.5-4) contains. Unlike the temperature dependent of H_{c2}, the field H_0 does not go to zero at $T = T_c$ but rather increases as the temperature increases.

Finally, if one also allows for possible thermal fluctuations of vortices, then a fluctuation term should be added to M in the equation (2.2.5-30). The fluctuation term has the form $\delta M = (k_B T/\phi_o s) \ln(C\kappa^2 k_B T/\phi_o sB)$, where s (= $c/2$) is the interlayer spacing and the constant $C \approx 10.2$.[46] So, which local London theory gives a constant slope from the linear relationship between M and $\ln(B)$ as we know, the nonlocal London formalism yields a nonlinear slope

$$S = d(M)/d(\ln B) = M_0/(1 + B/H_0)^2 - k_B T/\phi_o s. \qquad (2.2.5\text{-}31)$$

On the other hand, in the case of strongly anisotropic materials (polycrystalline), although we do not use, the nonlocal London formula of the reversible magnetization M can be derived as

$$M = -(M_0/2)\{\ln[(H_0+B)/B] + (H_0^2/B^2)\ln[(H_0+B)/H_0] - H_0/B + \zeta\} + \delta M, \qquad (2.2.5\text{-}32)$$

where $\delta M = (k_B T/2\phi_o s) \ln(C\sqrt{e}\kappa^2 k_B T/\phi_o sB)$. In addition, in the dirty case or near T_c for any mean free path ℓ,

$$M = -(M_0/2) \ln(\eta \sqrt{e} H_{c2}/B) + (k_B T/2\phi_o s) \ln(C\sqrt{e}\kappa^2 k_B T/\phi_o sB). \qquad (2.2.5\text{-}33)$$

2.3 Experimental Results and Analysis

2.3.1 Magnetization Studies in the Superconducting State

In this work, magnetization studies have been carried out in order to understand the superconducting properties of YNi_2B_2C single crystal and its magnetic phase diagram in the *H-T* plane. In previous magnetic studies, Ming Xu et al. found that YNi_2B_2C appears to be a relatively conventional low-T_c superconductor.[67] R. Movshovich et al. concluded that there is modestly strong coupling and a conventional pairing mechanism in YNi_2B_2C.[68] However, the superconducting length scales and characteristic magnetic fields are not well established for this material. In addition, the magnetic field-temperature (*H vs. T*) phase diagram for the system has not been fully established. There are still many controversies and complicated problems.[69-71] In this section, the superconducting length scales and non-local effect will be treated. In the following sections, the normal state properties and the critical magnetic fields - the thermodynamic critical field H_c, lower critical field H_{c1}, and upper critical field H_{c2} - will be discussed.

Previous magnetization measurements on the single crystal of YNi_2B_2C were analyzed using Ginzburg-Landau and simple London-limit theories.[67] The analysis yielded the value $\kappa (= \lambda/\xi) = 13 \sim 15$ for the GL-parameter,[67] indicating type-II superconductivity. Generally, Ginzburg-Landau theory is applicable in a temperature regime near the critical temperature T_c. Although conventional London theory is valid for all temperatures, there is no simple macroscopic description far from T_c, as V. G. Kogan et al. pointed out.[46] High κ ($>>1$) materials, in the intermediate field regime with $H_{c1} << H << H_{c2}$, are described

relatively well by standard London-limit theory; however, this theory does not account for the kinetic energy and the condensation energy terms arising from a suppression of the order parameter in vortex cores.[45,49,72,73] A complete microscopic formalism should be employed to suitably describe the vortex cores.[46]

Recently, small angle neutron scattering (SANS) studies have shown that the flux line lattice (FLL) in borocarbides can change from square to hexagonal symmetry as a function of vortex density, i.e. magnetic field.[31-35] When the magnetic field H is applied parallel to the tetragonal (00c)-axis, the local supercurrent density $j(r)$ of a vortex circulates in the square crystallographic basal plane. At first, the FLL is nearly hexagonal in low field H, where the vortices are far apart and interact weakly. At larger but still modest field levels, the FLL becomes rhombohedral and appears to undergo a first order structural transition. Finally, at higher field, the FLL becomes square. This seemingly unusual behavior of the vortex lattice is difficult to explain within the conventional standard London theory, which cannot account for either the symmetry of the FLL or features in the equilibrium magnetization that deviates significantly from simple London predictions. This standard London theory is local, with $a(r) \propto j(r)$. However, for clean type-II superconductors with a long electronic mean free path, the current density j is determined non-locally by an integral over a region of the size of coherence length (ξ_o). Non-local London theory[46] has provided a good description of the FLL transformation at low fields.[43] Below we show that the equilibrium magnetization of the single crystal of YNi_2B_2C, which deviates significantly from simple London predictions, is well described by non-local London theory.[41]

When the electronic mean free path is long in clean type-II superconducting materials with high κ, Kogan et al. suggested that non-local theory should be used.[46] The standard London-limit expression,

$$M = -(\phi_o/32\pi^2\lambda^2)\ln(\eta H_{c2}/H), \qquad (2.3.1\text{-}1)$$

contains the upper critical field $H_{c2} \propto \phi_o/\xi^2$ as the field scale. For clean materials at low temperature, they argued that the field scale should be $H_0 \propto \phi_o/\rho^2$, where ρ is the non-locality range on the order of $\xi_o(T=0\ \mathrm{K})$.[46] Thus, when non-locality is important, the resulting expression for M is[46]

$$M = -M_0[\ \ln(H_0/H + 1) - H_0/(H_0+H) + \zeta\ ] + \delta M. \qquad (2.3.1\text{-}2)$$

Here $H_0 = \phi_o/(\rho^2 2\pi^2\sqrt{3})$, $\delta M = (k_B T/\phi_o s)\ln(C\kappa^2 k_B T/\phi_o s H)$ and $\zeta(T) = \eta_1 - \ln(H_0/\eta_2 H_{c2} + 1)$, where both η_1 and η_2 are constants of order unity. In previous sections (2.2.4 and 2.2.5), local and non-local relations have been treated in detail theoretically. In contrast with H_{c2} that decreases as temperature increases, H_0 increases gradually as temperature increases. Thus, the non-local expression (2.3.1-2) reduces to the local equation (2.3.1-1) as T approaches T_c. Furthermore, for dirty superconducting materials, where ρ is small and H_0 is very large, the non-local form collapses to the local form at all temperatures. Consequently, the non-local theory predicts that the equilibrium magnetization should vary logarithmically with field H near T_c, but deviate significantly from logarithmic behavior at low temperatures (well below T_c).

In this work, the equilibrium magnetization of a clean single crystal of YNi_2B_2C is shown to deviate significantly from simple London predictions, but it is well described by the non-local theory. Prior to experimental studies in low magnetic fields, the

superconducting magnet in the magnetometer was "reset" to release trapped flux in its windings, by heating it above its T_c. The Meissner state magnetic moment m was measured under zero-field-cooled (ZFC) and field-cooled (FC) conditions in an applied field H = 10 G. In all case, the magnetization M[G] = m[Gcm^3]/V[cm^3] was based on the volume V, using the theoretical mass density ($\rho_{x\text{-}ray}$ = 6.05 g/cm^3), calculated from the lattice parameters.[23,24] Figure 2-10 shows ZFC and FC magnetization $M(T)$ curves with an applied field H = 10 G. The superconductive transition temperature T_c was determined as the point at which the linearly varying FC magnetization $M(T)$ extrapolates to zero, which ignores a very slight "tail" at higher temperature. The value of T_c is 14.5 K (onset 15.6 K). Hysteresis loops $M(H)$ in the mixed state were measured in fields up to 6.5 T. In the following, the values of magnetization (M) are corrected for the normal state magnetization, measured at a temperature of 20 K. To obtain the equilibrium magnetization in the presence of weak hysteresis, we average the increasing- and decreasing-field values. Overall, however, this material is remarkably reversible, magnetically. Figure 2-11-(a) and -(b) show the magnetization curve at T= 3 K and 5 K with magnetic field parallel to c-axis.

According to the standard local London theory, the equilibrium magnetization M should be linear in ln(H). The non-local theory predicts, however, a nonlinear dependence at low temperature. Figure 2-12 shows plots of M versus ln(H) at various temperatures. The linear dependence for T near T_c is clear. Well below T_c, however, the data progressively deviate from a simple linear dependence, where non-local effects should be significant. In analyzing the experimental data the fluctuation term (δM) is not considered, as it is expected to be small for this low-T_c material. The fitting procedure for the experimental equilibrium

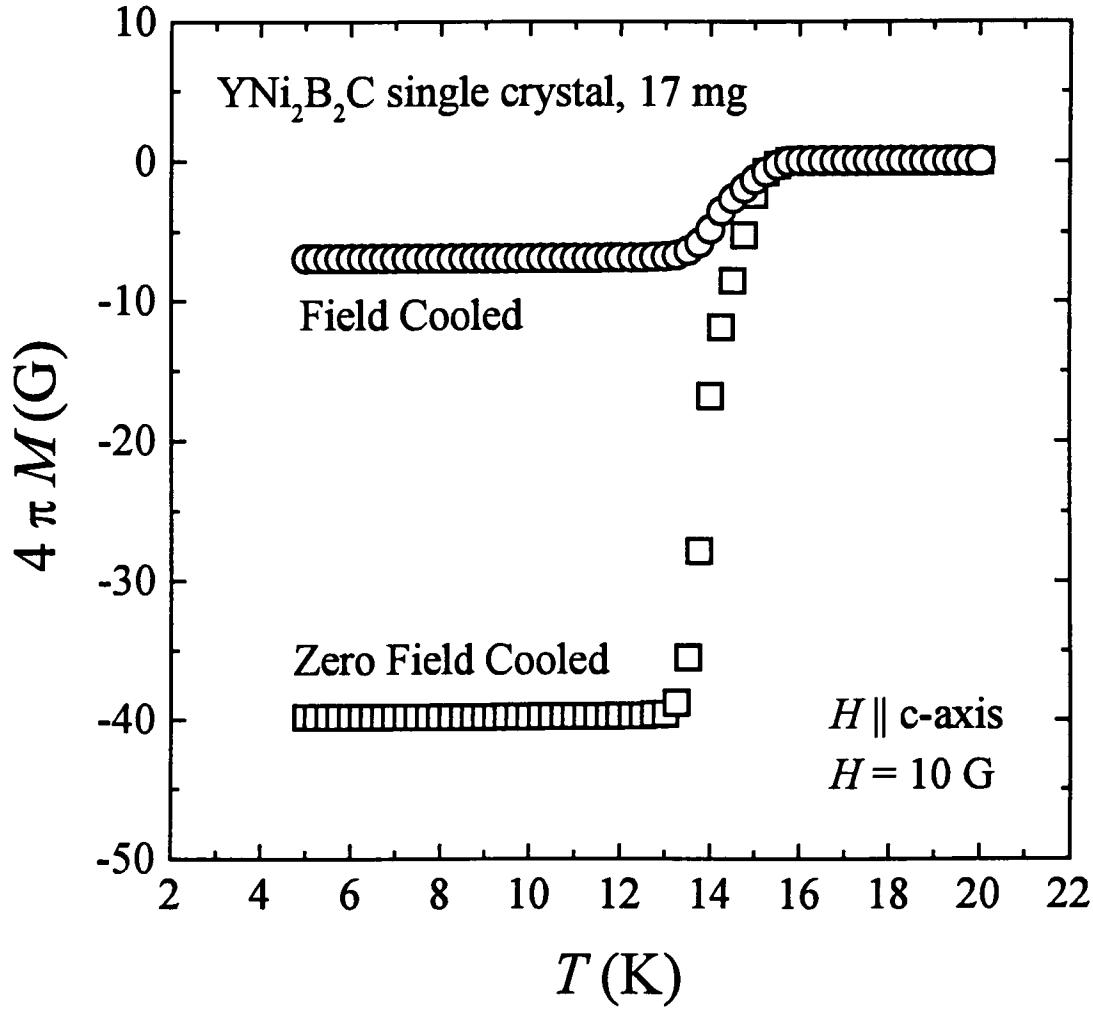


Figure 2-10. ZFC and FC magnetization curves as the function of temperature, for YNi_2B_2C.

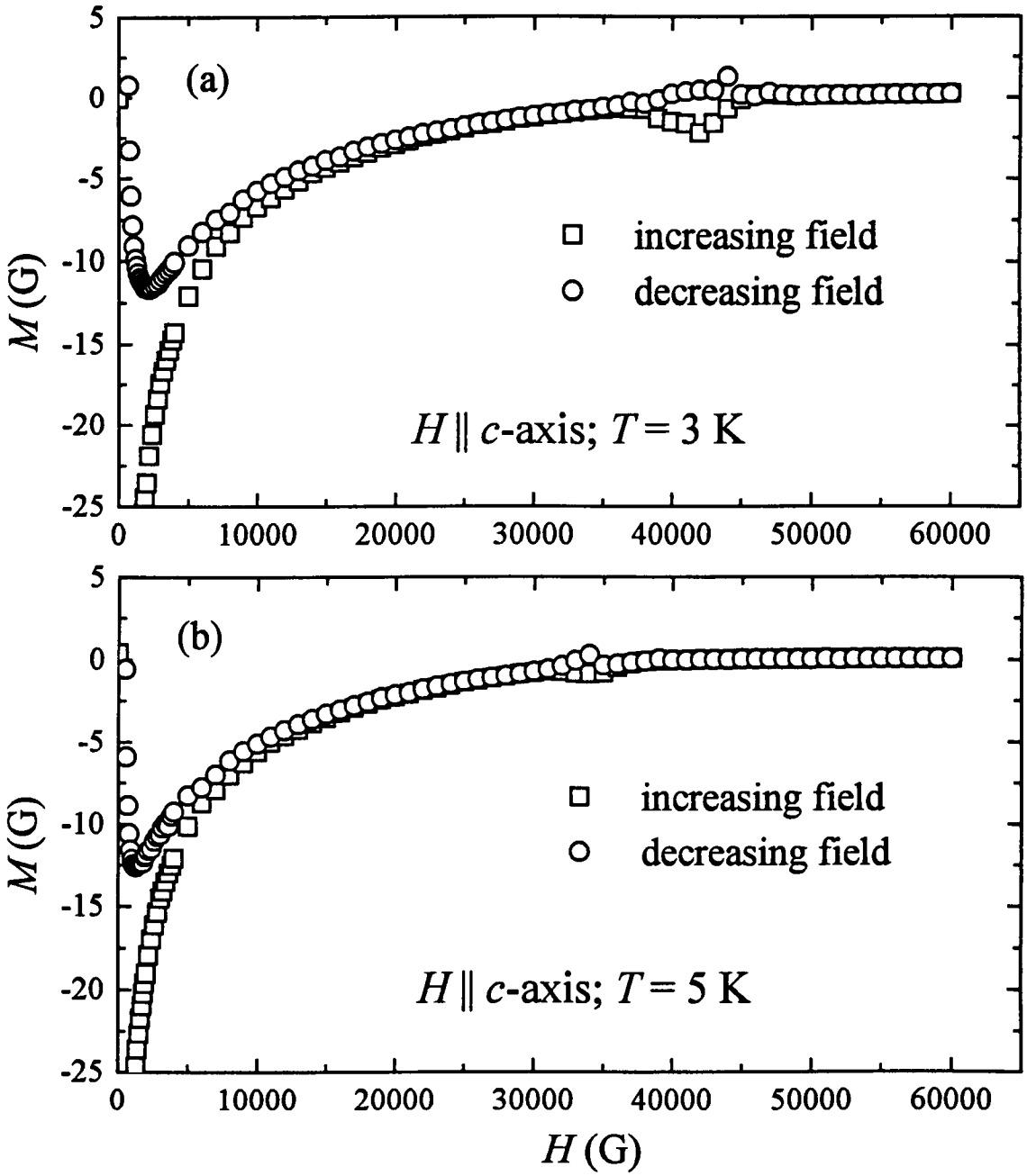


Figure 2-11. The magnetization M of YNi_2B_2C versus H (a) at $T = 3$ K and (b) $T = 5$ K, for magnetic field H applied parallel to c-axis (001).

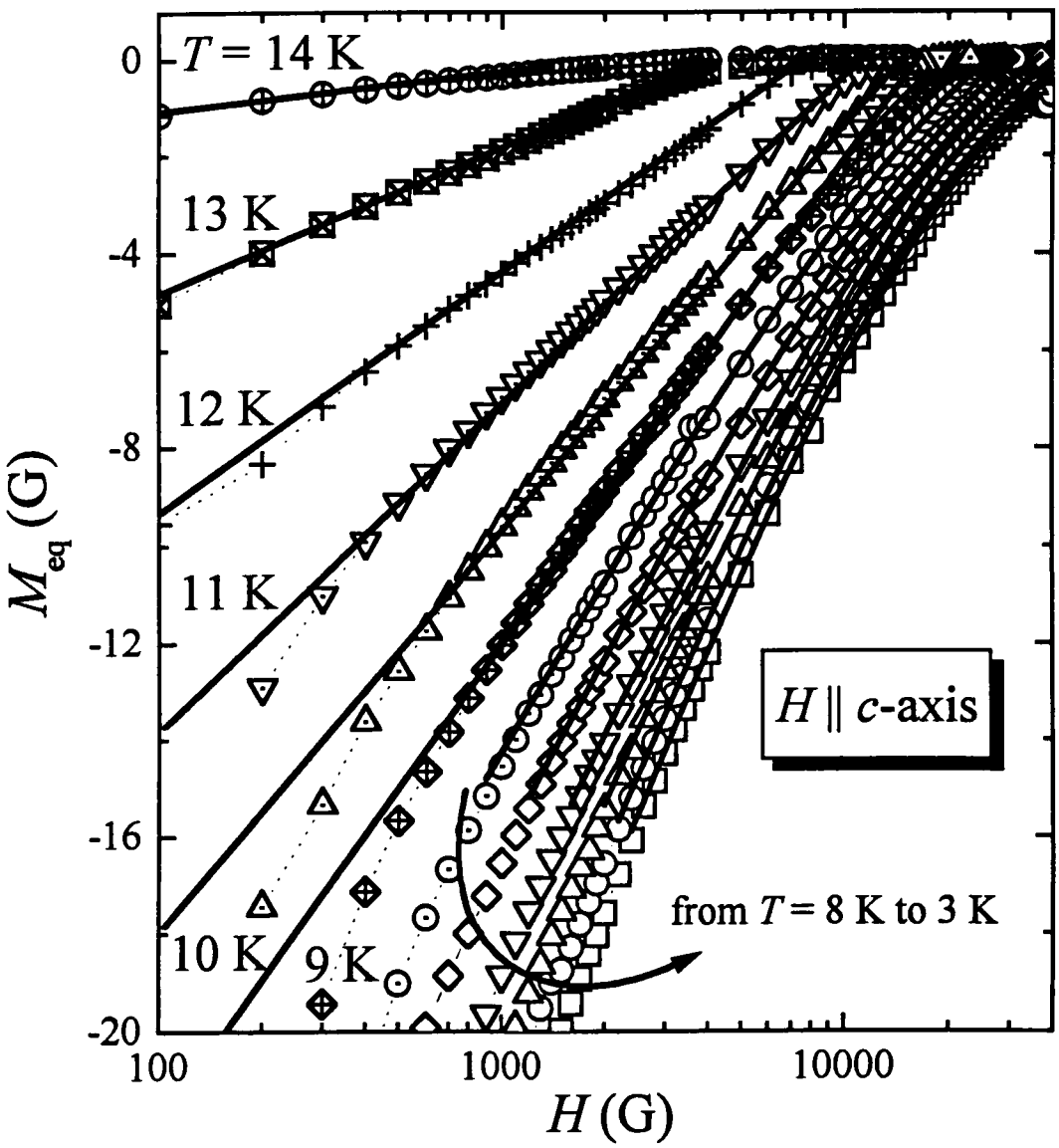


Figure 2-12. A semilogarithmic plot of equilibrium magnetization M_{eq} versus H, for temperatures from 14 K to 3 K. The local London theory, equation (2.3.1-1), predicts the linear dependence seen at higher temperature (above 10 K). The nonlocal London theory, equation (2.3.1-2), describes the data well at lower temperatures.

magnetization M[G] at a given temperature (T) is as follows. First, we note that equation (2.3.1-2) contains three fitting parameters M_0, H_0, and ζ, corresponding to the three length scales λ, ρ, and ξ. For each fixed value of T, the experimental data (M[G]) have been fitted using a nonlinear regression routine to the non-local equation (2.3.1-2). Figure 2-13 shows an example of the non-local analysis of data T = 3 K, 5 K, and 7 K. In Figure 2-12, the solid lines at low temperature region are calculated using the same methods.

To see the behavior of three fitting parameters, their temperature dependencies are presented in Figure 2-14 for magnetic field H parallel to (001)-direction. First, the temperature dependence of $H_0(T)$ is shown in Figure 2-14-(a). As this figure shows, $H_0(T)$ increases with T as the formalism predicts, because the non-local radius (ρ) decreases with T. In addition, the quantity $\gamma(T)H_0(T)$, where $\gamma(T)$ gives the temperature dependence of the non-local radius ρ, is temperature independent. This major consistency test for the non-local analysis follows from the theory which predicts that $\gamma(T)H_0(T) \propto \phi_0/\xi_0^2$. Second, Figure 2-14-(b) shows the resulting parameter $M_0 = \phi_0/32\pi^2\lambda^2(T)$. The temperature dependence of λ can be derived from M_0 for a wide range of temperature. Third, the parameter $\zeta(T)$ is shown in Figure 2-14-(c). Overall, the temperature dependencies of M_0 and ζ are qualitatively similar to those found for the high-T_c materials studied earlier.[46] So far, the non-local London formalism of Kogan et al.[46] has described the data well and has provided a good consistency check with the quantity $\gamma(T)H_0(T)$.

As mentioned above, the temperature dependence of the London penetration depth λ can be obtained from the parameter $M_0 = \phi_0/32\pi^2\lambda^2(T)$. Figure 2-15-(a) shows the T dependence of λ obtained from both non-local London analysis at low temperature region

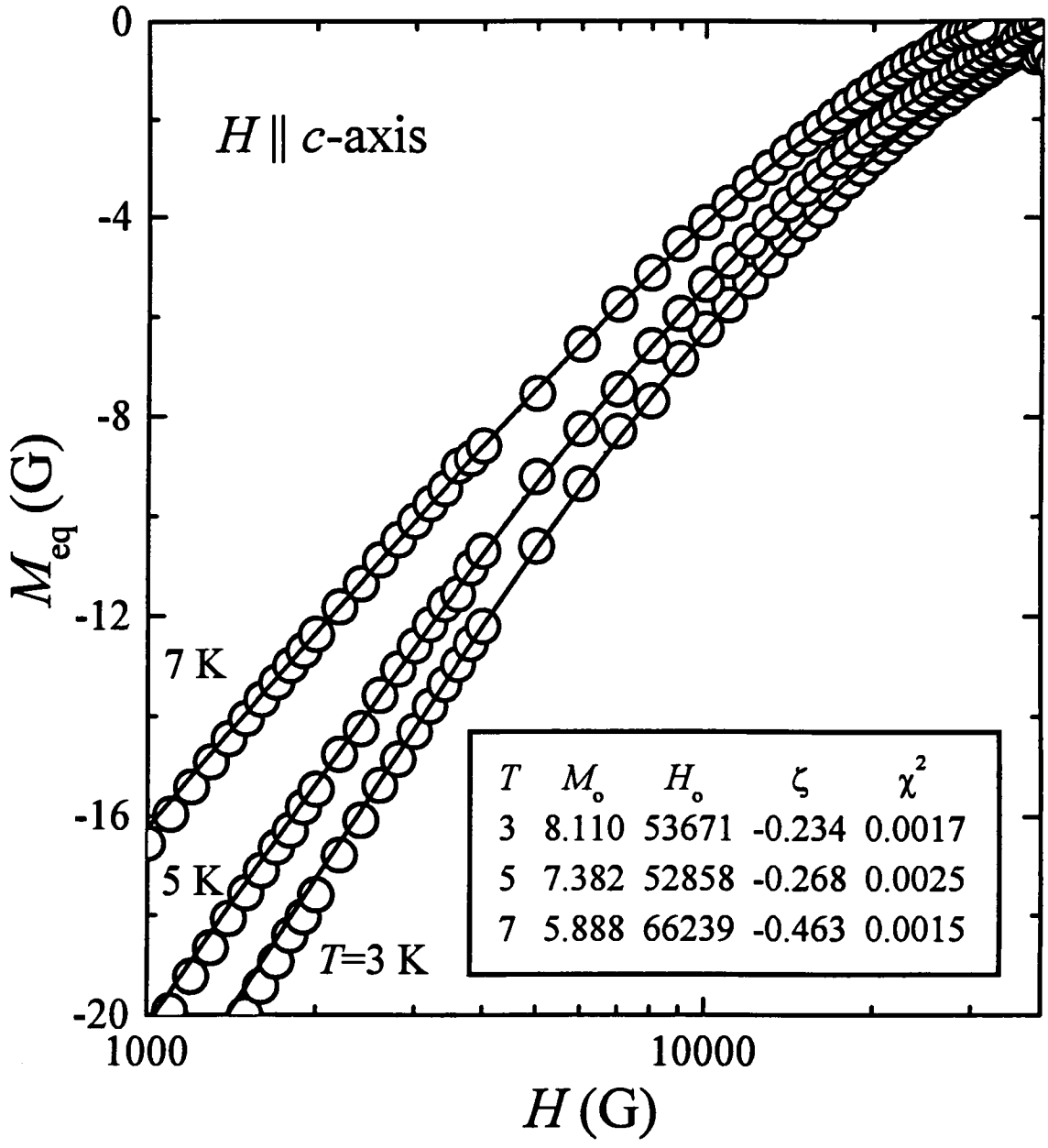


Figure 2-13. A semilogarithmic plot of equilibrium magnetization M_{eq} versus H at several temperatures. The solid lines show the non-local London theory fitted to the data, with parameters M_o, H_o, and ζ.

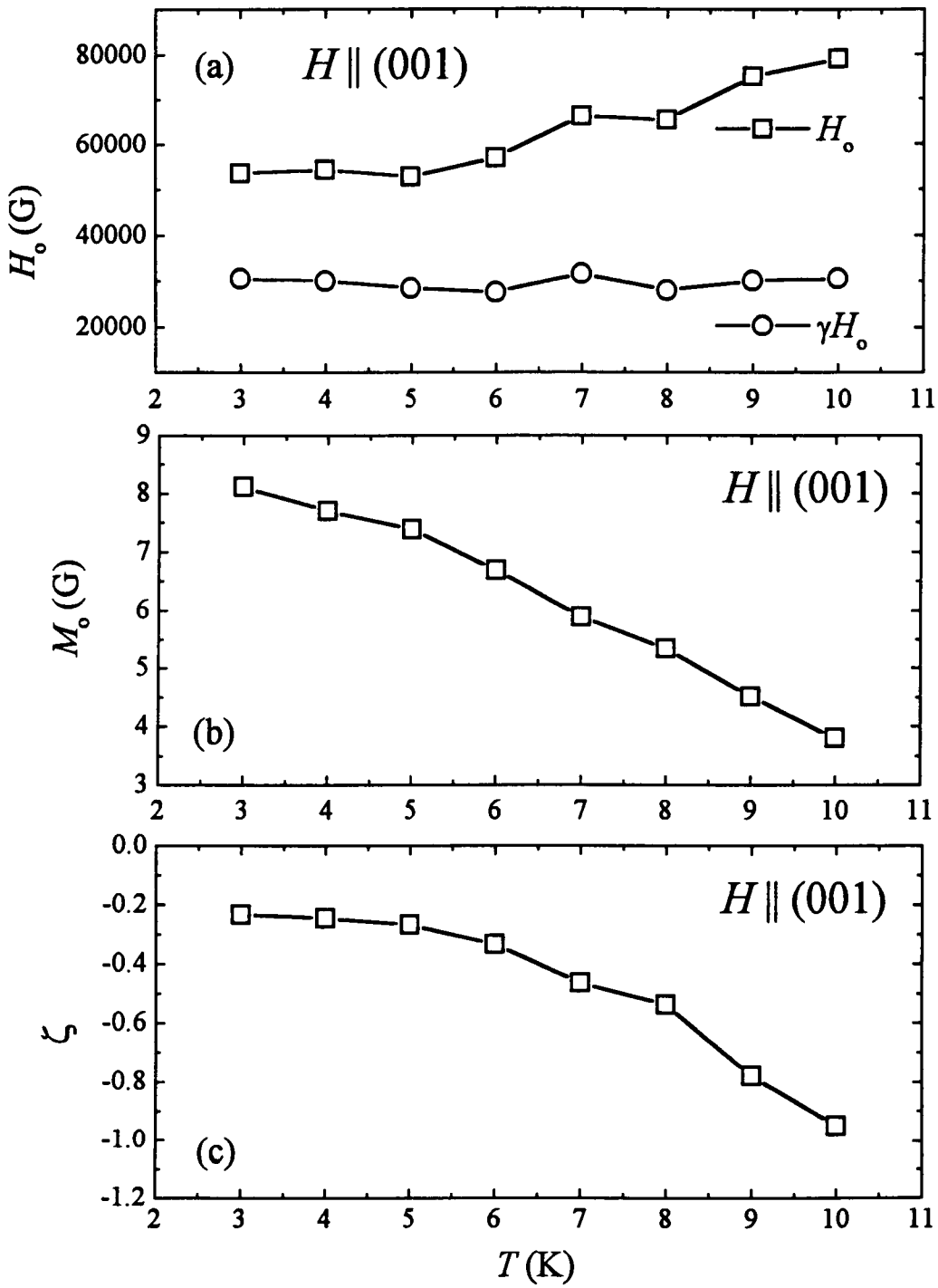


Figure 2-14. Parameters from non-local London analysis versus temperature T: (a) the field scale $H_o \sim \phi_o/\rho^2$ and product $\gamma(T)\, H_o(T) \sim \phi_o/\xi_o^2$, (b) the magnetization $M_o = \phi_o/32\pi^2\lambda^2$, and (c) dimensionless quantity ζ.

and a standard local London analysis near T_c. At first, we tried to fit the data for $1/\lambda^2$ using some power-law functions of $t = T/T_c$, and found $t^{3/2}$ to provide a good fit. Contrary to the exponential dependence expected for s-wave pairing, the nearly T^3 behavior for $\lambda(T)$ below 10 K in the single crystal of YNi_2B_2C seems to give evidence for a non-s-wave pairing scheme, perhaps similar to the dependencies in $HgBa_2CuO_4$, where $\lambda_{ab} \propto T$ and $\lambda_c \propto T^5$, which is consistent with d_{x2-y2} symmetry of the order parameter.[74,75] Another example is the dependence T^2 in YBCO at low temperature.[74,75] Using $1/\lambda^2 \sim (1 - t^2)$, the London penetration depth extrapolates to about 90 nm at $T = 0$ K for field H parallel to (001)-direction; this is considerable smaller than the value 150 nm deduced by Ming Xu et al.,[67] who analyzed their results using a simple London and Ginzburg-Landau formalisms near T_c. Figure 2-15-(a) shows that the plot of $1/\lambda^2$ versus T is linear near T_c, as expected from Ginzburg-Landau theory. Furthermore, there is reasonably good agreement between the magnetization results in this study and neutron scattering results, which come from the intensity I of neutrons diffracted from the FLL.[33] The diffraction intensity of the (01) reflection is

$$I \propto (1/\lambda^2)^2 \times (1 - H/H_{c2})^2 \times \exp(-\pi H/H_{c2}). \qquad (2.3.1\text{-}3)$$

Thus, $[\lambda(0)/\lambda(T)]^2$ can be estimated from above equation (2.3.1-3), using values for $H_{c2}(T)$ from the magnetization study, where $dH_{c2}(T)/dT = -3.8$ kG/K near T_c. Figure 2-15-(a) shows that the values deduced from the neutron scattering intensity agree fairly well with the penetration depth values from the magnetization study. In addition, Figure 2-15-(b) shows $\lambda^2(0)/\lambda^2(T)$ plotted versus $t=T/T_c$ comparing the experimental temperature dependence with several theories. The data fairly well agree with the traditional, empirical

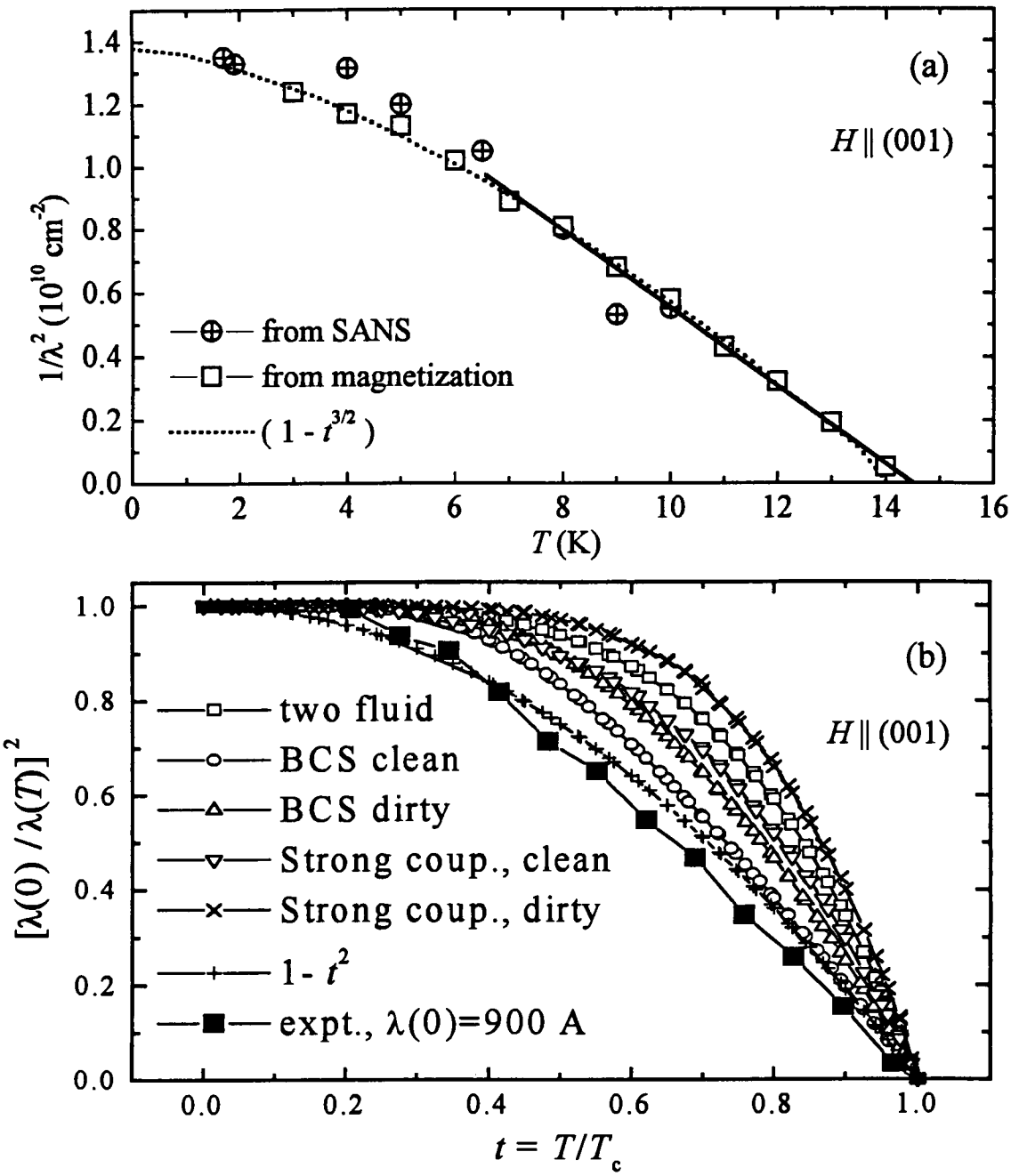


Figure 2-15. The London penetration depth λ, obtained with field $H \parallel (001)$; (a) open squares came from magnetization analysis, standard London near T_c and nonlocal London far below T_c (below 10 K), dotted line from empirical function $(1-t^{3/2})$, cross circles from neutron scattering intensity, and straight solid line is Ginzburg-Landau dependence near T_c. (b) $[\lambda(0)/\lambda(T)]^2$ versus $t = T/T_c$, with several theoretical lines.

$(1-t^2)$ dependence.

Let us recall that the equilibrium magnetization M is linear in $\ln(H)$ in the standard local-London theory, with slope $S = dM/d(\ln H) \propto 1/\lambda^2$. As showed previously, the equilibrium magnetization M[G] of this crystal is not linear in $\ln(H)$ at low temperature. In the non-local London theory, the modified expression is

$$1/\lambda^2 \propto S = dM/d(\ln H) = [M_0/(1+H/H_0)^2] - k_B T/\phi_o s, \qquad (2.3.1\text{-}4)$$

where again we neglect the last term due to fluctuations. In Figure 2-16, the upper panel shows the field H dependence of $S = dM/d(\ln H)$ with the field H parallel to the (001)-direction, and the lower panel shows the temperature T dependence of dS/dH, where the fluctuation term is ignored. As the T increases, the dS/dH decreases. The quantity dS/dH is a measure of the curvature of the $M(\ln H)$ curves. At low temperature, where $M(\ln H)$ has large curvature, the dS/dH is large. Conversely, at high temperature, the dS/dH is small, the $M(\ln H)$ is nearly linear, and the standard London theory describes the data accurately.

It is often difficult to determine precisely the upper critical field, H_{c2}, for type-II superconducting materials. From the non-local London theory,[46] we have $\zeta(T) = \eta_1 - \ln(H_0/\eta_2 H_{c2} + 1)$; however, one cannot directly extract H_{c2} because η_1 and η_2 are unknown. The quantity H_{c2}, however, can be estimated roughly, if one assumes values for η_1 and η_2, as in the next (2.3.6) section. Meanwhile, the irreversibility field H_{irr} where $J_c \to 0$, shown versus T in Figure 2-17, can be obtained from results similar to those in Figure 2-18-(b), using the criterion that $\ln(J) = 1$ A/cm^2; at this level, the isothermal J vs. H has decreased by factors of 10^3 or 10^4 from its low field values and is falling off precipitously. This H_{irr} can be described by the power-law relation $H_{irr}(T) = H_{irr}(0)(1-T/T_c)^n$ with n=1.35 and n=1.61 for

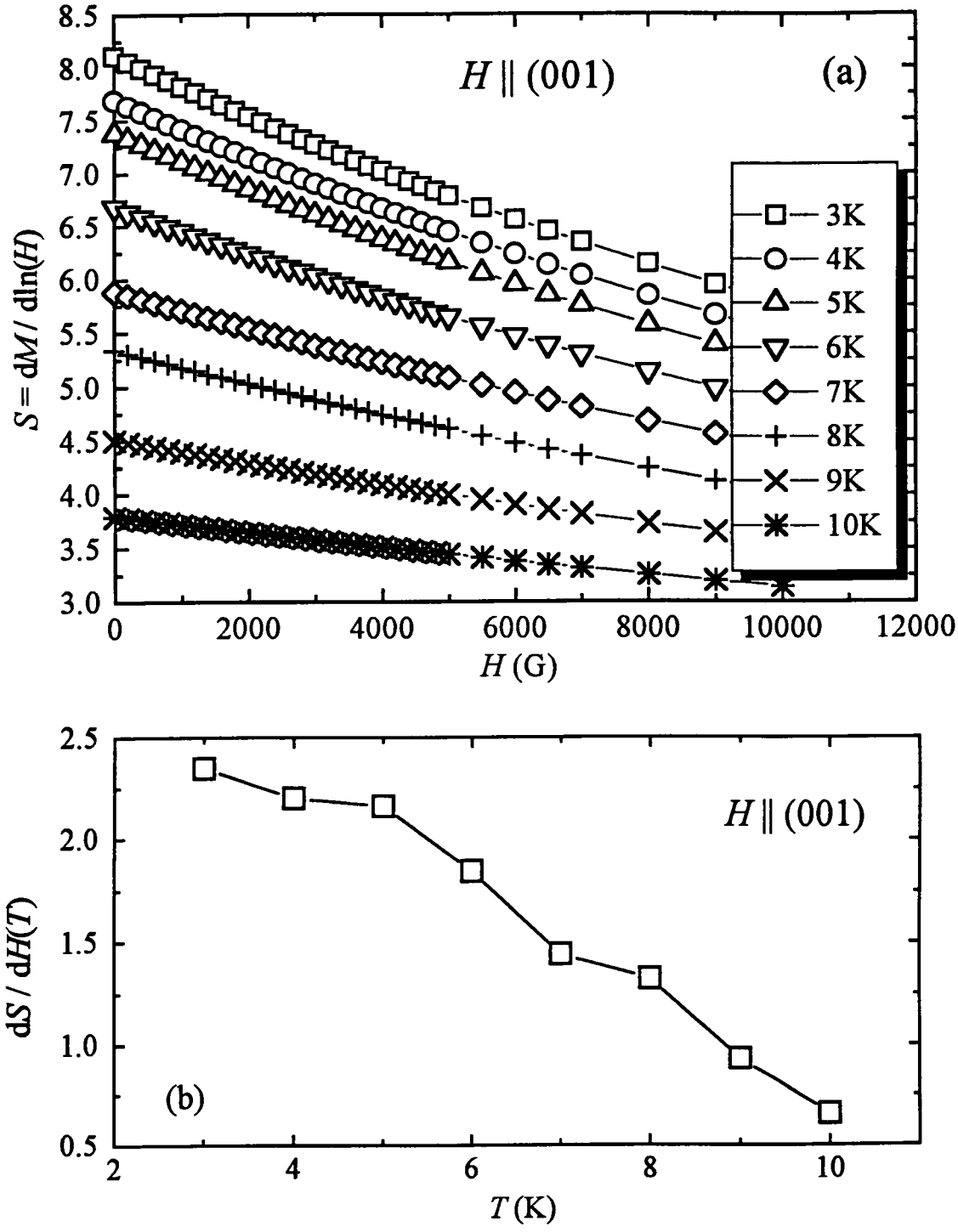


Figure 2-16. (a) The plots of $S = dM/d\ln H$, as the function of the field H. (b) The temperature dependence of dS/dH. See text.

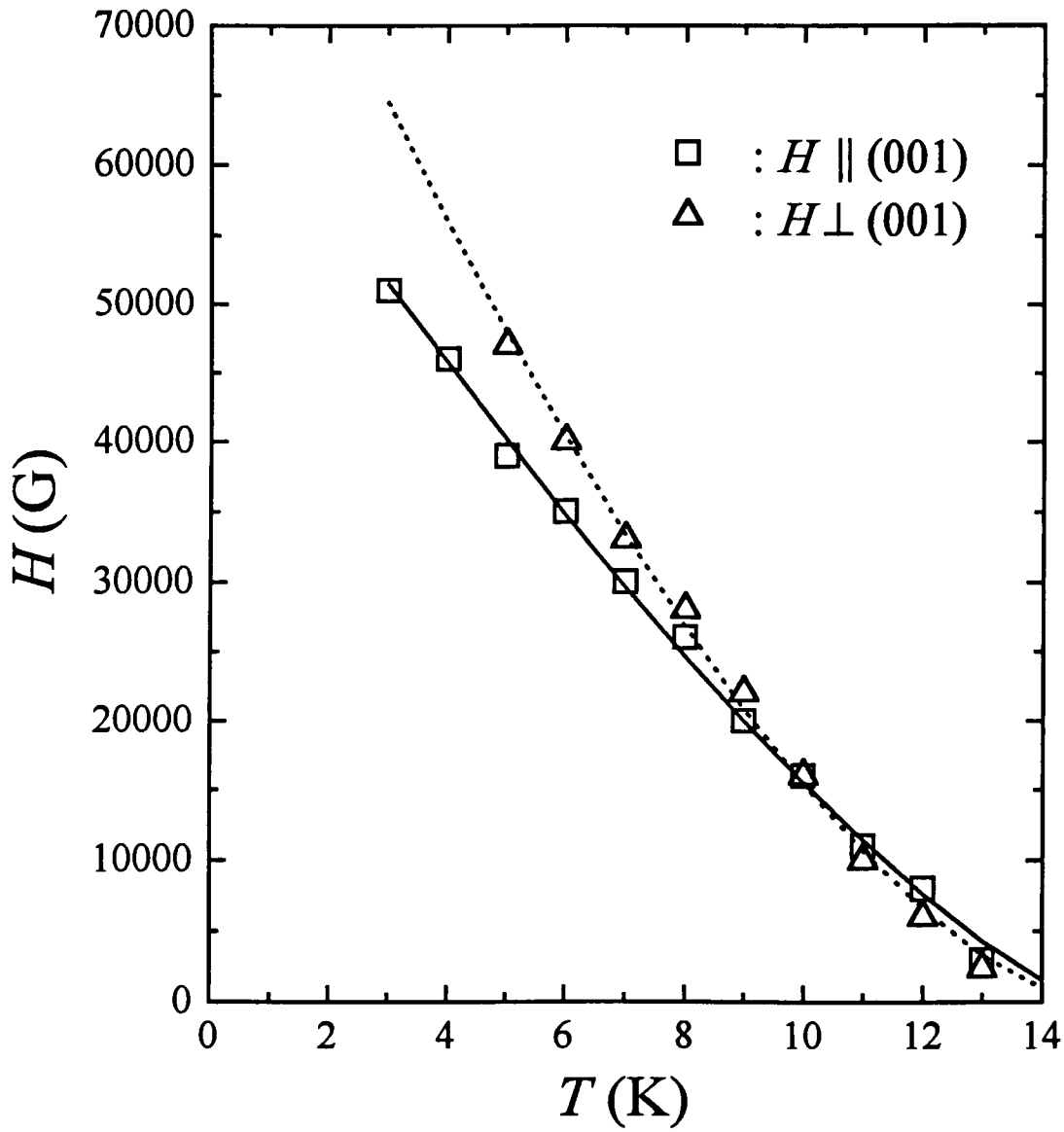


Figure 2-17. Temperature dependence of the irreversibility field, H_{irr}, for the field H parallel to (open squares) and perpendicular to (open triangles) (001)-axis. Solid and dot lines are fits to the function $H_{irr}(T) = H_{irr}(0)(1-T/T_c)^n$. See text.

magnetic field H parallel to and perpendicular to (001)-direction, respectively. As seen in Figure 2-17, the irreversibility field of the single crystal of YNi_2B_2C is nearly isotropic near T_c ($0.6T_c < T < T_c$), but somewhat anisotropic far away T_c ($T < 0.6T_c$).

Figure 2-18-(a) and -(b) show the "anomalous peak effect" in M vs. H and in ln(J) vs. H, respectively. Here, we can observe this phenomenon clearly slightly below H_{c2}. The formation of the peak in the superconductor YNi_2B_2C can be attributed to a sharp transition from week to strong pinning of vortices. There are a many possible mechanisms to explain this magnetization anomaly, which are the formation of a modulated "FFLO" state,[76,77] matching effects of the vortex lattice spacing and the pinning center spacing,[78] synchronization through the softening of the shear modulus of the FLL and the vortex lattice defect structure,[78,79] collective pinning which leads to extra softening of the lattice,[80] and a variation of the pinning threshold,[78] etc. From the previous discussion, measurements of the electrical resistivity presented below, and the reports of other research groups,[67, 81-83] it is clear that YNi_2B_2C is generally a quite clean ($\ell_o >> \xi_o \sim 9$ nm) type-II superconductor. In Figure 2-18-(a), the magnetization curve is nearly reversible over an extended field range, which indicates that the pinning force for vortices is very weak; then the anomalous peak effect with a stronger pinning force occurs just below H_{c2}. Therefore, a simple interpretation in terms of the conventional "peak effect" in the critical current density often observed for *dirty* type-II superconductors can be dismissed in this case. Long ago, Fulde and Ferrell (FF)[76] as well as Larkin and Ovchinnikov (LO)[77] proposed the existence of a non-uniform superconducting state, an "FFLO" state, in conventional superconductors. Recently, K. Samokhin showed possible types of non-uniform states in *d*-wave

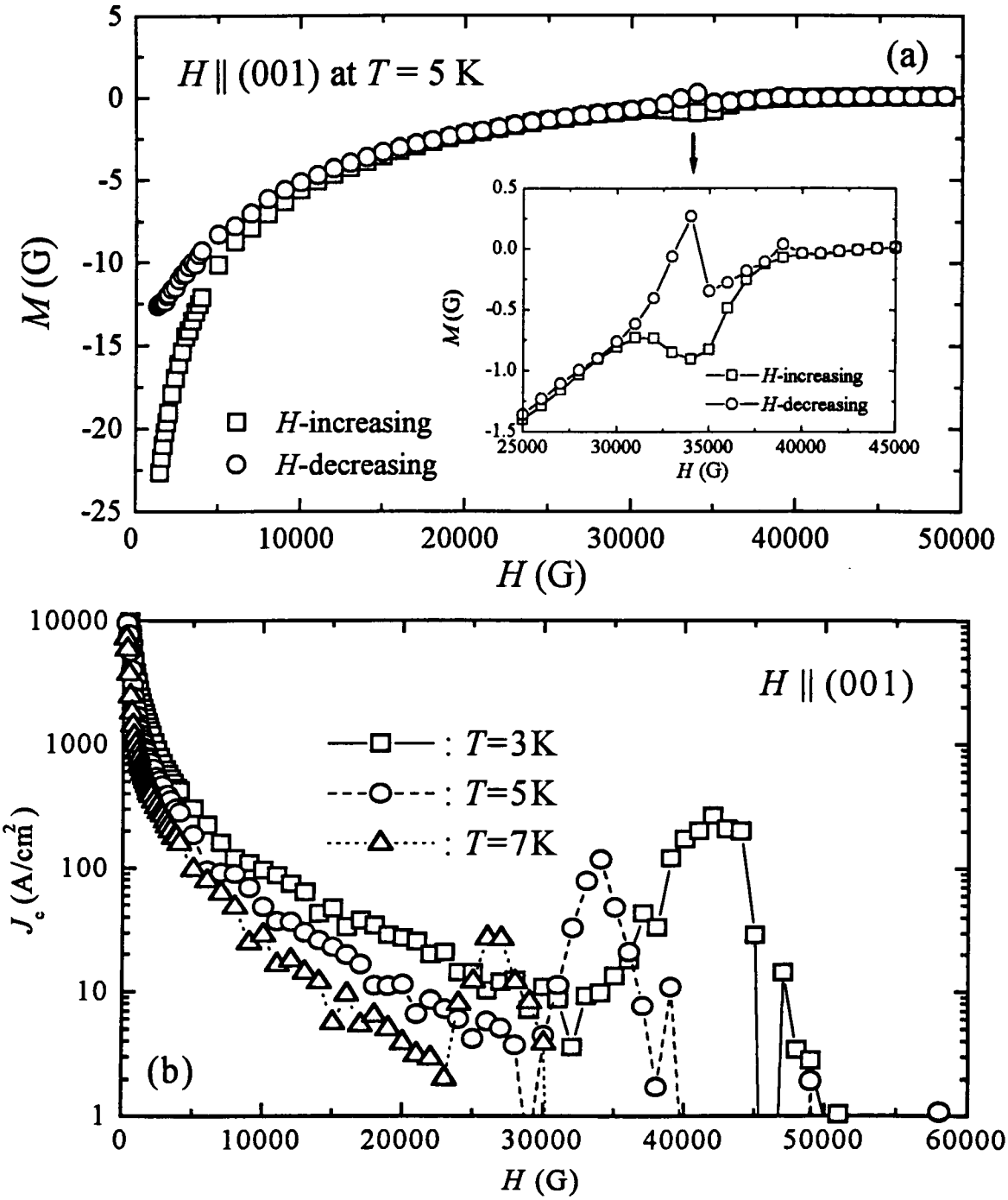


Figure 2-18. (a) Isothermal *dc*-magnetization M versus field H for $H \parallel c$-axis at $T = 5$ K. Inset indicates the "anomalous peak effect" in an expanded scale. The open squares and circles denote values for increasing and decreasing field history. (b) Semilogarithmic plot of the critical current density (J_c) versus field H at several temperatures.

superconductors.[84] In order for the "FFLO" state to be observed, the materials should be (1) an extreme clean limit of a type-II superconductor with (2) strong Pauli limiting.[85] Recently, it has been suggested that the "FFLO" state exists in certain heavy-fermion superconductors.[86-90] For example, UPt_3, UBe_{13}, $PbMo_6S_8$, and UPd_2Al_3 are good candidates to exhibit the "FFLO" state, but $CeRu_2$ is not. In the original theory dealing with a BCS superconductor, the "FFLO" state should be restricted to $T < 0.56T_c$.[85,91] However, R. Modler et al. found a greatly enhanced existence range, $T < 0.9T_c$, for both UPd_2Al_3 and $CeRu_2$.[89] These YNi_2B_2C data are similar to the results on $CeRu_2$[87-89,92] and UPd_2Al_3.[86,89] Thus, we can check simply whether this YNi_2B_2C can be a good candidate for observing the "FFLO" state or not. The YNi_2B_2C is a clean superconductor. The characteristic parameter $\beta = (\sqrt{2})H_{c2}(0)/H_p$, where $H_{c2}(0) = 0.7T_c(-dH_{c2}/dT)$ near T_c and $H_p = \Delta_o/(\sqrt{2}\mu_B) = 1.8[\text{Tesla/Kelvin}]\cdot T_c$, is the Clogston paramagnetic limit (where Δ_o is the BCS energy gap at $T = 0$ K).[93] The β value of YNi_2B_2C is estimated as 0.3. This is small compared with the criterion ($\beta = 1.8$) for the "FFLO" state to exist.[85] Thus YNi_2B_2C may be not a good candidate for an "FFLO" superconductor, but the similarities of the superconducting phase diagrams are interested nonetheless. Figure 2-19 shows the region of "anomalous peak effect", slightly below H_{c2}, which came from both Ginzburg-Landau or standard London limit analysis near T_c and non-local London analysis at low temperature region (well below T_c). In addition, near $T = 0$ K, the arrow ($H_c(0)$) is due to WHH[94] analysis. The generalized "FFLO" state can be introduced to this YNi_2B_2C system. Therefore, the generalized "FFLO" state can exist in the extended regions $T < 0.7T_c$ in the single crystal of YNi_2B_2C superconductor. This generalized "FFLO" state can push up the $H_{c2}(T)$ and cause an

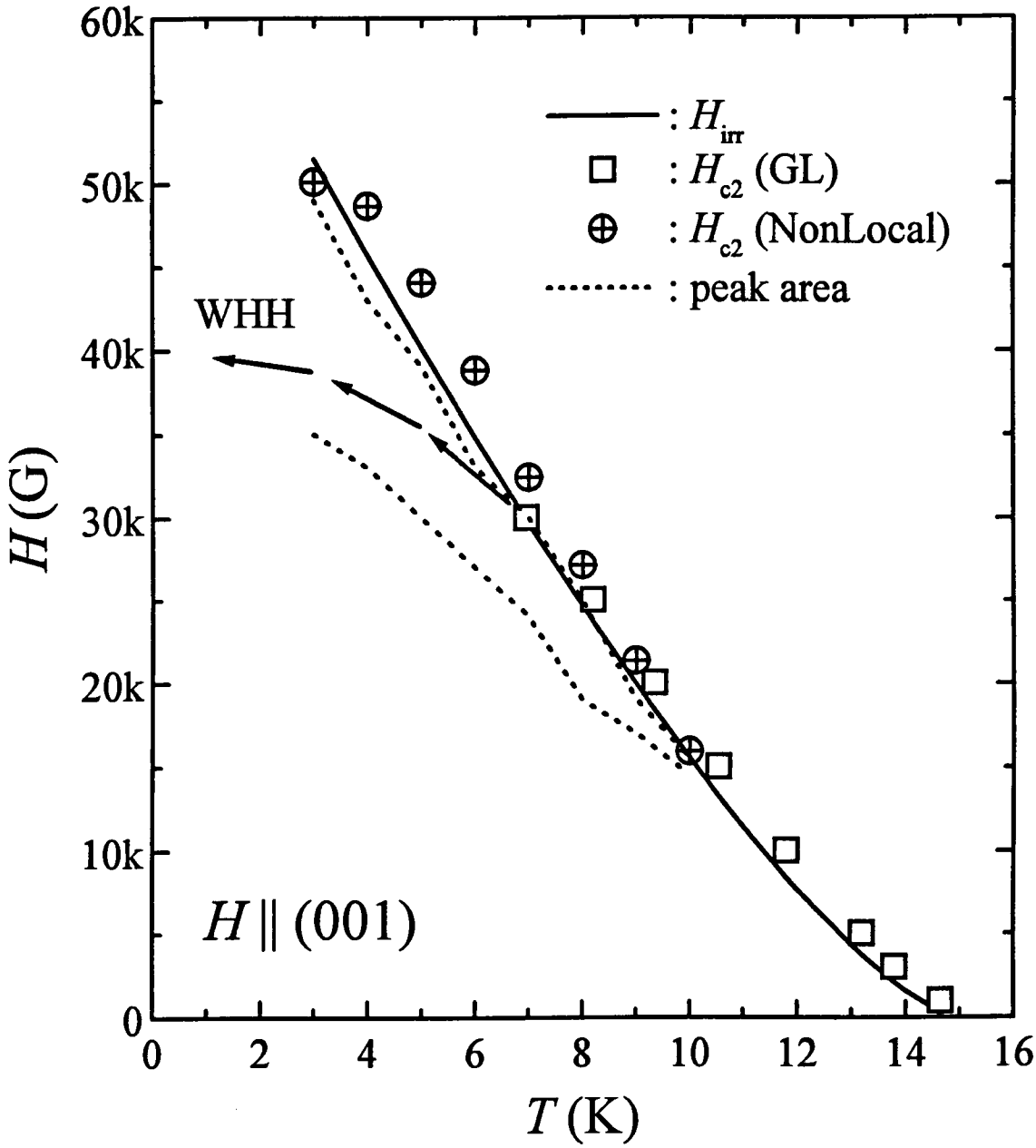


Figure 2-19. *H* versus *T* phase diagram in the high field region, from *dc*-magnetization measurements with field *H* parallel to *c*-axis. See text.

unconventional positive curvature of the $H_{c2}(T)$. However, these phenomena cannot be explained fully to current theory.

2.3.2 Magnetic Susceptibility (χ), Magnetization (M), and Electrical Resistivity (ρ) in Normal State

It is difficult to determine precisely the superconductive magnetic properties for the YNi_2B_2C system, because of its normal state paramagnetic signal.[95,96] To complement studies of YNi_2B_2C in the superconducting state, we have investigated the magnetization and electrical resistivity in the normal state above T_c. The normal state magnetic susceptibility was measured in the temperature regime between 16 K and 295 K in an applied field of 10 kG, for the magnetic field applied parallel and perpendicular to the crystalline (001)-direction. The temperature dependence of magnetic susceptibility, $\chi = M/H$, for the two field orientations is shown in Figure 2-20. The magnetic susceptibility is anisotropic for the entire temperature range. With the field perpendicular to (001)-direction, the susceptibility follows a Curie-Weiss temperature dependence, whereas the susceptibility is significantly smaller with the field parallel to the (001)-direction. The large anisotropy between magnetic field parallel to and perpendicular to (001)-direction in the low temperature regime is a common phenomenon in the RNi_2B_2C materials containing magnetic rare earth ions R = Er, Ho, Tb, and Dy;[29,97] however, the origin of such behavior is less obvious in the present compound containing yttrium, for which no local magnetic moment is expected.

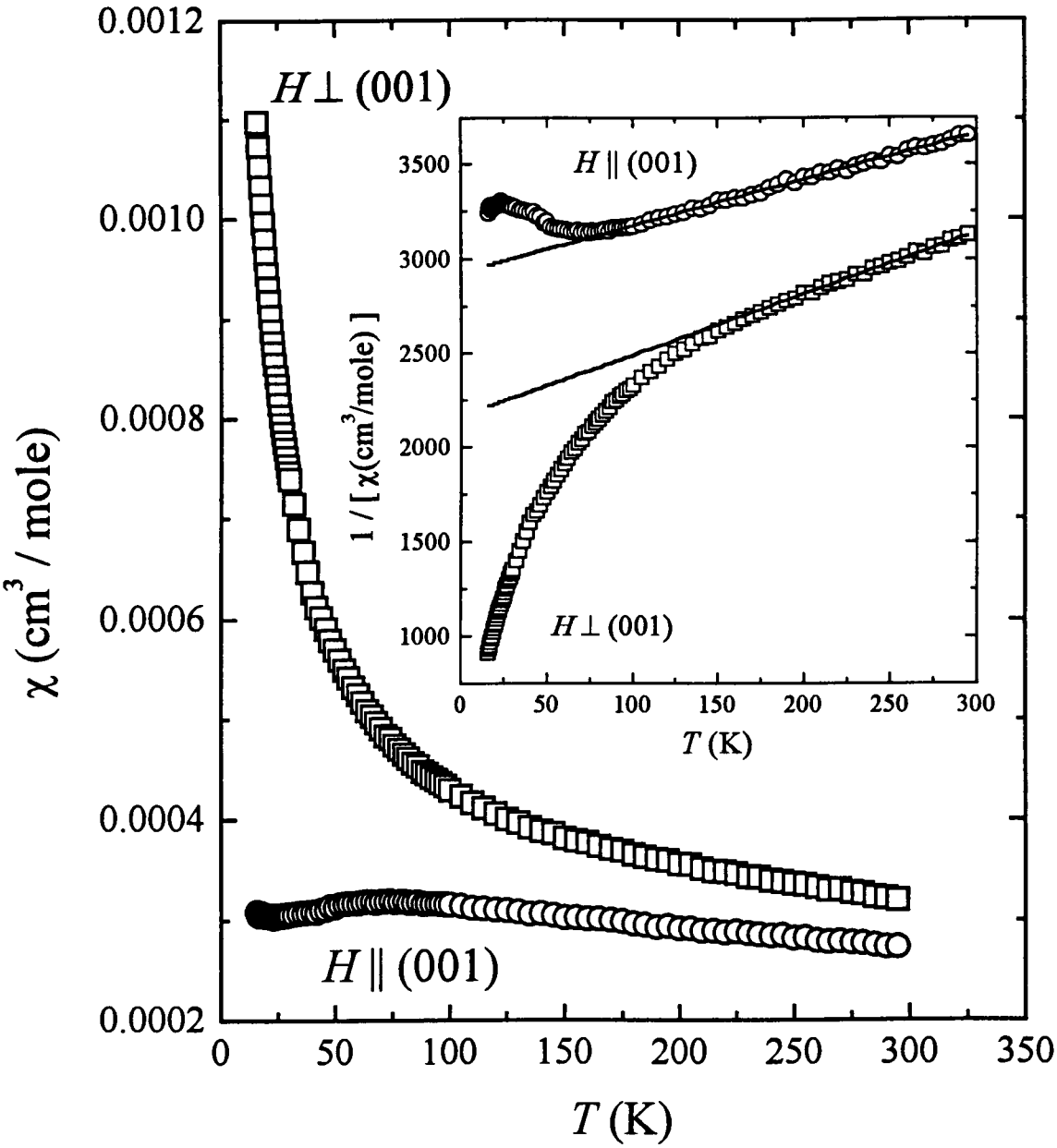


Figure 2-20. Susceptibility ($\chi = M/H$) versus temperature T measured in magnetic field $H = 10$ kG, parallel and perpendicular to (001)-direction. The inset shows the temperature dependence of $1/\chi$, where lines are linear curves above $T = 200$ K.

The inset to Figure 2-20 shows $1/\chi$ plotted versus T for both directions of applied field. The data at $T > 200$ K for both field directions show a Curie-Weiss-like behavior,

$$\chi^{molar} = N_A p^2 \mu_B^2 / 3k_B (T+\theta) = C / (T+\theta), \qquad (2.3.2\text{-}1)$$

where C is Curie constant, θ is Weiss temperature, N_A is Avogadro's number, k_B is Boltzmann constant, μ_B is Bohr magneton, and p is the effective number of Bohr magneton. From the high temperature (200 K $\leq T \leq$ 295 K) slopes in the inset, one finds $\mu_{eff} = 1.83\mu_B$ and $1.56\mu_B$ for the applied field parallel to and perpendicular to (001)-direction, respectively. These values are somewhat smaller than the theoretical value[98] of $2.83\mu_B$ for the Hund's rule ground state of Ni^{2+}, assuming that the orbital moments are quenched by crystalline electric field (CEF) effects. The Weiss temperature, θ, is found to be about 1235 K and 652 K for an applied field parallel to and perpendicular to the (001)-direction, respectively. On the other hand, the constant term in the magnetic susceptibility of the single crystal of YNi_2B_2C seems to be come from Pauli spin paramagnetism. Figure 2-21 shows the magnetic susceptibility χ versus $1/T$, which emphasizes the data at low temperatures. According to Figure 2-21, the Pauli spin susceptibility, χ^{Pauli}, can be estimated about 3.2×10^{-4} cm^3 / mol, which is very similar to several previous studies.[30,99,100]

The large anisotropy of the single crystal of YNi_2B_2C may be due to CEF effects as observed commonly in the RRh_4B_4 compounds[101] for R = rare earth elements and RNi_2B_2C materials for R = Ho, Tm, and Dy.[29,82,102] Plots of the magnetization versus applied field at several different temperatures (above T_c) for both directions of applied field are shown in Figure 2-22. For the field parallel to (001)-direction, the magnetization $M(H)$ is linear in the applied field H for over the whole temperature regime. However, the $M(H)$ curves for

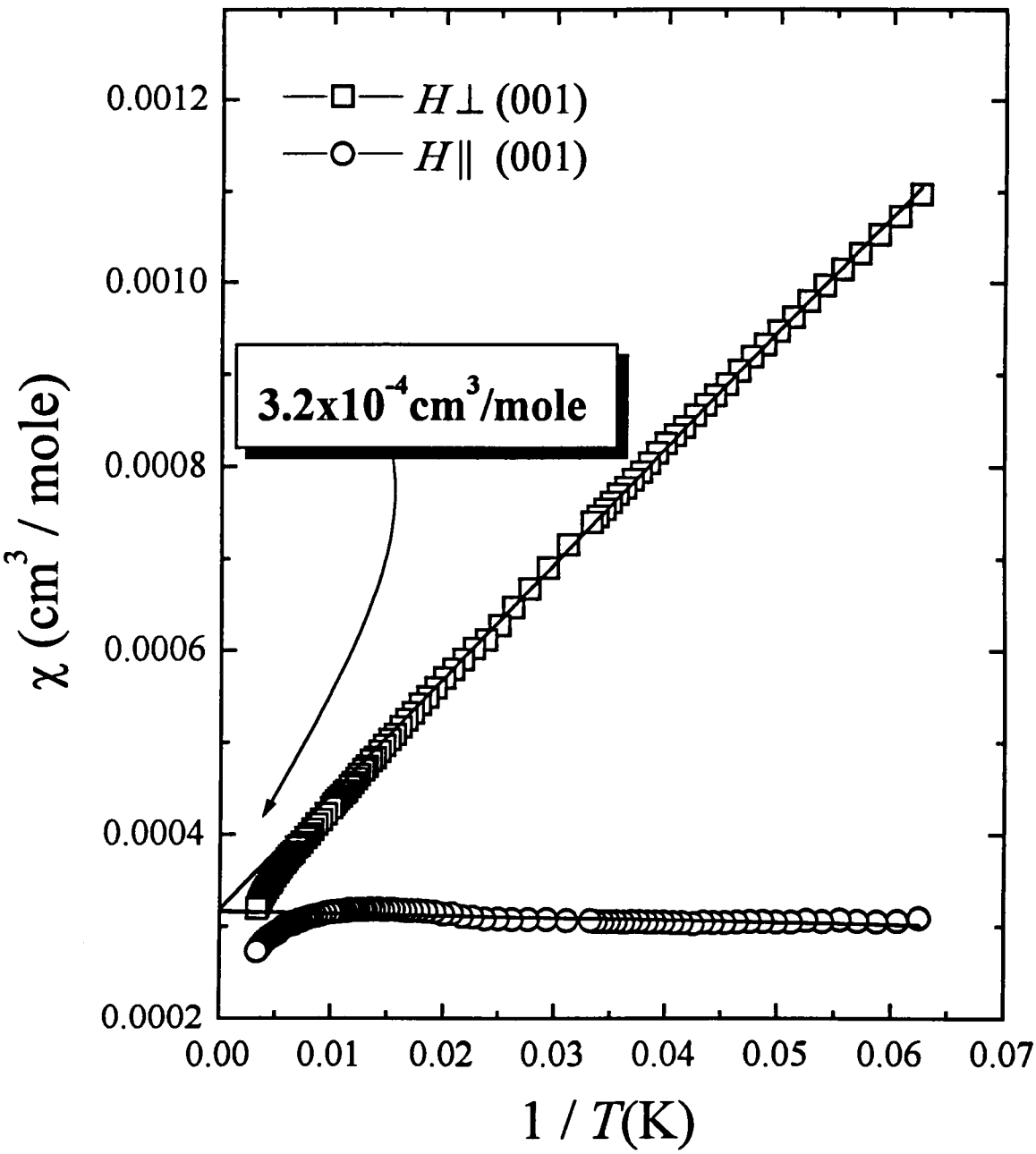


Figure 2-21. Susceptibility(χ) versus $1/T$, for both field directions.

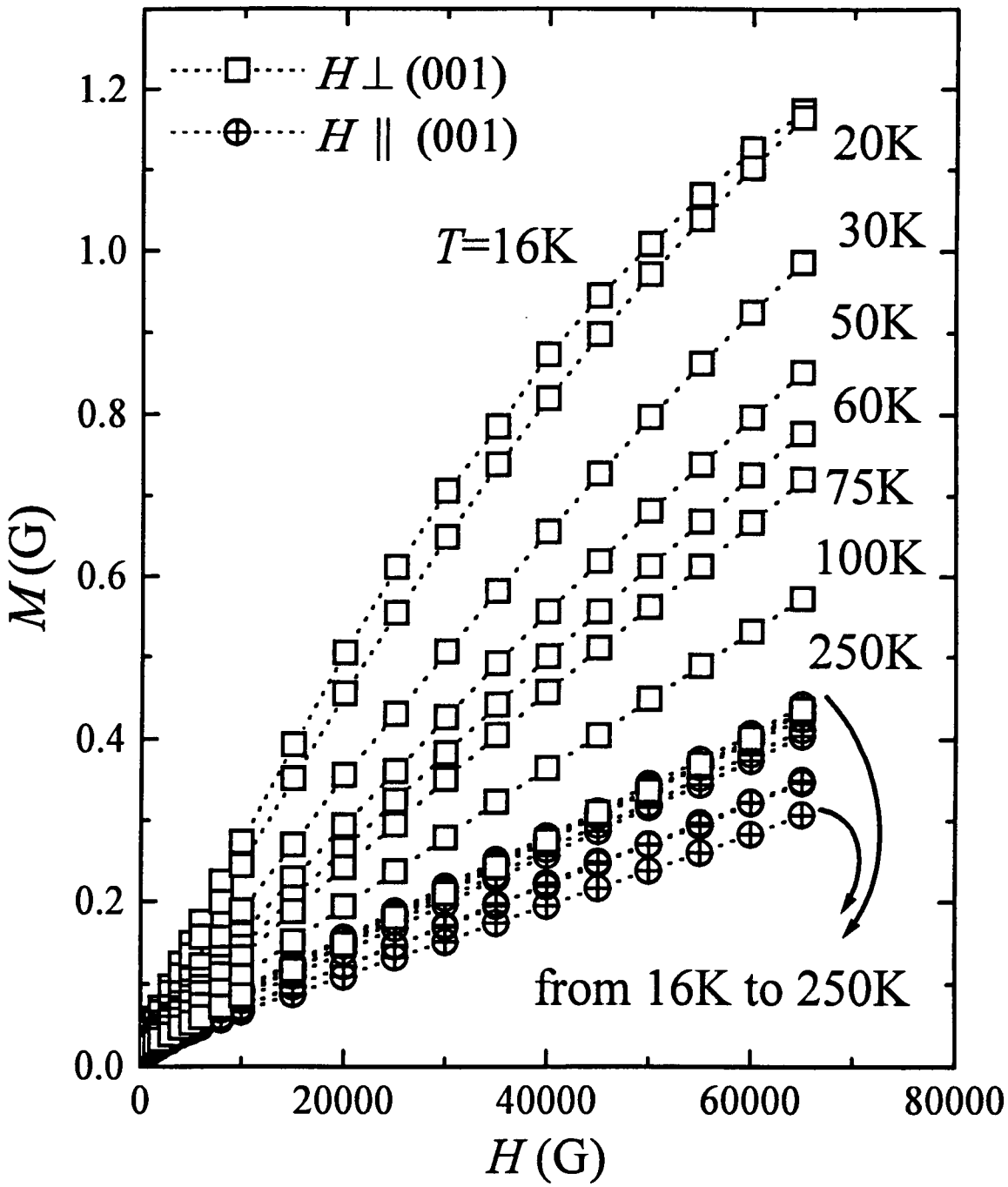


Figure 2-22. The magnetization M versus magnetic field H at several temperatures (above T_c) for fields applied parallel to or perpendicular to (001)-direction.

the field applied perpendicular to the (001)-direction become nonlinear below 50 K, and more strongly nonlinearity as the temperature decreases. This is likely due to CEF effects of Ni^{2+} ions. The normal state paramagnetic signal from paramagnetic Ni^{2+} ions is relatively weak, compared with the normal state paramagnetic signal due to rare earth ions in RNi_2B_2C compounds. The YNi_2B_2C, however, contains no rare earth ions. The Y as well as B and C are non-magnetic elements. Therefore, the paramagnetic signal due to Ni^{2+} ions can be become a significant factor in this compound.

The anisotropic magnetization of the single crystal of YNi_2B_2C most likely comes from the CEF splitting of the $\mathbf{J} = 4$ ground multiplet ($^3F_4$) of the Ni^{2+} ion. The magnetic moment due to Ni^{2+} is more sensitive to applied field perpendicular to (001)-direction (H // ab-plane) than that with the field applied parallel to the (001)-direction (H // c-axis). Therefore, the CEF effects of the single crystal of YNi_2B_2C may come from the Ni magnetic moment to lie predominantly within the ab-plane at low temperatures. In addition, the deviations from Curie-Weiss behavior and the large Weiss temperatures for the paramagnetic susceptibility of the single crystal of YNi_2B_2C can indicate that the Ni $3d$ bands may be critically associating with the conduction electrons. Electron band structure calculations for RNi_2B_2C materials[103,104] show that the bands near the Fermi level display predominant Ni $3d$ bands, with a relatively high density of states at E_F, and that the superconductivity may come from the conventional mechanism with strong electron-phonon coupling, in the contrast to the analysis of heat capacity for the single crystal of YNi_2B_2C (following next section 2.3.3).

Measurements of the electrical resistivity were conducted using a van der Pauw

method[105,106] in the normal state, for temperatures from 20 K to 300 K. Figure 2-23 shows the electrical resistivity of the single crystal of YNi_2B_2C. The temperature dependence of the electrical resistivity shows the typical behavior of decreasing linearly with temperature, as for temperatures from 300 K to 70 K. The measurements yielded an electrical resistivity of 4 μΩ-cm at 20 K and a residual ratio (= $\rho_{\text{Room Temp.}} / \rho_{\text{Low Temp.}}$) of 10.

2.3.3 Heat Capacity for Normal and Superconducting State

Figure 2-24 shows the heat capacity [C_p / T] as a function of [T^2] in the temperature regime from 2 K to 30 K, with no applied magnetic field and with $H = 7$ T. There is a jump of heat capacity in zero applied field at $T_c \approx 14.5$ K. In the high magnetic field ($H = 7$ T), however, the jump in heat capacity disappeared: the superconductivity is completely suppressed. For the normal state data with $H = 7$ T, the heat capacity C_p can be fitted in the temperature range 2 K < T < 14 K to the relation

$$C_p / T = \gamma + \beta T^2 \text{ (or } \gamma + \beta T^2 + \delta T^4), \qquad (2.3.3\text{-}1)$$

where γ is the coefficient of the electronic heat capacity (Sommerfeld parameter), and β describes the lattice heat capacity.[57,58,107] Fitting the data without the anharmonic term (δT^4) gives $\gamma \approx 19.1$ [mJ/(mol K^2)] and $\beta \approx 0.097$ [mJ/(mol K^4)]; including the anharmonic term gives $\gamma \approx 20.6$ [mJ/(mol K^2)], $\beta \approx 0.037$ [mJ/(mol K^4)], and $\delta \approx 0.00033$ [mJ/(mol K^6)]. Inclusion of the anharmonic term provides much better fitting than without the anharmonic term; the need is evident, from the significant curvature in the plot of C/T vs T^2 (Figure 2-24).

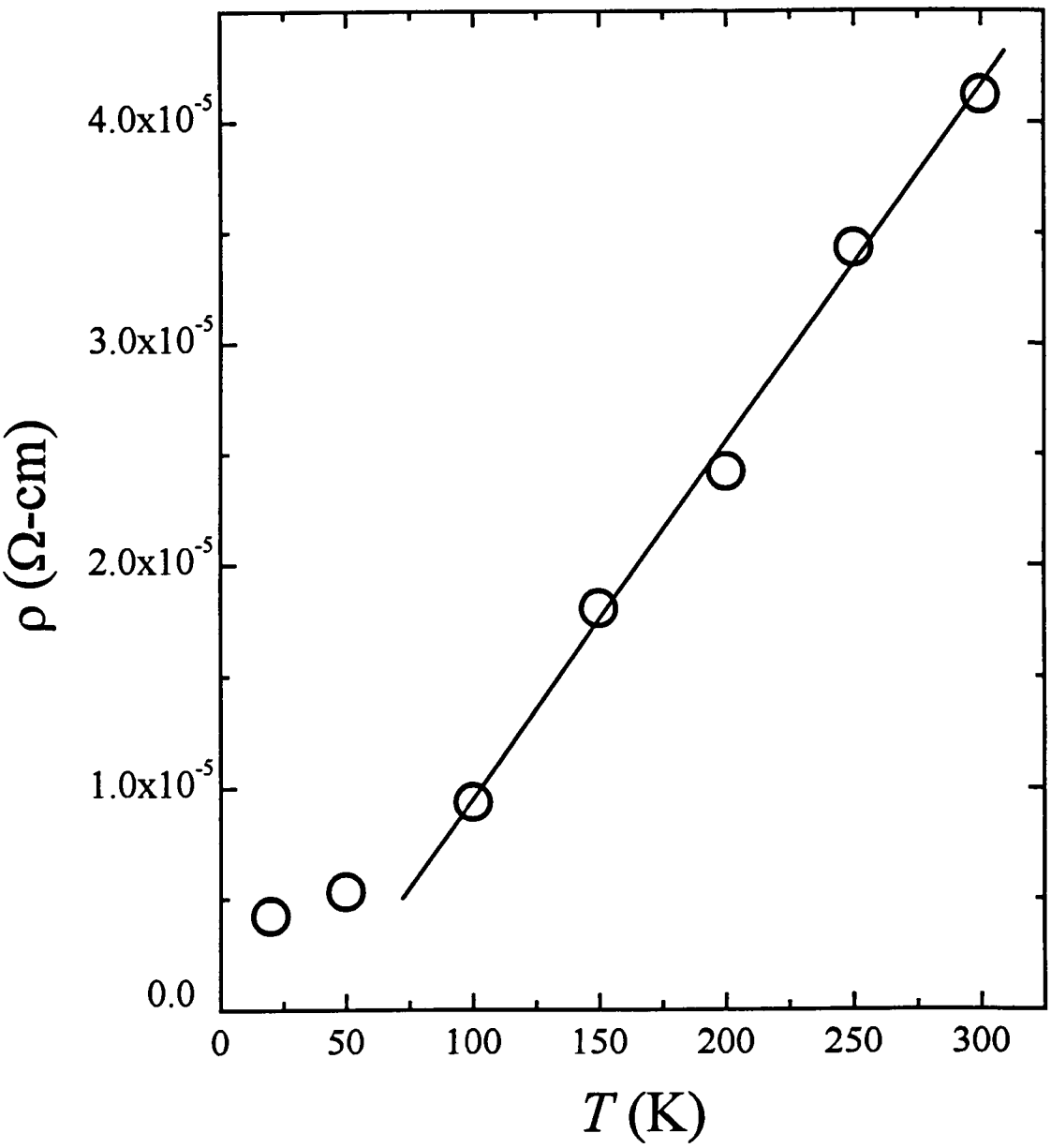


Figure 2-23. The electrical resistivity ρ versus temperature T, for YNi_2B_2C.

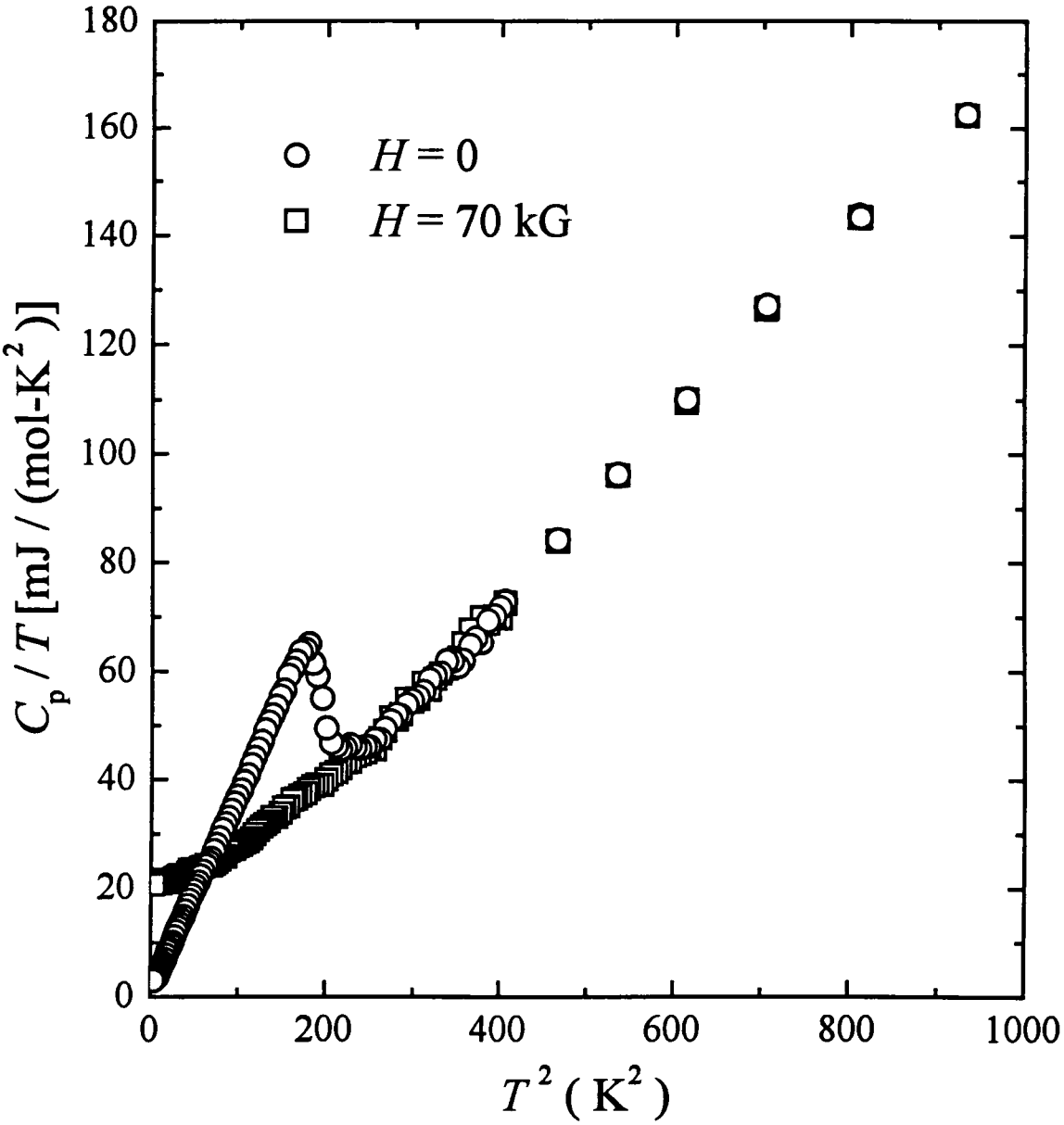


Figure 2-24. C_p / T versus T^2 in the temperature regime 2 K to 30 K for normal state (with $H = 70$ kG) and superconducting state with zero magnetic field.

The value of the Debye temperature Θ_D can be obtained from the relation $\beta = 1944Z/\Theta_D^3$ (where Z is the number of atoms per formula unit). The resulting values are $\Theta_D \approx 495$ K without and $\Theta_D \approx 680$ K with the anharmonic term, respectively. The origin of the large anharmonic effect is not be understood completely. However, this apparent anhamonicity may be due to the shape of the phonon density of states departing from the Debye model or to the crystalline electric field (CEF) splitting of Ni^{2+} ions. The coefficient of the electronic heat capacity γ is much better defined, with values 20.6 [mJ/(mol K^2)] (or 19.1 [mJ/(mol K^2)] with anharmonic term) that are similar to the results of other groups.[59,68]

To compare the predictions of the BCS theory with heat capacity measurements, the electronic heat capacity (C_{es}) in the superconducting state is needed. In general, one can assume that the lattice heat capacities in the normal (C_{ln}) and superconducting state (C_{ls}) are the same at the same temperature with $C_{ln} = C_{ls} = \beta T^3$, as based on measurements of the lattice terms above and below the transition temperature.[109] Therefore, C_{es} can be obtained by subtracting the lattice heat capacity in the normal state, C_{ln} ($H = 7$ T), from the total heat capacity in superconducting state, C_p ($H = 0$ T), below T_c:

$$C_{es} = C_p - C_{ln}. \qquad (2.3.3\text{-}2)$$

Various relationships between C_{es} and T have been tried. In contrast to the predictions of BCS theory, an exponential temperature dependence of C_{es} does not agree well to the data. However, the data of the YNi_2B_2C single crystal can be fitted relatively well to an empirical t^3 dependence, where $t = T/T_c$ is reduced temperature. A similar t^3-dependence for C_{es} was reported by N. M. Hong, et al.[81] for their YNi_2B_2C compound: $C_{es} = 3\gamma T_c t^{2.75}$. The plot of C_{es} vs T is shown in Figure 2-25. The inset of Figure 2-25 shows the t^3-dependence of C_{es}.

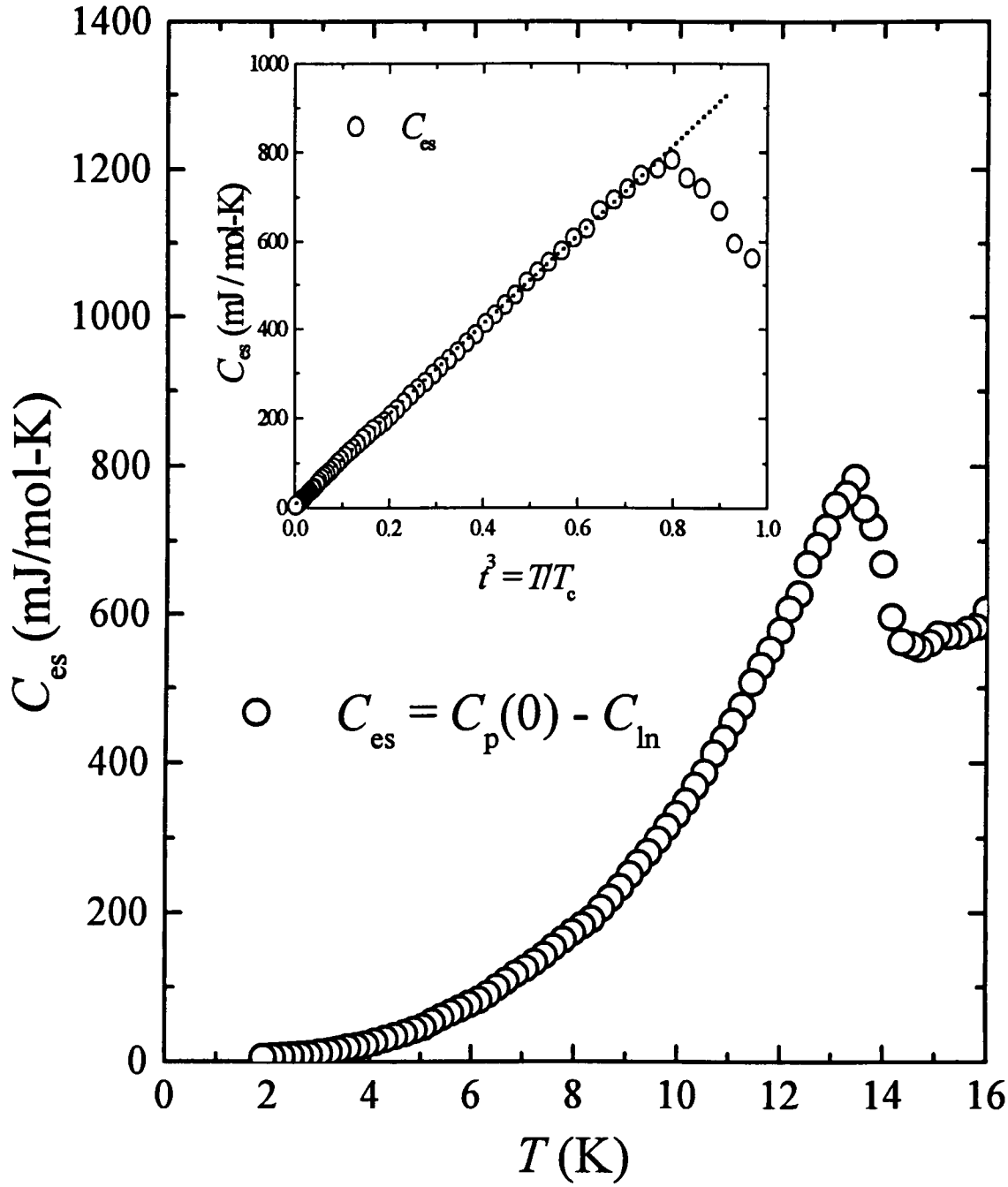


Figure 2-25. The electronic heat capacity C_{es} versus T in superconducting state with $H = 0$. The inset shows the t^3-dependence of C_{es}, where $t = T/T_c$.

This t^3-dependence for C_{es} seems curiously simple; it comes from the two-fluid model which gives the following simple relations for medium-coupling superconductors with electron-phonon coupling constant $\lambda \approx 1$,[57,107]

$$C_{es} = 3\gamma T_c t^3, \text{ where } t = T / T_c, \tag{2.3.3-3}$$

$$\Delta C / \gamma T_c = 2, \tag{2.3.3-4}$$

$$d(C_{es} / T) / dT = 6\gamma / T_c \text{ (at } T = T_c). \tag{2.3.3-5}$$

Thus γ values can be deduced from above simple relations, using the derived C_{es} data. This gives $\gamma \approx 23.1$ [mJ/mol K^2] from the measured $d(C_{es})/d(t^3) \approx 1010$ [mJ/mol K]; $\gamma \approx 18.6$ [mJ/mol K^2], from $\Delta C \approx 540$ [mJ/mol K]; and $\gamma \approx 19.0$ [mJ/mol K^2], from $d(C_{es}/T)/dT \approx 7.85$ [mJ/mol K^3] near T_c. These γ values agree relatively well, within 5~15 %, with the results of fitting of the heat capacity data in H = 7 T and the calculations based on magnetization data.

On the other hand, there are a number of BCS relationships involving T_c and various normal state quantities (details are given in Appendix 2):[108]

$$-(dH_{c2} / dT)_{Tc} = 9.55 \times 10^{24} T_c (n^{2/3} S/S_F)^{-2} \text{ [G/K]}, \tag{2.3.3-6}$$

$$\lambda_{L0} = 1.33 \times 10^8 \gamma (n^{2/3} S/S_F)^{-1} \text{ [cm]}, \tag{2.3.3-7}$$

$$N(0) = 7.97 \times 10^{30} \gamma \text{ [state/(cm}^3 \text{ erg spin)]}, \tag{2.3.3-8}$$

where $N(0)$ is the density of one spin direction. Thus $\gamma \approx 5420$ [erg/(cm^3 K^2)] ≈ 21.5 [mJ/(mol K^2)] can be deduced using the above relations[108] and these magnetization results:[41] $-(dH_{c2} / dT)_{Tc} \approx 3400$ [G/K], $\lambda_{L0} \approx 89.5 \times 10^{-7}$ [cm], and T_c =14.5 [K]. In addition, $\gamma \approx 5885$ [erg/(cm^3 K^2)] ≈ 23.3 [mJ/(mol K^2)] can be estimated from Pauli spin susceptibility, χ^{Pauli} (about 3.2×10^{-4} cm^3/mol) from Figure 2-21, with uncertainties due to the Stoner

enhancement factor, core diamagnetism, the van Vleck (orbital) paramagnetism, the electron-phonon enhancement factor, and so on. These results fairly agree well with the value obtained directly from the normal state heat capacity. From γ and the jump of the zero field heat capacity data, we get $\Delta C_p / (\gamma T_c) \approx 1.81$, indicating that this YNi_2B_2C single crystal deviates from the BCS weak-coupling value of 1.43.

Continuing, the entropy S and the free energy F of the single crystal of YNi_2B_2C can be estimated from the experimental heat capacity data. First, from the relation between heat capacity C_p and entropy S,

$$C_p = T\,(dS/dT) \text{ or } S = \int (C_p / T)\, dT, \qquad (2.3.3\text{-}9)$$

the entropy of this system is estimated experimentally. Figure 2-26 shows the entropy S in the normal and superconducting states as a function of temperature. In general, the entropy measures the disorder of a system. Because the entropy in the superconducting state is lower than in the normal state, just as the Figure 2-26 shows, the electrons in superconducting state are more ordered than in the normal state. Second, from the relation between the entropy S and the free energy F,

$$dF(T) = -S(T)\, dT \text{ or } F = -\int S\, dT, \qquad (2.3.3\text{-}10)$$

the free energy of this system was estimated experimentally as well. Figure 2-27 shows experimental values of the free energy as a function of temperature in the superconducting and normal states. Just as the Figure 2-27 shows, the two curves of the free energy merge at the transition temperature T_c. This means that there is no latent heat of transition at T_c and the phase transition is second order.

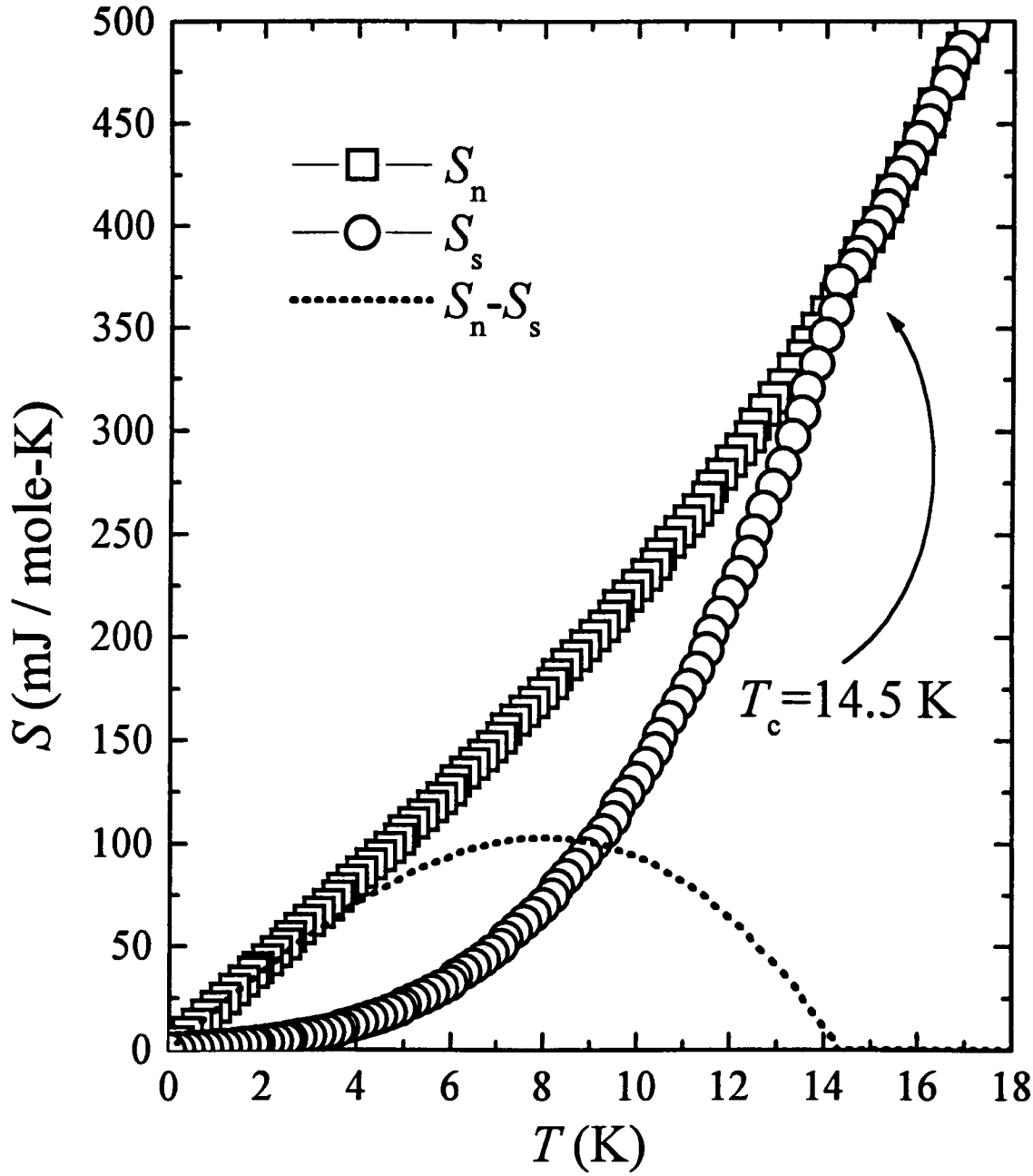


Figure 2-26. A plot of entropy S as a function of temperature T for both normal and superconducting states.

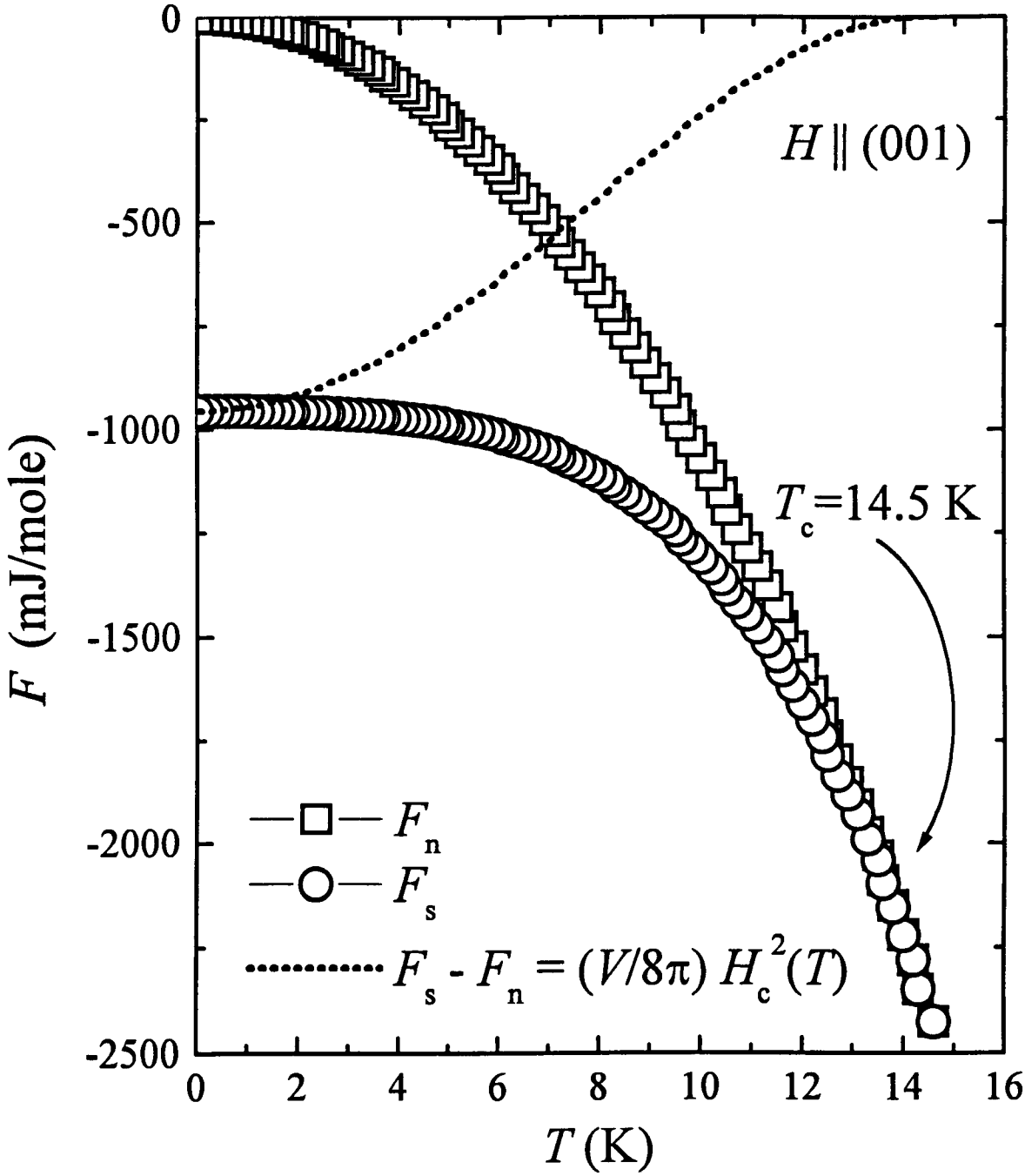


Figure 2-27. A plot of free energy F as the function of temperature T for both normal and superconducting states.

2.3.4 Thermodynamic Critical field H_c

Let us further examine the thermodynamic properties discussed in the previous section 2.2.3. For both type-I and type-II superconductors, the thermodynamic critical field is defined by the relation,[49,57,58]

$$H_c^2(T)/8\pi = [F_n(T) - F_s(T)]/V_{molar}, \qquad (2.3.4\text{-}1)$$

where $F_n(T)$ (or $F_s(T)$) is molar free energy of the normal state (or superconducting state) and V_{molar} is the molecular volume. In addition, the molar specific heat is defined by $C_p = T\cdot[dS/dT]$. Finally, one obtains that

$$C_n - C_s = T(\partial/\partial T)[S_n(T) - S_s(T)] = -(T V_{molar}/8\pi)(\partial^2/\partial T^2)[H_c(T)]^2, \qquad (2.3.4\text{-}2)$$

where C_n, S_n, and F_n are the specific heat, the entropy, and the free energy of the normal state, and C_s, S_s, and F_s are the specific heat, the entropy, and the free energy of the superconducting state. In the framework of thermodynamics, one can deduce the thermodynamic critical field from the specific heat using following relation,[57,59]

$$H_c^2(T) = (8\pi/V_{molar})\int_T^{Tc} dT' \int_{T'}^{Tc} dT'' \{[C_s(T'') - C_n(T'')]/T''\}. \qquad (2.3.4\text{-}3)$$

The resulting temperature dependence of $H_c(T)$ is shown in Figure 2-28. The experimental results have been fitted to the standard relation, $H_c(T) = H_c(0)[1-(T/T_c)^2]$, which describes the data well. This yields the value $H_c(0) \approx 2556$ G. The slope of H_c near T_c can be derived to be $-[dH_c/dT]_{Tc} \approx 320$ G/K. Then the following relation[110] for the superconducting energy gap $\Delta(0)$,

$$-[(T/H_c(0))(dH_c(T)/dT)]_{T=Tc} = \Delta(0)/k_B T_c, \qquad (2.3.4\text{-}4)$$

gives the estimate $\Delta(0)/k_B T_c \approx 1.82$ and $\Delta(0) \approx 2.26$ meV. It seems to describe these results for the single crystal of YNi_2B_2C superconductor fairly well, giving a value for $\Delta(0)/k_B T_c$

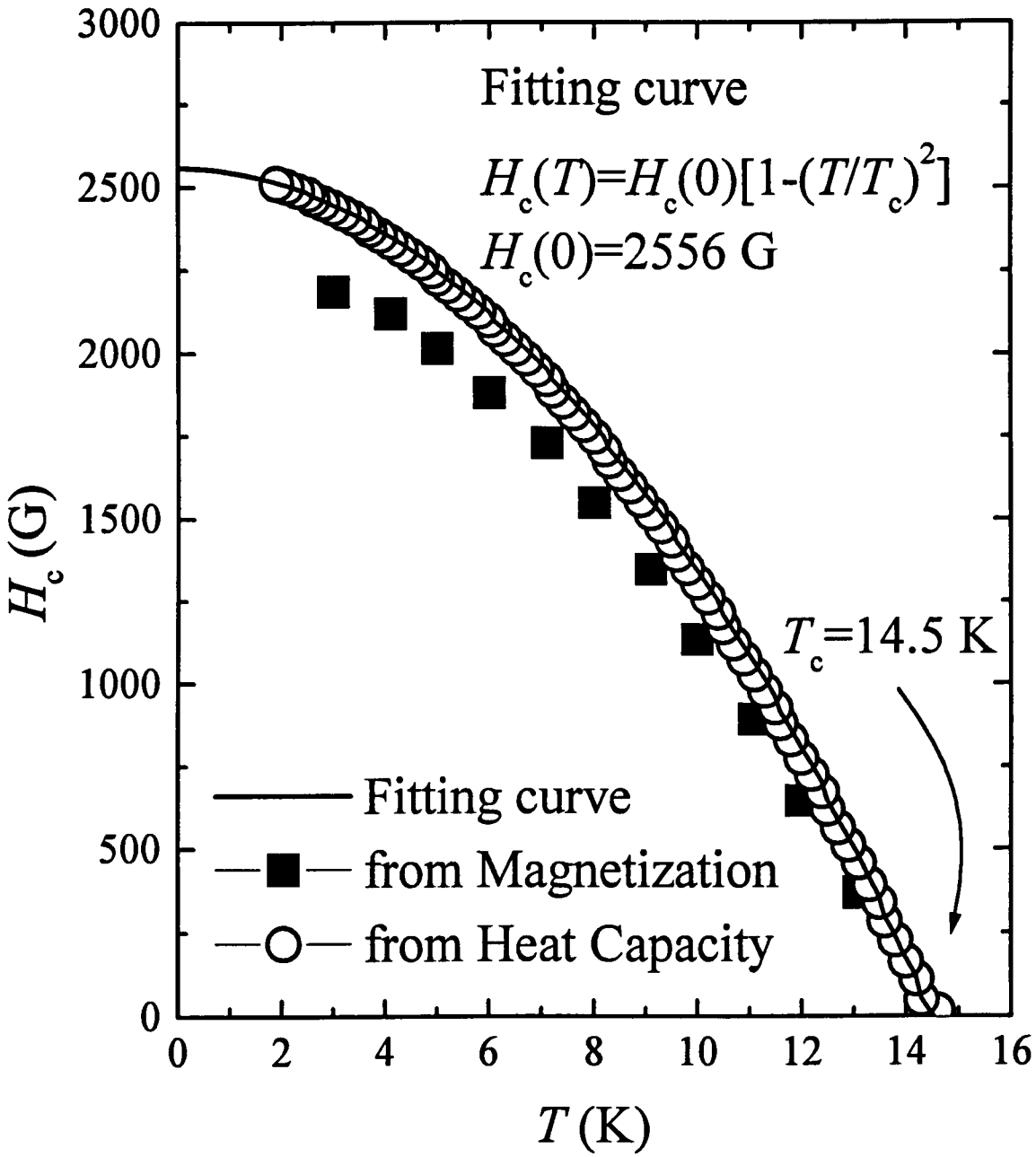


Figure 2-28. The temperature dependence of thermodynamic critical field H_c. The fitting curve is given by $H_c(T) = H_c(0)\ [1 - (T/T_c)^2\ ]$, according to heat capacity results, where H_c is about 2556 G, and T_c = 14.5 K. Open circles results from heat capacity study, and close squares come from the magnetization analysis.

that is slightly larger than the BCS prediction ($\Delta(0)/k_BT_c \approx 1.76$). The t^3-dependence of C_{es}, shown in the previous section (2.3.3), implies a parabolic variation of thermodynamic critical field H_c with temperature,[57,107] which is also observed experimentally. The same t^3-dependence of C_{es} implies that the coefficient of electronic heat capacity, $\gamma = H_o^2/(2\pi T_c^2)$ where $H_o = H_c(0)$.[57,107] Evaluating this with $H_o = H_c(0) \approx 2556$ G gives the values $\gamma \approx 19.6$ [mJ/mol K^2]. This agrees fairly well to previous evaluations, too. In addition, the deviation function $D(t)$,

$$D(t) = [H_c(T)/H_c(0)] - (1-t^2) \qquad (2.3.4\text{-}5)$$

where $t = T/T_c$ and $H_c(0) \approx 2556$ G, of the single crystal of YNi_2B_2C is shown in Figure 2-29. For comparison, the Figure 2-29 also contains the calculated BCS weak coupling deviation function.[57] Here the experimental data clearly deviates from the BCS weak coupling theory, as with Nb and other "simple" superconductors.

Meanwhile, strong coupling theory predicts the following relation: $\Delta(0)/(k_BT_c) = 1.76[(\Delta C_p/\gamma T_c)/1.43]^{1/2}$. For the YNi_2B_2C single crystal with $\Delta C_p \approx 540$ [mJ/mol K] and $\gamma \approx 20$ [mJ/mol K^2], this predicts that $\Delta(0)/(k_BT_c) \approx 1.98$ which significantly exceeds the value of 1.82 obtained from equation (2.3.4-4). Therefore, the strong coupling theory seems not to explain well these heat capacity data. As discussed previously, the above results for the single crystal of YNi_2B_2C superconductor seem to be consistent with the medium coupling formalism.

Let us now evaluate the condensation energy, or equivalently the thermodynamic critical field, from an entirely different experiment study of the magnetization. This is possible because the magnetization of this material is remarkably reversible magnetically in

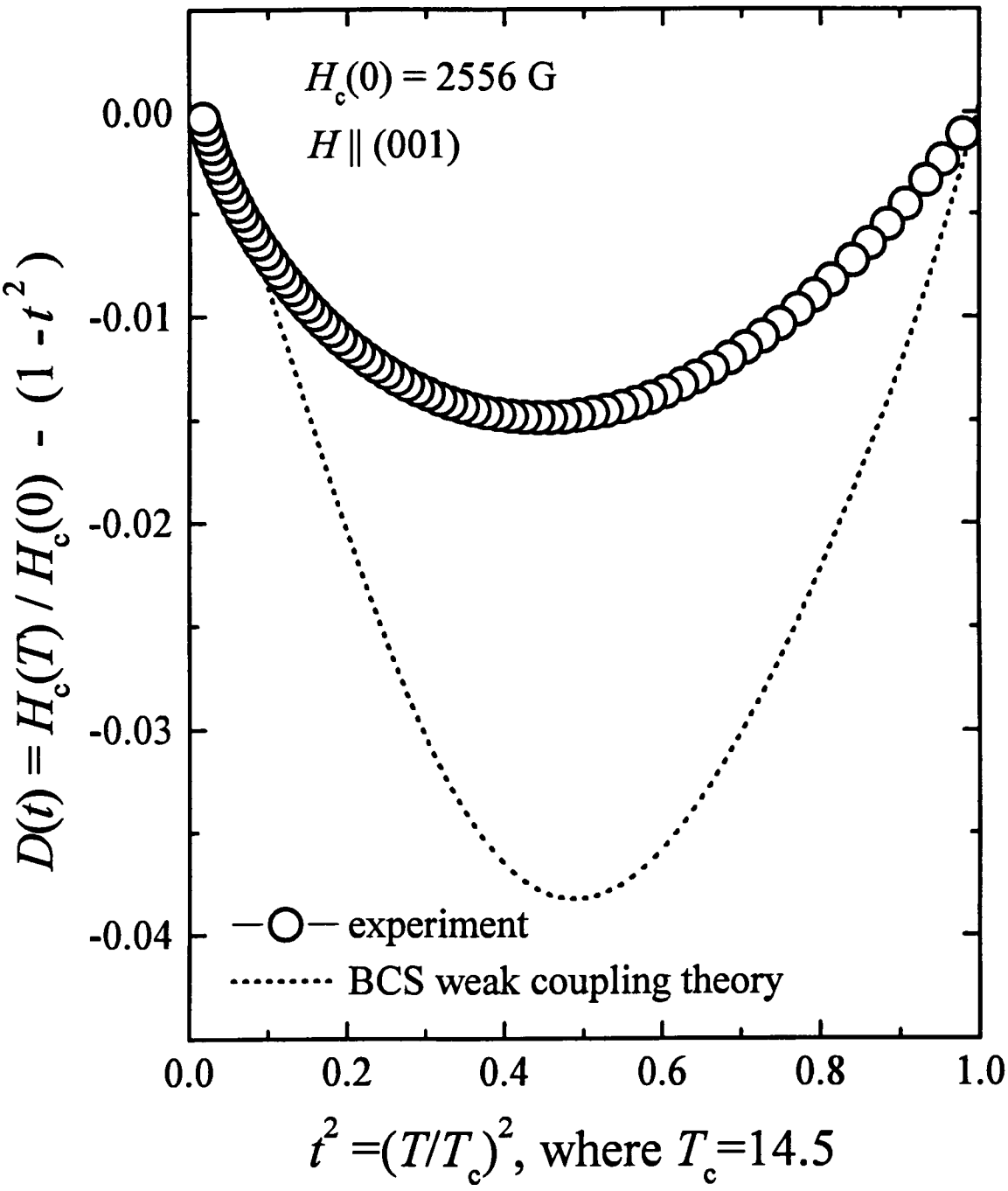


Figure 2-29. A plot of the deviation function $D(t)$ as the function of $t = T/T_c$.

the superconducting state. The previous Figure 2-11 shows the magnetization curve at T = 3 K and 5 K with magnetic field parallel to (001)-direction. At this relatively low temperature ($\approx T_c/3$), one can see a wide reversible region. Thus it is possible to apply thermodynamics to these data. Thermodynamically, the area under the magnetization curve gives the condensation energy, $H_c^2/8\pi$, whatever is the shape of the magnetization curve. Therefore, the thermodynamic critical field, H_c (T), can be obtained from integrating the magnetization $M(H)$ curve, as noted in equation (2.2.3-9) previously,[49,57]

$$-\int M\,dH = F_n(0) - F_s(0) = H_c^2/8\pi. \qquad (2.3.4\text{-}6)$$

One complication, however, is that the magnetization is not completely reversible in the low field regime. Also, the magnetization curves for the single crystal of YNi_2B_2C obviously deviate from simple standard London theory at low temperatures. Thus, at low temperature, the magnetization $M(H)$ data were extrapolated to lower fields using the non-local London formalism, which was described previously.[41] At the lowest fields, we used for $M(H)$ the Meissner state slope. These contributions were added to the area under the reversible magnetization curve to obtain the full integral in equation (2.3.4-6). The resulting values of $H_c(T)$ using this method are shown in the Figure 2-28. There is some difference between the results from heat capacity and magnetization; the evaluations of H_c differ systematically by ~ 10 %. However, we can see fairly good agreements of both thermodynamic critical fields, as the temperature dependencies and overall behavior are remarkably similar.

2.3.5 Lower Critical field H_{c1}

It is generally difficult to determine the lower critical field H_{c1} at which flux first enters a superconductor reversibly. In a magnetization curve, strong pinning effectively prevents magnetic flux from entering the sample, especially in low fields. However, with sufficiently low hysteresis and critical current density J_c, one can find H_{c1} as the field at which the magnetization deviates from the initial linear slope of diamagnetism. Experimentally, the magnetization difference ΔM is investigated in order to establish the field at which M first deviates from linearity. Here ΔM is the difference between the experimental magnetization and an extrapolation of the initial linear dependence of the magnetization on field (Meissner state slope), as determined by a least squares fit to the low field data points. Figure 2-30 shows an expanded plot of the low field regime. In addition, the inset of Figure 2-30 shows the square root of the deviations from linearity $(\Delta M)^{1/2}$, plotted versus applied field H.

One must correct, however, for demagnetization effects due to the geometric shape of sample. The effective field H_{eff} is related by $H_{eff} = H_{appl} - 4\pi DM$, where H_{appl} is the applied field and D is demagnetizing factor. In the Meissner state, one has

$$\chi_{true} = -1/(4\pi) = dM/dH_{eff}, \qquad (2.3.5\text{-}1)$$

and with linear magnetic response, one has

$$\chi_{obs} = dM/dH_{appl} = \chi_{true} / (1 + 4\pi D\chi_{true}). \qquad (2.3.5\text{-}2)$$

Thus the demagnetizing factor D can be determined. For the single crystal of YNi_2B_2C, the values $D_{H//(001)} = 0.725$ and $D_{H\perp(001)} = 0.135$ are estimated from the experimental data. In general, the demagnetizing factor D can not be easily determined analytically for a

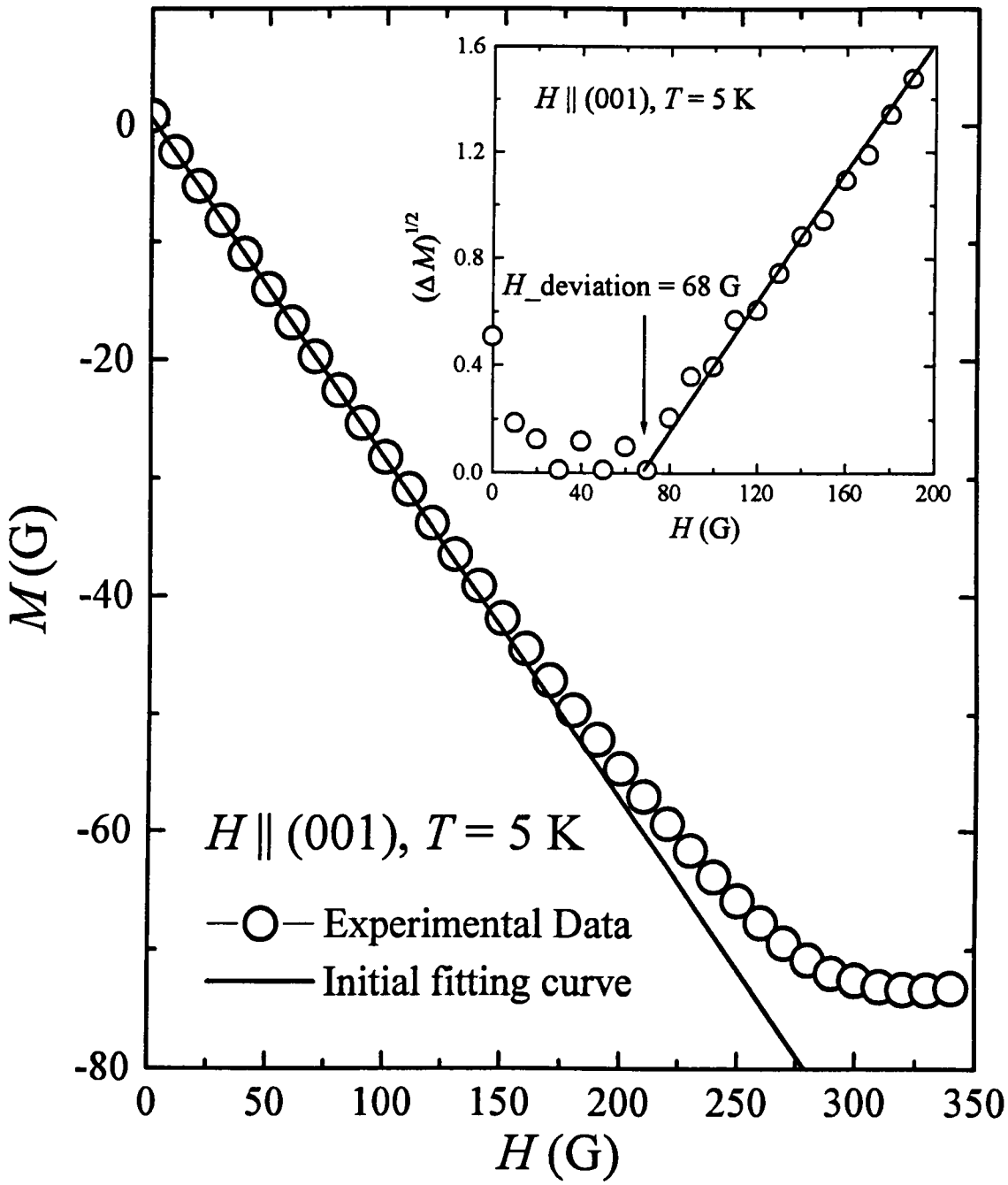


Figure 2-30. The magnetization M versus field H with the applied field parallel to c-axis in an expanded low field region. The inset shows $(\Delta M)^{1/2}$ versus H, which indicate the deviation point from linearity.

complicated sample shape. Alternatively, one can use the relation, $B = H_{eff} + 4\pi M$ and the fact that the lower critical field, H_{c1}, is the field at which the magnetic induction B first increases from zero. Thus, with $B = 0$, then H_{c1} can be obtained from the relation $H_{eff} = -4\pi M$, where M is the value at first deviation from linearity.

Using this method, the results for H_{c1} versus temperature shown in Figure 2-31 were obtained. Data are shown for H both parallel and perpendicular to the crystalline c-axis. Experimentally, the deduced values of H_{c1} approximately follow a parabolic dependence $H_{c1}(T) = H_{c1}(0)\,[\,1 - (T/T_c)^2\,]$, similar to the thermodynamic critical field H_c. Previously, the YNi_2B_2C system was reported to be remarkably isotropic in torque magnetometry measurements[111] and magnetization studies.[67] Subsequently, Yethiraj et al. found that the Y-based borocarbide compound exhibits complex angular dependencies.[33] For the data in Figure 2-31 with fields applied along orthogonal directions, it is likely that the observed differences arise from a superconductive mass anisotropy $\gamma = \sqrt{(m_c/m_{ab})} = \lambda_c/\lambda_{ab} = \xi_{ab}/\xi_c$. Table 2.3.5-1 shows a comparison between reported values of γ in the literature and our determinations from H_{c2} (from next section (2.3.6) and $\gamma = \xi_{ab}/\xi_c$).

Table 2.3.5-1 The comparison of superconductive mass anisotropy for YNi_2B_2C: $\gamma = \sqrt{(m_c/m_{ab})} = \lambda_c/\lambda_{ab} = \xi_{ab}/\xi_c = H_{c2\text{-}ab}/H_{c2\text{-}c}$.

	γ
This work: from H_{c2} (standard London analysis)	1.148
This work: from H_{c2} (Abrikosov analysis)	1.165
Ref.: torque magnetometry measurements[111]	1.005

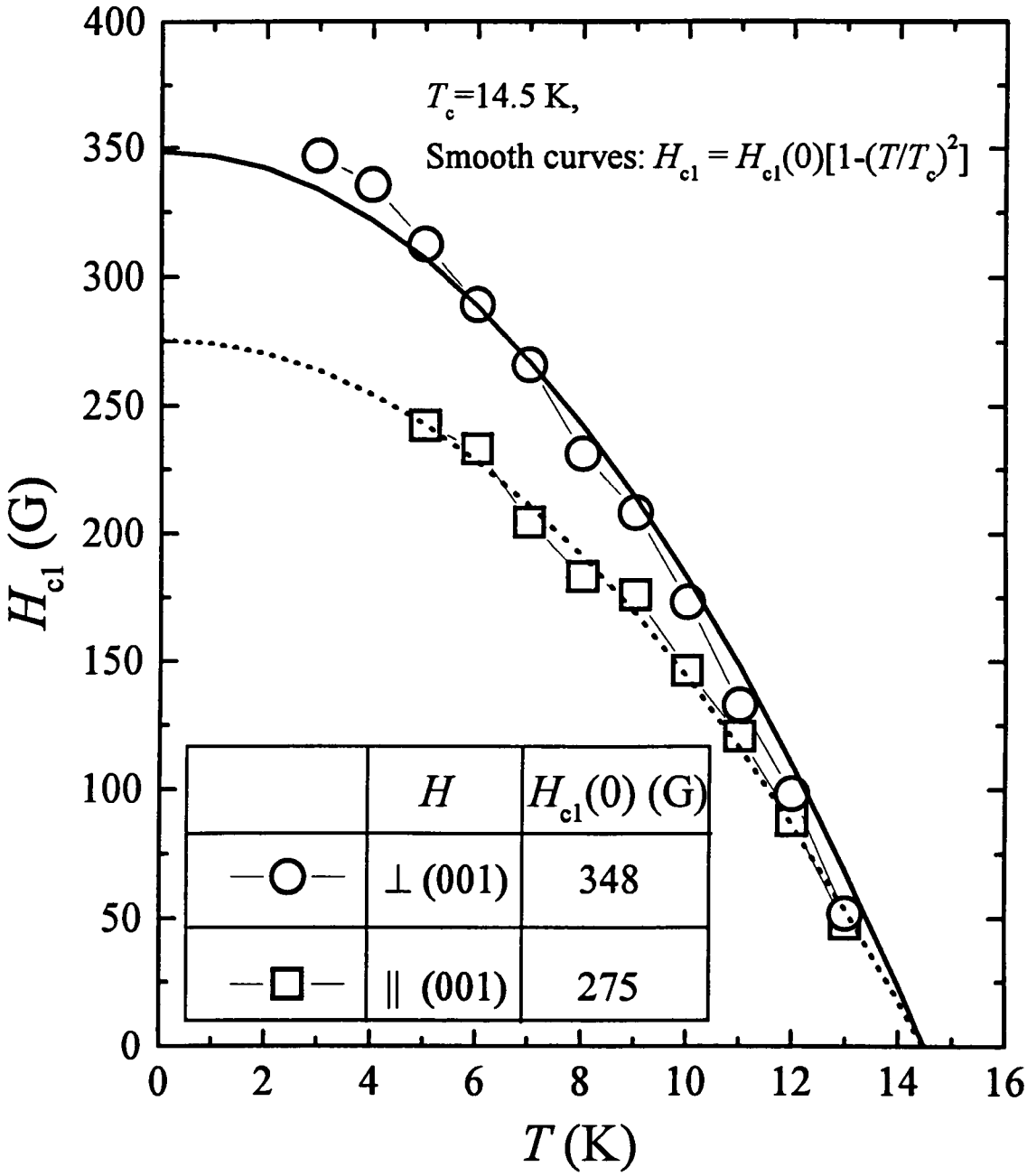


Figure 2-31. The temperature dependence of H_{c1} for both field directions. The smooth curves are given by $H_{c1} = H_{c1}(0)\ [\ 1-(T/T_c)^2\ ]$.

2.3.6 Upper Critical field H_{c2}

The quaternary intermetallic compound YNi_2B_2C has been described as a conventional, isotropic type-II superconductor.[67,111] However, the upper critical field, H_{c2}, of single crystal of YNi_2B_2C has an unconventional behavior. At low temperatures, a positive curvature of H_{c2} has been found by several research groups.[30,95,96,112,113] There are many controversies regarding the upper critical field in this material. Determining H_{c2} is made more complex by the paramagnetic background signal and non-locality of the single crystal. Two approaches for extracting H_{c2} from magnetization data rely on Ginzburg-Landau and standard London-limit theories.[45,49,67,72,73]

In the reversible (H,T) region near $H_{c2}(T)$, according to Abrikosov, standard Ginzburg-Landau relation predicts[49]

$$-4\pi M = [H_{c2}(T)-H]/(2\kappa^2-1)\beta_A . \qquad (2.3.6\text{-}1)$$

Here κ is the Ginzburg-Landau parameter and β_A is a constant which is 1.16 for a triangular vortex lattice.[49] Since H_{c2} is linear in T near T_c,

$$d(-4\pi M)/dT] = [dH_{c2}(T)/dT][1/(2\kappa^2-1)\beta_A], \qquad (2.3.6\text{-}2)$$

one should obtain a linear dependence of M on T near T_c. Therefore, Figure 2-32-(a) and -(b) contain plots of equilibrium magnetization M as a function of temperature (a) in the reversible region and (b) in the limited scale up to $4\pi M$ = -10 G. Indeed, the data in the Figure 2-32-(b) are nearly linear in T and have similar slopes for a wide region of field. A linear extrapolation of the reversible data in Figure 2-32-(b) to M = 0 yields values for $H_{c2}(T)$ directly. These values shown as open diamonds in Figure 2-33. One uncertainty, however, relates to the slope dM/dT in Figure 2-32: according to equation (2.3.6-1 and -2),

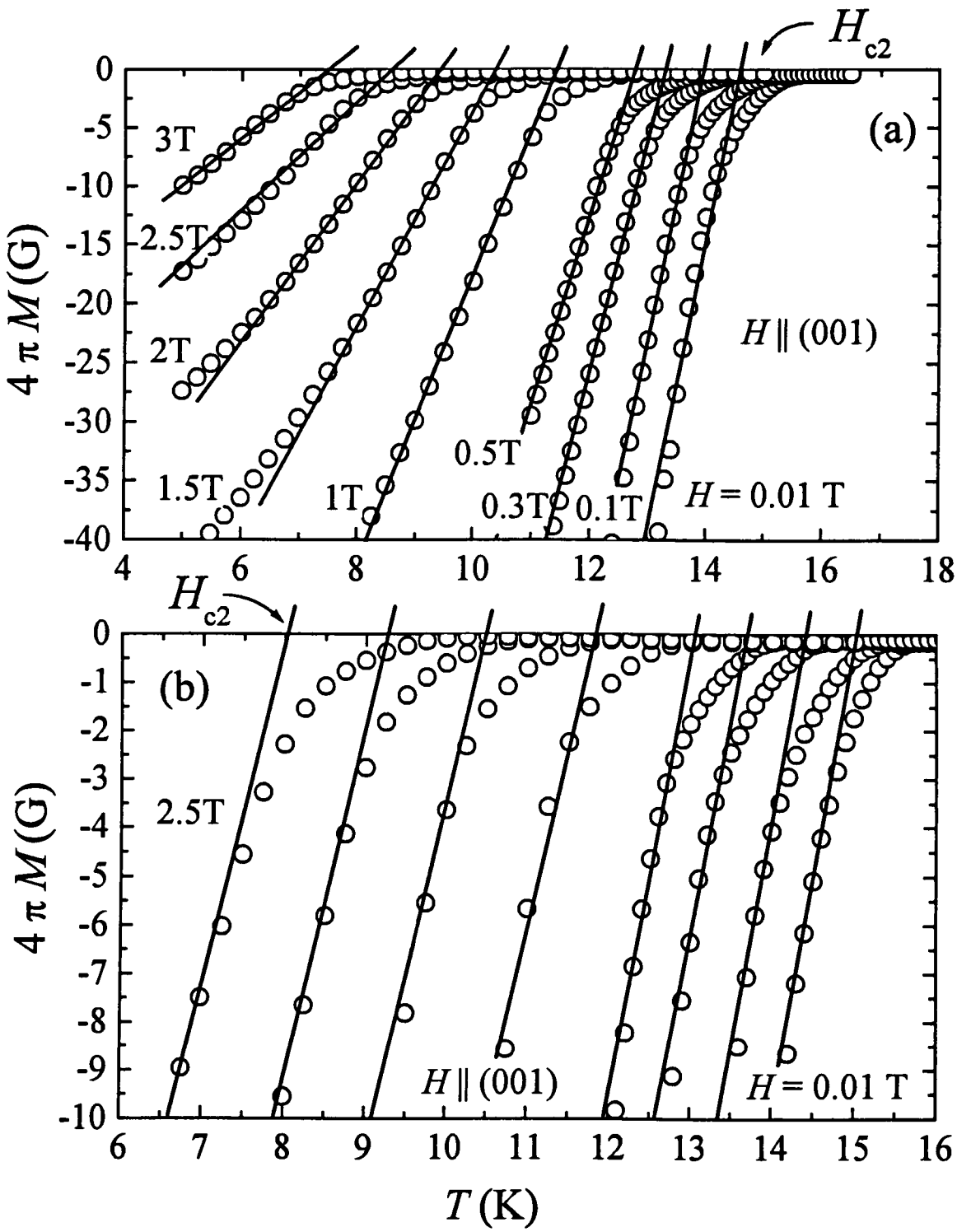


Figure 2-32. Plots of equilibrium magnetization M as a function of temperature T (a) in the reversible region and (b) in the limited scale up to $4\pi M = -10$ G.

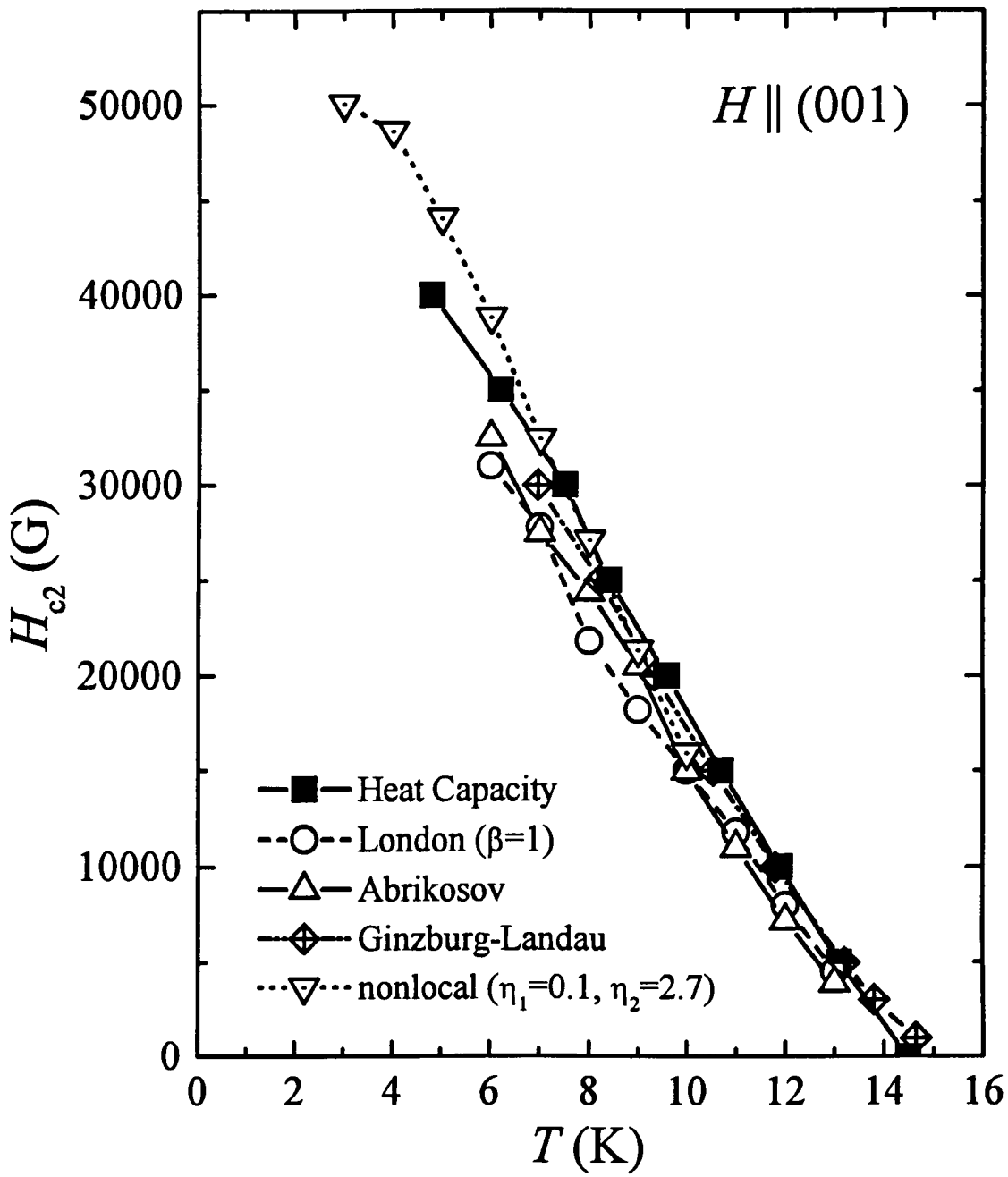


Figure 2-33. The temperature dependence of H_{c2} using several analytic methods.

the slopes should be temperature and field independent near $T_c(H = 0)$. In contrast, the slopes do vary with temperature, beyond what can be expected from the dH_{c2}/dT factor, suggesting that κ may be T-dependent. In addition, the $M(T)$ data with $|4\pi M| < |-10\ G|$ may be affected by fluctuations. Thus it is desirable to assess $H_{c2}(T)$ by some complementary method.

Several alternative approaches are available for estimating H_{c2}. One is the standard London limit formalism for the reversible equilibrium magnetization in the intermediate field region, equation (2.3.1-1), which provides that $M \sim \ln(\beta H_{c2}/H)$. Thus Figure 2-34-(b) shows plots of M versus $\ln(H)$ at several temperatures. Linear extrapolations of $M(\ln H)$ to $M = 0$ gives values for $\beta H_{c2}(T)$; taking $\beta = 1$ gives the results shown as open circles in Figure 2-33. Well below T_c, however, the electrodynamics in the material becomes non-local, as discussed extensively in an earlier section; there the standard London-limit theory, as shown in Figure 2-12, is inadequate and the equilibrium M vs. $\ln(H)$ relation is non-linear. In the low temperature region, the non-local London formalism of Kogan et al.[46] was applied to the data, as shown in section (2.3.1). From the fitting parameter $\zeta(T) = \eta_1 - \ln(H_0/\eta_2 H_{c2} + 1)$ of the non-local theory,[46] one cannot directly extract H_{c2} because of the two unknown constants η_1 and η_2, both of order unity. Arbitrarily setting $\eta_1 \approx 0.1$ and $\eta_2 \approx 2.7$ gives the values H_{c2} shown in Figure 2-33 as open down-triangles. The resulting temperature dependence is qualitatively reasonable.

Another approach is based on the Abrikosov relation, equation (2.3.6-1), for $M(H)$ for H near H_{c2}, which provides that $-M \sim (H_{c2}(T) - H)$. We test this direct proportionality by plotting M versus H in Figure 2-34-(a). The data at low temperature exhibit a credible

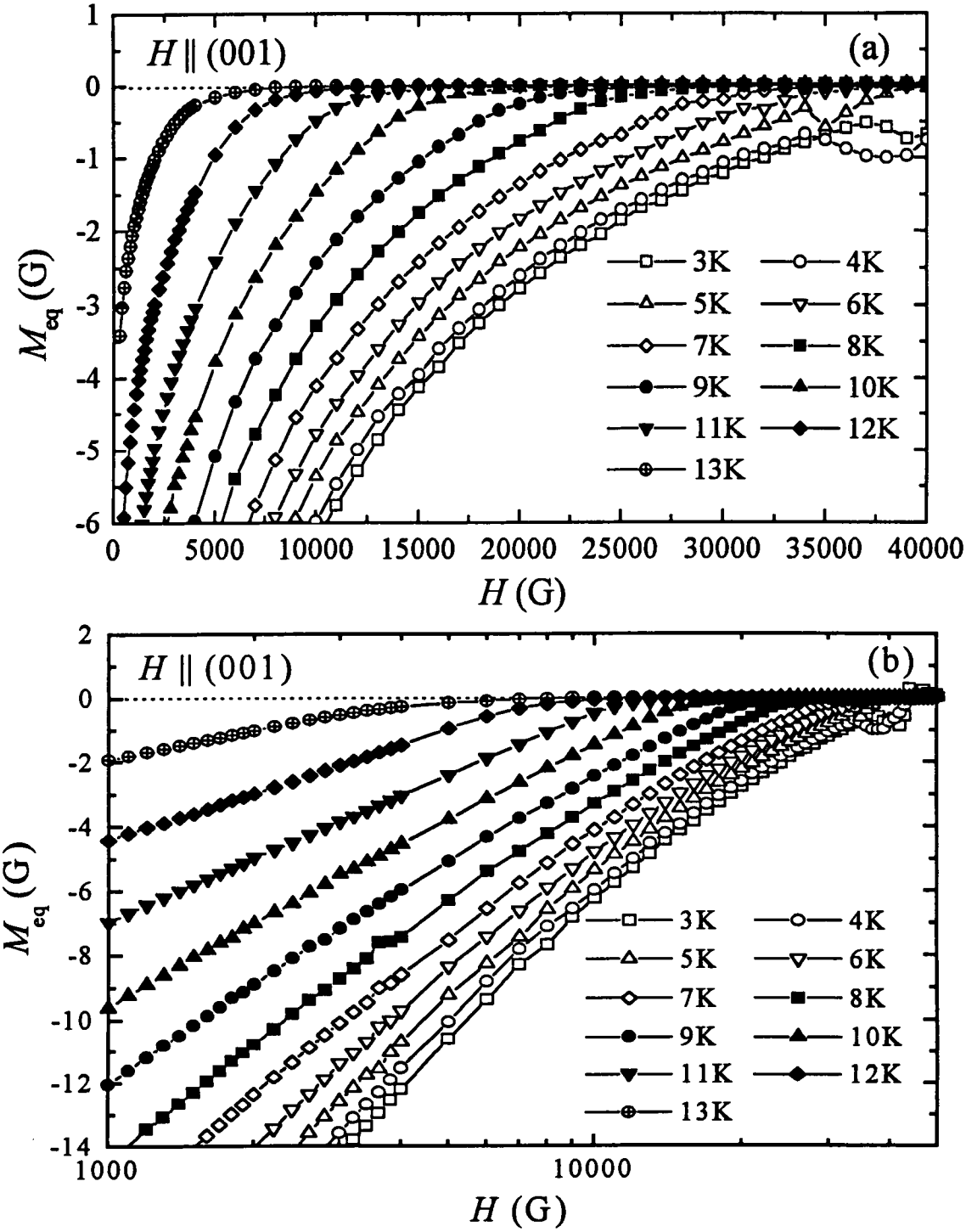


Figure 2-34. Plots of (a) M_{eq} vs. H and (b) M_{eq} vs. ln(H) at several temperatures.

linear dependence for M near zero, yielding values for H_{c2} via linear extrapolations to M = 0 (ignoring data in the "peak effect" where M is irreversible). These values shown as open up-triangles in Figure 2-33. For temperatures nearer T_c, the predicted linear dependence is poorly defined and the resulting values for H_{c2} are less reliable.

Finally, measurements of the heat capacity $C_p(H,T)$ provide completely independent values for the upper critical field H_{c2}. These measurements were conducted in several fixed fields H // (001)-axis. At H_{c2}, there is a jump in C_p due to the second order phase transition; experimentally, we defined the field H_{c2} to be at the mid point of this jump. The resulting values, shown as solid squares in Figure 2-33, agree relatively well with the aggregate results from magnetization studies.

2.3.7 Ginzburg-Landau parameter κ, beyond the constant - κ approximation

In the original formulation of Ginzburg-Landau theory, the parameter κ was defined as the ratio of λ/ξ, near T_c. As is evident in the preceding discussion, this dimensionless parameter appears frequently with the theory of the mixed state. Experimentally, it is often assumed that κ is constant for a given (sample of) superconducting material. To illustrate a typical argument, the Ginzburg-Landau parameter κ can be estimated to be about 15, deduced from equation (2.3.6-2), in single crystal of YNi_2B_2C, with magnetic field H parallel to the (001)-axis. From WHH theory,[94] one has $H_{c2}(0) = 0.7T_c(-dH_{c2}/dT)$ near T_c, which predicts $H_{c2}(0)$ = 3.8 T based on the experiment result dH_{c2}/dT = -0.36 T/K near T_c. Then,

with the simple relation $H_{c2}(0) = \phi_o/2\pi\xi^2$, a coherence length ξ of about 9.3 nm can be determined, which gives in turn a penetration depth λ = 139 nm, from $\kappa = \lambda/\xi$. Using these values, the lower critical field H_{c1} can be estimated from the relation $H_{c1}(0) = (\phi_o/4\pi\lambda^2)(\ln\kappa + 1/2)$ to be about 273 G, which is consistent with the value (for magnetic field H parallel to (001)-axis) in Figure 2-31. However, this typical analysis with a constant Ginzburg-Landau parameter κ oversimplifies the experimental and theoretical reality.

Extensions beyond the constant-κ approximation are needed for lower temperatures. In 1964, K. Maki first studied this problem theoretically.[47] The generalized work contains three parameters κ_1, κ_2, and κ_3, associated with the three relations

$$H_{c2} = (\sqrt{2})\kappa_1 H_c, \tag{2.3.7-1}$$

$$(4\pi)(dM/dH)_{Hc2} = (2\kappa_2^2 - 1)^{-1}\beta_A^{-1}, \tag{2.3.7-2}$$

and

$$H_{c1} = H_c [ln\kappa_3] / [(\sqrt{2})\kappa_3]. \tag{2.3.7-3}$$

At T_c, one has $\kappa_1 = \kappa_2 = \kappa_3 = \kappa$ as in the original formulation. Below T_c, however, the κ_i exhibit different temperature dependencies, with the size of the variation depending on the cleanliness of the material. The various κ_i values can be estimated from the respective experimental data: the thermodynamic critical field H_c from magnetization and heat capacity measurements, the upper critical field H_{c2} and dM/dH near H_{c2} from equilibrium magnetization measurement, and the lower critical field H_{c1} from flux-entry field measurement. Figure 2-35 shows determinations of κ_i of the single crystal of YNi_2B_2C as a function of temperature. The κ_1 is best determined, as it is based on data for H_{c2} and H_c, each of which is well established by both magnetic and calorimetric studies. Experimentally

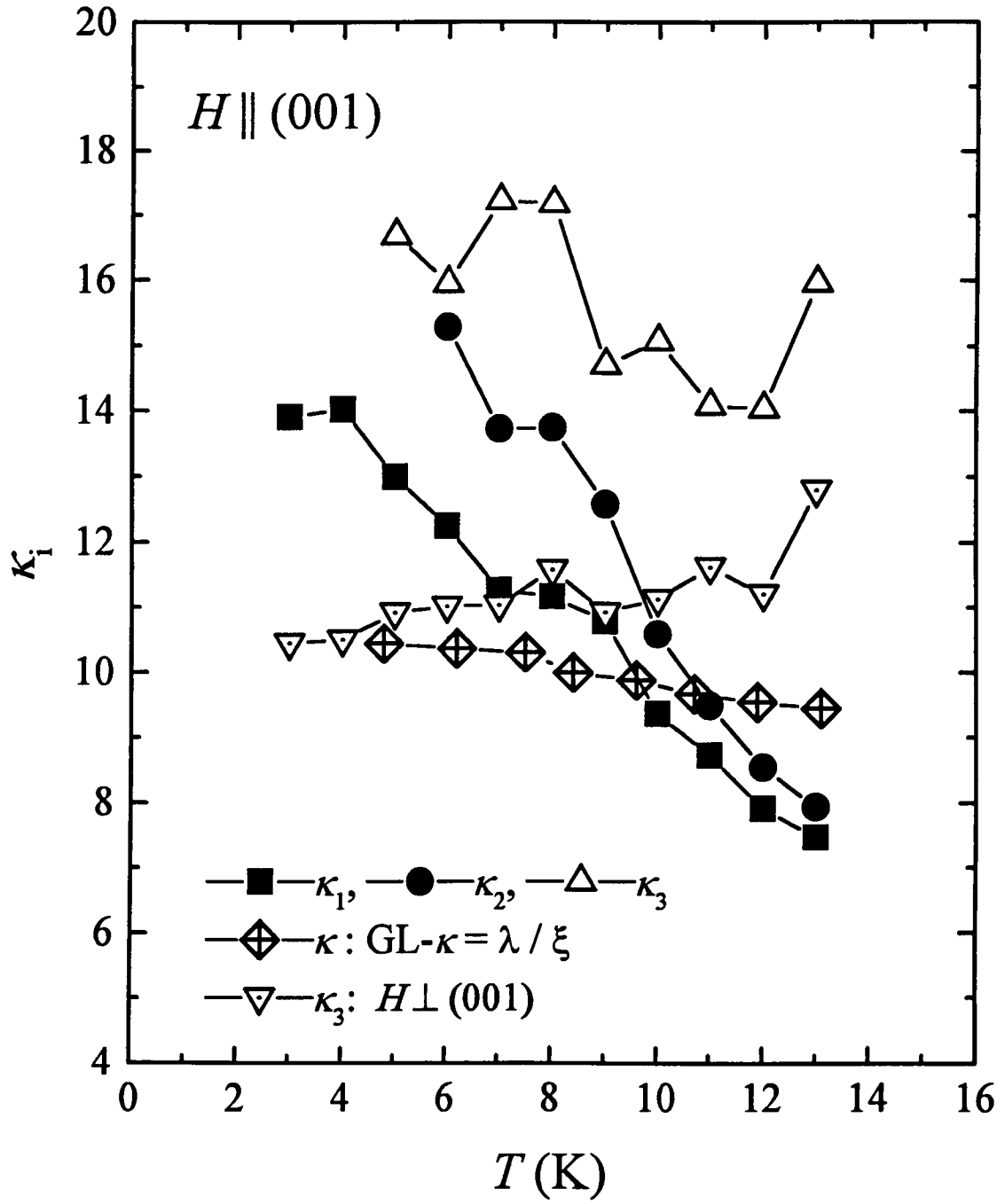


Figure 2-35. The temperature dependence of Ginzburg-Landau parameters κ_i.

$\kappa_i(T)$ increased by nearly a factor-of-2 over its value near T_c, $\kappa_1(T_c) \approx 8$. The second parameter κ_2, which is based on the slope of $M(H)$ near H_{c2}, has a very similar value near T_c. Like κ_1, it increases significantly as the temperature is reduced. The least well defined is κ_3, as it is based on the field of first penetration, which is affected by surface feature that can either promote the entry of flux (e.g. sharp edges) or inhibit flux entry (e.g. pinning or surface barrier effects). The experimental value of κ_3 near T_c is much larger than the similar values for κ_1 and κ_2.

According to Eilenberger,[114] the relative temperature dependencies of the κ's depends on the quantity (ℓ /ξ_o) and the anisotropy due to impurity scattering. As the electronic mean free path ℓ becomes longer, the generalized Ginzburg-Landau parameters exhibit a more pronounced variation with temperature; with relatively short ℓ, the κ_i lose their temperature dependence and retain their values at T_c. Since this YNi_2B_2C crystal displays pronounced effects of non-local electrodynamics that requires a long mean free path, it is only natural that the non-locality should be accompanied by temperature dependent κ values, as observed.

2.4 Summary

In summary, the YNi_2B_2C crystal is a clean ($\ell_o >> \xi_o \sim 9$ nm), type-II superconductor. The anisotropic London equations derived by V. G. Kogan et al. for describing nonlocal effects in clean high-κ superconducting materials well represent the magnetization data for the single crystal. There is an "anomalous peak effect" slightly below

H_{c2}. It may be possible to consider the formation of a generalized FFLO state, a suitable first-order phase transition from weak to strong pinning near H_{c2}, in the YNi_2B_2C system. The temperature dependence of $1/\lambda^2$, which is obtained using non-local theory at low temperature and local theory near T_c, is $1/\lambda^2 \propto t^n$ with $n = 3/2$ and $t = T/T_c$. Contrary to the exponential dependence expected for s-wave pairing, the nearly T^3 behavior for $\lambda(T)$ below $T = 10$ K in the single crystal suggests the possibility of a non-*s*-wave pairing mechanism. However, the parabolic relation between $\lambda^2(0)/\lambda^2(T) = (1-t^2)$, with $t = T/T_c$, describes the experimental values fairly well, also. More direct and precise methods are needed to investigate the temperature dependence of λ near $T = 0$ K, to understand whether the pairing in YNi_2B_2C differs from *s*-wave.

The normal state magnetization and paramagnetic susceptibility of YNi_2B_2C likely comes from paramagnetic Ni^{2+} ions. In addition, the anisotropy of the magnetic susceptibility of this material can be attributed to CEF effects on Ni^{2+} ions. Meanwhile, in the framework of thermodynamics, the thermodynamic critical field, $H_c(T)$, of YNi_2B_2C is described well by the parabolic relation, $H_c(T) = H_c(0)\,[1 - (T/T_c)^2\,]$, with $H_c(0) \approx 2556$ G. Other aspects of the heat capacity data deviate from predictions of both the weak- and strong-coupling theories, but agree fairly well with the medium-coupling analysis. It seems inevitable to make a more comprehensive study of microscopic mechanisms, such as medium or strong electron-phonon coupling, for YNi_2B_2C. Using various methods, the coefficient of electronic heat capacity $\gamma \approx 20$ [mJ/mol K^2] is obtained, values come from heat capacity data, from integration of the magnetization curves and normal state parameters, and from the medium-coupling analysis.

Overall, the YNi_2B_2C crystal exhibits little irreversibility in the superconducting state and significant angular variation of magnetization in normal state. Near T_c, the equilibrium magnetization M for YNi_2B_2C is standard London-like with $M \propto \ln(H)$. Well below T_c, however, M deviated from this simple "local" form and follows accurately the more general nonlocality relation of Kogan et al. The deduced values of the Ginzburg-Landau parameters κ_1 and κ_2 (from Maki theory) increase considerably as the temperature decreases. This is consistent with the material's long electronic mean free path and the observation of non-local electrodynamics.

CHAPTER 3

THE MIXED STATE PROPERTIES OF HIGH-T_C SUPERCONDUCTORS

High-T_c superconducting (HTS) materials are unconventional type-II superconductors which have a much larger upper critical field (H_{c2}) and consequently a much shorter coherence length (ξ) than those of conventional low-T_c superconductors. Overall, the mixed (vortex) state in HTS materials covers a very large part of the magnetic phase diagram. The mixed state plays a key role in practical applications of HTS materials. However, there are many obstacles to be overcome in obtaining practical applications of HTS materials. First, the high-T_c superconductors are ceramics, which are brittle and generally not flexible. It is not easy to develop applications such as superconducting wires, magnets, and so on. Second, the high-T_c superconductors have highly anisotropic properties, weak link current flow, and giant flux creep (magnetic relaxation or decay of the

electric current with time) in the mixed state. Usually, the conventional low-T_c superconductors exhibit only a small magnetic relaxation effect, which is explained by the classical Anderson-Kim model:[115] the irreversible magnetic moment decreases logarithmically with time, which is referred to as "magnetic flux creep" since it occurs via hopping of vortices. However, the high-T_c superconductors show a much large rate of magnetic relaxation, so called "giant flux creep."[116] In the presence of a large magnetic field, an easy movement of flux lines generates heat and makes the current conduction to be dissipative. Therefore, magnetic relaxation in HTS materials can be an important limitation, from the point of the view of practical applications. To overcome the specific shortcomings of giant flux creep and a weak current density (J_c) in the mixed state, the pinning effects of flux lines (vortices) in HTS materials has been studied. Fortunately, vortices can be pinned in the mixed state by intrinsic or extrinsic imperfections (defects), which prevent the motion of flux lines. In 1991, L. Civale et al. showed that introducing columnar tracks, made by heavy-ion irradiation, greatly increases the critical current density J_c in single crystals of $YBa_2Cu_3O_7$.[37] More recently, T. Hwa et al. suggested that splayed columnar defects (with an angular dispersion of several degrees) should create much stronger pinning effects than those of simple, parallel columnar defects,[38] since splay forces an entanglement of vortex lines that further constrains their motion. Therefore, L. Krusin-Elbaum et al. devised a mechanism to produce splayed columnar defects using a fission process, in which heavy constituent nuclei (Hg, Tl, Pb, etc.) inside HTS materials were induced to fission by high energy (0.8 GeV) proton irradiation.[39,40] They found remarkable increases in the critical current density J_c and decreases in the decay rate of magnetic

relaxation, due to strong vortex pinning effects. Overall, a key requirement for useful applications lies in making methods to pin the vortices against dissipative motion, due to a current flow in a magnetic field.

3.1 The Influence of Ag-Additions to $HgBa_2CuO_{4+\delta}$ Materials

3.1.1 Experimental Aspects

As mentioned, the high-T_c superconductors are ceramics which are brittle and inflexible. To get some metallic properties in the HTS materials, many scientists investigated the effects of adding some kinds of metallic elements to the HTS materials. Usually, metallic silver (Ag) seems to be favorable in the fabrication of high-T_c superconducting tapes, wires, and materials as it is one of the few elemental metals that does not "poison" the superconductor. The Hg-based cuprate $HgBa_2CuO_{4+\delta}$, which has high-T_c values near 90 K,[14] is one of the simplest materials, in which it has only one CuO_2 layer in the unit cell. The Hg-1201 compound has a tetragonal structure and P4/mmm space group, with one planar Cu site as shown in Figure 3-1.[117]

The synthesis of the $Ag_xHgBa_2CuO_{4+\delta}$ materials was as following. To begin, a precursor Ba_2CuO_3 was prepared from BaO and CuO powders after mixing, grinding, pressing, and heat treatment. Then the superconductor $HgBa_2CuO_{4+\delta}$ was prepared by heat

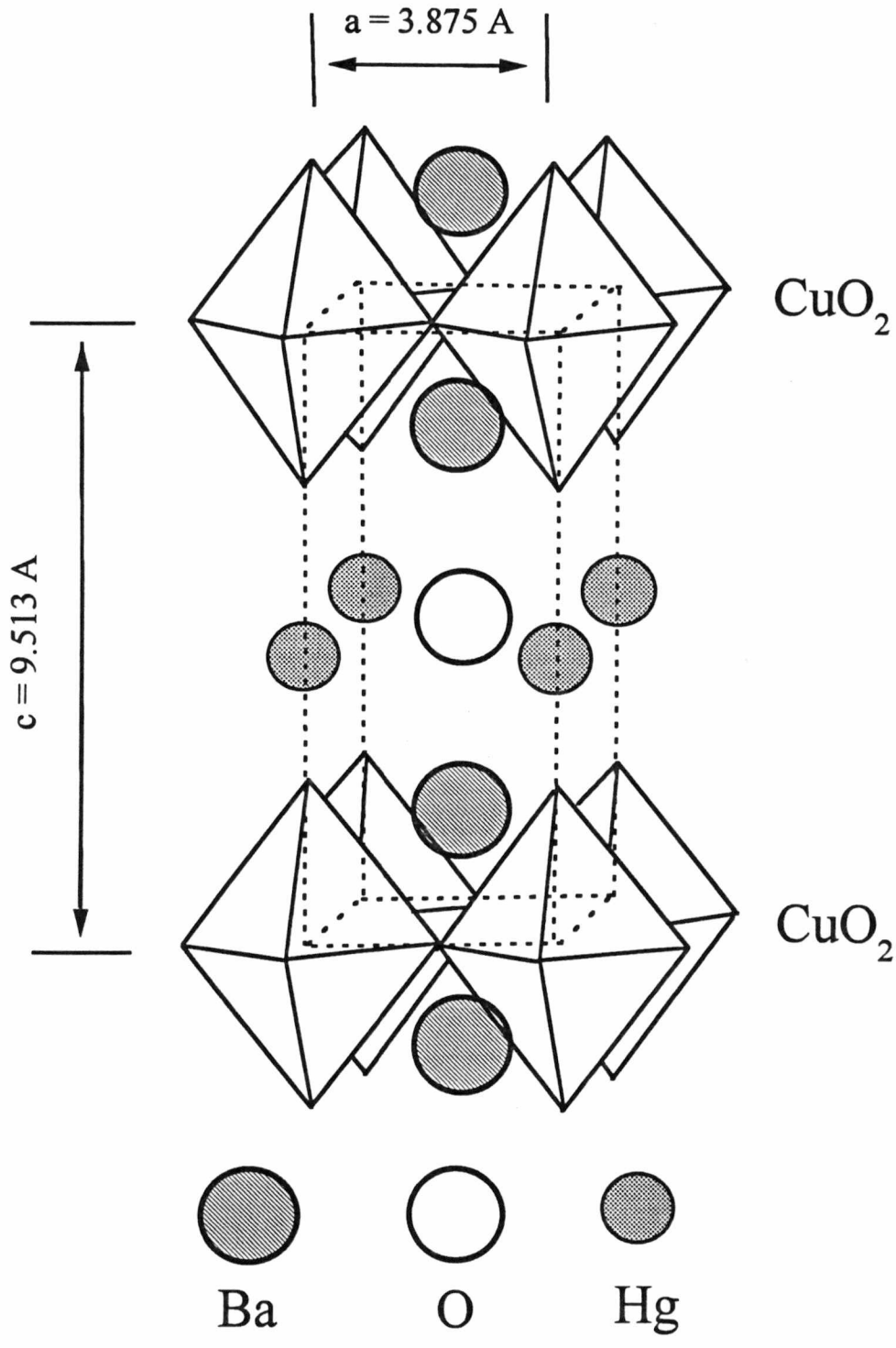


Figure 3-1. The structure of Hg-1201 in the unit cell.

treatment of mixtures of powders of the precursor and HgO. Finally, to make $Ag_xHgBa_2CuO_{4+\delta}$ materials containing metallic silver (Ag), portions of the $HgBa_2CuO_{4+\delta}$ stoichiometric material were mixed and ground together with Ag_2O in Ag-mole fractions $x = 0$, 0.05, 0.1, 0.3, and 0.5. Each material was pressed into a pellet. This was wrapped in Ag foil and sealed in an quartz tube that was evacuated to 0.1 mbar pressure. The assembly was annealed at temperature 840 °C for 5 hours. The detailed synthesis and structure properties of this materials have been described elsewhere.[118]

The magnetic studies were carried out using a SQUID-based magnetometer (Quantum Design MPMS-7). The randomly oriented polycrystalline $Ag_xHgBa_2CuO_{4+\delta}$ materials (mass 98.7, 86.5, 105.9, 106.7, and 98.0 mg for x = 0, 0.05, 0.1, 0.3, and 0.5, respectively) were glued onto a thin Al-disk using a *Duco* cement and mounted in a *Mylar* tube for measurement. Prior to studies in low magnetic fields, the superconducting magnet in the magnetometer was "reset" to release trapped flux in its windings, by heating it above its T_c. The Meissner state magnetic moment m was measured under zero-field-cooled (ZFC) and field-cooled (FC) conditions in an applied field $H = 4$ G. In all case, the magnetization $M(\mathrm{G}) = m(\mathrm{G{\cdot}cm^3})/V(\mathrm{cm^3})$ was based on the volume V, calculated from the mass of superconductor accounting for any free Ag component (Appendix 3).

The superconductive transition temperature T_c was determined by extrapolating to zero the linearly varying Field Cooling (FC) magnetization $M(T)$ curve. For studies in the mixed state, at first the sample was cooled from above T_c in zero magnetic field and stabilized at the target temperature. At this temperature, the sample magnetization $M(H)$ was measured in fields up to 6.5 T for both increasing and decreasing field history. In

addition, to correct for the paramagnetic background signal, the normal state magnetic moment was measured for temperatures from above T_c to 295 K for each samples and extrapolated to lower temperatures. From the studies of reversible and irreversible magnetization in the mixed state, the superconducting properties, such as London penetration depth λ, characteristic temperature T_o for thermally induced current decay, and so on, of the $Ag_xHgBa_2CuO_{4+\delta}$ materials were investigated, according to the mole fraction $x = 0$, 0.01, 0.1, 0.3, and 0.5, respectively. The properties are consistently understood in terms of the superconducting hole density and thermally activated tunneling of pancake vortices through a surface barrier.[119]

3.1.2 Experimental Results and Analysis

Silver is one of the very few metals that is chemically compatible with high temperature superconductors. As such, it is often used as a matrix or substrate. One may expect, however, that the presence of silver (Ag) at high temperature during the synthesis of the HTS materials may play some role in changing the superconducting properties. The basic intra-granular properties of Hg-1201 superconducting material may be modified by adding Ag into $HgBa_2CuO_{4+\delta}$ superconductor. For example, the *X*-ray diffraction studies of these $Ag_xHgBa_2CuO_{4+\delta}$ showed that the crystalline unit cell volume was reduced, with contractions of both the *a*- and *c*-lattice parameters.[118] As mentioned in the previous section (3.1.1) and shown in Figure 3-2, the superconductive transition temperature T_c was determined by the linearly extrapolating to zero in field cooled (FC) magnetization $M(T)$ curve. This procedure ignores the slight tail at higher temperature due to thermal

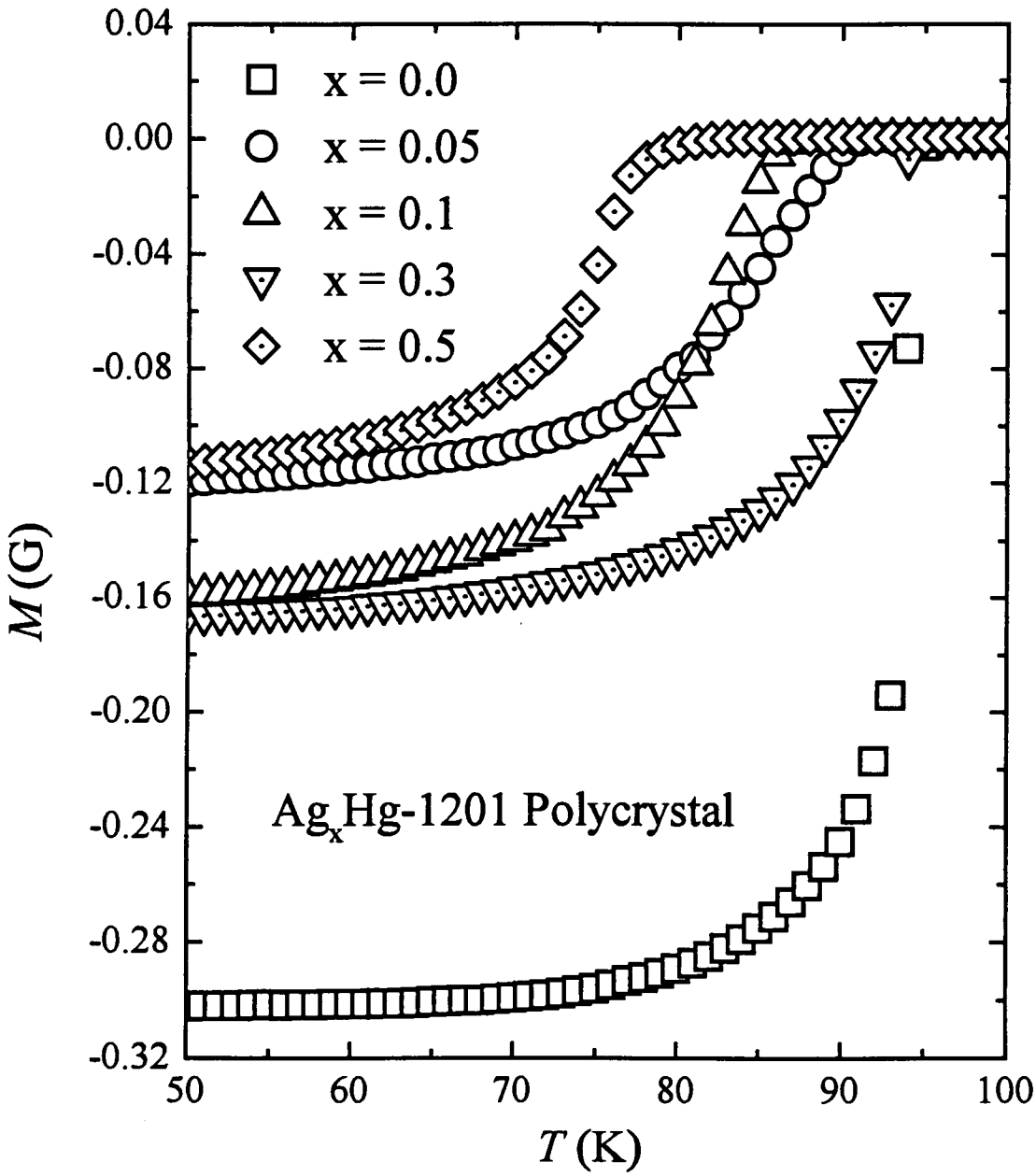


Figure 3-2. Field Cooled magnetization M versus temperature T in an applied field $H = 4$ G.

fluctuation effects. As a function of the mole fraction of Ag-content, the T_c and persistent current density J_p (at T = 10 and 30 K for H = 1 T) values are shown in Figure 3-3-a and -b. The T_c values were determined by the FC magnetization $M(T)$ curve, and the J_p values were obtained from the Bean critical state model, assuming the value r = 1 μm for the average radius of the circulating currents. Figure 3-3-a shows that T_c generally decreases with Ag-content with the only exception the material with x = 0.3 case. Meanwhile, Figure 3-3-b shows no clear trend for J_p versus Ag-content.

While the FC transitions in Figure 3-2 change smoothly with temperature, the zero field cooled (ZFC) magnetization $M(T)$ curve has more structure as seen in Figure 3-4. This "two step" transition is due to decoupling of current flow between grains.[120] The figure shows the Meissner state magnetic moment under ZFC condition in an applied field 4 G. It is evident that the structure gradually disappears as the Ag-content increases. This means that increasing the Ag-content diminishes the supercurrent flow between grains and weakens the inter-grain coupling.

After correction for the normal state magnetic moment that was measured from 295 K to near T_c and extrapolated to lower temperature, the mixed state magnetization was obtained. Figure 3-5-a and -b show $M(H)$ curves for one sample of $Ag_xHgBa_2CuO_{4+\delta}$ with x = 0.05. In Figure 3-5-a, the magnetization M is irreversible at the low temperature of 10 K. However, Figure 3-5-b shows that the magnetization M is nearly reversible at higher temperatures. As noted in the previous section (2.2.5), the standard local limit London theory should describe fairly well HTS materials with high κ-values.[45] According to Kogan's standard London limit theory in the intermediate field regime $H_{c1} << H << H_{c2}$, the

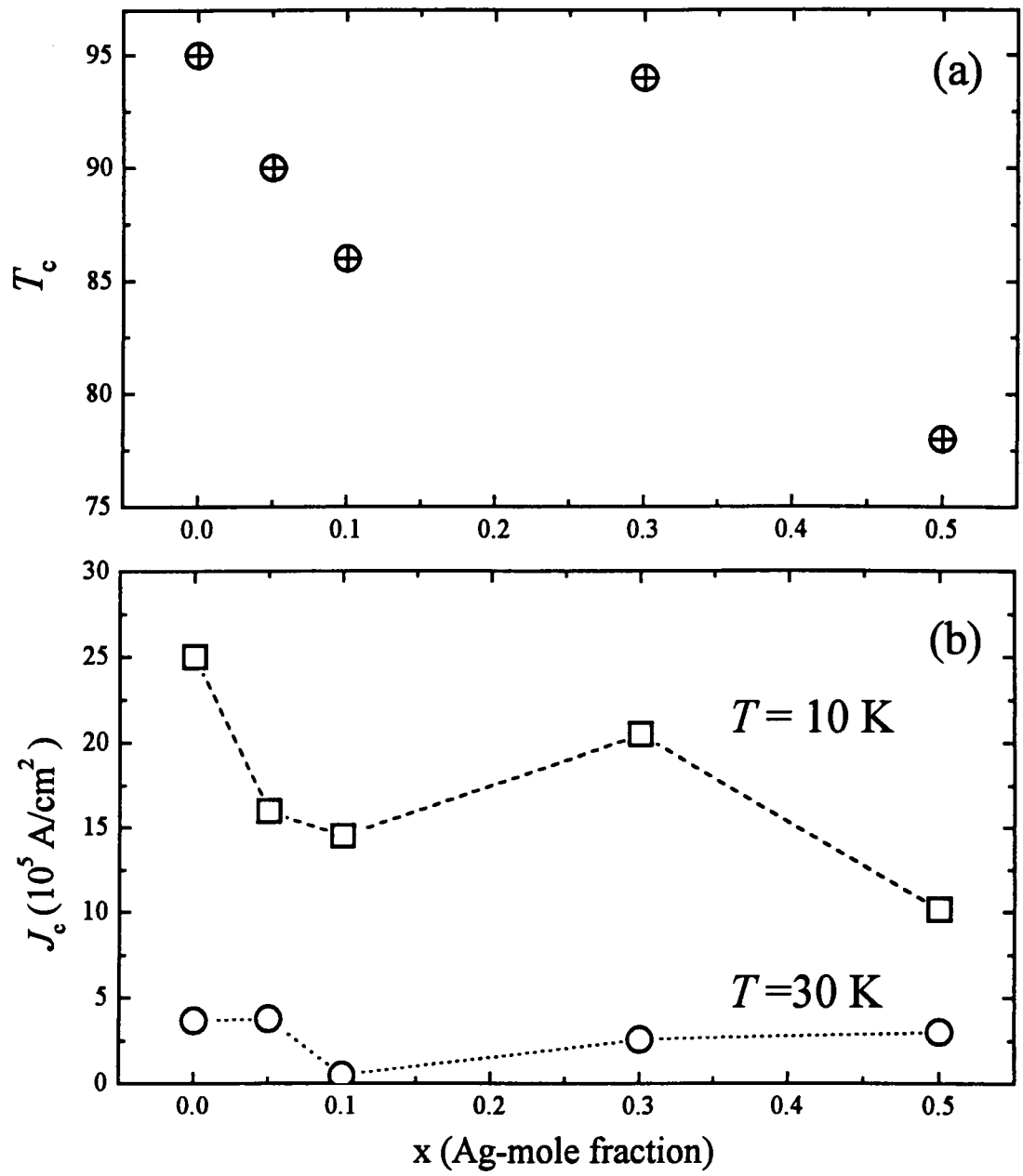


Figure 3-3. (a) T_c versus x (Ag-mole fraction) and (b) J_c versus x (Ag-mole fraction) at T = 10 and 30 K for H = 1 T.

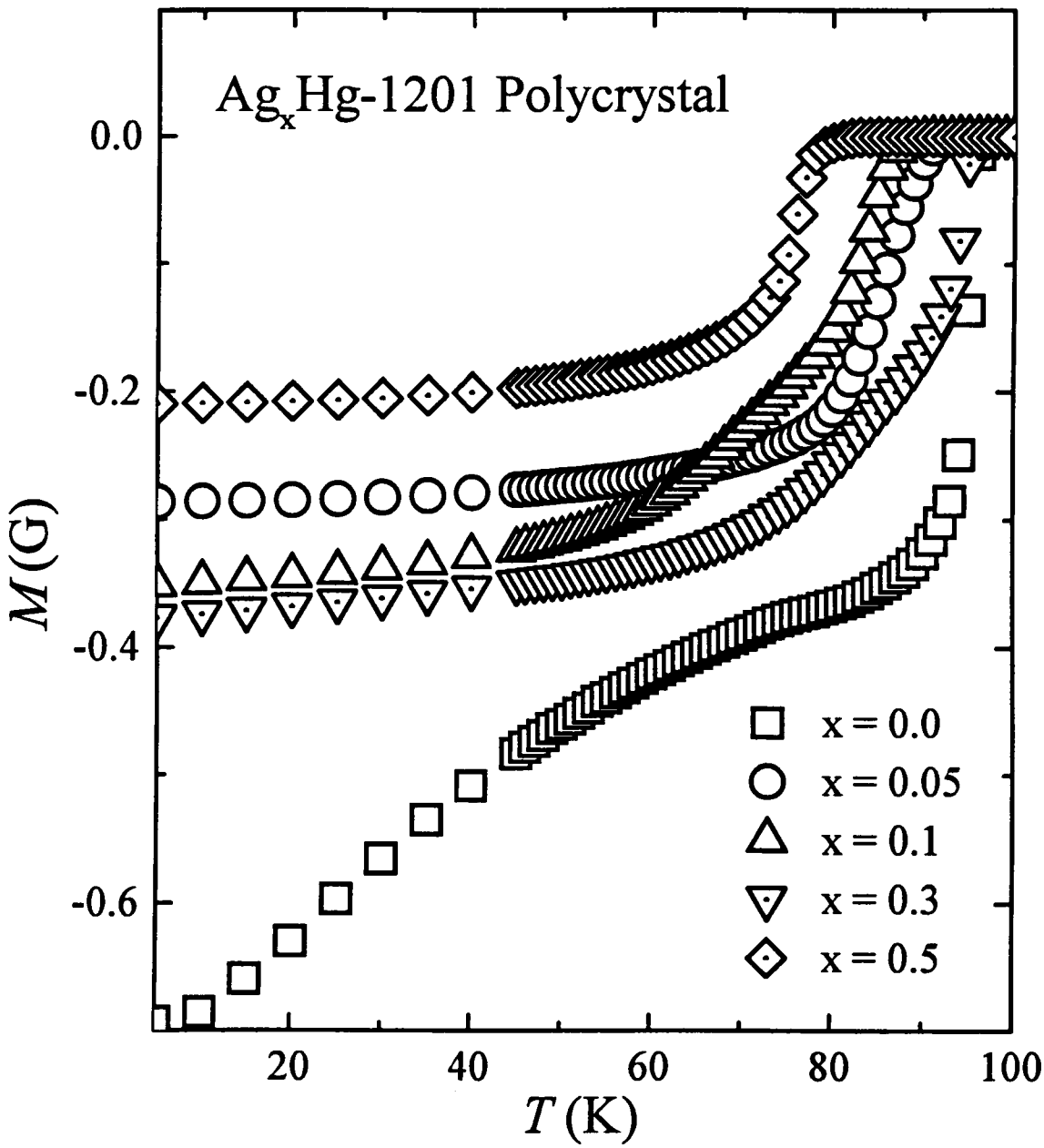


Figure 3-4. Zero Field Cooled magnetization M versus temperature T in an applied field $H = 4$ G.

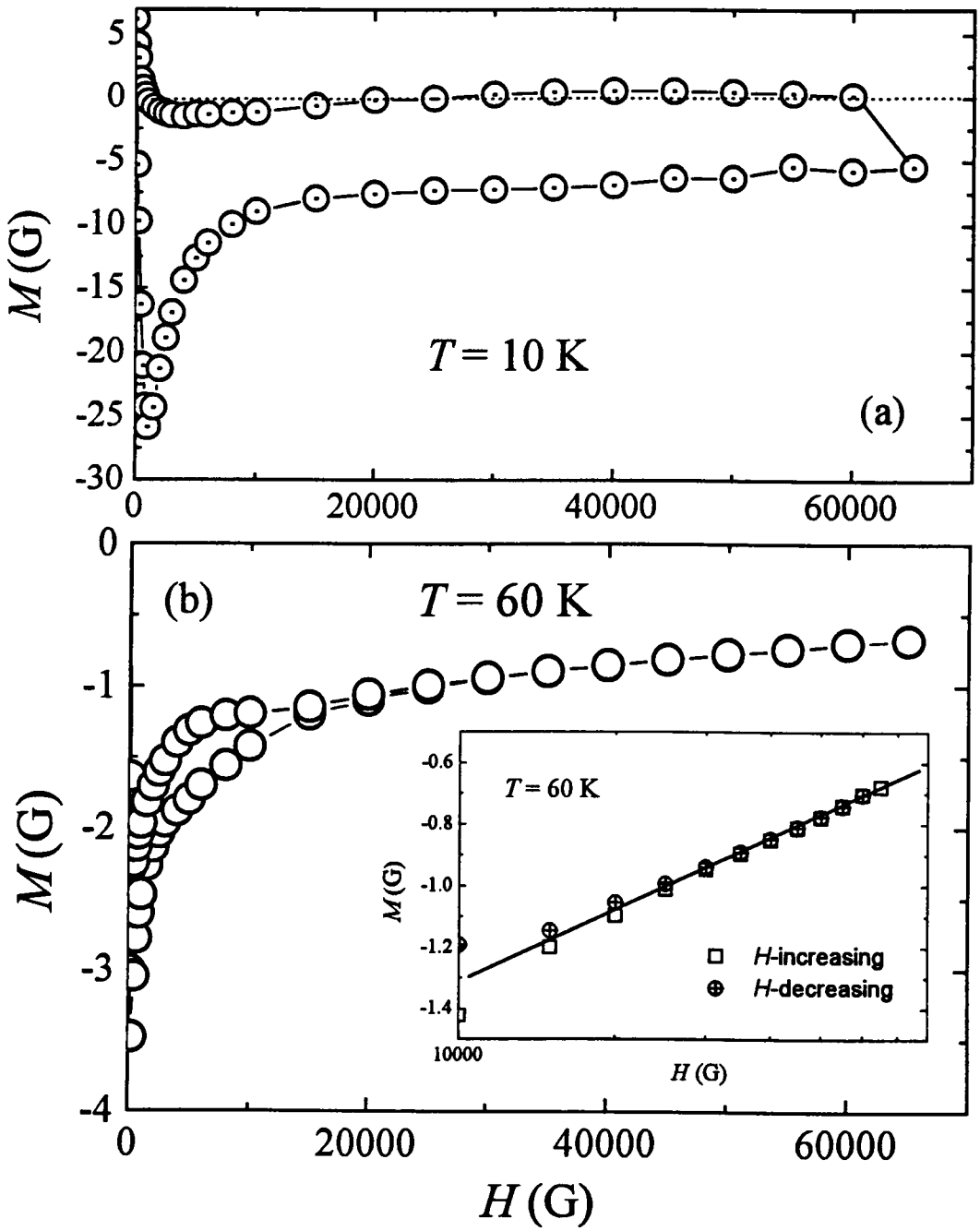


Figure 3-5. The magnetization M versus magnetic field H, for polycrystalline $Ag_xHgBa_2CuO_{4+\delta}$ superconductor with x = 0.05. Inset in (b) shows a semilogarithmic plot of M versus H.

equilibrium magnetization M is given by equation (2.3.1-1):[45]

$$M = - [\phi_o /(32\pi^2 \lambda(T)^2)] \ln(\eta H_{c2} /H), \qquad (3.1.2\text{-}1)$$

which means that the equilibrium magnetization M should be linear when plotted versus the logarithmic of field $\ln(H)$. Thus its slope $dM / d\ln(H)$ is proportional to $1/\lambda^2$. The standard London theory for the reversible magnetization is based on thermodynamic equilibrium. Often, fluctuation effects near T_c in HTS materials contribute considerable entropy and can significantly modify the equilibrium magnetization. In this study, fluctuation effects are ignored because the analysis focuses on the data well below T_c where such effects are very small. The equilibrium magnetization M, at low temperature and low field region, was approximated by the average of both field histories, increasing and decreasing field. The $1/\lambda^2$ dependencies as a function of temperature for various samples are shown in Figure 3-6. Both Ginzburg-Landau and BCS theories predict the linear relationship between $1/\lambda^2$ and temperature (T) near T_c only. However, as shown in Figure 3-6, the linear variation of the experimental $1/\lambda^2$ with temperature extends down to temperature far below T_c. This suggests that the superconducting mechanism in these materials is more complex than simple s-wave pairing.

Whatever is its temperature dependence, the density of superconducting charge carriers, n_s, can be estimated using London theory in previous section (2.2.4):

$$(\lambda_L)^2 = m^* c^2 / 4\pi n_s e^2 \qquad (3.1.2\text{-}2)$$

These values and the corresponding T_c values can be composed with the universal empirical curve of $(T_c/T_{c,max})$ versus hole density p, which was formulated and discussed by Presland et al.[121] and Tallen and Flower:[122]

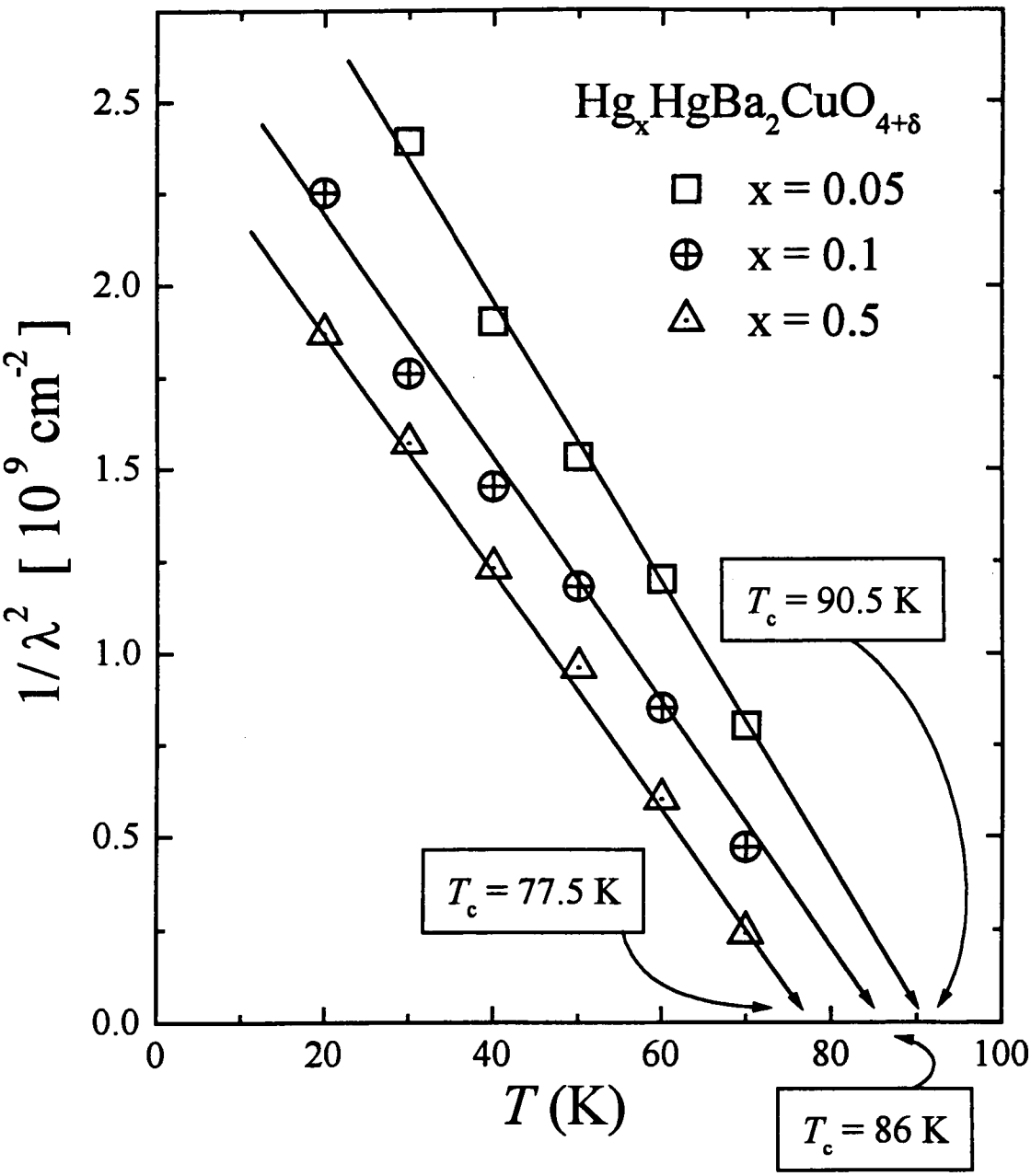


Figure3-6. Plots of $1/\lambda^2$ as a function of temperature T, for polycrystalline Ag_xHg-1201 materials. The intersections at $[1/\lambda^2] = 0$ show T_c, which are very similar to the values measured in low fields (Field Cooled measurement).

$$T_c / T_{c,\,max} = 1 - 82.6\,(p - 0.16)^2. \qquad (3.1.2\text{-}3)$$

In Figure 3-7, this parabolic relation is fitted to the experiment data for the Ag-Hg-1201 materials.[119] The overall consistency strongly suggests that the hole doping effects play a significant role in establishing the observed properties of these $Ag_xHgBa_2CuO_{4+\delta}$ superconductors.

In addition to the reversible magnetization, there is also irreversibility which comes from the present of macroscopic currents in the superconductors that flows in the bulk, on surfaces, or both. Often, as-prepared Hg-based cuprates show an asymmetric curve $M(H)$, with $M \approx 0$ in the decreasing field branch. This is a characteristic feature of a surface barrier-dominated system.[123-126] Figure 3-5-a shows an example, this characteristic asymmetry in $Ag_xHgBa_2CuO_{4+\delta}$ with $x = 0.05$. Recently, the theory for thermal flux creep of "pancake" vortices through a Bean-Livingstone surface barrier was developed by Burlachkov et al.[127] Instead of the transmission of a vortex line through a surface,[128] the theory considered 2-D pancake vortices,[129] which form in the mixed state when the interlayer coupling is weak and small compared with other energies in the system. When the magnetic field is first applied, the pancake vortices do not penetrate into the superconductor until H reaches the penetration field H_p, where

$$H_p = H_c \exp(-T/T_o). \qquad (3.1.2\text{-}4)$$

Here H_c is the thermodynamic critical field and T is the temperature. The factor T_o is a characteristic temperature for a given superconducting material,[127]

$$T_o = \epsilon_o d/\ln(t/t_o) = (\phi_o/4\pi\lambda)^2\, d/\ln(t/t_o), \qquad (3.1.2\text{-}5)$$

where $d = 0.95$ nm is the distance between sets of Cu-O planes, $\epsilon_o = (\phi_o/4\pi\lambda)^2$ is the vortex

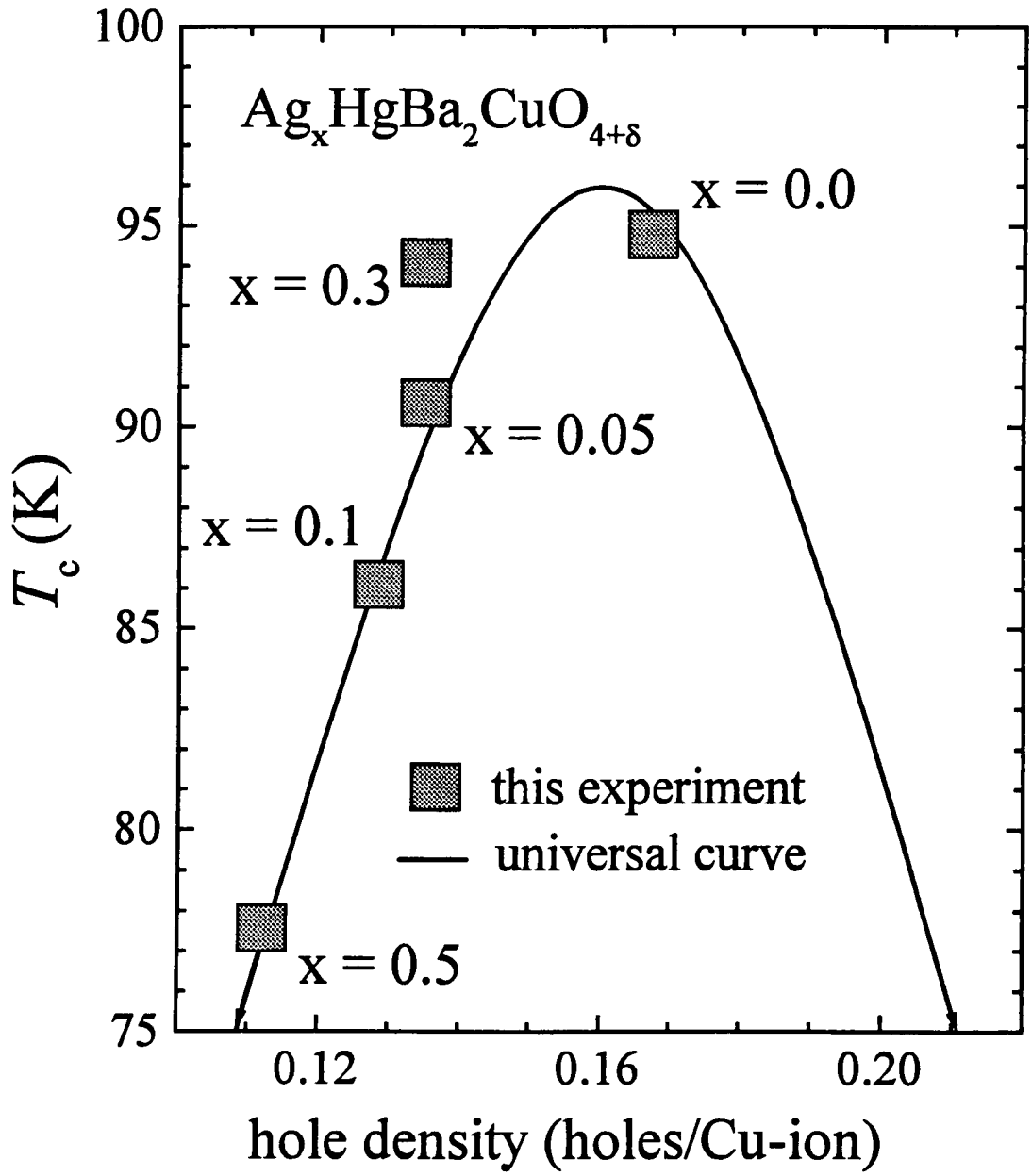


Figure 3-7. T_c of the materials versus hole density p, deduced from the London penetration depth using effective mass ratio $(m^*/m_e) = 1.07$. The solid line shows the general relation, Eq. (3.1.2-3), with $T_{c,max} = 96$ K. (J. R. Thompson et al., Physica C **272**, 171 (1996))

line energy, and t/t_o is the ratio of the experimental time (since application of the field) to the fundamental time scale t_o for vortex oscillations. At $T = 0$ K, the equation (3.1.2-4) reduced to the traditional result that $H_p \approx H_c$. However, for $T > 0$ K, thermally activated creep of pancake vortices into the superconductor leads to the exponential factor, $\exp(-T/T_o)$, and causes H_p to fall off much more rapidly with T than expected classically from the temperature dependence of $H_c(T)$. Although surface imperfections often reduce the magnitude of the prefactor in equation (3.1.2-4), they do not change the value of T_o.

Let us consider further an asymmetric magnetization curve like Figure 3-5-a, with the field increasing beyond the penetration field H_p. In this region, the magnetization M is predicted to decrease as $M \sim 1/H$. Furthermore, in the decreasing field region, the magnetization is expected to be field independent with $M \sim 0$, as observed. Consequently, the width ΔM of the magnetization loop for $H >> H_p$, using $B = (H^2 - H_p^2)^{1/2}$ for $H > H_p$ and $-4\pi M = H - B = H - (H^2 - H_p^2)^{1/2} \approx H_p^2/2H$,[127] is

$$\Delta M \approx H_p^2/H \propto \exp(-2T/T_o). \qquad (3.1.2\text{-}6)$$

At sufficiently high temperature or high field, the pancake vortex hopping distance becomes comparable with the thickness of the vortex-free surface layer. Then penetration by pancake vortices becomes reversible and ΔM (≈ 0) decreases to a noise-limited values, which serves to define the irreversibility line.

We can determine easily the penetration field H_p, as the point of minimum magnetization ($-M_{max}$) in the initial, increasing field part of an $M(H)$ curve. Using values determined by this method, T_o can be estimated by the slope ($d\ln H_p/dT$). Figure 3-8 shows semilogarithmic plots of H_p versus temperature T. The resulting values are T_o = 18 - 21 K,

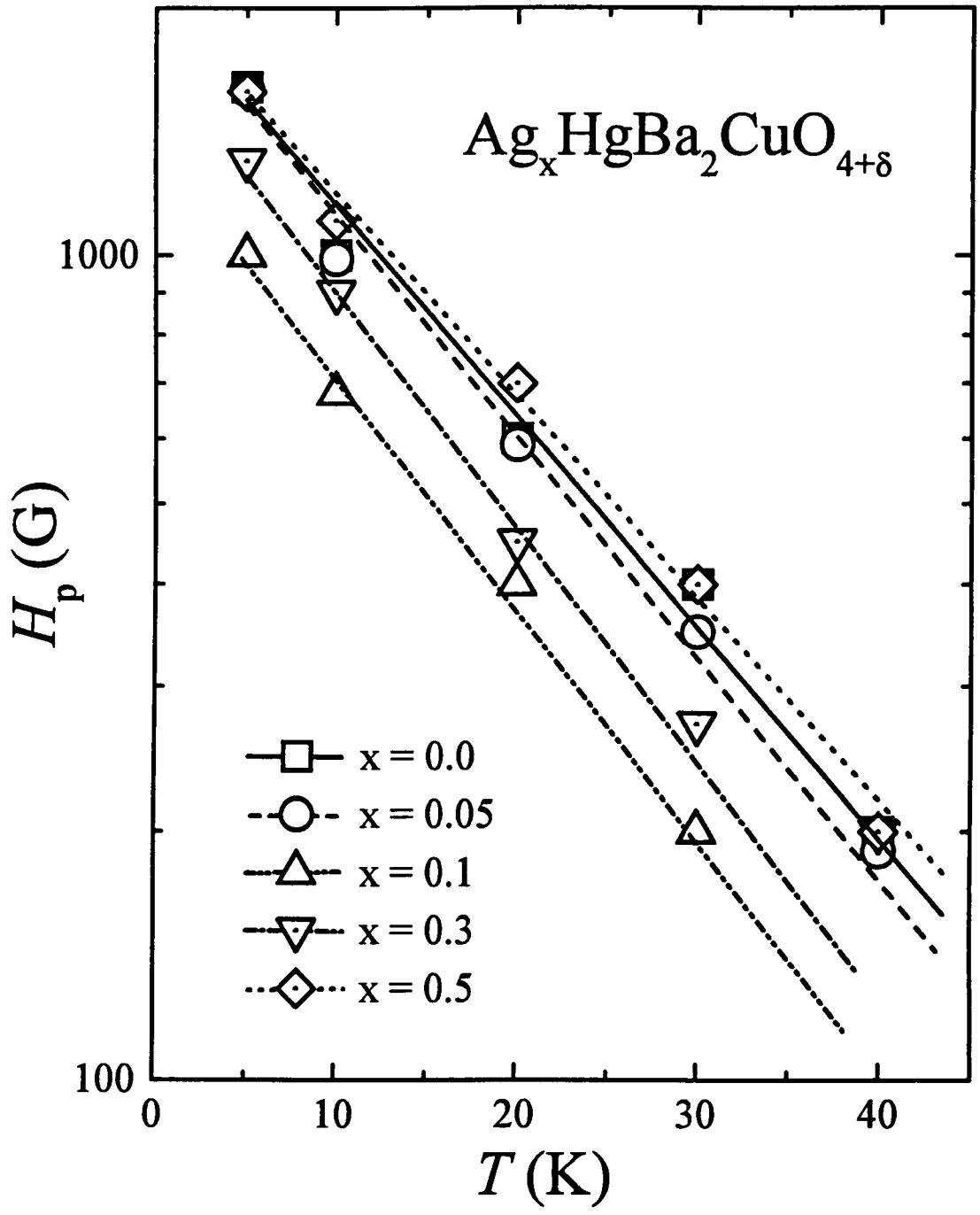


Figure 3-8. Semilogarithmic plot of the penetration field H_p versus T.

18 K, 16 K, 16 - 18.5 K, and 14.5 - 16.5 K for $Ag_xHgBa_2CuO_{4+\delta}$ with x = 0, 0.05, 0.1, 0.3, and 0.5, respectively. Using equation (3.1.2-5) with the typical experimental value, $\ln(t/t_o)$ ~ 30, and values of λ from the London analysis, we obtain for $Ag_xHgBa_2CuO_{4+\delta}$ with x = 0.1 the value $T_o \approx 18$ K; this is comparable with the experimental value from $H_p(T)$. Similar results are obtained for the other samples. Continuing, equation (3.1.2-6) predicts an exponential falloff of ΔM with temperature T. So Figure 3.9 shows semilogarithmic plots of ΔM versus T for $Ag_xHgBa_2CuO_{4+\delta}$ with x = 0.1 in several fields. Thus complementary values for T_o can be obtained from the slope of the lines in Figure 3-9. For the field range H = 2 ~ 20 kG, the estimated values for T_o by this method are T_o = 19 - 16 K, 26 - 22 K, 19 - 10 K, 21 - 12 K, and 28 - 27 K for $Ag_xHgBa_2CuO_{4+\delta}$ with x = 0, 0.01, 0.1, 0.3, and 0.5, respectively. These values are overall similar to the values obtained from the penetration field H_p. However, the values of T_o exhibit a field dependence which is not included in the existing theory. In summary, the results for $Ag_xHgBa_2CuO_{4+\delta}$ materials seem to be reasonable and consistent. Some complexities remain, such small "fishtail" effect in the $M(H)$ curve and the variation of J_p with Ag-content.

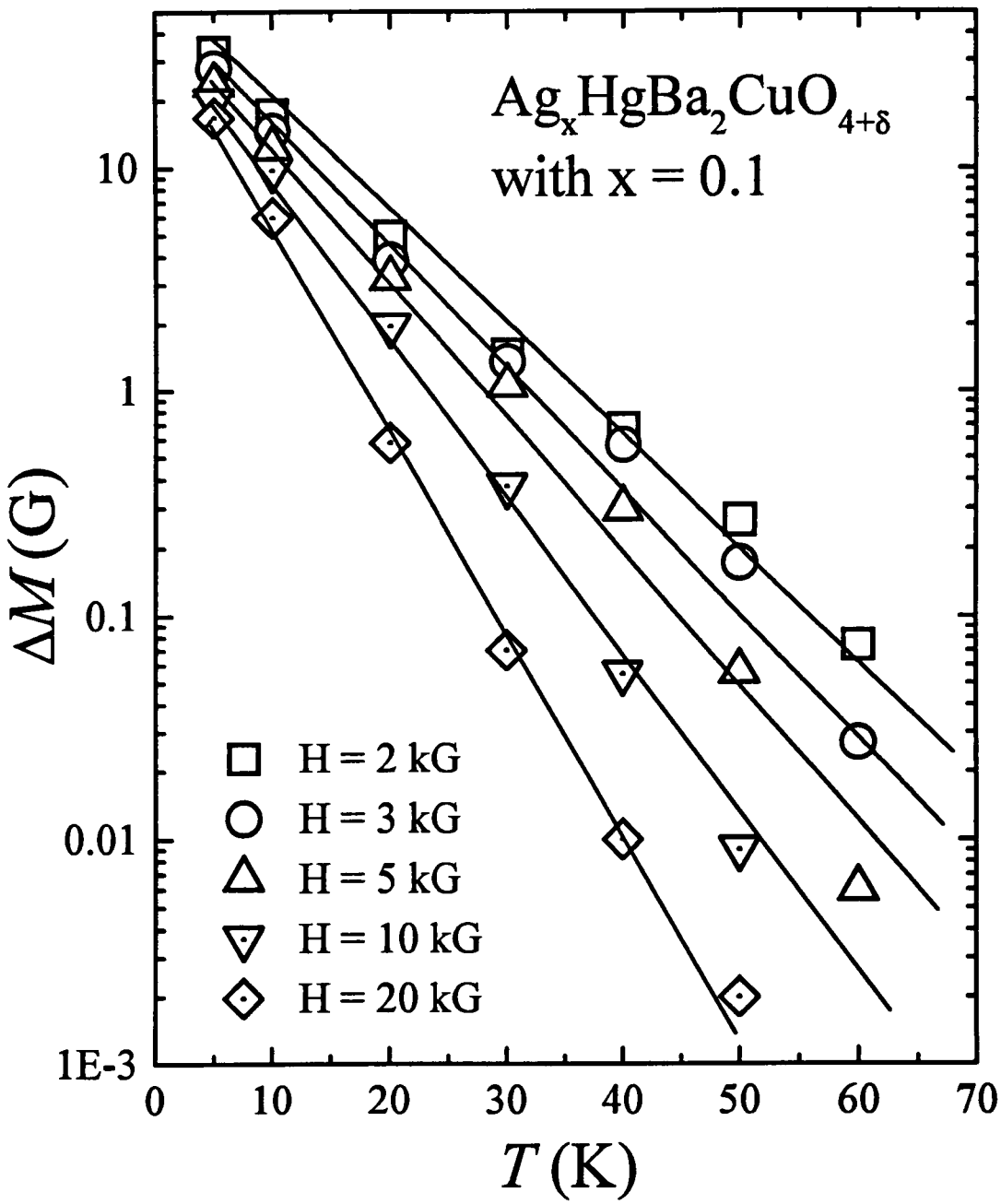


Figure 3-9. Semilog plot of the magnetic hysteresis ΔM, measured in different magnetic fields, versus T.

3.2 The Effects of Artificially Created Defects by Irradiation Methods: Splayed Columnar Effects in Several HTS Materials

3.2.1 Experimental Aspects

All of the HTS materials are type-II superconductors, which exhibit a wide mixed state region in their magnetic phase diagram. Figure 3-10 shows a simplified, schematic magnetic phase diagram for type-II superconductors. Two critical fields are seen, the lower critical field H_{c1} and the upper critical field H_{c2}. The Meissner state, in which the magnetic field inside superconductor is completely screening out ($B = 0$), only exists below H_{c1}. The magnetic flux lines, so-called vortices ($\phi_0 = ch/2e = 2.07 \times 10^{-7}$ G·cm^2), begin to enter into the superconductor when the applied field exceeds H_{c1}. The field regime between H_{c1} and H_{c2} is called the mixed state or vortex state. Within the vortex state, there may be a variety of vortex structural or dynamical phases. Especially, important phases are vortex solid and vortex liquid phases, which are divided by the irreversibility (melting) line, at which $J_c = 0$.[36]

The flux lines can be pinned inside a type-II superconductor by natural or artificial defects. Vortex pinning is a very important factor in practical applications requiring a large magnetic field ($H_{c1} < H < H_{c2}$), since vortices permeate the HTS material. The core of a vortex is an almost normal conductor. Because a superconductor conducts a macroscopic current J in the presence of a magnetic field, vortices experience a Lorentz-like force:[36,49]

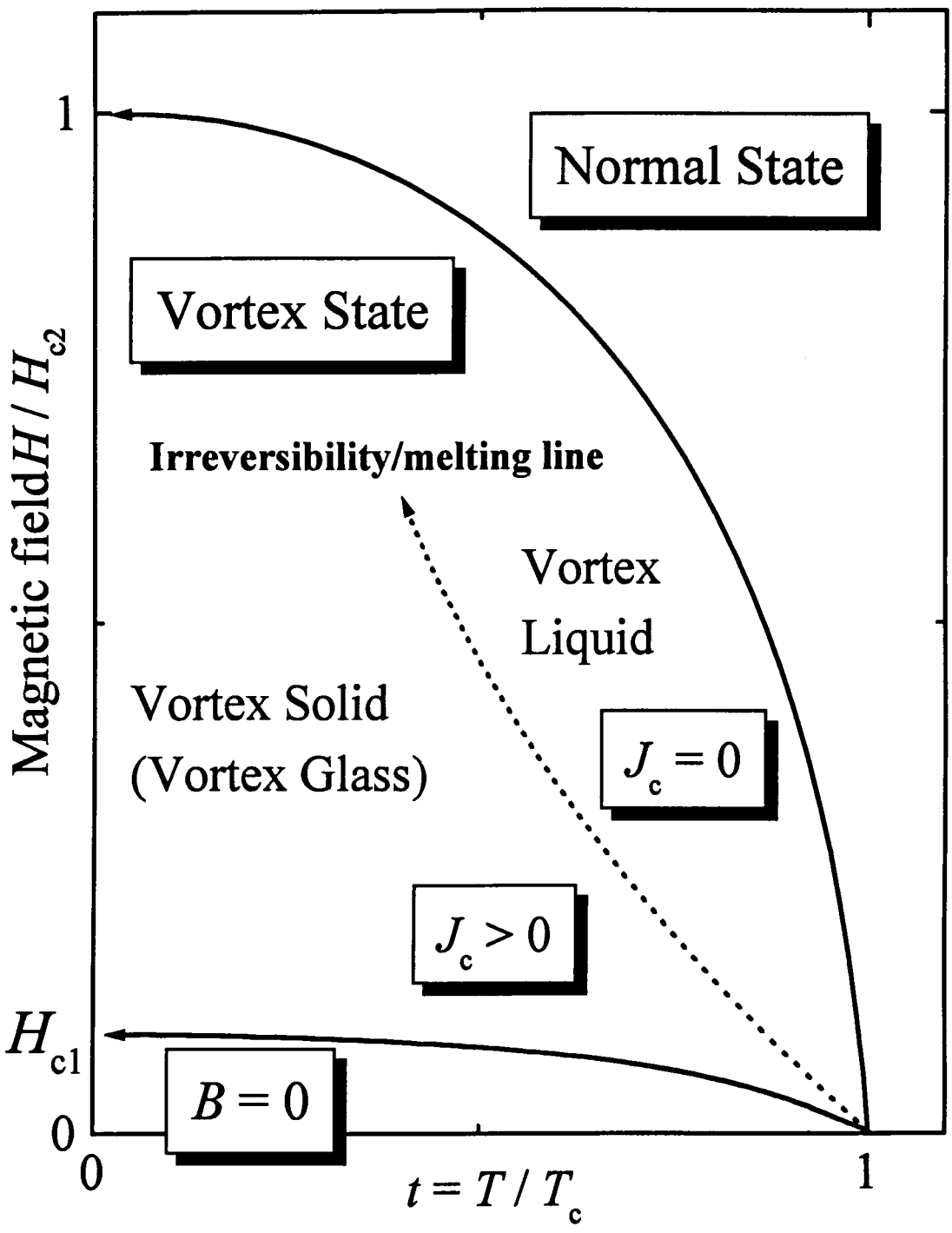


Figure 3-10. A schematic magnetic phase diagram for type-II, high-T_c superconductors.

$$\boldsymbol{F} = \boldsymbol{J} \times \boldsymbol{B}/c, \tag{3.2.1-1}$$

where J is the macroscopic current density, and $\boldsymbol{B}$ ($= \boldsymbol{H} + 4\pi\boldsymbol{M}$) is the magnetic induction. The movement of vortices in a superconductor is viscous. Usually the vortex velocity (**v**) due to the Lorentz driving force is perpendicular to the magnetic induction $\boldsymbol{B}$. Therefore, there exists an electric field,

$$\boldsymbol{E} = \boldsymbol{B} \times \mathbf{v}/c, \tag{3.2.1-2}$$

and this electric field $\boldsymbol{E}$ is parallel to the macroscopic current density J. This makes power dissipation[36,49]

$$\boldsymbol{P} = \boldsymbol{J} \cdot \boldsymbol{E}. \tag{3.2.1-3}$$

Therefore, vortex motion in a viscous medium dissipates energy, unless **v** (the velocity of a vortex) = 0. Consequently, vortices (flux lines) must be pinned in the material to obtain a loss-free current.

For most practically applications of HTS wire and tape, one must overcome the obstacle of dissipative current conduction, which is particularly pronounced at higher temperatures (above 77 K). Fortunately, microscopic inhomogeneities ("defects") of various configurations help to immobilize vortices. The defects can become "pinning centers" which are energetically very favorable sites for vortices. In other words, the defects act like potential wells that tend to immobilize vortex lines, so long as the Lorentz force ($\boldsymbol{F}_L$) is less than pinning force ($\boldsymbol{F}_{pin}$). Thus the defects provide vortex pinning, which is essential for the loss-free critical current density. The discovery of columnar defects provided a particularly effective type of potential well, since their linear geometry and transverse size closely match the properties of a vortex.

Recently, T. Hwa et al. suggested that splayed columnar defects should create even more strong pinning effects than those of simple columnar defects.[38] Therefore, L. Krusin-Elbaum et al. devised a mechanism to produce the splayed columnar defects using the fission process, in which heavy constituent nuclei inside materials were induced to fission by high energy proton (0.8 GeV) irradiation.[39,40] They found remarkable increases in the critical current density J_c and decreases in the decay rate of magnetic relaxation, due to strong vortex pinning. This new procedure creates the splayed columnar tracks in HTS materials using deeply penetrating (with a range of 0.6 meters) 0.8 GeV protons. The next section (3.2.2.1) will treat briefly the mechanism of defect formation.

In the present work, the effects of the splayed columnar tracks have been investigated in several HTS materials, including bulk polycrystalline $(TlPb)(SrBa)_2Ca_2Cu_3O_{9+\delta}$ materials, which are labeled as [(TlPb)(SrBa)-1223]; epitaxial thin films $(Tl_{0.8}Bi_{0.2})Ba_2Ca_2Cu_3O_{9+\delta}$ on $LaAlO_3$ or $Y_{0.2}Zr_{0.8}O_2$ (YSZ) substrates: [(TlBi)-1223 thin film]; thick films of $TlBa_2Ca_2Cu_3O_9$ on polycrystalline YSZ substrate: [Tl-1223 film]; bulk polycrystalline $Tl_2Ba_2CaCu_2O_{8+\delta}$: [Tl-2212]; thin films and bulk polycrystalline $HgBa_2Ca_2Cu_3O_8$: [Hg-1223 film, Hg-1223]; single crystal or tape (deposited on Ag with 3.4 μm thickness) $Bi_2Sr_2CaCu_2O_8$: [Bi-2212, Bi-2212 tape/Ag]; and so on. The magnetic studies of these materials were conducted in a superconducting quantum interference device (SQUID)-based magnetometer (Quantum Design MPMS-7). After pre-characterization, the samples were irradiated in air by the 0.8 GeV protons beam from Los Alamos Meson Production Facility (LAMPF) at the Weapons Neutron Research (WNR) facility. At first, loss-free current density J is derived from $M(H)$ data and analyzed using Bean critical state

model:[130]

$$J = 15 \times \Delta M/r, \qquad (3.2.1\text{-}4)$$

where $\Delta M = (|M_- - M_+|)$ is difference between M_- in decreasing field branch and M_+ in increasing field branch of the hysteresis loop; r is the radius of a cylindrical sample. Second, the measured magnetic relaxation data are analyzed using several flux creep theories such as classical Anderson-Kim,[115] collective flux creep,[36,131] or interpolation formula.[36,131] Third, the effective pinning energy $U(J,T)$ from $M(T,t)$ data is studied employing the Maley analysis of flux creep.[132] In addition, evidence of quantum creep, that is quantum tunneling of vortices,[36] is discussed.

3.2.2 Experimental and Theoretical Background

3.2.2.1 The Formation of Defects in HTS Materials by Particle Irradiation

One of the most interesting technological properties of type-II superconductors is the conduction of a current density with no dissipation. According to Maxwell's equation ($\nabla \times \boldsymbol{B} = (4\pi/c)J$), there is a relationship between current density J and the vortex density gradient ($\nabla \times B$), which is caused by a vortex pinning. From a thermodynamic point of view, the macroscopic current in materials can decay, due to thermally activated motion of the vortices; i.e. magnetic relaxation. Therefore, to overcome the shortcomings of giant flux creep and weak current density J_c in the mixed state of HTS materials, many scientists have studied vortex pinning in these materials.

The most direct method to make defects in materials is by irradiation with energetic

particles such as electrons, protons, neutrons, heavy ions, and so on. The relationships between bulk damage and incident energy of irradiation (using heavy ions: Kr, Xe, Pb, U, etc.) were studied by F. Studer and M. Toulemonde.[133] They showed the damage evolution and the corresponding damage morphology was dependent on the electronic stopping power (dE/dx) in the material. The evolution of the damage efficiency ($\epsilon = A/[dE/dx]$, here A is a damage cross section) versus the electronic stopping power (dE/dx) and the damage morphology in five specified categories are shown Figure 3-11. In range I (below the threshold stopping power T_e), the damage results only from the nuclear elastic collisions. At range II (between T_e and T_s), the damage is induced by inelastic collisions, giving a defect morphology of small spherical regions. At range III (between T_s and T_c), the damage efficiency increases very fast as the electronic stopping power increases, and the defects extend along the particle path and become discontinuous and cylindrical in shape. At range IV (between T_c and T_m), the discontinuous cylindrical defects gradually become continuous. Finally, at range V (above T_m), the defects become latent tracks with a homogenous cylindrical shape. Therefore, we can make point-like defects with light ions (electrons, protons) irradiation of MeV energy, or blob-like defects by neutron irradiation to the HTS materials.[134] Even better, we can produce nominally parallel columnar defects[37] in HTS materials by irradiation with GeV energy heavy ions, Xe, Sn, Pb, Cu, Au, etc., and the splayed columnar defects[39] by fission fragments produced by irradiation with GeV energy protons, which penetrate deeply in materials.

It is clear that to pin flux lines, strongly columnar defects are better than point-like defects. Linear vortex pinning sites match the linear shape of the vortex core. To obtain

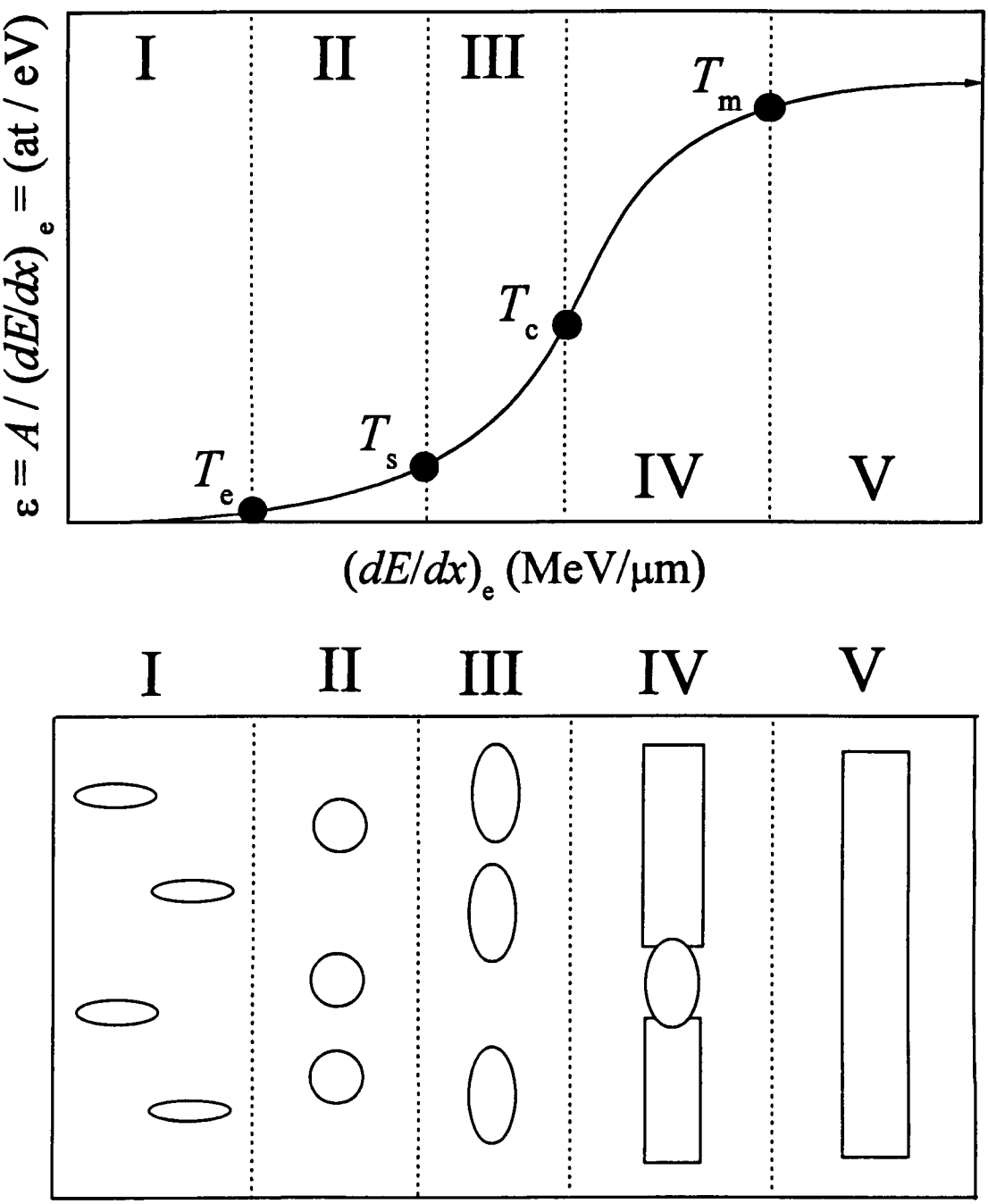


Figure 3-11. General behavior of the damage efficiency as observed in magnetic insulators. In the upper part of the figure, the evolution of the damage efficiency versus (dE/dx) is shown. F. Studer and M. Toulemonde, Nucl. Inst. & Meth. in Phys. Research B **65**, 560 (1992).

the maximum pinning force, the transverse size of the defects should be similar to the coherence length ξ_{ab} since the pinning force = - ∇U_{pin} ~ U_{pin}/ξ_{ab}, and ξ_{ab} is the shortest relevant length scale. In addition, to pin every vortex within a material, B_ϕ (number of pins per area) must larger than B (number of flux quanta ϕ_o per area). In 1991, L. Civale et al. showed that introducing columnar defects, made by heavy-ion irradiation, greatly increases the critical density J_c in single crystals of $YBa_2Cu_3O_7$.[37] In other words, the columnar defects produce strong vortex pinning and reduce the decay rate of magnetization. Usually, the columnar defects, made by irradiation with GeV energetic heavy ions, are very popular method to pin optimally vortices in HTS materials. This method, which has a limited penetration range (a few tens of μm ≈ 20 ~ 30 μm), seems to be most useful for increasing vortex pinning in relatively thin materials.

More recently, T. Hwa et al. suggested that splayed columnar defects should create more strong pinning effects than those of simple columnar defects.[38] Therefore, L. Krusin-Elbaum et al. devised a mechanism to produce splayed columnar defects using a fission process, in which heavy constituent nuclei inside materials were induced to fission by a high energy proton irradiation.[39] This new procedure creates an array of splayed columnar defects in HTS materials using deeply penetrating (with a range of about 0.6 meters) 0.8 GeV protons. Figure 3-12 shows briefly the mechanism of this procedure.[40] At first, an incident proton can be absorbed by a heavy nucleus, such as Bi, Hg, Tl, Pb, Au, and so on, in several HTS materials. The probability of this process is substantial, with a fission cross-section σ_f ≈ 100 ~ 200 mbarns. Therefore, the nucleus, highly excited by the energetic proton, fissions (splits) into two fragments. Each has energy of about 100 ~ 200 MeV and

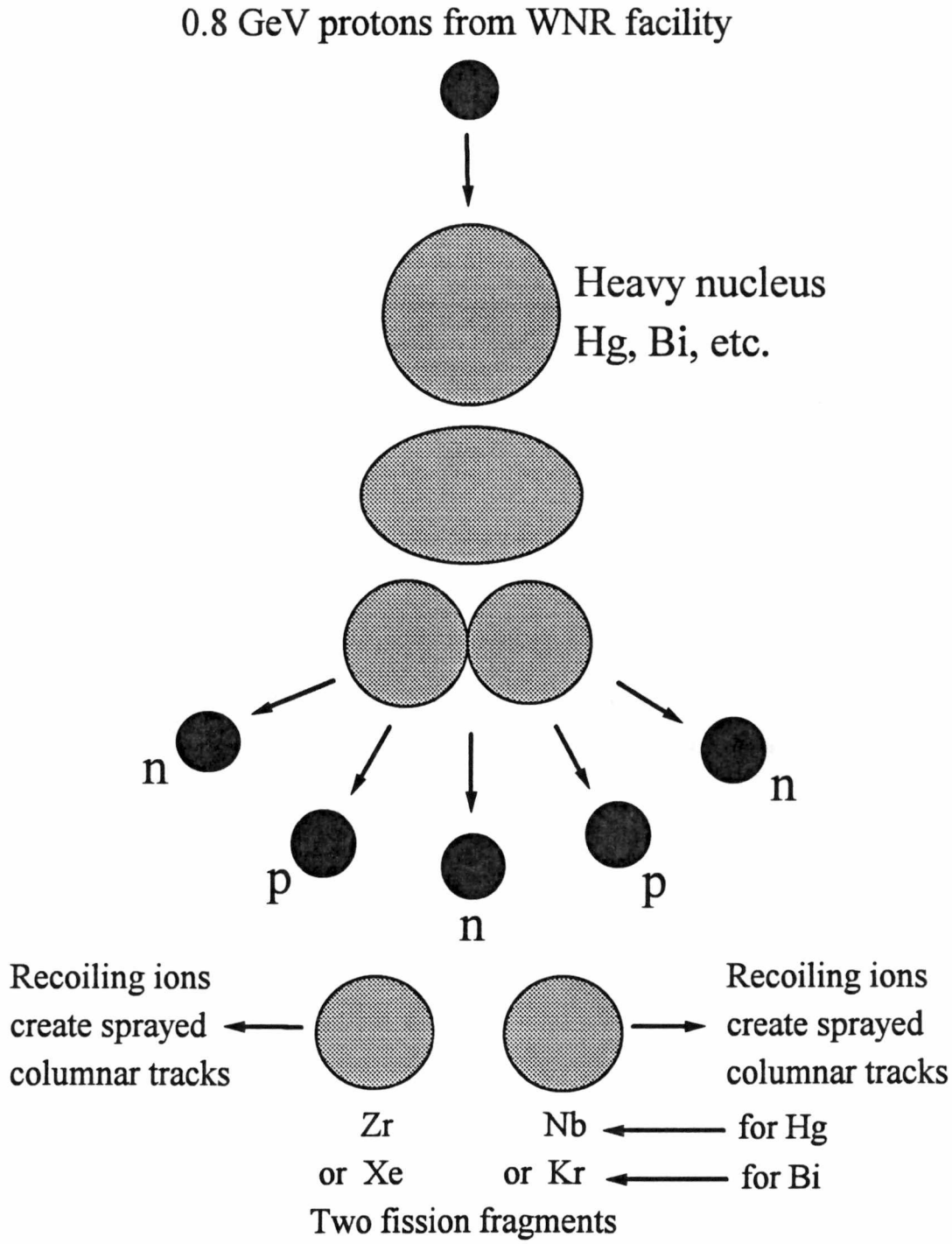


Figure 3-12. The formation of splayed columnar defects by the fission process. Krusin-Elbaum, et al., Nature (London) **389**, 243 (1997).

approximately half of the mass and charge of the parent nucleus. Typical fission fragments, such as $^{131}Xe_{54}$ and $^{84}Kr_{36}$ at about 100 MeV from fission of $^{209}Bi_{83}$, can make columnar tracks deeply within the thick or bulk HTS materials. Another example is $^{90}Zr_{40}$ and $^{93}Nb_{41}$ at about 100 MeV from fission of $^{200}Hg_{80}$. In addition to fission fragments, there remains several hundred MeV of energy in evaporated neutrons and protons from spallation. Thus, these fission fragments create randomly aligned columnar damage tracks. Figure 3-13 shows the splayed columnar tracks due to fission fragments.

3.2.2.2 Bean Critical State Model

There is an important relationship between the measured hysteretic magnetization, due to the vortex pinning, and bulk critical current density J_c. In 1962, the "critical state model" was introduced by C. P. Bean.[130] The idea of the critical state model was characterized by "critical current density J_c" in the mixed state of a type-II superconductor. The model provides a simple relation between the measured irreversible magnetization ΔM and the critical current density J_c of the sample: $J_c \propto \Delta M/r$, where r is the width or diameter of the superconducting sample. Therefore, it is possible to estimate the current density for arbitrarily small and irregularly shaped samples for which the typical transport measurements are sometimes very difficult.

In this model, C. P. Bean has set two key assumptions.[130] First, the lower critical field H_{c1} is usually ignored. Second, the critical current density J_c is independent of field: the possible current densities in the materials are $+J_c$, $-J_c$ or 0. Figure 3-14 shows schematically the profiles of B and J in the Bean critical state model, for a long cylindrical

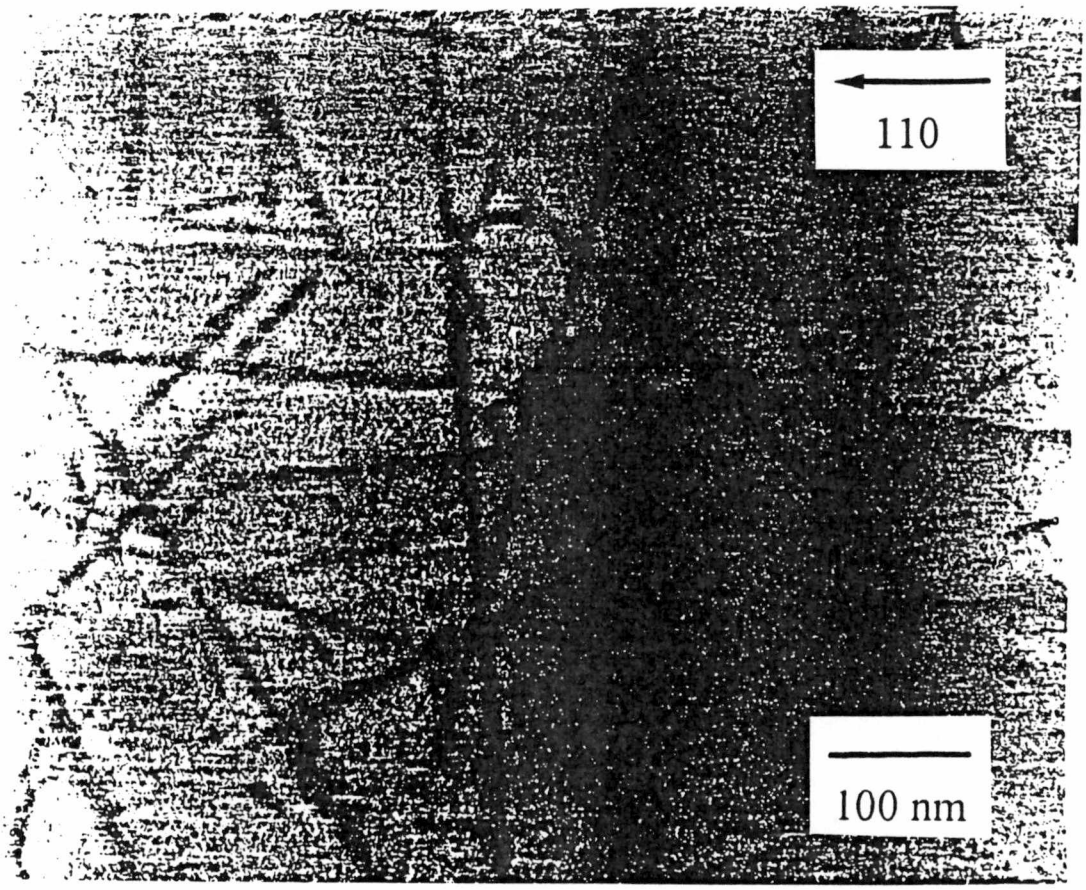


Figure 3-13. TEM of 0.8 GeV proton-induced splayed columnar defects in Bi-2212.

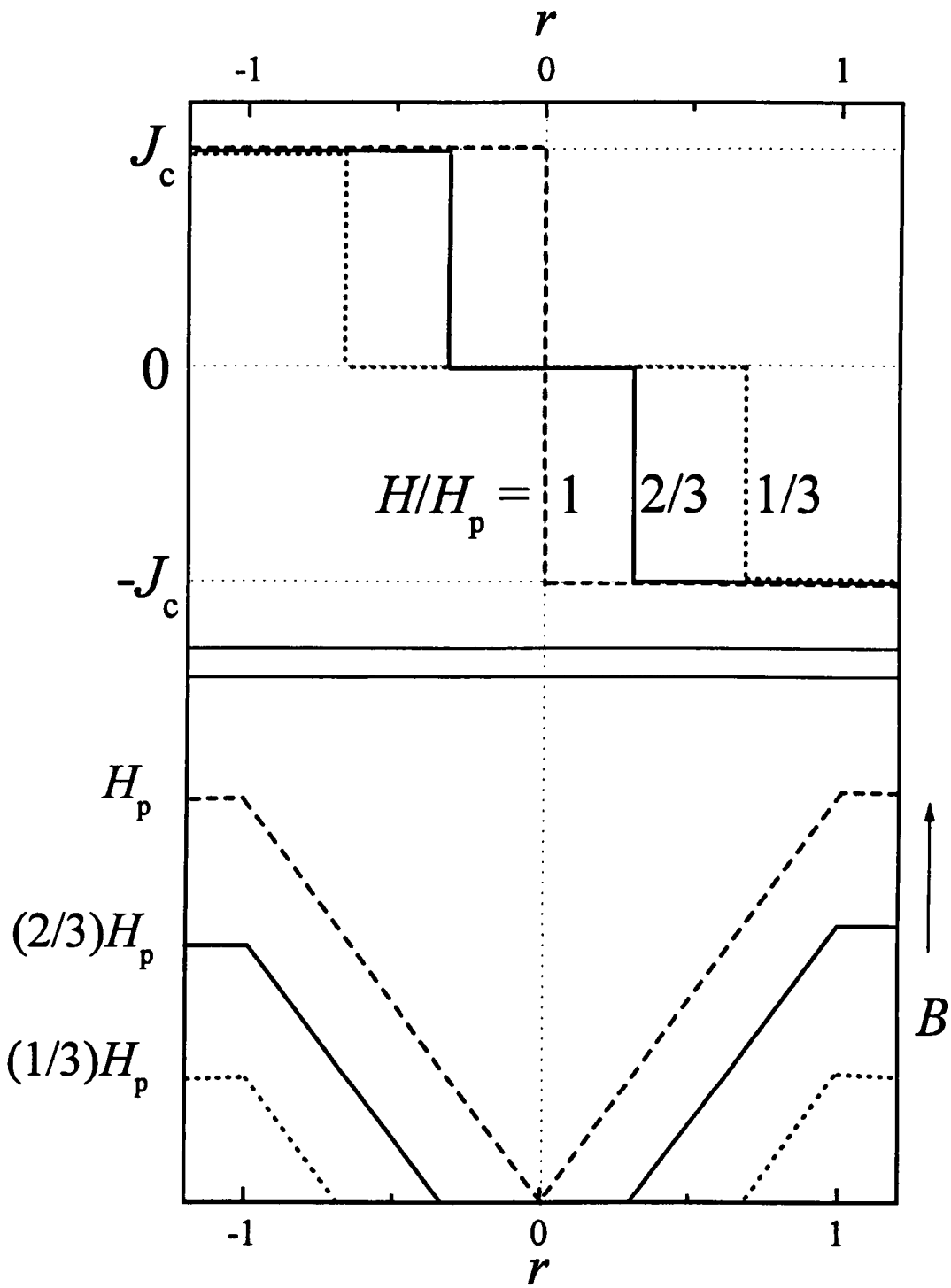


Figure 3-14. The Bean Critical State Model.

sample in a parallel magnetic field. In addition, Figure 3-15 shows the hysteresis loop, a $M(H)$ curve, and flux profiles for a slab of thickness r in an applied field parallel to its plane. The current density J_c always flows to some depth for a non-zero applied magnetic field. This depth increases as the applied magnetic field increases. The magnetic flux density $B(x)$ can be explained as a function of the distance from the center of the sample: $B(x)$ decreases linearly from the surface, where $x = 1$ represents to the surface and $x = 0$ stands for the center of the sample. When the magnetic flux fully penetrates into the center of the sample at the penetration field H_p, the whole sample is in the critical state and the critical current density $\pm J_c$ flows everywhere in the sample. We can calculate the penetration distance of the magnetic flux, x, into the slab using Maxwell's equation

$$\nabla \times H = (4\pi/c)J, \text{ so } H/x = (4\pi/c)J_c \text{ and } x = cH/(4\pi J_c). \quad (3.2.2.2\text{-}1)$$

To calculate the magnetization curves of the sample, we have that

$$B(x) = [\int(H\,dV)] / [\int(dV)] = (H\,x)/r = H\,(cH/4\pi J_c)/r = cH^2/(4\pi J_c r) \quad (3.2.2.2\text{-}2)$$

and

$$4\pi M = B(x) - H = [cH^2/(4\pi J_c r)] - H. \quad (3.2.2.2\text{-}3)$$

Using $H = 2\pi J_c r / c$ from $H/(r/2) = (4\pi/c)\,J_c$ at the center ($x = r/2$) of the sample, when the flux front reach the center, the maximum diamagnetic magnetization can be calculated by the equation (3.2.2.2-3):

$$4\pi M = B(r/2) - H = H/2 - H = -\pi J_c r/c, \quad (3.2.2.2\text{-}4)$$

where $B(r/2) = H \cdot (r/2)/r = H/2 = \pi J_c r/c$, so

$$M = -J_c r / (4c). \quad (3.2.2.2\text{-}5)$$

Finally, $J_c = -4cM / r$: this is a typical relation for the simplest case from the Bean critical

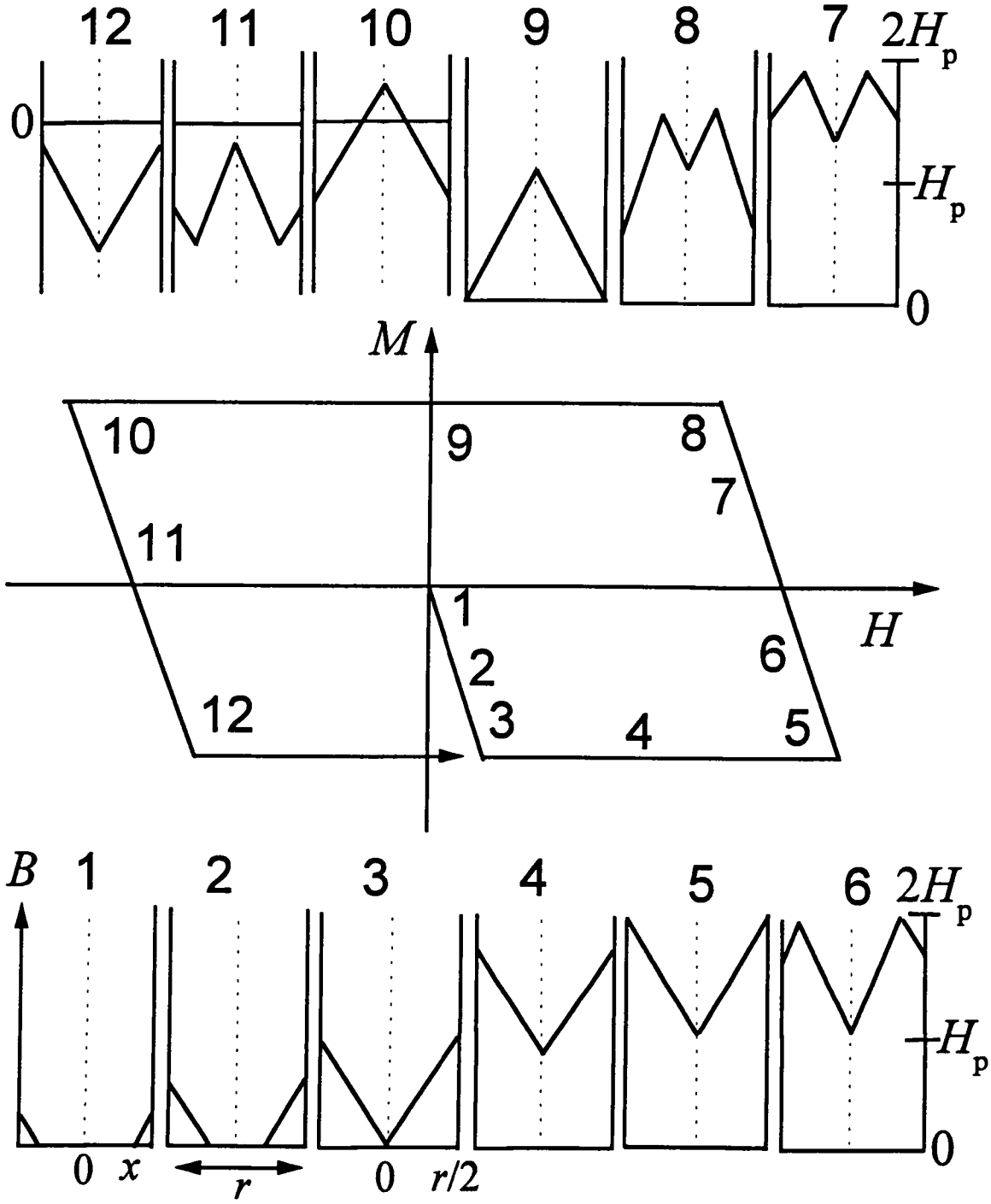


Figure 3-15. The hysteresis loop ($M(H)$ curve) and profiles for a slab of thickness r.

state model.[135] The more detailed calculation of the critical current density J_c for a spherical superconducting sample is treated in Appendix 4.

3.2.2.3 The Measurement of Magnetic Relaxation

A non-equilibrium state can arise from a variety of processes, such as changing of the magnetic field or temperature. This leads to a redistribution of vortices, whose configuration tends to relax toward an equilibrium arrangement in the superconductor. As the redistribution of vortices takes place, the magnetic moment will change with time because the instantaneous current density J decreases as the flux profile flattens. This is the basic concept of magnetic relaxation in superconductors. Thus we can understand that the magnetic relaxation is a consequence of the spontaneous motion of vortices out of their pinning sites due to thermal activation, quantum tunneling, or some other depinning processes.

From a thermal point of view, the macroscopic current in materials decays due to thermally activated motion of the vortices. Thus the magnetic relaxation in HTS materials can be one of the important factors in practical applications. Usually, the conventional low-T_c superconductors have a very small magnetic relaxation effect, which can be explained by the Anderson-Kim model,[115] where a magnetic moment decays logarithmically with time, which is referred as "magnetic flux creep." However, the high-T_c superconductors exhibit a large rate of magnetic relaxation, so called "giant flux creep."[116]

Magnetic relaxation in HTS materials is an interesting experimental study. It is not easy to obtain correctly the measurement of magnetic relaxation in HTS materials; for

example, experimental effects such as sample inhomogeneities and field inhomogeneities in SQUID magnetometers can lead to spurious results. According to the Bean critical state model,[130] the measured irreversible magnetization $M_{irr}(H)$, defined as (1/2) of the hysteresis ΔM obtained from the hysteresis loop, is proportional to the current density J. Thus the measured magnetization must be corrected for the equilibrium magnetization and background effects. Then we can obtain the relaxation rate and perform the evaluation of the pinning energy from the irreversible magnetization $M_{irr}(H)$. After establishing the full penetration for field in HTS materials, the magnetic relaxation can be measured by monitoring the magnetic moment versus time.

Figure 3-16 shows briefly the procedure for measurement of magnetic relaxation. The following is a step-by-step procedure for the measurement of magnetic relaxation.[135] (1) At first, we must make sure the quality of sample, magnetic field homogeneity, and magnetic field orientation according to the sample axes. (2) Second, measure the magnetic hysteresis full loop at fixed temperature T for which magnetic relaxation is going to be measured. (3) Third, determine the field H_m corresponding to the minimum magnetization from the hysteresis loop, which was started from $M = 0$ and $H = 0$, of the second step. Thus we can estimate the first field for full magnetic flux penetration (H^*) that is approximately $H^* \approx 1.5 \times H_m$. (4) Fourth, estimate the irreversibility field H_{irr} at which $\Delta M = |M_- - M_+| \approx 0$. (5) Fifth, determine the irreversible component $M_{irr}(H)$: $M_{irr} = | M_{meaure} - M_{average} |$, where $M_{average} = (M_+ + M_-)/2$. (6) Sixth, redo zero field cooling of the sample from above T_c to the target temperature T. (7) Seventh, apply a magnetic field H smaller than H_{irr} to allow for magnetic relaxation after making full flux penetration, which is obtained by

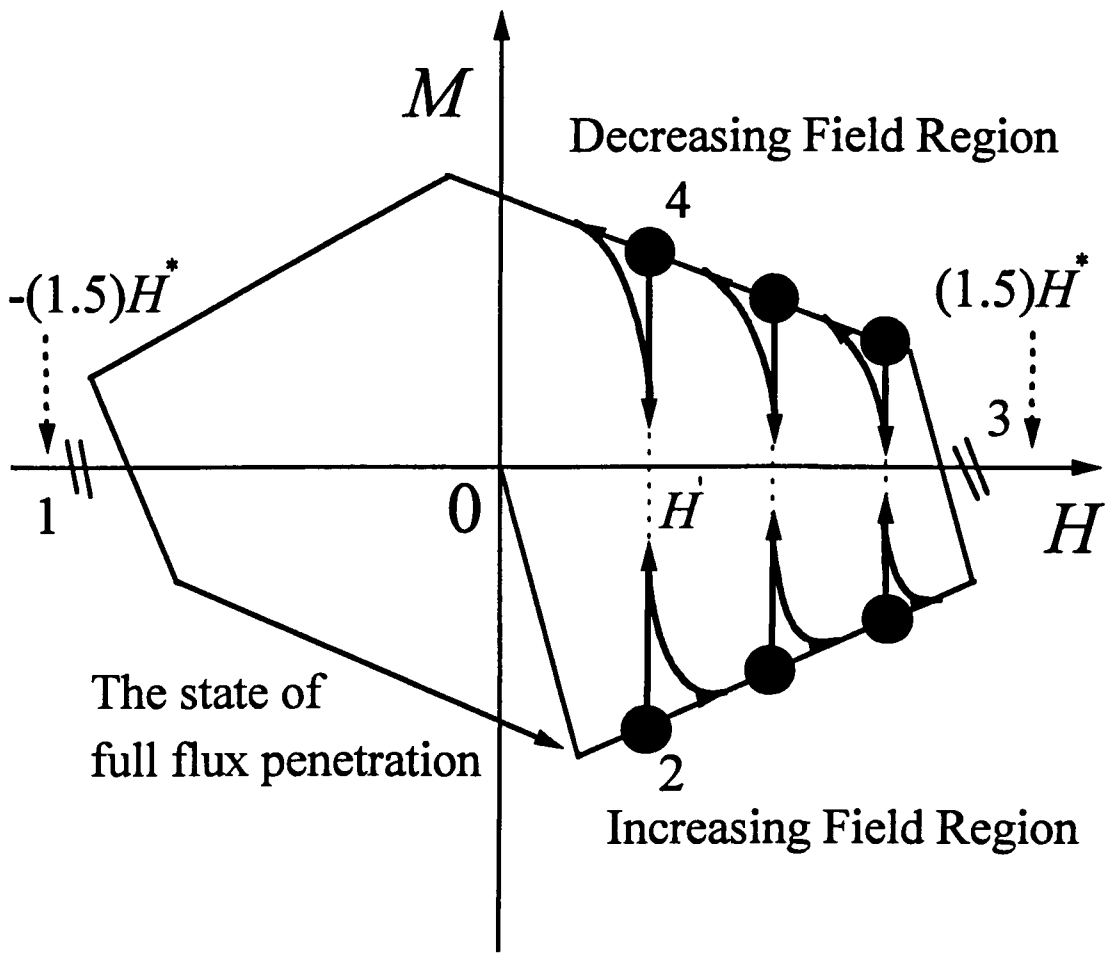


Figure 3-16. The procedure for measurement of magnetic relaxation: At starting point, (1) apply field $H = (1.5)H^*$. After full flux penetration into sample, (2) apply a target field H'. Keeping the field H' constant, measure the decay of magnetic moment in increasing field region. Before starting measurement in decreasing field region, (3) apply a larger field, e.g. $(1.5)H^*$. Finally, go to a target field in decreasing field region. (4) Measure the decay of magnetic moment just as (2).

starting a negative applied field ($-H$). (8) Eighth, measure the magnetization (M) as a function of time t. (9) Ninth, obtain the irreversible magnetization $M_{irr}(t) = M(t) - (M_{eq} + M_{bkg})$. (10) Tenth, go back to step (6) or (7) according to a different target temperature T or field H. In this way, one obtains a reliable set of data for $J(H,T,t) \propto M_{irr}(H,T,t)$. The data can then be analyzed for the creep rate $S(T)$, the effective pinning energy $U(J,T)$, etc., employing the Maley analysis[132] and other theoretical results, including corrective creep theory,[36,131] the interpolation formula,[36,131] and classical Anderson-Kim theory.[115]

3.2.2.4 From Classical Anderson-Kim to Collective Flux Creep Theory

At finite temperatures, flux lines can jump from one pinning site to another by thermal energy. This causes the macroscopic screening current in a HTS material to decay, under the combined action of thermally activated motion of the flux lines in association with the driving force of the current and flux density gradient. Usually, the flux creep, movement of vortices out of their pinning sites, is evident in two ways: (1) the slow changing of magnetic moment in a magnetic measurement and (2) the current-voltage dependence for the longitudinal resistive voltage (related to the average creep velocity of the vortex motion) in a resistive measurement. In the present study, creep of the magnetic moment will be treated.

The classical theory of thermally activated flux creep has been treated by Blatter et al.[36] recently. Let us assume that the magnetic flux density $B \approx H$ (the applied field) and consider a simple slab geometry with the field B // z-axis, v (the velocity of flux lines or flux-line bundles) // x-axis, and the current density J // y-axis. According to Maxwell's equation,

$\nabla \times \boldsymbol{B} = (4\pi/c)\boldsymbol{J}$, the current density J is related to the flux density gradient, as noted above:

$$\partial B_z/\partial x = -(4\pi/c)J_y. \qquad (3.2.2.4\text{-}1)$$

The flux lines should move with the velocity v_x by the Lorentz force, $\boldsymbol{F}_x = (1/c)(\boldsymbol{J}_y \times \boldsymbol{B}_z)$. Using Maxwell's equation, $\nabla \times \boldsymbol{E} = -(1/c)\partial \boldsymbol{B}/\partial t$,

$$\partial E/\partial x = -(1/c)\partial B/\partial t, \qquad (3.2.2.4\text{-}2)$$

and the relation between the electric field and the flux motion, $\boldsymbol{E} = (1/c)\boldsymbol{B} \times \mathbf{v}$,

$$E_y = (1/c)B_z v_x. \qquad (3.2.2.4\text{-}3)$$

Thus we can get the equation of continuity for the flux lines from equations (3.2.4-2 and -3),

$$\partial B/\partial t = -(\partial/\partial x)(vB). \qquad (3.2.2.4\text{-}4)$$

In addition, using the equation after taking the derivative with respect to time (t) of equation (3.2.2.4-1), we obtain the corresponding dynamic equation for the current density J:

$$\partial J/\partial t = (c/4\pi)(\partial^2/\partial x^2)(vB). \qquad (3.2.2.4\text{-}5)$$

The velocity of flux lines due to thermal activation over the pinning barrier is given by

$$v = v_o \exp[-U(J)/kT], \qquad (3.2.2.4\text{-}6)$$

where $U(J)$ is the pinning energy barrier, like a potential energy barrier U. Finally, after integration, we obtain the decay or dynamic equation for the current density J,

$$\partial J/\partial t \approx -(J_c/\tau_o)\exp[-U(J)/kT], \qquad (3.2.2.4\text{-}7)$$

where $U(J)$ is the activation energy. If we use the mathematical trick, $dJ/dt = (dU/dt)(dJ/dU)$, we can get the dynamic equation for the activation energy $U(J)$,

$$dU/dt = -(J_c/\tau_o)(dU/dJ)\exp[-U(J)/kT]. \qquad (3.2.2.4\text{-}8)$$

This equation was solved with logarithmic accuracy by Geshkenbein and Larkin,[136] providing

$$U(J) = kT \ln(1+t/t_o), \qquad (3.2.2.4\text{-}9)$$

where $t_o = \tau_o T / (J_c |dU/dJ|)$, and additive factor (1+), which is inserted to obtain a valid expression at $t = 0$, can normally be dropped because $1 << (t/t_o)$.

The hopping of flux lines or flux-line bundles out of their pinning-potential wells due to thermal activation was introduced first by P. W. Anderson and Y. B. Kim in 1962 and 1964.[115] According to the conventional Arrhenius relation, the vortex hopping time t is given by

$$t = t_o \exp(U/kT), \qquad (3.2.2.4\text{-}10)$$

where U is the potential energy barrier. Because the hopping is activated by the driving Lorentz force, $\boldsymbol{F} = (1/c)\boldsymbol{J} \times \boldsymbol{B}$, there is a relation between U and J, such as U decreases as J increases. In Anderson-Kim flux creep theory, they assume a linear $U(J)$, that is the linear J-dependence of the activation energy U:

$$U = U_o (1 - J/J_{co}), \qquad (3.2.2.4\text{-}11)$$

where $J_{co} = J_c$ is critical current density at which the activation energy is zero. Using equations (3.2.2.4-9 and -11), we can obtain the famous logarithmic time decay of the current density:

$$J = J_{co} [1- (kT/U_o) \ln(1 + t/t_o)]. \qquad (3.2.2.4\text{-}12)$$

According to Bean model,[130] the magnetization $\boldsymbol{M} \propto J$. Thus the magnetization should decay logarithmically with time. From equation (3.2.2.3-12), we can determine the normalized creep rate S:

$$S \equiv (1/M_{irr}) [dM_{irr} / d\ln(t)] = d\ln(J) / d\ln(t), \qquad (3.2.2.4\text{-}13)$$

(where these, $(1/M_{irr}) [dM_{irr} / d\ln(t)] = d\ln(M_{irr}) / d\ln(t)$, are the same only if $dM_{irr} \approx 0$.)

$$S \simeq - kT / [U_o - kT \ln(1 + t/t_o)]. \qquad (3.2.2.4\text{-}14)$$

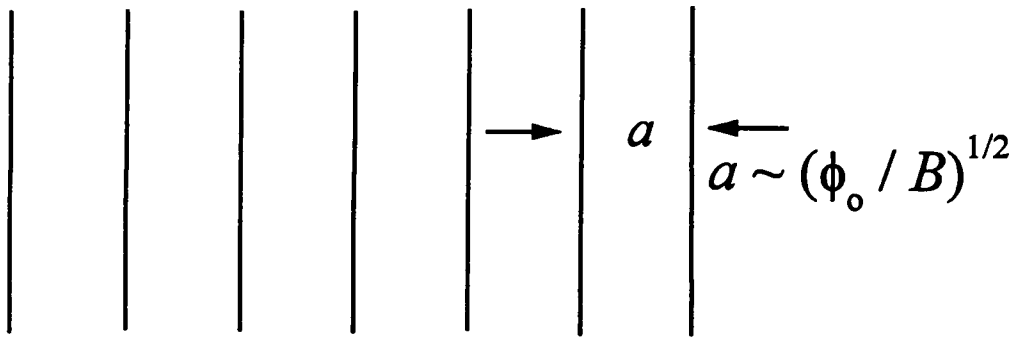
A low temperatures (usually low-T_c superconductors) in which $U_o >> kT \ln(1 + t/t_o)$,

$$S \simeq -kT / U_o. \qquad (3.2.2.4\text{-}15)$$

This logarithmic relaxation relation based on Anderson-Kim theory explained well the flux creep for conventional low temperature superconductors. More recently, however, Thompson et al. showed significant deviations from logarithmic-time behavior for an $YBa_2Cu_3O_7$ crystal.[137] In addition, this basic Anderson-Kim theory can not explain the typical plateau phenomenon[138-140] of the normalized relaxation rate, in which S is independent of temperature in the intermediate temperature range for many HTS materials. Therefore, many scientists have looked for modifications of Anderson-Kim theory or have searched for some other formalism to explain adequately the above shortcomings.

Before treating the formalism beyond of the basic Anderson-Kim theory, let us briefly review the concept of collective pinning by Larkin and Ovchinnikov.[141] When there are no pinning sites in a material, the flux line lattice (FLL) should be the ideal periodic arrangement of Abrikosov.[62] If there is a random array of pinning sites, the individual flux lines, which have the properties of mutually repulsive elastic strings, would like to take lower their energy by passing through the favorable pinning sites. That is collective pinning-one vortex is pinned by many randomly located "point" defects. Thus the FLL becomes a deformed and distorted array. Figure 3-17 showed a schematic diagram for collective pinning.[49] Usually, the distortion of the FLL is described in terms of a correlation volume, V_c, which is characterized by both a correlation length L_c along the field direction and a transverse dimension R_c. In addition, the distortions of the FLL in a correlation volume,

(a) With no pinning, the FLL is periodic.



(b) With random attractive pinning sites, the local direction of the FLL is modulated slightly.

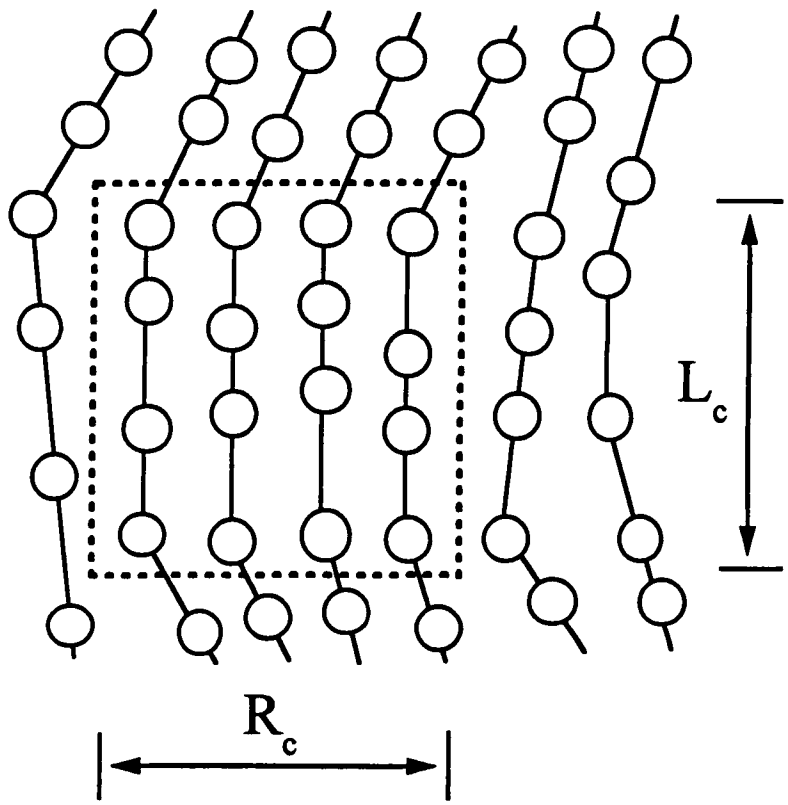


Figure 3-17. The schematic diagram about the collective pinning. (from M.Tinkham, "Introduction to Superconductivity")

which generally contains several or many collective pinning sites, can be described by using the elastic moduli of the FLL, such as the shear modulus (C_{66}) and tilt modulus (C_{44}).

Extending the idea of a linear $U(J)$ relation in Anderson-Kim theory, the concept of a nonlinear $U(J)$ relation was first introduced by Beasley et al. in 1969.[142] Within the framework of collective pinning theory, Feigel'man et al. introduced an inverse-power-law form of $U(J)$, assuming weak random pinning and flux lines that act as an elastic medium:[131]

$$U = U_o [(J_{co}/J)^{\mu} - 1]. \qquad (3.2.2.4\text{-}16)$$

According to this collective creep theory, the correlation volume V_c of a thermally activated flux bundles depends on the current density J. In addition, if the current density J goes to zero, then the volume V_c becomes infinitely large and the barrier U diverges. Using equations (3.2.2.4-9 and -16), we can obtain the "interpolation formula,"[36,131]

$$J(T, t) = J_{co} / [1 + (\mu kT/U_o) \ln(1 + t/t_o)]^{1/\mu}, \qquad (3.2.2.4\text{-}17)$$

where the dimensionless μ is called a glassy exponent. This interpolation formula is valid both for $J \sim J_c$, which may be found at low temperatures (close to Anderson-Kim theory), as well as for $J << J_c$ which can result from giant flux creep in unconventional HTS materials. Specially, the numerical values of glassy exponent μ, obtained by the elastic theory, play a role as an indicator for the type of pinning-depinning process;[36,135] in three dimensions with random point-like defects, (1) $\mu = 1/7$ represents the motion of individual flux lines in low-field and low-temperature region; (2) $\mu = 3/2$ means the collective creep of small bundles in higher field and higher temperature; (3) $\mu = 1$ stands for the collective creep of intermediate size bundles; and (4) $\mu = 7/9$ corresponds to collective creep of large bundles. Finally, from equation (3.2.2.4-17), we obtain the normalized creep rate,

$$S = d\ln(J) / d\ln(t) = - kT / [U_o + \mu kT \ln(1 + t/t_o)]. \quad (3.2.2.4\text{-}18)$$

At higher temperature where $U_o << \mu kT \ln(1 + t/t_o)$, then

$$S \approx 1/ [\mu \ln(1 + t/t_o)]. \quad (3.2.2.4\text{-}19)$$

This result provides an explanation for the temperature T-independent plateau phenomena[138-140] of S for HTS materials, so long as μ and t_o are independent of T.

In 1990, Zeldov et al. introduced another nonlinear $U(J)$ barrier, a logarithmic dependence on J:[143]

$$U = U_o \ln(J_{co} / J). \quad (3.2.2.4\text{-}20)$$

From combining equation (3.2.2.4-20) and equation (3.2.2.4-9), one can derive

$$J = J_{co} \exp[- (kT/U_o) \ln(t/t_o)]. \quad (3.2.2.4\text{-}21)$$

Thus the normalization creep rate S can be obtained by

$$S = d\ln(J) / d\ln(t) = - kT/U_o. \quad (3.2.2.4\text{-}22)$$

However, the plateau phenomena[138-140] of S for HTS materials cannot be explained using the theory based logarithmic $U(J)$ relation because of the direct relationship of $S \propto T$.

With many different $U(J)$ dependencies possible, Maley et al. developed a model independent method for determining the dependence experimentally. By inverting equation (3.2.2.4-7), they obtained the following,[132] assuming only thermally activated current decay:

$$U = - kT [\ln(dJ/dt) + C], \quad (3.2.2.4\text{-}23)$$

where $C = \ln(J_c/\tau)$ is determined experimentally by requiring that U becomes a smooth function of J. Alternatively, this Maley analysis arises from the flux conserving equation,

$$dM/dt = (B\omega a/2\pi r) \exp(-U/T), \quad (3.2.2.4\text{-}24)$$

where B is the magnetic induction, ω is the attempt frequency for vortex hopping, a is the

hopping distance, r is the radius of the sample, and U is the energy measured in temperature (K) units. This provides a net pinning barrier $U = -T[\ln(dM/dt) - C]$, where $M \propto J_c$ from Bean critical state model and $C = \ln(B\omega a/2\pi r)$.

3.2.3 Experimental Results and Analysis

The most direct method to make defects in materials is by irradiation with particles such as protons, neutrons, heavy ions, and so on. Thus, we can make the point-like defects by irradiation with light ion of MeV energy or blob-like defects by energetic neutron irradiation of the HTS materials,[134] which also have naturally occurring defects. In addition, we can produce columnar defects[37] in HTS materials by irradiation with GeV energy heavy ions such as Xe, Sn, Pb, Cu, Au, etc. Alternatively, splayed columnar defects[39] can be formed by GeV energy protons, which penetrate deeply into materials. In 1991, L. Civale et al. showed that introducing columnar defects, formed by heavy-ion irradiation, greatly increases the critical density J_c in single crystals of $YBa_2Cu_3O_7$.[37] Columnar defects, made by irradiation with GeV energetic heavy ions, have been a very popular method for strong pinning of vortices in HTS materials. This method, however, has the disadvantage of a limited penetration range (a few tens of μm ≈ 20 ~ 30 μm). More recently, T. Hwa et al. suggested that splayed columnar defects should create stronger pinning effects than those of simple parallel columnar defects.[38] Therefore, L. Krusin-Elbaum et al. devised a mechanism to produce splayed columnar defects using a fission process, in which heavy constituent nuclei inside materials are induced to fission by high energy (0.8 GeV) proton

irradiation.[39] They found remarkable increases in the critical current density J_c and decreases in the decay rate of magnetic relaxation, due to strong vortex pinning. This new procedure creates the splayed columnar defects in HTS materials using deeply penetrating 0.8 GeV protons (with a range of about 0.6 meters). In the present work, the effects of the splayed columnar tracks, which are actually made by fission fragments, are studied in several HTS materials, including bulk polycrystalline high-T_c superconductors, epitaxial thin films, tapes, single crystals, etc. Sometimes, to increase the areal density of splayed columnar defects, an "amplifier foil" of heavy metal could be set in front of a thin film. For example, in the Hg-1223 films, a 40 μm foil of Pb was used to create additional splayed defects due to Pb fission fragments that escape from the last 2 - 3 μm of foil.

Magnetization data ($M(H,T,t)$) on the HTS materials were obtained using a SQUID-based magnetometer. Precharacterized samples were irradiated in air by the 0.8 GeV protons beam (at a beam density of less than 1 $\mu A/cm^2$) at the Los Alamos Meson Production Facility (LAMPF) at the Weapons Neutron Research (WNR) branch. We can estimate the area density of defects,[144] which is conveniently expressed in units of flux density, as

$$B_\phi = \Phi_p \times \sigma_f \times (N/V) \times \ell \times \phi_o, \qquad (3.2.3\text{-}1)$$

where Φ_p is proton fluence, $\sigma_f \sim \exp(Z^2/A)$ is the fission cross-section, N/V is the number density of fissionable nuclei, ℓ is the track length (~ 7 μm in bulk material), and ϕ_o is the flux quantum. Figures 3-18-a and -b illustrate the effects on the materials, showing M versus H at temperature T = 30 K for polycrystalline $Tl_2Ba_2CaCu_2O_{8+\delta}$ [Tl-2212] and, at T = 60 K, corresponding results for bulk polycrystalline $HgBa_2Ca_2Cu_3O_9$ [Hg-1223]. In Figures

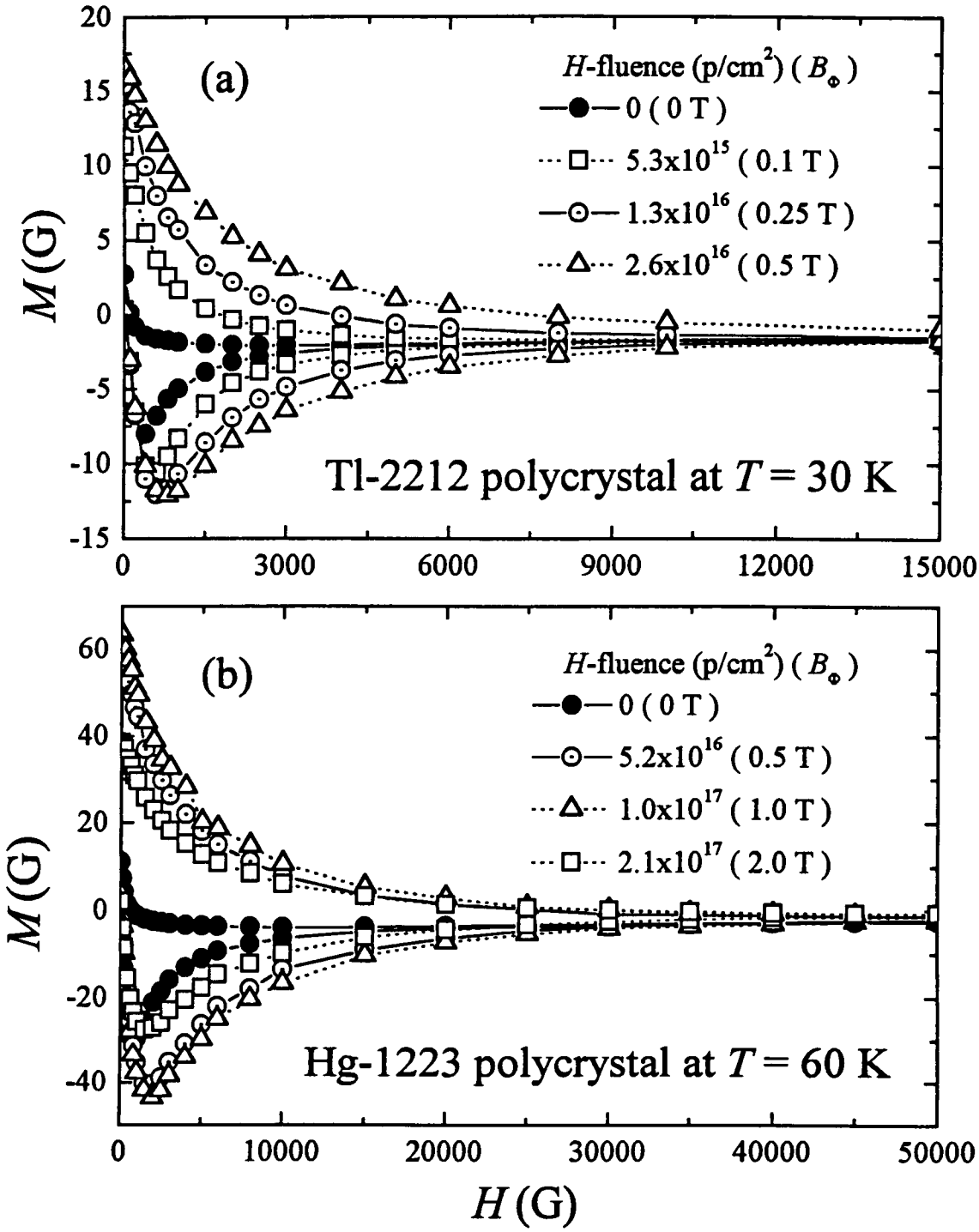


Figure 3-18. Magnetization M versus field H for both virgin and irradiated samples.

3-18-a and -b, results are shown both for the sample as grown (virgin) and after irradiation with progressive fluencies of 0.8 GeV protons. It is evidence that the magnetic hysteresis ΔM is greatly increased by the splayed columnar defects. Note too a change in the overall shape of the hysteresis curve for the bulk polycrystalline $HgBa_2Ca_2Cu_3O_9$: [Hg-1223]. The virgin material has an asymmetric shape of $M(H)$ curve with features indicating a surface barrier-dominated system.[123-126] The curve gradually changes to a symmetric shape as the irradiation fluence and defect density increases. The surface barrier effects in these Hg-based cuprates seem to disappear; at minimum, it become unmasked by the irreversibility of bulk currents with increased bulk pinning by the sprayed columnar defects. In addition, from the irreversible component of magnetization $M(H)$, the loss-free current density J is obtained and analyzed using Bean critical state model (from previous section 3.2.2.2):[130]

$$J = 15\Delta M/r \approx 30(M - M_{eq})/r, \qquad (3.2.3\text{-}2)$$

where ΔM is the difference ($|M_- - M_+|$) between M_- in decreasing field region and M_+ in increasing field region, and r is an appropriate transverse dimension, and the last equality is useful at the highest temperatures where the equilibrium magnetization M_{eq} becomes important. Figure 3-19-a and -b present J versus H at the temperature $T = 77$ K for bulk polycrystalline $(TlPb)(SrBa)_2Ca_2Cu_3O_{9+\delta}$: [(TlPb)(SrBa)-1223], and J versus T in field $H =$ 5 and 10 kG for a thin film of $Tl_{0.8}Bi_{0.2}Ba_2Ca_2Cu_3O_9$: [TlBi-1223 film]. In both figures, the results are shown for the samples both virgin (as grown) and after irradiation by 0.8 GeV protons. It is evidence that the current density J is greatly increased by the splayed columnar defects formed by fission fragments. There is, however, an optimal proton fluence Φ_p for enhancing the current density in these HTS materials. The current density J first

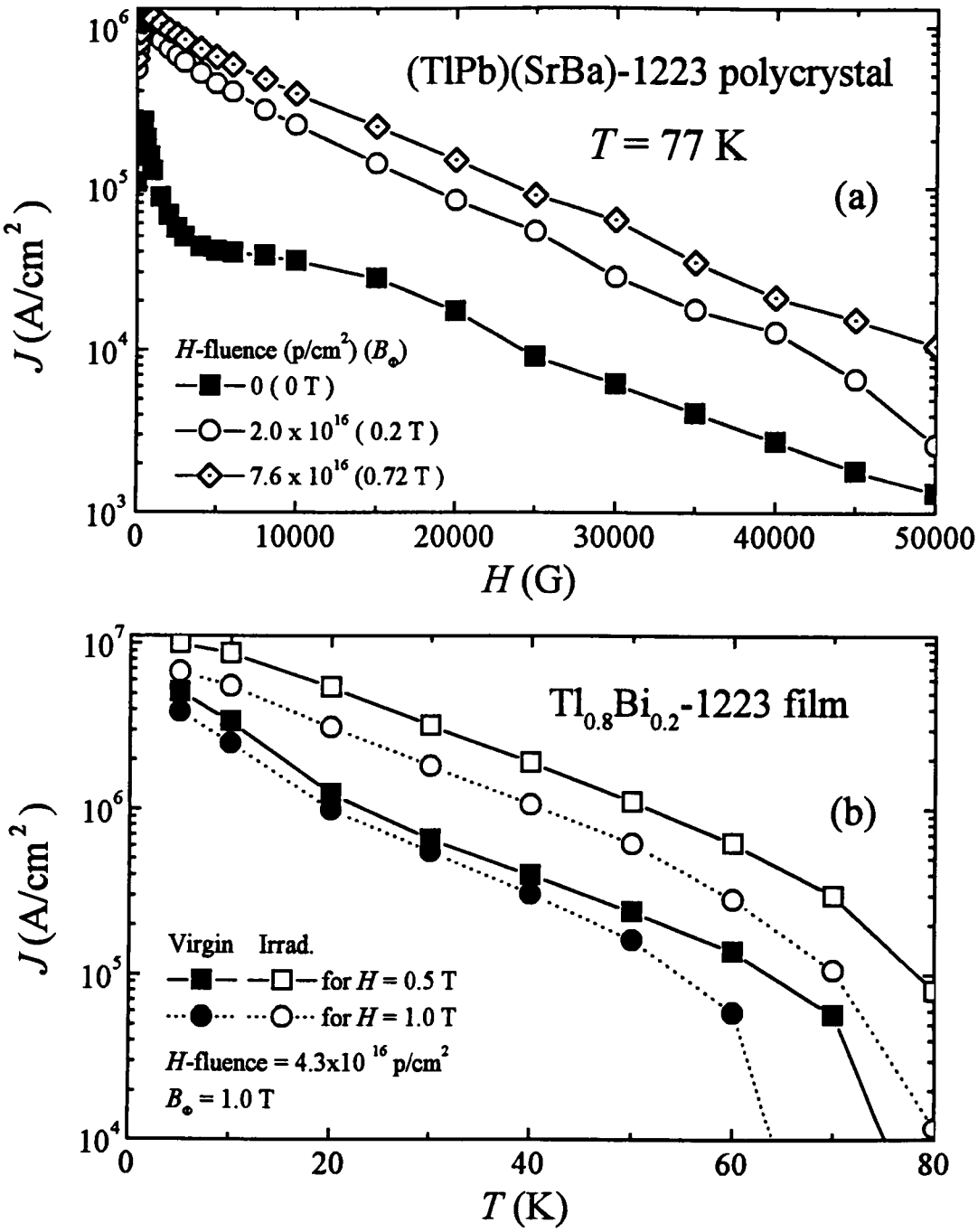


Figure 3-19. The persistent current density $J = (15 \times \Delta M) / r$ versus (a) the magnetic field H and (b) the temperature T, for both virgin and irradiated samples.

increases with increasing proton fluence Φ_p, then decreases at much higher Φ_p. This is illustrated in Figure 3-20, plots of the current density J versus the proton fluence Φ_p for polycrystalline HTS Hg-1223 materials in H = 1 T. While the current density J can be increased significantly by introducing optimal densities of defects such as point-like defects, parallel simple columns, and splayed columnar tracks within the HTS materials, the superconducting transition temperature T_c is suppressed somewhat by the added defects. To demonstrate this, Figure 3-21 shows the variation of T_c for several HTS materials as a function of the proton fluence Φ_p. The slopes $dT_c/d\Phi_p$ for the different HTS materials differ significantly. One expects that the depression rate for T_c should depend on the fission rate per volume:

$$dT_c/d\Phi_p \sim \text{fission rate / volume} \sim \sigma_f \times (N/V)_f . \qquad (3.2.3\text{-}3)$$

Qualitatively, this empirical relation appears to describe the process, as the rate is higher for materials containing two fissionable nuclei per unit all (Bi-2212 and Tl-2212) and lower for nuclei with smaller σ_f, e.g. Hg-1223.

In general, the $M(H)$ curves provide the persistent current density from Bean critical state model. Thus we can define the irreversibility field H_{irr} at which the hysteresis in the $M(H)$ curves tends toward zero ($\Delta M \sim 0$) in the $M(H)$ curves, or correspondingly, when the current density drops precipitously below some criterion value; this is conveniently done on plots of log(J) versus H. The irreversibility line $H_{irr}(T)$ determined using the criterion ($J_{criterion} = 10^3$ A/cm^2), is shown in Figure 3-22 for polycrystalline (TlPb)(SrBa)$_2$Ca$_2$Cu$_3$O$_{9+\delta}$: [(TlPb)(SrBa)-1223]. According to the relation for 3D line vortices,

$$H_{irr}(T) = H_{irr}(0)\,(1\text{-}T/T_c)^n, \qquad (3.2.3\text{-}4)$$

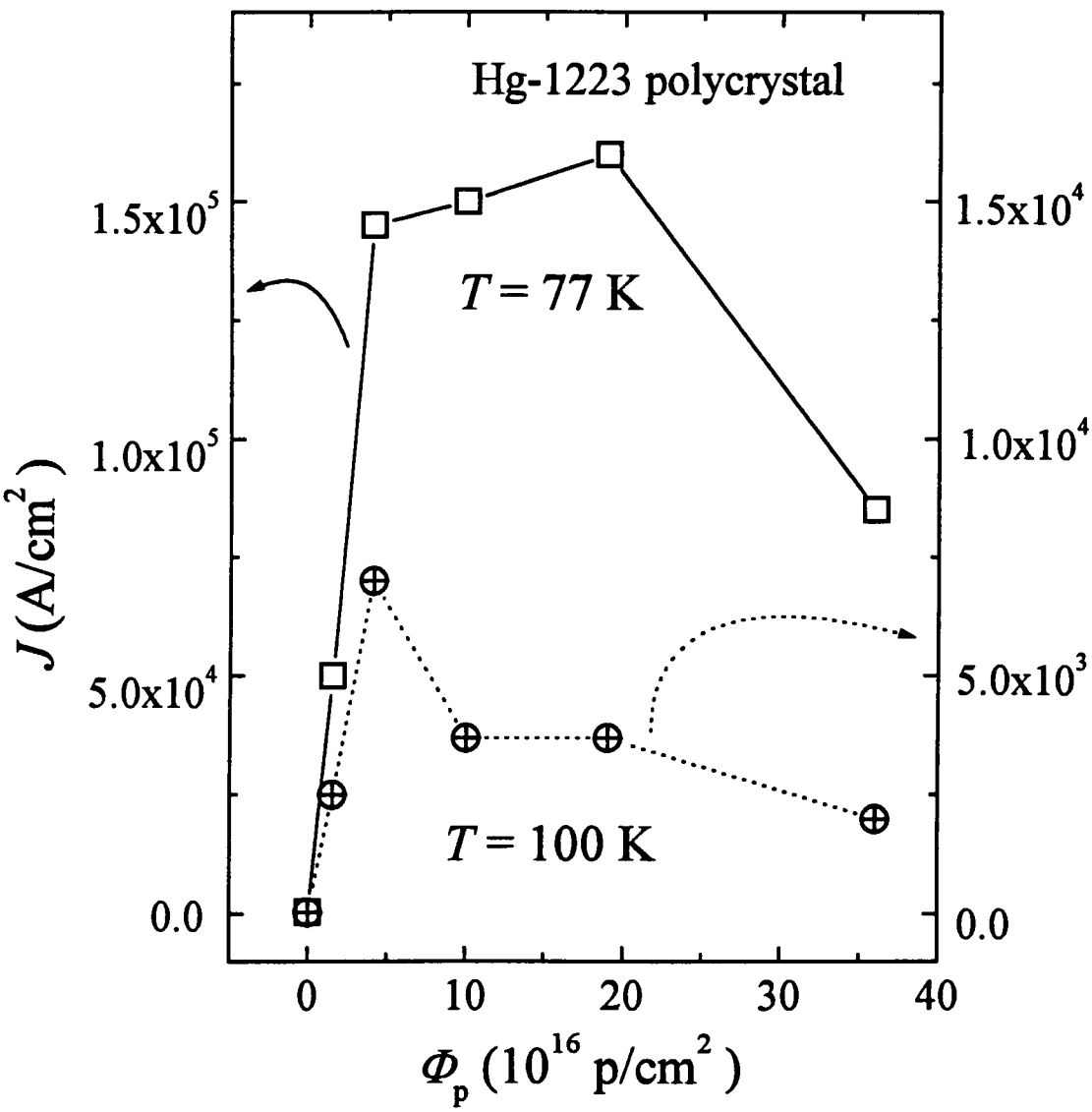


Figure 3-20. The current density J versus proton fluence Φ_p. Results are for Hg-1223 polycrystalline HTS with $H = 1$ T.

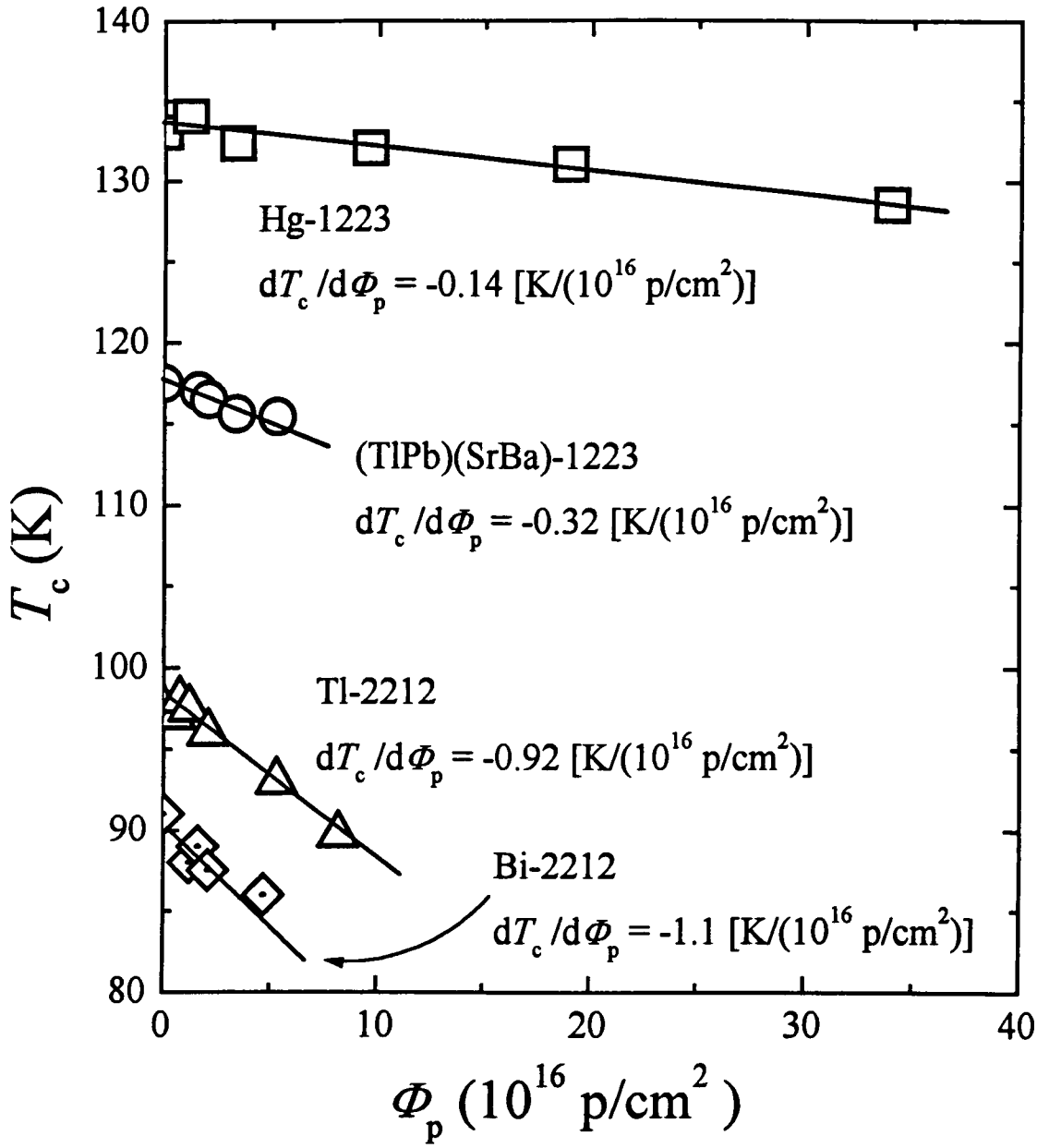


Figure 3-21. The dependence of T_c on the fluence of 0.8 GeV protons, for several cuprate HTS materials.

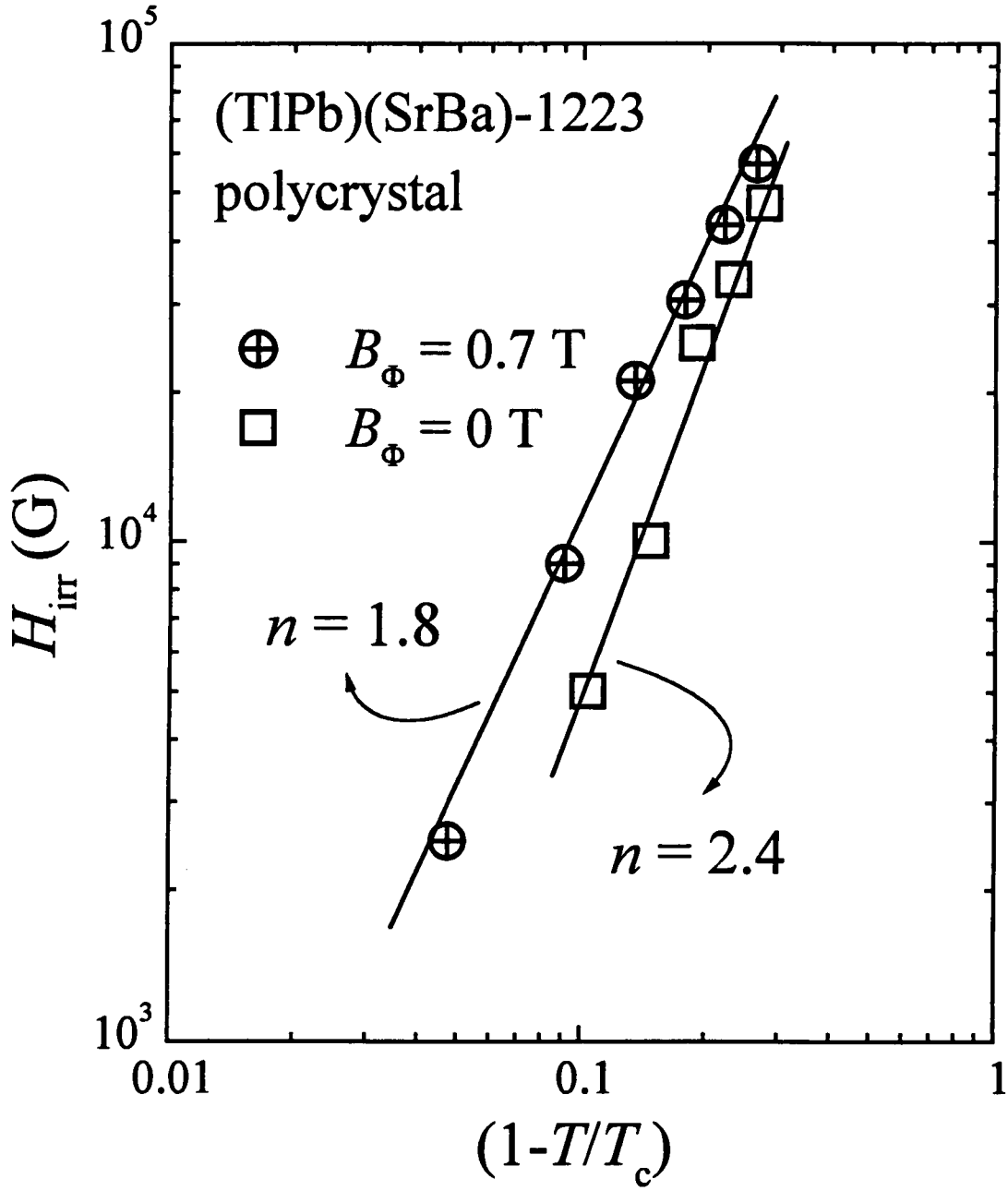


Figure 3-22. The irreversibility field H_{irr} versus $(1-T/T_c)$, where H_{irr} is defined by $J_{criterion} = 10^3$ A/cm^2.

the irreversibility line $H_{irr}(T)$ should be linear when plotted on double logarithmic axes, and the exponent n can be obtained from the linear slope. While the virgin sample (before irradiation) has $n = 2.4$, the irradiated sample has a reduced slope with $n = 1.8$. Thus the HTS materials with splayed columnar tracks have higher irreversibility fields. Also, H_{irr} fall off less rapidly with increasing temperature, compared with the virgin HTS materials, as shown in Figure 3-22.

Next we consider the region below the irreversibility field, where M_{irr} is finite and non-zero persistent currents flow. Then from time dependent studies, one can obtain the decay rate S and an evaluation of the pinning energy. A plot of the logarithmic decay rate $S = d\ln(M_{irr})/d\ln(t) = d\ln(J)/d\ln(t)$ as a function of temperature is shown in Figure 3-23. The materials are superconducting tapes of $Bi_2Sr_2CaCu_2O_8$/Ag (deposited on Ag with 3.4 μm thickness): [Bi-2212 tape/Ag], both virgin (as grown) and after irradiation by 0.8 GeV protons. The decay rate S for the persistent currents is reduced, especially at high temperature, by the splayed columnar defects, which were formed by Bi-fission fragments. The enhanced vortex pinning gives increased stability to the supercurrents in the irradiation materials. Especially at low temperature, the temperature independent behavior of the logarithmic decay rate S for the irradiated samples shows the presence of quantum creep, which means the tunneling of vortices from the pinning wells.[36] For the samples with the splayed columnar tracks, the constant decay rate S (≈ 0.03 - 0.05) at low temperature is strong evidence of quantum creep effects, which extend up to temperatures T near 10 K. This evidence of the temperature independence of the decay rate S at low temperatures is associated with a flattening of the supercurrent density $J(T)$, whose limited magnitude is an

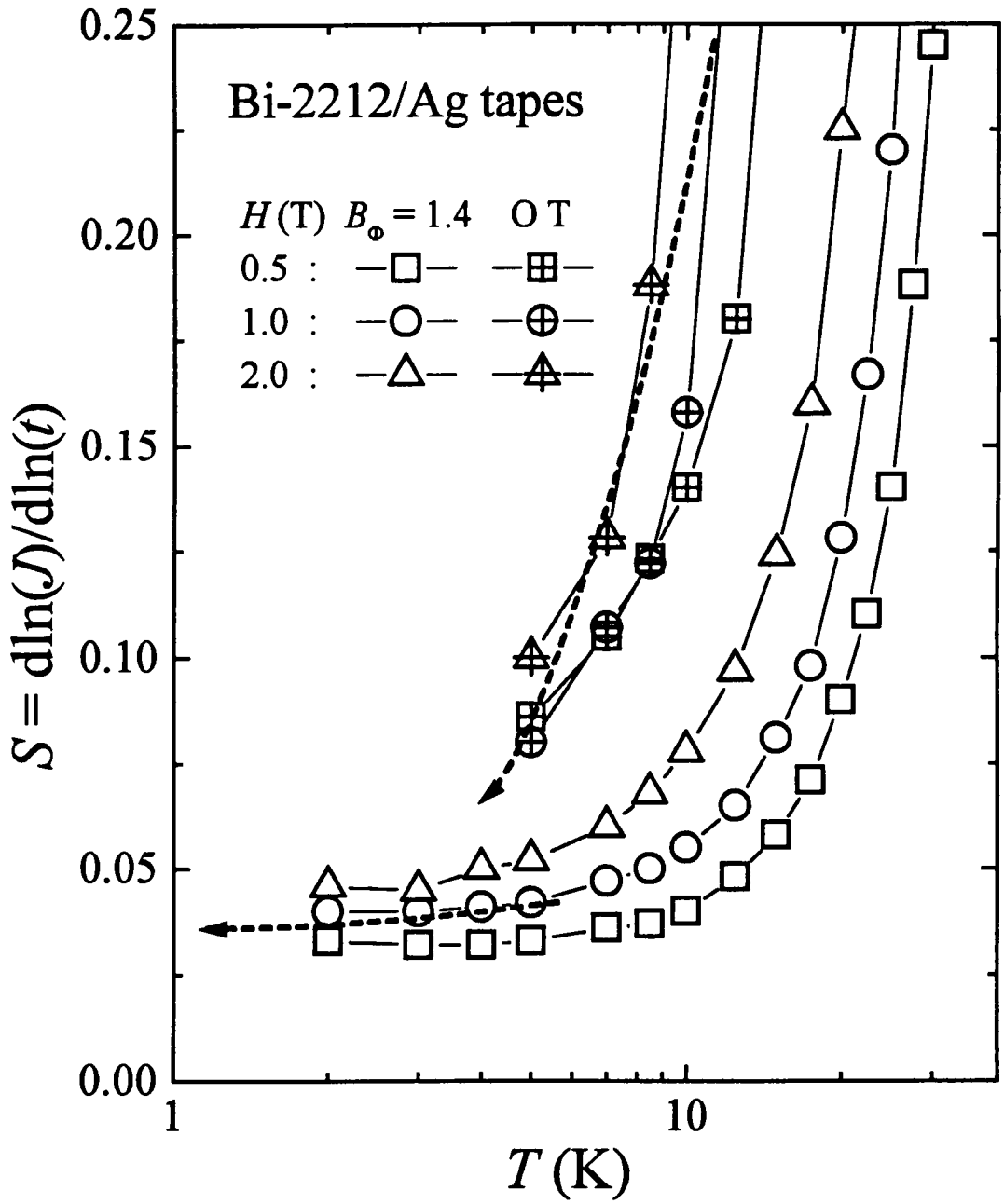


Figure 3-23. The flux creep rate S versus temperature T for Bi-2212/Ag tapes, both virgin and proton-irradiated with 4.7×10^{16} p/cm^2.

apparent consequence of large quantum creep in the Bi-2212 containing splayed columnar defects.[145]

In long-term measurements of the magnetization $M(t)$ at fixed field and temperature, Thompson et al.[137] showed that the data deviated significantly from the Anderson-Kim model. This model predicts a magnetic moment changing logarithmically with time (from previous section 3.2.2.4),[115]

$$M(t) \propto J(t) = J_{co} [1 - (k_B T/U_o) \ln(t/t_o)]. \qquad (3.2.3\text{-}5)$$

They analyzed the curvature of their data in terms of the dependence of the pinning potential energy U_o on the current density J. In contrast to the linear $U(J)$ relation of the Anderson-Kim theory,[115] the concept of a nonlinear $U(J)$ relation was treated first by M. R. Beasley et al. in 1969.[142] However, they did not include a dependence of pinning potential energy U_o on current density J in their Anderson-Kim formulation. Subsequently, a nonlinear dependence of $U(J)$ on J was introduced in the vortex-glass model by D.S. Fisher et al.[146] and in collective pinning theory by M. V. Feigel'man et al.[131] Thus they obtained an "interpolation formula" (from previous section 3.2.2.4),

$$M(t) \propto J(t) = J_{co} / [1 + (\mu k_B T/U_o) \ln(t/t_{eff})]^{1/\mu}, \qquad (3.2.3\text{-}5)$$

which reduces to the Anderson-Kim expression when $(k_B T/U) << 1$. In general, the interpolation formula describes very well the experimental results.

To understand giant flux creep in HTS materials, the current dependence of the vortex pinning potential energy $U(J)$ is a very important microscopic property. The effective pinning energy $U(J,T)$ from $M(T,t)$ data can be studied and determined experimentally by employing the procedure of M. P. Maley et al.,[132] as described earlier.

This gives a net pinning barrier U,

$$U = - T[\ln(dM/dt) - C], \qquad (3.2.3\text{-}6)$$

where $M \propto J_c$ from Bean critical state model and $C = \ln(B\omega\alpha/2\pi r)$. Thus equation (3.2.3-6) is an explicit expression for $U(J)$ at temperature T. Some results of such an analysis are given in Figure 3-24 showing $U(J,T_i)$ as a function of $M \propto J$ for bulk polycrystalline $HgBa_2Ca_2Cu_3O_9$: [Hg-1223]. In constructing these curves, the value of C is assumed to be temperature independent and is chosen to make the segments at several low temperatures to form a continuous curve. The resulting values of C are 22 (80) for virgin sample in increasing (decreasing) field history; for the irradiated sample, the corresponding values are C = 26 (30). It is evident that the increased stability of the vortices in the irradiated materials comes from the enhancement of the net pinning potential barrier of the vortices. Before concluding, two features should be noted. First, Figure 3-24 shows that the segments of the data at low temperature region do not lie well on a continuous curve. This effect likely comes from quantum flux creep, which can be sometimes significant at low temperature. This is a limitation of the Maley analysis, which considers only thermally activated flux creep. Second, for the unirradiated sample, we can see the large differences between increasing and decreasing field region. This is particularly evident in Figure 3-25, a semilog plot of the effective pinning potential. It is likely that this difference and widely differing values of C (given above) arise from surface barrier effects, where the barriers to flux entry and flux exit differ greatly. Just as shown in a Figure 3-18-b, the surface barrier effects gradually disappear by introducing splayed columnar defects, that are formed by irradiation with 0.8 GeV protons.

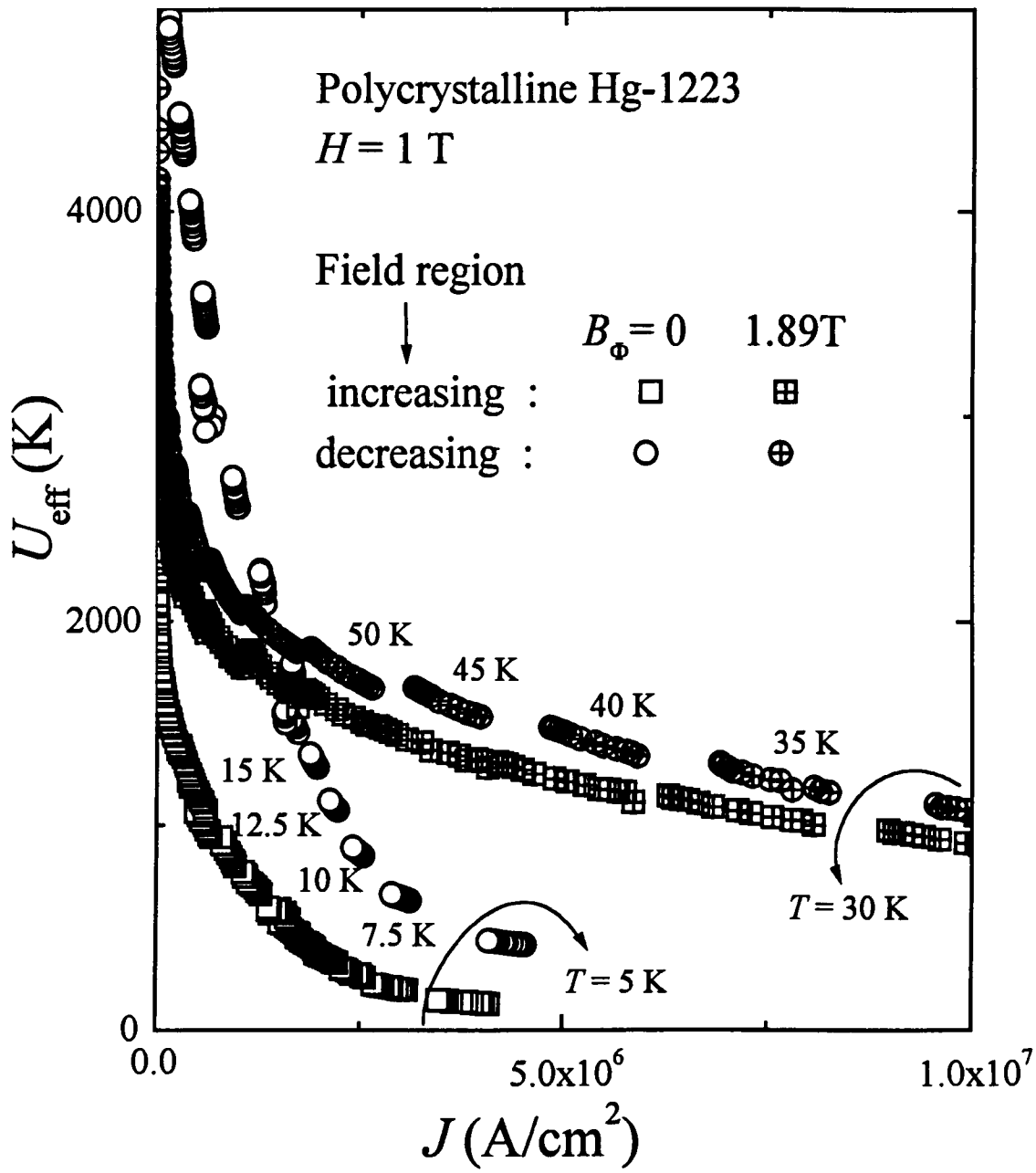


Figure 3-24. The pinning potential energy U versus current density J in both increasing and decreasing field history for magnetic field $H = 1$ T. See text.

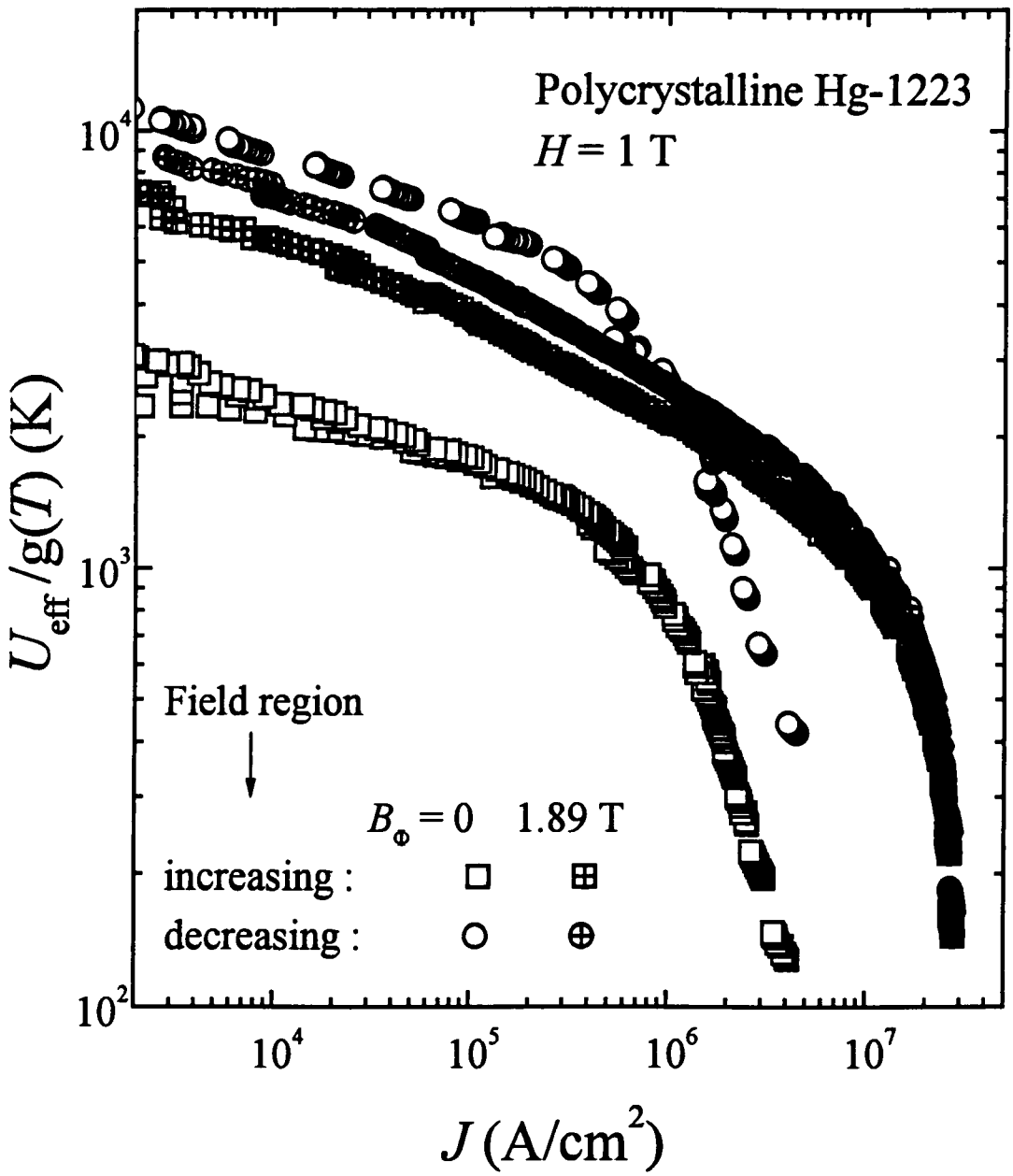


Figure 3-25. The log plots of U_{eff} / g(T) versus J in both increasing and decreasing field regions for magnetic field H = 1 T, where g(T) = $[1-(T/T_c)^2]^m$ with T_c = 135 K, m = 0.4(inc.), 0.8(dec.) for unirradiated sample, and m = 0.8(inc.), 1.0(dec.) for irradiated sample.

3.3 Summary

The $Ag_xHgBa_2CuO_{4+\delta}$ superconductors, fabricated by adding elemental Ag to the single Cu-O_2 layer superconductor $HgBa_2CuO_{4+\delta}$, have been studied in order to understand a role of Ag, which is often used for contacts, wire or tape fabrication, etc., in ceramic HTS materials. The ZFC magnetization $M(T)$ curve has structure, a "two step" transition, due to characteristic decoupling between grains. The structure, however, gradually disappears as Ag-content increases. This means that the increasing Ag-content diminishes the decoupling transition, which indicates a weakening of inter-grain coupling. The T_c for $Ag_xHgBa_2CuO_{4+\delta}$ decreases with Ag-content which is associated with changes in the supercarrier density. The carrier density was obtained from the equilibrium superconducting properties.

In particular, from an analysis of the reversible equilibrium magnetization data, a linear variation of $1/\lambda^2$ with temperature was found to extend down to temperature far below T_c; the hole density was estimated from the London penetration depth using standard London limit theory. The hole doping significantly affects the observed properties of the $Ag_xHgBa_2CuO_{4+\delta}$ superconductors. The processing of $HgBa_2CuO_{4+\delta}$ by addition of elemental Ag led to significant variation of the hole concentration. The irreversible magnetization $M(H)$ curves of the $Ag_xHgBa_2CuO_{4+\delta}$ superconductors were asymmetric about the line $M = 0$, indicating a surface barrier-dominated system. An analysis based on the theory for thermal flux creep of pancake vortices through a Bean-Livingstone surface barrier led to reasonable and consistent values of the characteristic temperature T_o, where

experimental data for the penetration field H_p and ΔM were analyzed.

In studies of enhanced pinning of vortices, splayed columnar tracks were formed by fission fragments due to the irradiation of 0.8 GeV protons. Several HTS materials were studied, including bulk polycrystalline (TlPb)$(SrBa)_2Ca_2Cu_3O_{9+\delta}$: [(TlPb)(SrBa)-1223], epitaxial thin films $(Tl_{0.8}Bi_{0.2})Ba_2Ca_2Cu_3O_{9+\delta}$ on $LaAlO_3$ or $Y_{0.2}Zr_{0.8}O_2$ (YSZ) substrates: [(TlBi)-1223 thin film], thick film $TlBa_2Ca_2Cu_3O_9$ on polycrystalline YSZ substrate: [Tl-1223 film], bulk polycrystalline $Tl_2Ba_2CaCu_2O_{8+\delta}$: [Tl-2212], thin film or bulk polycrystalline $HgBa_2Ca_2Cu_3O_9$: [Hg-1223 film, Hg-1223], single crystal or tape (deposited on Ag with 3.4 μm thickness) $Bi_2Sr_2CaCu_2O_8$: [Bi-2212, Bi-2212 tape/Ag], and so on. The HTS materials with splayed columnar tracks have higher irreversibility fields and the slower fall off of H_{irr} with increasing temperature, compared with the virgin HTS materials. The current density was greatly increased by the splayed columnar defects. There is, however, an optimal proton fluence Φ_p for enhancing the current density in these materials. The current density J first increases with increasing proton fluence Φ_p, then decreases at much higher Φ_p. While the current density J can be increased significantly by introducing optimal densities of defects such as point-like defects, simple parallel columnar or splayed columnar tracks within the HTS materials, the superconducting transition temperature T_c is suppressed somewhat by introducing defects. The depression rate for T_c is proportional to the number density and fission cross-section of the heavy fissionable nucleus in the material.

The decay rate S for the persistent currents is reduced, especially at high temperature, by the splayed columnar defects, formed by the fission fragments due to the irradiation of 0.8 GeV protons. In other words, the increasing stability of the supercurrents

in the irradiated materials comes from the enhancement of the vortex pinning. Especially, at low temperature, the temperature independent behavior of the logarithmic decay rate S for the irradiated samples of Bi-2212/Ag points to the presence of quantum creep, i.e., tunneling of vortices from the pinning wells. In addition, the effective pinning energy $U(J,T)$ has been obtained experimentally from $M(T,t)$ data by employing the procedure of M. P. Maley et al., which is based on thermally activated flux creep. The engineered microstructures give significantly enhanced vortex pinning.

CHAPTER 4

CONCLUSIONS

The single crystal of YNi_2B_2C is a clean type-II superconductor (mean free path $\ell > \xi_o$). Overall, the material is remarkably reversible, with a critical current density (at a field H = 10 kG) of ~ $10^{-6} \times J_o$, the depairing current density. Near T_c, the equilibrium magnetization M of this clean, type-II, reversible material follows the standard London relation $M \propto \ln(H)$. Well below T_c, the equilibrium magnetization deviates significantly from traditional local London theory, but it is described well by the more general non-local London formalism of Kogan et al. [Phys. Rev. B **54**, 12386 (1996)]. The resulting parameters in this theory (H_o, M_o, and ζ) are well behaved. The temperature T dependence of the London penetration depth λ was obtained from both non-local London analysis at low temperatures and a standard local London analysis near T_c. The quantity $1/\lambda^2$ follows a $t^{3/2}$ dependence (where $t = T/T_c$) for all temperatures, and its behavior is consistent with the intensity of neutron diffraction from the square vortex lattice, reanalyzed using parameters from this study. Near T_c, the material exhibits a linear dependence with $1/\lambda^2 \propto (1-t)$, as expected from both Ginzburg-Landau and BCS theories. At low temperature, however, $\lambda(T)$ seems to deviate from the simple BCS exponential dependence, and varies approximately as $\lambda(T) \propto T^3$.

The normal state magnetic susceptibility of the single crystal of YNi_2B_2C exhibited

large anisotropy depending on whether the magnetic field was applied parallel or perpendicular to the crystalline (001)-axis. For the field parallel to the crystalline (001)-axis, the magnetization $M(H)$ in the normal state is linear in the applied field H for over the whole temperature region, 5 ~ 300 K. However, for the field applied perpendicular to the crystalline (001)-axis, the $M(H)$ curves become nonlinear below 50 K, and progressively more nonlinearity as the temperature decreases. Measurement of the electrical resistivity using a van der Pauw method yielded an electrical resistivity of 4 μΩ-cm at 20 K and a residual ratio of 10. Analysis of heat capacity data for the single crystal of YNi_2B_2C agrees relatively well with a medium-coupling formalism. The electronic heat capacity in the superconducting state has t^3-dependence [$C_{e,super} \propto t^3$, where $t = T/T_c$]. Values for the Sommerfeld constant γ (the coefficient of the electronic heat capacity in the normal state) were obtained in a number of ways. These several evaluation all yielded values near 20 mJ/(mol K^2), showing good consistency in the data sets and analyses. In addition, from magnetization and heat capacity studies, the deduced values of the Ginzburg-Landau parameters κ_1 and κ_2 increase considerably as temperature decreases. This is consistent with the long mean free path and the observation of non-local electrodynamics in the single crystal of YNi_2B_2C.

In further work, a series of materials $Ag_xHgBa_2CuO_{4+\delta}$ containing Ag addition (with molar fraction x = 0, 0.05, 0.1, 0.3, and 0.5) to the single CuO_2 layer superconductor $HgBa_2CuO_{4+\delta}$ were studied. Overall, the processing with Ag-element led to general reductions in superconducting transition temperature T_c. The superconducting properties can be consistently interpreted in terms of the superconducting hole density as obtained from

the London penetration depth λ by standard London analysis. The magnetic properties are dominated by surface barrier effects. Therefore, the irreversible magnetic properties are reasonably well described by theory for thermally activated tunneling of pancake vortices through a surface barrier. In addition, there is "fishtail" behavior, with a local maximum in the $M(H)$; and values for the characteristic temperature T_0 exhibit a field dependence, reflecting further complexity to these materials.

In the third area of study, the vortex pinning effects due to sprayed columnar tracks, created by high energy (0.8 GeV) proton irradiation, were studied. For most practical applications, it is important to pin strongly vortices within high-T_c superconducting (HTS) materials. The magnetic hysteresis ΔM ($\propto J$) of HTS materials is increased significantly by introducing an optimal density of sprayed columnar defects. The superconducting transition temperature T_c, however, is suppressed somewhat by the radiation damage. Overall, irradiation with deeply penetrating 0.8 GeV protons, which create sprayed columnar tracks via a fission process, enhances the current conduction properties of HTS materials. The normalized current decay rate $S = - d\ln(J) / d\ln(t)$ is stabilized greatly in time, especially at high temperature, by the sprayed columnar defects. In addition, at low temperature, there is evidence of quantum flux creep (vortex tunneling) as S becomes temperature independent. Finally, analyses using the method of Maley show that these sprayed columnar defects effectively pin vortices within a variety of HTS materials and increase the net pinning potential. They make significant increases in the persistent current density J and elevate the irreversibility line $H_{irr}(T)$. These features suggest a good future and progress toward practical applications.

REFERENCES

and

BIBLIOGRAPHY

REFERENCES

1. H. Kamerlingh-Onnes, Leiden Comm. 120b, 122b, 124c (1911).
2. W. Meissner and R. Ochsenfeld, Naturwissenschaften **21**, 787 (1933).
3. F. London and H. London, Proc. Roy. Soc. (London) **A149**, 71 (1935).
4. V. L. Ginzburg and L. D. Landau, Zh. Eksperim. i Teor. Fiz. **20**, 1064 (1950).
5. J. Bardeen, L. N. Cooper, and J. R. Schrieffer, Phys. Rev. **108**, 1175 (1957).
6. L. N. Cooper, Phys. Rev. **104**, 1189 (1956).
7. J. R. Gavaler, Appl. Phys. Lett. **23**, 480 (1973).
8. L. R. Testardi, R. L. Meek, J. M. Poate, W. A. Royer, A. R. Storm, and J. H. Wernick, Phys. Rev. **B 11**, 4304 (1975).
9. J. G. Bednorz and K. A. Muller, Z. Phys. **B 64**, 189 (1986).
10. M. K. Wu, J. R. Achburn, C. J. Torng, P. M. Hor, R. L. Meng, L. Gao, Z. J. Huang, Y. Q. Wang, and C. W. Chu, Phys. Rev. Lett. **58**, 908 (1987); C. W. Chu, P. H. Hor, R. L. Meng, L. Gao, Z. J. Huang, Y. Q. Wang, Phys. Rev. Lett. **58**, 405 (1987).
11. R. J. Cava, B. Batlogg, R. B. van Dover, D. W. Murphy, S. Sunshine, T. Siegrist, J. P. Remeika, E. A. Rietman, S. Zahurak, and A. P. Espinosa, Phys. Rev. Lett. **58**, 1676 (1987).
12. H. Maeda, Y. Tanaka, M. Fukutomi, and T. Asano, Jpn. J. Appl. Phys. Lett. **27**, 209 (1988).
13. Z. Z. Sheng and A.M. Hermann, Nature (London) **332**, 138 (1988).

14. N. Putilin, E. V. Antipov, O. Chmaissem, and M. Marezio, Nature (London) **362**, 226 (1993).

15. A. Schilling, M. Cantoni, J. D. Guo, and H. R. Ott, Nature (London) **363**, 56 (1993).

16. K. Heine, J. Tenbrink, and M. Thoner, Appl. Phys. Lett. **55**, 2441 (1989).

17. Y. Iijima, N. Tanabe, O. Kohno, and Y. Ikeno, Appl. Phys. Lett. **60**, 769 (1992).

18. R. P. Reade, P. Burdahl, R. E. Russo, and S. M. Garrison, Appl. Phys. Lett. **61**, 2231 (1993).

19. X. D. Wu, S. R. Foltyn, P. Arendt, J. Townsend, C. Adams, I. H. Campbell, P. Tivari, Y. Coulter, and D. E. Peterson, Appl. Phys. Lett. **65**, 1961 (1994).

20. A. Goyal, D. P. Norton, J. D. Budai, M. Paranthaman, E. D. Specht, D. M. Kroeger, D. K. Christen, Qing He, B. Saffian, F. A. List, D. F. Lee, P. M. Martin, C. E. Klabunde, E. Hatfield, and V. K. Sikka, Appl. Phys. Lett. **69**, 1795 (1996).

21. D. P. Norton, A. Goyal, J. D. Budai, D. K. Christen, D. M. Kroeger, E. D. Specht, Qing He, B. Saffian, M. Paranthaman, C. E. Klabunde, D. F. Lee, B. C. Sales, and F. A. List, Science **274**, 755 (1996).

22. R. Nagarajan, Chandan Mazumdar, Zakir Hossain, S. K. Dhar, K. V. Gopalakrishnan, L. C. Gupta, C. Godart, B. D. Padalia, and R. Vijayaraghavan, Phys. Rev. Lett. **72**, 274 (1994).

23. R. J. Cava, H. Takagi, H. W. Zandbergen, J. J. Krajewski, W. F. Peck Jr., T. Siegrist, B. Batlogg, R. B. van Dover, R. J. Felder, K. Mizuhashi, J. O. Lee, H. Eisaki, and S. Uchida, Nature (London) **367**, 252 (1994).

24. T. Siegrist, H. W. Zandbergen, R. J. Cava, J. J. Krajewski, and W. F. Peck Jr., Nature (London) **367**, 254 (1994).

25. H. C. Ku, C. C. Lai, Y. B. You, J. H. Shieh, and W. Y. Guan, Phys. Rev. **B 50**, 351 (1994).

26. J. L. Sarrao, M. C. de Andrade, J. Herrmann, S. H. Han, Z. Fisk, M. B. Maple, and R. J. Cava, Physica **C 229**, 65 (1994).

27. H. Eisaki, H. Takagi, R. J. Cava, B. Batlogg, J. J. Krajewski, W. F. Peck, K. Mizuhashi, J. O. Lee, and S. Uchida, Phys. Rev. **B 50**, 647 (1994).

28. R. Movshovich, M. F. Hundley, J. D. Thomson, P. C. Canfield, B. K. Cho, and A. V. Chubukov, Physica **C 227**, 381 (1994).

29. P. C. Canfield, B. K. Cho, D. C. Johnston, D. K. Finnemore, and M. F. Hundley, Physica **C 230**, 397 (1994).

30. C. Godart, L. C. Gupta, R. Nagarajan, S. K. Dhar, H. Noel, M. Potel, C. Mazumdar, Z. Hossain, C. Levy-Clement, G. Schiffmacher, B. D. Padalia, and R. Vijayaraghavan, Phys. Rev. **B 51**, 489 (1995).

31. U. Yaron, P. L. Gammel, A. P. Ramirez, D. A. Huse, D. J. Bishop, A. I. Goldman, C. Stassis, P. C. Canfield, K. Mortensen, and M. R. Eskildsen, Nature (London) **382**, 236 (1996).

32. M. R. Eskildsen, P. L. Gammel, B. P. Barber, U. Yaron, A. R. Ramirez, D. A. Huse, D. J. Bishop, C. A. Bolle, C. M. Lieber, S. Oxx, S. Sridhar, N. H. Andersen, K. Mortensen, and P. C. Canfield, Phys. Rev. Lett. **78**, 1968 (1997).

33. M. Yethiraj, D. McK. Paul, C. V. Tomy, and E. M. Forgan, Phys. Rev. Lett. **78**,

4849 (1997).

34. D. McK. Paul, C. V. Tomy, C. M. Aegerter, R. Cubitt, S. H. Lloyd, E. M. Forgan, S. L. Lee, and M. Yethiraj, Phys. Rev. Lett. **80**, 1517 (1998).

35. M. Yethiraj, D. McK. Paul, C. V. Tomy, and J. R. Thompson, Phys. Rev. **B 58**, R14767 (1998).

36. G. Blatter, M. V. Feigel'man, V. B. Geshkenbein, A. I. Larkin, and V. M. Vinikur, Rev. Mod. Phys. **66**, 1125 (1994) and references therein.

37. L. Civale, A. D. Marwick, T. K. Worthington, M. A. Kirk, J. R. Thompson, L. Krusin-Elbaum, Y. Sun, J. R. Clem, and F. Holtzberg, Phys. Rev. Lett. **67**, 648 (1991).

38. T. Hwa, P. LeDoussal, D. R. Nelson, and V. M. Vinokur, Phys. Rev. Lett. **71**, 3545 (1993).

39. L. Krusin-Elbaum, J. R. Thompson, R. Wheeler, A. D. Marwick, C. Li, S. Patel, D. T. Shaw, P. Lisowski, and J. Ullmann, Appl. Phys. Lett. **64**, 3331 (1994).

40. L. Krusin-Elbaum, D. Lopez, J. R. Thompson, R. Wheeler, J. Ullmann, C. W. Chu, and Q.M. Lin, Nature (London) **389**, 243 (1997).

41. K. J. Song, J. R. Thompson, M. Yethiraj, D. K. Christen, C. V. Tomy, D. McK. Paul, Phys. Rev. **B 59**, R6620 (1999).

42. M. R. Eskildsen, P. L. Gammel, B. P. Barber, A. P. Ramirez, D. J. Bishop, N. H. Andersen, K. Mortensen, C. A. Bolle, C. M. Lieber, and P. C. Canfield, Phys. Rev. Lett. **79**, 487 (1997).

43. V. G. Kogan, M. Bullock, B. Harmon, P. Miranovic, Lj. Dobrosavljevic-Grujie, P.

L. Gammel, and D. J. Bishop, Phys. Rev. **B 55**, R8693 (1997).

44. Y. De Wilde, M. Lavarone, U. Welp, V. Metlushko, A. E. Koshelev, I. Aranson, and G. W. Crabtree, Phys. Rev. Lett. **78**, 4273 (1997).

45. V. G. Kogan, M. M. Fang, and Sreeparna Mitra, Phys. Rev. **B 38**, 11958 (1988).

46. V. G. Kogan, A. Gurevich, J. H. Cho, D. C. Johnston, Ming Xu, J. R. Thompson, and A. Martynovich, Phys. Rev. **B 54**, 12386 (1996-I) and references therein.

47. K. Maki, Physics **1**, 21 and 127 (1964).

48. F. London, "*Superfluids*" Vol. I, Wiley, New York (1950).

49. M. Tinkham, "*Introduction to Superconductivity*" 2nd Ed., McGraw-Hill, New York (1996).

50. V. G. Kogan, P. Miranovic, Lj. Dobrosavlievic, W. E. Pickett, and D. K. Christen, Phys. Rev. Lett. **79**, 741 (1997).

51. Quantum Design Inc., "*Magnetic Properties Measurement System Operating Manual*," Quantum Design, San Diego (1989).

52. Yang Ren Sun, "*Flux Creep Studies in* $Y_1Ba_2Cu_3O_{7-\delta}$ *Superconductors*," Ph. D. Thesis, University of Tennessee (May, 1993).

53. C. M. Aegerter, R. Cubitt, S. L. Lee, D. McK. Paul, M. Yethiraj, and H. A. Mook, Phys. Rev. **B 57**, 14511 (1998-II).

54. D. Cribier, B. Jacrot, L. Madhov Rao, and B. Farnoux, Phys. Lett. **9**, 106 (1964).

55. E. M. Forgan, D. McK. Paul, H. A. Mook, P. A. Timmins, H. Keller, S. Sutton, and J. S. Abell, Nature (London) **343**, 735 (1990).

56. R. Cubitt, E. M. Forgan, G. Yang, S. L. Lee, D. McK. Paul, H. A. Mook, M.

Yethiraj, P. H. Kes, T. W. Li, A. A. Menovsky, Z. Tarnawski, and K. Mortensen, Nature (London) **365**, 407 (1993).

57. R.D. Parks, "*Superconductivity*" Vol. 1 & 2, Marcel Dekker, New York (1969).

58. A. C. Rose-Innes and E. H. Rhoderick, "*Introduction to Superconductivity*" 2nd Ed., Pergamon, Oxford (1978).

59. H. Michor, T. Holubar, C. Dusek, and G. Hilscher, Phys. Rev. **B 52**, 16165 (1995-II).

60. C. J. Gorter and H. B. G. Casimir, Phys. Z. **35**, 963 (1934); Physica **1**, 306 (1934).

61. A. B. Pippard, Proc. Roy. Soc. (London) **A203**, 98 & 210 (1950); **A216**, 547 (1953).

62. A. A. Abrikosov, Zh. Eksperim. I Teor. Fiz. **32**, 1442 (1957): Sov. Phys. - JETP **5**, 1174 (1957).

63. P. de Gennes, "*Superconductivity in Metals and Alloys*," Benjamin, New York (1966).

64. V. G. Kogan, Phys. Rev. **B 24**, 1572 (1981).

65. L. J. Campbell, M. M. Doria, and V. G. Kogan, Phys. Rev. **B 38**, 2439 (1988).

66. G. Eilenberger, Z. Phys. **214**, 195 (1968).

67. Ming Xu, P. C. Canfield, J. E. Ostenson, D. K. Finnemore, B. K. Cho, Z. R. Wang, and D. C. Johnston, Physica C **227**, 321 (1994); Ming Xu, B. K. Cho, P. C. Canfield, D. K. Pinnemore, D. C. Johnston, and D. E. Farrell, Physica C **235-240**, 2533 (1994).

68. R. Movshovich, M. F. Hundley, J. D. Thomson, P. C. Canfield, B. K. Cho, and A.

V. Chubukov, Physica **C 227**, 381 (1994).

69. Mi-Ock Mun, Sung-Ik Lee, W. C. Lee, P. C. Canfield, B. K. Cho, and D. C. Johnston, Phys. Rev. Lett. **76**, 2790 (1996).

70. S. Oxx, D. P. Choudhury, Balam A. Willemsen, H. Srikanth, S. Sridhar, B. K. Cho, and P. C. Canfield, Physica **C 264**, 103 (1996)

71. T. V. Chandrasekhar Rao, P. K. Mishra, G. Ravinkumar, V. C. Sahni, K. Ghosh, Gautam I. Menon, S. Ramakrishnan, A. K. Grover, and Girish Chandra, Physica **B 223-224**, 86 (1996); S. Kalavathi, T. Geetha Kumari, Y. Hariharan, M. C. Valsakumar, M. P. Janawadkar, T. S. Radhakrishnan, Z. Hossain, R. Nagarajan, L. C. Gupta, and R. Vijayaraghavan, Physica **B 223-224**, 96 (1996); K. Ghosh, S. Ramakrishnan, A. K. Grover, Girish Chandra, T. V. Chandrasekhar Rao, P. K. Mishra, G. Ravikumar, and V. C. Sahni, Physica **B 223-224**, 109 (1996).

72. V. G. Kogan, M. Ledvij, A. Yu. Simonov, J. H. Cho, and D. C. Johnston, Phys. Rev. Lett. **70**, 1870 (1993).

73. Zhidong Hao and John R. Clem, Phys. Rev. Lett. **67**, 2371 (1991).

74. T. Xiang and J. M. Wheatley, Phys. Rev. Lett. **77**, 4632 (1996).

75. C. Panagopoulos, J. R. Cooper, T. Xiang, G. B. Peacock, I. Gameson, and P. P. Edwards, Phys. Rev. Lett. **79**, 2320 (1997).

76. Peter Fulde and Richard A. Ferrell, Phys. Rev. **135**, A550 (1964).

77. A. I. Larkin and Yu. N. Ovchinnikov, Sov. Phys. - JETP **20**, 762 (1965).

78. A. M. Campbell and J. E. Evetts, Adv. Phys. **21**, 327 (1972).

79. A. B. Pippard, Phil. Mag. **19**, 217 (1969).

80. A. I. Larkin and Yu. N. Ovchinnikov, J. Low Temp. Phys. **34**, 409 (1979).

81. N. M. Hong, H. Michor, M. Vybornov, T. Holubar, P. Hundegger, W. Perthold, G. Hilscher, and P. Rogl, Physica **C 227**, 85 (1994).

82. B. K. Cho, Ming Xu, P. C. Canfield, L. L. Miller, and D. C. Johnston, Phys. Rev. **B 52**, 3676 (1995-I).

83. F. Bommeli, L. Degiorgi, P. Wachter, B. K. Cho, P. C. Canfield, R. Chau, and M. B. Maple, Phys. Rev. Lett. **78**, 547 (1997).

84. K. V. Samokhin, Physica **C 274**, 156 (1997).

85. Leonard W. Gruenberg and Leon Gunther, Phys. Rev. Lett. **16**, 996 (1966).

86. K. Gloos, R. Modler, H. Schimanski, C. D. Bredl, C. Geibel, F. Steglich, A. I. Buzdin, N. Sato, and T. Komatsubara, Phys. Rev. Lett. **70**, 501 (1993).

87. Takao Nakama, Masato Hedo, Tsunehisa Maekawa, Miyuki Higa, Roland Resel, Hitoshi Sugawara, Rikio Settai, Yoshichika Onuki, and Katsuma Yagasaki, J. Phys. Soc. Japan **64**, 1467 (1995).

88. H. Sugawara, T. Yamazaki, N. Kimura, R. Settai, and Y. Onuki, Physica **B 206-207**, 196 (1995).

89. R. Modler, P. Gegenwart, M. Lang, M. Deppe, M. Weiden, T. Luhmann, C. Geibel, F. Steglich, C. Paulsen, J. L. Tholence, N. Sato, T. Komatsubara, Y. Onuki, M. Tachiki, and S. Takahashi, Phys. Rev. Lett. **76**, 1292 (1996).

90. F. Thomas, B. Wand, T. Luhmann, P. Gegenwart, G. R. Stewart, and F. Steglich, J. Low Temp. Phys. **102**, 117 (1996).

91. D. Saint-James, G. Sarma and E. J. Thomas, "*Type II Superconductivity*,"

Pergamon, Oxford (1969).

92. N. R. Dilley, J. Herrmann, S. H. Han, and M. B. Maple, Phys. Rev. **B 56**, 2379 (1997-I).

93. A. M. Clogston, Phys. Rev. Lett. **9**, 266 (1962).

94. N. R. Werthamer, E. Helfand, and P. C. Hohenberg, Phys. Rev. **147**, 295 (1966).

95. S. B. Roy, Z. Hossain, A. K. Pradhan, P. Chaddah, R. Nagarajan, and L. C. Gupta, Physica **C 256**, 90 (1996).

96. Mi-Ock Mun, Mun-Seog Kim, Sung-Ik Lee, B. K. Cho, In-Sang Yang, W. C. Lee, and P. C. Canfield, Physica **C 303**, 57 (1998).

97. B. K. Cho, P. C. Canfield, L. L. Miller, D. C. Johnston, W. P. Beyermann, and A. Yatskar, Phys. Rev. **B 52**, 3684 (1995); B. K. Cho, P. C. Canfield, and D. C. Johnston, Phys. Rev. **B 52**, R3844 (1995).

98. C. Kittel, "*Introduction to Solid State Physics*," 5th Ed., John Wiley & Sons, New York (1976).

99. I. R. Fisher, J. R. Cooper, and R. J. Cava, Phys. Rev. **B 52**, 15086 (1995).

100. B. J. Suh, F. Borsa, D. R. Torgenson, B. K. Cho, P. C. Canfield, D. C. Johnston, J. Y. Rhee, and B. N. Harmon, Phys. Rev. **B 53**, R6022 (1996).

101. B. D. Dunlap, L. N. Hall, F. Behroozi, G. W. Crabtree, and D. G. Niarchos, Phys. Rev. **B 29**, 6244 (1984).

102. C. V. Tomy, M. R. Lees, G. Balakrishnan, D. T. Adroja, and D. McK. Paul, Physica **B 223-224**, 62 (1996).

103. L. F. Mattheiss, Phys. Rev. **B 49**, 13279 (1994).

104. W. E. Pickett and D. J. Singh, Phys. Rev. Lett. **72**, 3702 (1994); David J. Singh and Warren E. Pickett, Phys. Rev. **B 51**, 8668 (1995); David J. Singh, Solid State Comm. **98**, 899 (1996).

105. L. J. van der Pauw, Philips Res. Reports **13**, 1 (1958).

106. Yicai Sun, Oswin Ehrmann, Jurgen Wolf, and Herbert Reichl, Rev. Sci. Instrum. **63**, 3757 (1992).

107. Donald M. Ginsburg, "*Physical Properties of High Temperature Superconductors II*," World Scientific Publishing Co. (1990).

108. T. P. Orlando, E. J. McNiff, Jr., S. Foner, and M. R. Beasley, Phys. Rev. **B 19**, 4545 (1979).

109. M. K. Wilkinson, C. G. Shull, L. D. Roberts, and S. Bernstein, Phys. Rev. **97**, 889 (1955).

110. A. M. Toxen, Phys. Rev. Lett. **15**, 462 (1965).

111. E. Johnston-Halperin, J. Fiedler, D. E. Farrell, Ming Xu, B. K. Cho, P. C. Canfield, D. K. Pinnemore, and D. C. Johnston, Phys. Rev. **B 51**, 12852 (1995-II).

112. T. V. Chandrasekhar Rao, P. K. Mishra, G. Ravikumar, V. C. Sahni, K. Ghosh, S Ramakrishnan, A. K. Grover, and G. Chandra, Physica **C 249**, 271 (1995).

113. S. V. Shulga, S. L. Drechsler, G. Fuchs, K. H. Muller, K. Winzer, M. Heinecke, and K. Krug, Phys. Rev. Lett. **80**, 1730 (1998).

114. G. Eilenberger, Phys. Rev. **153**, 584 (1967).

115. P. W. Anderson, Phys. Rev. Lett. **9**, 309 (1962); P. W. Anderson and Y. B. Kim, Reviews of Modern Physics **36**, 39 (1964).

116. Y. Yeshurun and A. P. Malozemoff, Phys. Rev. Lett. **60**, 2202 (1988).

117. J. L. Wagner, P. G. Radaelli, D. G. Hinks, J. D. Jorgensen, J. F. Mitchell, B. Dabrowski, G. S. Knapp, and M. A. Beno, Physica **C 210**, 311 (1993).

118. H. R. Khan, O. Loebich, P. Fabbricatore, A. Sciutti, and B. Zhang, *Physica* **C 229**, 165 (1994); H. R. Khan and O. Loebich, Physica **C 254**, 15 (1995).

119. J. R. Thompson, H. R. Khan, and K. J. Song, Physica **C 272**, 171 (1996).

120. J. R. Thompson, D. K. Christen, H. R. Kerchner, L. A. Boatner, B. C. Sales, B. C. Chakoumakos, H. Hsu, J. Brynestad, D. M. Kroeger, J. W. Williams, Yang Ren Sun, Y. C. Kim, J. G. Ossandon, A. P. Malozemoff, L. Civale, A. D. Marwick, J. K. Worthington, L. Krusin-Elbaum, and F. Holtzberg in "*Magnetic Susceptibility of Superconductors and Other Spin Systems*," edited by R. A. Hein, T. Francavilla, and D. Liebenburg (Plenum, New York, 1992), p. 157.

121. H. R. Presland, J. L. Tallon, R. G. Buckley, R. S. Liu, and N. E. Flower, Physica **C 176**, 95 (1991)

122. J. L. Tallon and N. E. Flower, Physica **C 204**, 237 (1993).

123. Yang Ren Sun, J. R. Thompson, H. R. Kerchner, D. K. Christen, M. Paranthaman, and J. Brynestad, Phys. Rev. **B 50**, 3330 (1994).

124. Y. R. Sun, J. R. Thompson, J. Schwartz, D. K. Christen, Y. C. Kim, and M. Paranthaman, Phys. Rev. **B 51**, 581 (1995).

125. Y. C. Kim, J. R. Thompson, D. K. Christen, Y. R. Sun, M. Paranthaman, and E. D. Specht, Phys. Rev. **B 52**, 4438 (1995).

126. J. A. Lewis, V. M. Vinokur, J. Wagner, and D. Hinks, Phys. Rev. **B 52**, R3852

(1995).

127. L. Burlachkov, V. B. Geshkenbein, A. E. Koshelev, A. I. Larkin, and V. M. Vinokur, Phys. Rev. **B 50**, 16770 (1994).

128. C. P. Bean and J. D. Livingston, Phys. Rev. Lett. **12**, 14 (1964).

129. John R. Clem, Phys. Rev. **B 43**, 7837 (1991).

130. C. P. Bean, Phys. Rev. Lett. **8**, 250 (1962), and Rev. Mod. Phys. **36**, 31 (1964).

131. M. V. Feigel'man, V. B. Geshkenbein, A. I. Larkin, and V. M. Vinokur, Phys. Rev. Lett. **63**, 2303 (1989); M. V. Feigel'man and V. M. Vinokur, Phys. Rev. **B 41**, 8986 (1990); M. V. Feigel'man, V. B. Geshkenbein, and V. M. Vinokur, Phys. Rev. **B 43**, 6263 (1991).

132. M. P. Maley, J. O. Willis, H. Lessure, and M. E. McHenry, Phys. Rev. **B 42**, 2639 (1990).

133. F. Studer and M. Toulemonde, Nuclear Instruments and Methods in Physics Research **B 65**, 560 (1992).

134. J. R. Thompson, D. K. Christen, M. Paranthaman, L. Krusin-Elbaum, A. D. Marwick, L. Civale, R. Wheeler, J. G. Ossandon, P. Lisowski, and J. Ullmann, "*Springer-Verlag Lectures in Physics series*," edited by B. Veal, B. Dabrowski, P. Klamut, and J. Klamut (1996).

135. Y. Yeshurun, A. P. Malozemoff, and A. Shaulov, Rev. Mod. Phys. **68**, 911 (1996) and references therein.

136. V. B. Geshkenbein and A. I. Larkin, Sov. Phys. JETP **68**, 639 (1989).

137. J. R. Thompson, Yang Ren Sun, and F. Holtzberg, Phys. Rev. **B 44**, 458 (1991).

138. L. Civale, A. D. Marwick, M. W. McElfresh, T. K. Worthington, A. P. Malozemoff, F. H. Holtzberg, J. R. Thompson, and M. A. Kirk, Phys. Rev. Lett. **65**, 1164 (1990).

139. I. A. Campbell, L. Fruchter, and R. Cabanel, Phys. Rev. Lett. **64**, 1561 (1990).

140. L. Fruchter, C. Aguillon, I. A. Campbell, and B. Keszei, Phys. Rev. **B 42**, 2627 (1990).

141. A. I. Larkin, Zh. Eksp. Teor. Fiz. **58**, 1466 (1970), or Sov. Phys. JETP **31**, 784 (1970); A. I. Larkin and Yu. V. Ovchinnikov, J. Low Temp. Phys. **34**, 409 (1979); A. I. Larkin and Yu. V. Ovchinnikov, Zh. Eksp. Tero. Fiz. **65**, 1704 (1973), or Sov. Phys. JETP **38**, 854 (1974).

142. M. R. Beasley, R. Labusch, and W.W. Webb, Phys. Rev. **181**, 682 (1969).

143. E. Zeldov, N. M. Amer, G. Koren, A. Gupta, N. W. McElfresh, and R. J. Gambino, Appl. Phys. Lett. **56**, 680 (1990).

144. J. R. Thompson, L. Krusin-Elbaum, D. K. Christen, K. J. Song, M. Paranthaman, J. L. Ullmann, J. Z. Wu, Z. F. Ren, J. H. Wang, J. E. Tkaczyk, and J. A. DeLuca, Appl. Phys. Lett. **71**, 536 (1997).

145. J. R. Thompson, J. G. Ossandon, L. Krusin-Elbaum, K. J. Song, D. K. Christen, and J. L. Ullmann, Appl. Phys. Lett. **74**, 3699 (1999).

146. D. S. Fisher, M. P. A. Fisher, and D. A. Huse, Phys. Rev. **B 43**, 130 (1991); M. P. A. Fisher, Phys. Rev. Lett. **62**, 1415 (1989).

BIBLIOGRAPHY

* F. London, "Superfluids" (Wiley, New York 1950), Vol. 1.

* P. de Gennes, "Superconductivity of Metals and Alloys" (Benjamin, New York 1966).

* A. C. Rose-Innes and E. H. Rhoderick, "Introduction to Superconductivity" (Pergamon Press, Oxford 1968).

* R. D. Parks, Ed., "Superconductivity" (Marcel Dekker, New York 1969), Vols. 1 and 2.

* D. Saint-James, G. Sarma, and E. Thomas, "Type-II Superconductivity" (Pergamon Press, Oxford 1969).

* A. Cambell and J. Evetts, "Critical currents in Superconductors" (Taylor, London 1972).

* D. M. Ginsberg, Ed., "Physical Properties of High-Temperature Superconductors" (World Scientific, 1989 & 1990), Vols. 1 and 2.

* D. R. Tilley and J. Tilley, "Superfluidity and Superconductivity" (Institute of Phys. Pub., Bristol ans Philadelphia, 1990).

* Vladimir Z. Kresin and Stuart A. Wolf, " Fundamentals of Superconductivity" (Plenum Press, New York 1990).

* Gerald Burns, "High-Temperature Superconductivity (An Introduction)" (Academic Press, Inc., San Diego 1992).

* V. L. Ginzburg and E. A. Andryushin, "Superconductivity" (World Scientific, Singapore 1994).

* M. Tinkham, "Introduction to Superconductivity" (McGraw-Hill, Inc., New York 1975, 1996)

APPENDICES

Appendix 1. The calculation of mass density of YNi_2B_2C.

Reference : R. J. Cava et. al., Nature **367**, 252 (1994)

T. Siegrist et. al., Nature **367**, 254 (1994)

For YNi_2B_2C single crystal, the Molecular weight is

$$MW = [\,88.91\,] + [\,2 \times (\,58.71\,)\,] + [\,2 \times (\,10.81\,)\,] + [\,12\,]$$

$$= 239.95\ [\ (\text{amu}) / (\text{Formula unit})\ ]$$

From the above references, the lattice parameters (constants) of YNi_2B_2C single crystal are $a = b = 3.53$ Å and $c = 10.57$ Å. The YNi_2B_2C single crystal has two formula units per unit cell. Therefore, the cell volume is $V = 131.7$ Å^3 $= 131.7 \times 10^{-24}$ cm^3.

Finally, we can get density of mass of YNi_2B_2C single crystal:

$$\rho_{\text{mass}} = \frac{M}{V} = \frac{[239.95\ \text{amu / Fu}] \times [2\ \text{Fu / cell}] \times [1.66 \times 10^{-24}\ \text{g / amu}]}{[\,131.7 \times 10^{-24}\ \text{cm}^3\ /\ \text{cell}\,]}$$

$$= \mathbf{6.05\ g / cm^3}$$

Appendix 2. BCS relationships;

Reference: T. P. Orlando et al, Phys. Rev. B 19, 4545 (1979).

Followings are several BCS results for the properties of a superconductor in terms of its T_c and three independent normal-state parameters: ρ, γ, and the Fermi-surface area S. The units and symbols used the relations: (a) Low temperature normal state resistivity, $\rho_{\Omega\,cm} = (1/9) \times 10^{-11}\, \rho_{cgs}$. (b) The normal state electronic specific heat coefficient, γ [erg / (cm^3 K^2)]. (c) The reduced temperature, $t = T/T_c$ where T_c is the superconducting transition temperature. (d) The jump at T_c in the specific heat = $C_S - C_N$. (e) The conduction electron density = n [1/cm^3]. (f) Fermi surface = S [1/cm^2]. (g) The Fermi surface of an electron gas of density n, $S_F = 4\pi\,(3\pi^2\,n)^{2/3}$. (h) The flux quantum = ϕ_o = 2.07×10^{-7} G·cm^2.

1. Average Fermi velocity; $< v_F > = 5.77 \times 10^{-5}\,(n^{2/3}\,S/S_F)\,/\gamma$ [cm / sec]
2. Electronic mean free path; $\ell_{tr} = 1.27 \times 10^{4}\,/\,[\,\rho_{\Omega\,cm}\,(n^{2/3}\,S/S_F)\,]$ [cm]
3. Density of states of one spin direction;

   $N(0) = 7.97 \times 10^{30}\,\gamma$ [states / (cm^3 erg spin)]
4. BCS coherence length; $\xi_o = 7.95 \times 10^{-17}\,(n^{2/3}\,S/S_F)\,/\,(\gamma T_c)$ [cm]
5. London penetration depth (at 0 K); $\lambda_{L0} = 1.33 \times 10^{8}\,\gamma^{1/2}\,/\,(n^{2/3}\,S/S_F)$ [cm]
6. Gor'kov χ function;

   $\chi(\lambda_{tr}) = R(\lambda_{tr})\,/\,(1+\lambda_{tr})$, where $R(0) = 1$ and $R(\infty) = \pi^2\,/\,[7\zeta(3)] = 1.17$

   $\lambda_{tr} = 0.882\,\xi_o\,/\,\ell_{tr} = 5.51 \times 10^{-21}\,\rho_{\Omega\,cm}\,(n^{2/3}\,S/S_F)\,/\,(\gamma T_c)$

7. Ginzburg-Landau coherence length;

Clean limit ($\lambda_{tr} << 1$): $\xi^{c}_{GL} = 0.739\xi_{o}/(1-t)^{1/2} = 5.87 \times 10^{-17}(n^{2/3}\, S/S_F)/(\gamma T_c)$ [cm]

Dirty limit ($\lambda_{tr} >> 1$):

$\xi^{d}_{GL} = 0.852\,(\xi_o \ell_{tr})/(1-t)^{1/2} = 8.57 \times 10^{-7}/[(\gamma\, \rho_{\Omega\,cm}\, T_c)\,(1-t)]^{1/2}$ [cm]

8. Ginzburg-Landau penetration depth;

Clean limit: $\lambda^{c}_{GL} = \lambda_{L0}/[2(1-t)]^{1/2} = 9.37 \times 10^{7}\gamma^{1/2}/[(\, n^{2/3}\, S/S_F\,)\,(1-t)^{1/2}]$ [cm]

Dirty limit:

$\lambda^{d}_{GL} = \lambda_{L0}\,(\xi_o/1.33\ell_{tr})^{1/2}/[2(1-t)]^{1/2} = 6.42 \times 10^{-3}\,(\rho_{\Omega\,cm}/T_c)^{1/2}/(1-t)^{1/2}$ [cm]

9. Ginzburg-Landau κ;

Clean limit: $\kappa^{c}_{GL} = 0.957\,\lambda_{L0}/\xi_o = 1.60 \times 10^{24}\, T_c\gamma^{3/2}/(\, n^{2/3}\, S/S_F\,)^2$

Dirty limit: $\kappa^{d}_{GL} = 0.720\,\lambda_{L0}/\ell_{tr} = 7.49 \times 10^{3}\,\gamma^{1/2}\,\rho_{\Omega\,cm}$

10. Thermodynamic critical field; $H_c = 4.23\,\gamma^{1/2}\,T_c\,(1-t)$ [Oe]

11. Slope of thermodynamic critical field;

$-(dH_c/dT)_{Tc} = [4\pi(C_s - C_n)/T_c]^{1/2} = 4.23\,\gamma^{1/2}$ [Oe/K]

12. Slope of upper critical field;

Clean limit: $-(dH_{c2}/dT)^{c}_{Tc} = 9.55 \times 10^{24}\,\gamma^2\,T_c/(\, n^{2/3}\, S/S_F\,)^2$ [Oe / K]

Dirty limit: $-(dH_{c2}/dT)^{d}_{Tc} = 4.48 \times 10^{4}\,\gamma\,\rho_{\Omega\,cm}$ [Oe / K]

13. Lower critical field; $H_{c1} = H_c \ln\kappa/[(2)^{1/2}\,\kappa]$

Appendix 3. The calculation of the mass of free Ag in $Ag_xHgBa_2CuO_{4+\delta}$ and the volume of $Ag_xHgBa_2CuO_{4+\delta}$ superconductor:

$M_{total} = M_{Hg\text{-}1201} + M_{Ag}$, where $M_{Hg\text{-}1201}$ = 603 g/mole

Ag element: 107.87 amu/mole

$\rho_{Hg\text{-}1201}$ = 7.0 g/cm^3 and ρ_{Ag} = 10.5 g/cm^3.

Because we can dissolve about 0.1 mole Ag into 1 mole of $HgBa_2CuO_{4+\delta}$, the mass of free Ag(M_{Ag}) = (x - 0.1)[# moles of $HgBa_2CuO_{4+\delta}$](107.87 g/mole Ag), where [# moles of $HgBa_2CuO_{4+\delta}$] = [(M_{total} - M_{Ag})/(603 g/mole $HgBa_2CuO_{4+\delta}$)]. Therefore,

$$M_{Ag} = (x - 0.1)[(M_{total} - M_{Ag})/(603)](107.87).$$

These samples contained Ag addition with mole fraction x = 0, 0.05, 0.1, 0.3, and 0.5, into the $Ag_xHgBa_2CuO_{4+\delta}$ material. In the cases of x = 0, 0.01, and 0.1, the mass of free Ag is almost zero. However, for x = 0.3 into $Ag_xHgBa_2CuO_{4+\delta}$ (mass = 106.7 mg),

$$M_{Ag=0.3} = (0.3 - 0.1)[(0.1067 - M_{Ag=0.3})/603](107.87) \text{ g}$$

finally,

$$M_{Ag=0.3} = 0.003686 \text{ g} = 3.686 \text{ mg}.$$

In addition, using $M_{total} = (\rho_{Hg\text{-}1201})(V_{superconductor}) + M_{Ag=0.3}$, we can get

$$V_{superconductor} = (0.1067 - 0.00368) / 7 = 0.01472 \text{ g/cm}^3.$$

Appendix 4. The calculation of the critical current density J_c of a spherical superconductor of radius R by Bean critical state model:

If we assume that $J(r, \theta)$ is the critical current density of a sphere in an applied field H, then the magnetic moment of the sphere sample is

$$m = (1/2c)\int (r \times J)\, dr. \tag{A.4-1}$$

In spherical coordinates,

$$m = (1/2c)\int rJ(r)\sin(\theta)\, 2\pi r^2 \sin(\theta)\, d\theta\, dr. \tag{A.4-2}$$

From mathematical tables, $\int_o^{\pi} \sin^2(nx)\, dx = \pi/2$, where n is integer,

$$m = (\pi^2/2c)\int r^3 J(r)\, dr. \tag{A.4-3}$$

Thus the magnetization is obtained to

$$M = (3\pi/8cR^3)\int r^3 J(r)\, dr. \tag{A.4-4}$$

Now $J(r)$ can expand about the point $r = R$ using Taylor series:

$$J(r) = J(R) + J'(R)\,(r - R) + J''(R)\,(r - R)^2/2! + \cdots\cdots, \tag{A.4-5}$$

where the primes represent derivatives with respect to r.

Plugging equation (A.4-5) in (A.4-4),

$$M = (3\pi/8cR^3)\int r^3\,[J(R) + J'(R)\,(r - R) + J''(R)\,(r - R)^2 + \cdots\cdots]dr$$

$$= (3\pi/8cR^3)[J(R)\int r^3 dr + J'(R)\int r^3(r - R)dr + J''(R)\int r^3(r - R)^2 dr + (\int \cdots\cdot)dr]$$

$$= (3\pi/8cR^3)\{J(R)[R^4/4] + J'(R)[R^5/5 - R^5/4] + J''(R)[R^6/6 - 2R^6/5 + R^6/4] + \cdot\cdot\ \}$$

$$= (3\pi/8cR^3)\{J(R)[R^4/4] - J'(R)[R^5/20] + J''(R)[R^6/60] + \cdots\}. \quad \text{(A.4-6)}$$

If we take the first derivative of $4\pi M$ with respect to the applied field H,

$$4\pi M' = 4\pi(\partial M/\partial H)$$

$$= (3\pi^2/2cR^3)[J'(R)\,(\partial R/\partial H)(R^4/4) - J''(R)\,(\partial R/\partial H)(R^5/20) + \cdots], \quad \text{(A.4-7)}$$

where the primes indicate derivatives with respect to the applied field H.

On the other hand, using one of Maxwell's equation: $\nabla \times H = (4\pi/c)\,J$, so $\partial R/\partial H = -\,c/(4\pi J)$. If we eliminate $\partial R/\partial H$ from equation (A.4-7),

$$4\pi M' = (3\pi^2/2cR^3)\{J'(R)\,[-\,c/(4\pi J)]\,(R^4/4) - J''(R)\,[-\,c/(4\pi J)]\,(R^5/20) + \cdots\cdots\}$$

$$= (-3\pi/8R^3)[1/J(R)]\,[\,J'(R)\,(R^4/4) - J''(R)\,(R^5/20) + \cdots\cdots], \quad \text{(A.4-8)}$$

and solve about $J'(R)\,(R^5/20)$,

$$J'(R)\,(R^5/20) = (-32/15)\,R^4 J(R)M' + (1/100)\,R^6\,J''(R) + \cdots\cdots. \quad \text{(A.4-9)}$$

Substituting equation (A.4-9) into (A.4-6),

$$M = (3\pi/8cR^3)[J(R)[R^4/4] - (-32/15)R^4 J(R)M' - (1/100)R^6\,J''(R) - J''(R)[R^6/60] + \cdots]$$

$$= (3\pi/32c)R\,J(R)\{1 + (128/15)M' - (1/150)R^2\,[J''(R)\,/\,J(R)] + \cdots\cdots\}, \text{ so}$$

$$4\pi M = (3\pi^2/8c)R\,J(R)\{1 + (128/15)M' - (1/150)\,R^2[J''(R)/J(R)] + \cdots\}. \quad \text{(A.4-10)}$$

If the magnetization M changes with an applied field H, we get the following:

$$4\pi M = (3\pi^2/8c)\,R\,J(H)\{1 + (128/15)M' - (1/150)\,R^2\,[J''(H)\,/\,J(H)] + \cdots\cdots\}$$

$$\approx (3\pi^2/8c)\,R\,J(H)[1 + (128/15)(\partial M/\partial H)], \quad \text{(A.4-11)}$$

where the last terms are neglected. In the Bean critical state model, the possible values of critical current density are $+J_c$ or $-J_c$ according to the field history, either increasing or decreasing field, assuming $H >$ the penetration field H_p. This gives two branches of magnetization, for the increasing field region (M_+) or decreasing field region (M_-); these

have the same magnitude with the opposite signs and correspond to critical current densities $+J_c$ or $-J_c$, respectively. Finally, we can calculate the difference between M_+ and M_-:

$$(4\pi M_+) - (4\pi M_-) = (3\pi^2/8c)RJ_c(H)\{2+(128/15)[(\partial M_+)/(\partial H_+)+(\partial M_-)/(\partial H_-)]\}. \quad \text{(A.4-12)}$$

If we solve equation (A.4-12) for $J_c(H)$,

$$J_c(H) = (32c/3\pi R)[(M_+)-(M_-)]/\{2+(128/15)[(\partial M_+)/(\partial H_+)+(\partial M_-)/(\partial H_-)]\}. \quad \text{(A.4-13)}$$

After converting to laboratory units, where c is replaced by 10, expressing the magnetic field H in Gauss, and current density J in Amperes/cm^2, and neglecting the derivative term, we obtain the following simple relation:

$$J_c \simeq (17)\, \Delta M / R, \quad \text{(A.4-14)}$$

where $\Delta M = (M_+) - (M_-)$.

Appendix 5. Published papers and presentations in these works.

Published papers

1. "Superconducting and magnetic properties of single crystal YNi_2B_2C" K. J. Song, J. R. Thompson, D. K. Christen, D. G. Mandrus, M. Yethiraj, C. V. Tomy, and D. McK. Paul, **in preparation**
2. "Properties of Polycrystalline $Hg_{1-x}Bi_xBa_2Ca_2Cu_3O_y$ Superconductors, K. J. Song, H. R. Khan, H. J. Kim, and J. R. Thompson, 22nd International Conference on Low Temperature Physics, Espoo and Helsinki, Finland, August 4-11, 1999: submitted to **Physica B**.
3. "Quantum Tunneling of Vortices in Bi-2212 with Splayed Columnar Defects" J. R. Thompson, J. G. Ossandon, L. Krusin-Elbaum, K. J. Song, D. K. Christen, and J. L. Ullmann, 22nd International Conference on Low Temperature Physics, Espoo and Helsinki, Finland, August 4-11, 1999: submitted to **Physica B**.
4. "Non-local superconductivity and the vortex-state properties of YNi_2B_2C" K. J. Song, J. R. Thompson, D. K. Christen, D. G. Mandrus, M. Yethiraj, C. V. Tomy, and D. McK. Paul, 22nd International Conference on Low Temperature Physics, Espoo and Helsinki, Finland, August 4-11, 1999: submitted to **Physica B**.
5. "Quantum Constraints on Technological Superconductors", J. R. Thompson, J. G. Ossandon, L. Krusin-Elbaum, K. J. Song, D. K. Christen, J. L. Ullmann, **Appl.**

Phys. Lett. 74, 3699 (1999).

6. "Nonlocal current-field relation and the vortex-state magnetic properties of YNi_2B_2C", K. J. Song, J. R. Thompson, M. Yethiraj, D. K. Christen, C. V. Tomy, and D. McK. Paul, **Phys. Rev. B 59**, R6620 (1999).
7. "Stabilization of Magnetic Flux in BSCCO-2212/Ag Tapes Subjected to 0.8 GeV Proton Irradiation", J. G. Ossandon, J. R. Thompson, L. Kurusin-Elbaum, K. J. Song, D. K. Christen, and J. L. Ullmann, in **Science and Technology of HTS superconductivity: Advances in Science and Technology 23,** edited by P. Vincenzini (Techna, Faenza, Italy, 1998) pp 645 - 652.
8. "Thermal conversion of an iron nitride-silicon nitride precursor into a ferromagnetic nanocomposite", L. Maya, J. R. Thompson, K. J. Song, and R. J. Warmack, **J. Appl. Phys. 83**, 905 (1998).
9. "J_c and vortex pinning enhancements in Bi-, Tl-, and Hg-based cuprate superconductors via GeV proton irradiation", J. R. Thompson, J. G. Ossandon, L. Krusin-Elbaum, K. J. Song, D. K. Christen, M. Paranthaman, J. Z. Wu, and J. L. Ullmann, **Proceedings of 8th U.S. / Japan workshop on high-Temperature Superconductors** (Tallahassee, Florida, Dec. 7-10, 1997), edited by J. Schwartz (Rose Printing, Tallahassee, FL, 1998), pp. 146-152.
10. "Current-density enhancements of the highest-T_c superconductors with GeV protons", J. R. Thompson, L. Krusin-Elbaum, D. K. Christen, K. J. Song, M. Paranthaman, J. L. Ullmann, J. Z. Wu, Z. F. Ren, J. H. Wang, J. E. Tkaczyk, and J. A. DeLuca, **Appl. Phys. Lett. 71**, 536 (1997).

11. "Influence of Ag additions on the superconducting properties of $HgBa_2CuO_{4+\delta}$ materials - hole doping and surface barrier effects", J. R. Thompson, H. R. Khan, and K. J. Song, **Physica C 272**, 171 (1996).

Presentations

1. **The 22nd International Conference on Low Temperature Physics,** "Properties of Polycrystalline $Hg_{1-x}Bi_xBa_2Ca_2Cu_3O_y$ Superconductors" K. J. Song, H. R. Khan, H. J. Kim, and J. R. Thompson, Espoo and Helsinki, Finland, August 4-11, 1999.
2. **The 22nd International Conference on Low Temperature Physics,** "Quantum Tunneling of Vortices in Bi-2212 with Splayed Columnar Defects" J. R. Thompson, J. G. Ossandon, L. Krusin-Elbaum, K. J. Song, D. K. Christen, and J. L. Ullmann, Espoo and Helsinki, Finland, August 4-11, 1999.
3. **The 22nd International Conference on Low Temperature Physics,** "Non-local superconductivity and the vortex-state properties of YNi_2B_2C" K. J. Song, J. R. Thompson, D. K. Christen, D. G. Mandrus, M. Yethiraj, C. V. Tomy, and D. McK. Paul, Espoo and Helsinki, Finland, August 4-11, 1999.
4. **APS 99 Centennial Atlanta March Meeting:** K. J. Song, J. R. Thompson, D. K. Christen, D. G. Mandrus, M. Yethiraj, C. V. Tomy, and D. McK. Paul, Bull. American Phys. Soc., **44**, 1591 (1999).
5. **The Vortex Dynamics Workshop:** J. R. Thompson, K. J. Song, M. Yethiraj, D. K. Christen, C. V. Tomy, and D. MaK. Paul, The Vortex Dynamics Workshop, Hachimantai, Iwate Prefecture, Japan, June 21-26, 1998.

6. **The 9th CIMTEC - World Ceramics Congress and Forum on New Materials;** J. G. Ossandon, J. R. Thompson, L. Kurusin-Elbaum, K. J. Song, D. K. Christen, and J. L. Ullmann, Proceedings of 9th CIMTEC-World Ceramics Congress and Forum on New Materials, Florence, Italy, June 14 - 19, 1998.

7. **APS 98 L.A. March Meeting:** K. J. Song, J. R. Thompson, D. K. Christen, M. Yethiraj, C. V. Tomy, D. McK. Paul, Bull. American Phys. Soc., **43**, 503 (1998).

8. **The 8th US-Japan Workshop on High Temperature Superconductors:** J. R. Thompson, J. G. Ossandon, L. Krusin-Elbaum, K. J. Song, D. K. Christen, and J. L. Ullmann, Tallahassee, Florida, Dec. 8-10, 1997.

9. **Vortex Matter Workshop:** J. R. Thompson, L. Krusin-Elbaum, D. K. Christen, K. J. Song, M. Paranthaman, J. L. Ullmann, J. Z. Wu, Z. F. Ren, J. H. Wang, J. E. Tkaczyk, and J. A. DeLuca, Ascona, Switzerland, June 15-20, 1997.

VITA

Kyu Jeong Song was born in Cheonrabuk-Do, Korea on April 14, 1963. He received his basic education in Cheonju, Korea and was graduated from Cheonra high school in February 1982. In March of 1982 he entered Korea University, in Seoul, Korea and in February 1986 he received a Bachelor of Science degree in Physics. In March of 1986 he entered the graduate school of Korea University, in Seoul, Korea and began to study toward a Master of Science degree with the position of teaching assistantship at Korea University. He was awarded a Master of Science degree in physics in February 1988.

After a military duty with Korean army, he did research works for four years (1989-1993) as a research scientist in Physics Division at the Korea Basic Science Institute (KBSI), Korea. In January of 1994 he began study toward a Doctor of Philosophy degree at the University of Tennessee, Knoxville and accepted a teaching assistantship in September of 1994. In December of 1995 he accepted a graduate research assistantship at the Solid State Division of the Oak Ridge National Laboratory. He expects to receive the Doctor of Philosophy degree with a major in Physics in August of 1999.

Kyu Jeong Song is a member of Sigma Pi Sigma Physics Honor Society and also a member of the American Physical Society with membership in the Division of Condensed Matter Physics. He is an author or coauthor of 20 journal papers and 30 presentations on superconductivity for various high-T_c and intermetallic superconductors and point defects and impurity effects for ferroelectric materials, etc.